EFFECTS OF THE FLUID RHEOLOGY AND SURFACE TEXTURE ON THE FOOTPRINT OF PASSIVE DROPLETS

by

Gulraiz Ahmed

Submitted in accordance with the requirements for the the degree of

Doctor of Philosophy

The University of Canterbury

Mechanical Engineering Department

May 1, 2014

Abstract

Bloodstain pattern analysis has been used in criminal investigations for more than 100 years. It provides valuable information about the events that took place prior to the formation of bloodstains at a crime scene. Forensic scientists use empirical laws to make a deduction from bloodstains, but the validity of these conclusions has been challenged in courts due to a lack of understanding of the underlying fluid mechanics. With this motivation, this thesis illustrates how mathematical modeling and numerical simulation can help gain insight into the spreading of blood droplets which eventually leads to the formation of a bloodstain.

Understanding the fluid mechanics of droplet spreading and sliding has been accomplished with the help of the lubrication approximation which simplifies the Navier-Stokes equations to a more tractable form, i.e. a coupled set of non-linear partial differential equations. The resulting highly non-linear coupled set of equations is discretized using Finite-Difference. The resulting algebraic system is solved via an efficient Multigrid algorithm. These equations are modified to understand the effects of contact angle hysteresis, fluid rheology and absorptive properties of substrates on sliding dynamics.

Variations in the inclination of the substrate cause the droplets to attain different advancing and receding contact angles as they slide down the incline under gravitational pull. This work explores a new way to introduce contact angle hysteresis in the numerical simulation to predict the different phases of a sliding droplet. Experiments of fluid droplet spreading/sliding on inclined surfaces have been performed to measure the terminal sliding velocity. A simplified hysteresis model has been proposed. This model automatically locates the section of the contact line which is advancing and the section which is receding which enables the application of the contact angles for the advancing and receding fronts and therefore takes into account contact angle hysteresis. A simplified analytical model is also suggested for droplets moving down the incline with near circular footprints. With the inclusion of the contact angle hysteresis, simulation results were brought in closer agreement with the experimental ones and the results from both were compared with the results from the analytical model.

Blood is a shear-thinning fluid. One of the main objectives of this study is to investigate numerically the effect on the spreading and/or sliding of non-Newtonian fluid droplets on

surfaces. To achieve this, the effect of rheology on the leveling of thin fluid films on horizontal solid substrates is first investigated as a preliminary investigation since this problem does not involve a contact line and is therefore more tractable. A mathematical model based on the lubrication approximation which defines non-Newtonian rheology using a power-law model is presented. Results for the leveling of sinusoidal perturbations of the fluid film highlight important differences between the leveling of shear-thinning and shear-thickening fluids. Namely, the onset of leveling occurs earlier for the shear-thinning fluid than for the shear-thickening one. However, the rate of leveling is higher for the shear-thickening fluid than the shear-thinning one. An important aspect of this part of the work is the verification of the numerical implementation using the Method of Manufactured Solutions (MMS). This leveling study also highlights differences between the leveling of two-dimensional and three-dimensional perturbations.

This verified numerical formulation is then used to study the effects of rheology on the spreading/sliding of droplets. Results for the spreading of fully wetting droplets on a horizontal substrate show that, for all other quantities being equal, an increase of the flow index leads to a more rapid wetting. It also shows that, even for non-Newtonian fluids, the droplet velocity asymptotes to a constant value when sliding down an inclined substrate. This terminal velocity is strongly dependent on the rheological parameters and as it is reached, the droplets travel with a visibly constant profile. Finally, the numerical simulations revealed the formation of a tail at the rear of the droplet as it slides down the incline plane in the case of shear-thickening fluids.

Finally, a more complex dynamics of fluid being absorbed in a porous substrate as it slides/spreads is considered. A mathematical model based on the lubrication approximation which defines the absorptive property of a substrate using a Darcy's model is presented. This numerical model is verified with the help of comparison between the analytical and numerical solutions for the absorption of thin film on horizontal porous substrates. Results show that physical properties of the substrates, i.e. permeability, porosity, capillary pressure and equilibrium contact angle affect the rate of absorption of the fluid. Adding inclination to the problem, introduces the gravitational pull in the absorption dynamics. This directly shows its effects on the footprints formed inside the porous substrates.

The following papers, based on sections of this thesis, have appeared or been accepted for publication:

- Ahmed, G., Sellier, M., Lee, Y., Jermy, M., and Taylor, M. (2013). Modeling the spreading and sliding of power-law droplets. Colloids and Surfaces A: Physicochemical and Engineering Aspects, 432:2–7.

- Ahmed, G., Sellier, M., Lee, Y., Jermy, M., and Taylor, M. (2014). Rheological effects on the leveling dynamics of thin fluid films. Accepted for publication in the International Journal of Numerical Methods for Heat and Fluid Flow.

- Ahmed, G., Sellier, M., Jermy, M., and Taylor, M. (2014). Modelling the effects of contact angle hysteresis on sliding of droplets on inclined surfaces. Submitted for peer review in The European Journal of Mechanics - B/Fluids.

Dedicated to my family for all their love and support throughout my life...

Acknowledgments

I thank ALLAH Almighty for the strength, and health to accomplish this degree. It is ALLAH who has always kept me going in hard times.

I would like to thank and express my deepest appreciation to my supervisor Dr. Mathieu Sellier (UoC) for giving me the opportunity to work on this project. It is his excellent guidance, feedback and support that has made all this possible.

Many thanks to my associate supervisors Dr. Mark Jermy (UoC), Dr. Michael Taylor (ESR), and Dr. Yeaw Chu Lee (Herriot Watt University, UK) for their feedback and their support.

I would also like to thank my family, who never stopped encouraging and have always helped to keep my hopes high. They have lost a lot due to my research abroad. Without their understanding this work would not have been possible.

Lastly, I would like to acknowledge the patience, company, and support of my wife, Dr. Urooj Sania Paracha. She gave up her career to accompany me in New Zealand and she always encouraged me especially when I was really frustrated.

I would like to express my gratitude to all the authors, and researchers whose work has enabled me accomplish this task. A special note of thanks to all those who helped me personally with their expertise. I could be forgetting some vital contributors, but I appreciate the efforts of those who have lent a helping hand to me in the project.

Contents

List of Figures

List of Tables

Nomenclature

a	.....	Bloodstain major-axis
b	.....	Bloodstain minor-axis
Bo	.....	Bond number
Ca	.....	Capillary number
d	.....	Droplet diameter
F_{cl}	.....	Capillary force in the vicinity of contact line
F_r	.....	Viscous resistive force
h	.....	Droplet height
h^*	.....	Precursor film thickness
H_0, H_i	.....	Droplet/film thickness
h_p	.....	Penetration depth in porous medium
K	.....	Permeability
L_0	.....	Characteristic length of the substrate
m	.....	Droplet mass
n	.....	Flow behavior index power-law fluid
n_c	.....	Flow behavior index carreau fluid
n_d, m_d	.....	Exponents in the disjoining pressure term

n_t ..... Number of time steps

p ..... Liquid pressure

P_0 ..... Characteristic pressure scale

Pm ..... Permeability number

R_0, R_i ..... Droplet radius

R_c ..... Droplet contact radius

Re ..... Reynolds number

Su ..... Suction Number

t ..... Time

T_0 ..... Characteristic time scale

u', v', w', u, v, w ..... Velocity components

U'_d ..... Droplet sliding velocity

V_0 ..... Droplet volume

x', y', z', x, y, z ..... Cartesian coordinates

x, y, z ..... Cartesian coordinates

$x_{centroid}$ ..... Position of centroid of the sliding droplet

x_{cg} ..... Position of center of gravity of the sliding droplet

Abbreviations

ADI ..... Alternating Direction Implicit

BPA ..... Blood Pattern Analysis

CDA ..... Constant Drawing Area

CFD ..... Computational Fluid Dynamics

DDA ..... Decreasing Drawing Area

FAS ..... Full Approximation Storage

MG ..... Multigrid

ODE ..... Ordinary Differential Equation

RBC's ..... Red Blood Cells

WBC's ..... White Blood Cells

Greek Symbols

α ..... Angular position

Δt ..... Time-step size

ϵ ..... Aspect ratio of the droplet

ϵ_c ..... Cut-off length

λ_s ..... Slipping length for the slipping model

μ ..... Fluid viscosity

ϕ ..... Porosity

$\Pi(h)$ ..... Disjoining pressure term

ρ ..... Fluid density

σ ..... Fluid surface tension

θ_a ..... Advancing contact angle

θ_c ..... Contact angle droplet makes around the contact line

θ_e ..... Equilibrium contact angle

θ_i ..... Substrate inclination angle with the horizontal

θ_r ..... Receding contact angle

θ_{hys} ..... Contact angle hysteresis

θ_{impact} ..... Impact angle

A convention used throughout the thesis is that, unless otherwise stated, quantities with " $'$ " sign are dimensional and lower case quantities are dimensionless. Variables with multiple definitions are clearly distinguished in the text by the context in which they are used.

Chapter 1

Introduction to bloodstain pattern analysis

Contents

1.1 Bloodstain pattern analysis (BPA)

Bloodstain Pattern Analysis (BPA) is the science of interpreting bloodstain patterns at a crime scene. The formation of a bloodstain pattern is based on the principles of biology and physics. BPA is often used in court to provide evidence to prove the guilt or innocence of a suspect. The complex interplay between viscosity, surface tension, and other physical properties of blood influences the flight characteristics of blood droplets generated at the crime scene. The resulting bloodstains on a substrate are influenced by both physical properties of the blood as well as the substrate characteristics (James et al., 2005).

In a crime scene reconstruction, BPA can help investigators with useful investigative information on the area of origin of the spatter. The area of origin is the three-dimensional location from which the spatter originated. Bloodstains give valuable information about the directionality and the impact angle of blood droplets, but at a crime scene multiple bloodstains are present often in a regular or repetitive arrangement, depending on the manner in which they were deposited.

Bloodstain patterns are not straightforward. They depend largely on the event that generated the stains. In this passage, a few stain types are discussed to give an idea of the vast range of information stored in the shape of the stains. Blood droplet formation is not always straightforward and is often accompanied by small droplets which are produced as a by-product. These accompanying droplets might alter a valuable stain. Bloodstains can develop from droplets which travel in the same direction as the impact force (forward spatter pattern) or in the opposite direction (back spatter pattern). Classifying precisely the stain origin from forward or back spatter can be critical for an investigation. Sometimes air bubbles get trapped in blood droplets causing the formation of a bubble ring in the bloodstain. Smaller stains which come into existence during formation of the parent stain immediately after the blood droplet impact the substrate (known as satellite stains). Drip stains, trails and patterns originate from blood dripping from a wound or from the weapon involved in the crime. Stains which are transferred from one surface to another resulting from a contact are known as transfer stains. Thus a wide variety of stains are expected to be present at crime scenes (Attinger et al., 2013; Shaler, 2011).

Figure 1.1 shows a circular blood droplet having diameter, d, impacting a vertical substrate at an angle of impact, θ_{impact}. The trajectory assumed is linear. The resultant bloodstain on the substrate is elliptical in shape having a as major-axis and b as minor-axis, where b is usually greater than d, but in the sine rule these are assumed to be equivalent. By measuring the major and minor-axis of the bloodstain, the fraction (d/a) can be calculated. Evaluating the arcsine $(\sin^{-1})$ of the fraction gives θ_{impact} (Pizzola et al., 1986).

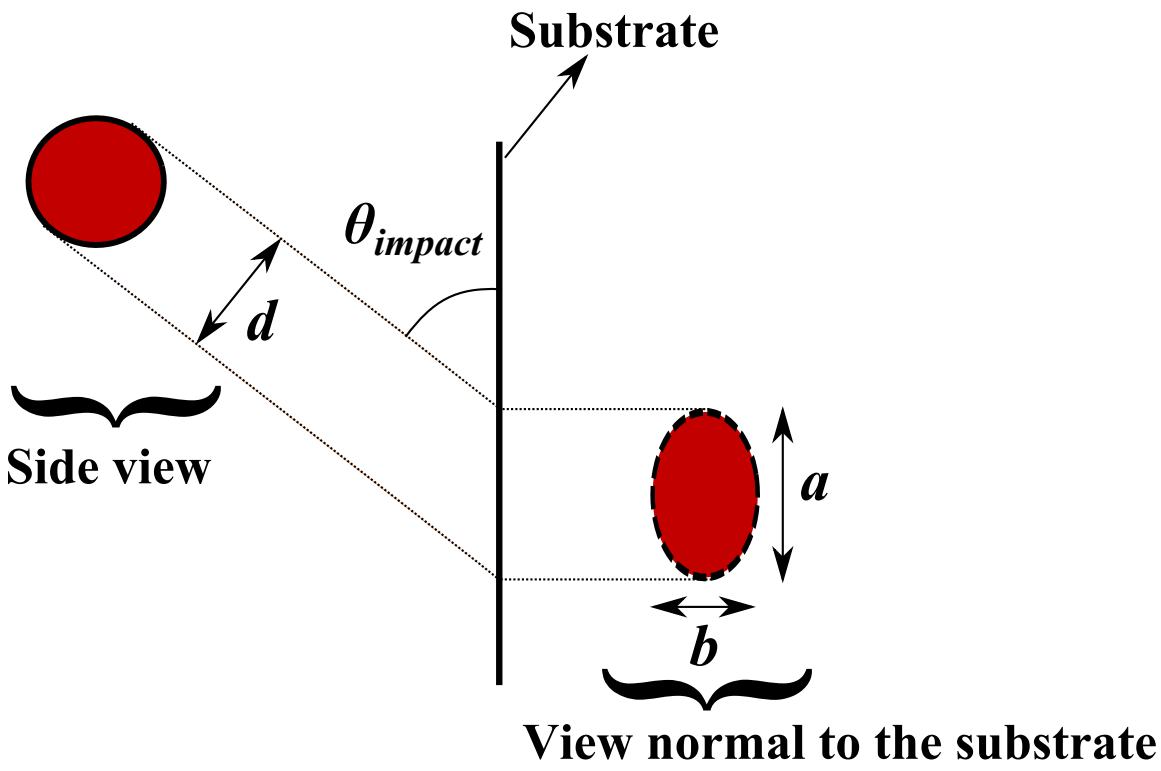

Figure 1.1: Sine rule

A considerable amount of error is introduced in determining the impact angle through measurement error and error in picking the pertinent bloodstain. The bloodstains which are more elongated tend to carry less error. The bloodstains that are more circular have a greater error (Shaler, 2011). The sine rule can reliably measure the impact angle in the range $20^{o} < \theta_{impact} < 40^{o}$. If $\theta_{impact} < 20^{o}$, it can be difficult to measure the major-axis due to splash. If $\theta_{impact} > 40^{o}$, the major-axis of the elliptic bloodstain cannot be measured accurately, because the minor-axis becomes large, but stays less than major-axis. On top of this substrate, characteristics such as absorption and roughness induce errors of up to 20% (Shaler, 2011; Dutelle, 2010). The sine rule is quite simple, but has some limitations in its applicability. It is an empirical relationship which has a geometric basis, but has no estab-

lished connection to fluid mechanics. Impact angle calculated with the help of the "sine rule" is just a first estimate, because the projectile approach of the blood droplet is completely ignored (Bevel and Gardner, 2008).

Blood droplet impact is of prime importance as it determines the type of stain generated at a crime scene. A recent review describes the blood droplet impact from BPA perspective (Adam, 2012). Early BPA researchers considered shape of blood spatters to be associated with the velocity of impact (James et al., 2005). The reason for this interpretation was solely the inverse correlation between the stain sizes and the magnitude of impact velocity. Later, this categorization was reconsidered after discovering stain overlapping between the medium and high velocity impacts. Different droplet volumes and impact velocities can produce similar stains. The contact surface plays a vital role in the formation of the stains. At a crime scene, there are a wide range of surfaces and surface properties can also vary over short distances, e.g. roughness, dust particles, prewetted, porosity, etc. It is difficult for the investigators to accurately describe the flight path of the droplet and to have a detailed knowledge of all the variables involved.

BPA frequently involves the interpretation of blood droplets that have impacted different surfaces: hard or soft, smooth or rough, porous or non-porous. The resultant stain shape depends upon density, viscosity, impact velocity, non-Newtonian effects, surface tension, roughness and wettability of the substrate, non-isothermal effects (e.g., solidification and evaporation), and trapped air. Surface roughness causes the blood droplet to rupture sooner than on a smooth substrate (Bevel and Gardner, 2008). MacDonell suggests in his publications that the substrate roughness can increase spatter, i.e. it promotes splashing (MacDonell and Bialousz, 1971; MacDonell, 2005).

Over time, blood spatter dries. How quickly this happens depends on the surface where the blood landed, how much blood is contained in the spatter, and the heat and humidity present at the crime scene. The outer edge dries first. A really dry bloodstain can skeletonize, flaking off and leaving a ring around the original diameter of the spatter. An analyst can sometimes help to pinpoint when the crime occurred based on the dryness of the blood (Dutelle, 2010). The drying of a droplet of human blood exhibits coupled physical

mechanisms, such as Marangoni flow, evaporation and wettability (Brutin et al., 2010). In forensics, the bloodstains that are observed are dried due to evaporation and form crack patterns depending upon health conditions as well as the age group of the victim. Bremmer et al. recently reviewed the physical processes involved in the ageing of bloodstains and the techniques which are present to determine precisely the age of bloodstains (Bremmer et al., 2012). An understanding of the drying process helps the investigators in reconstructing the events and to determine the time elapsed after the crime.

A careful examination of blood-stained clothing can potentially provide information regarding the movements and activities of the wearer during a bloodshedding event. Examination of blood stained clothing is a common request of the bloodstain pattern analyst. Given its potential to provide information about the movements and activities of the wearer, bloodstain pattern analysis may confirm or refute explanations for the presence of blood on his or her clothing. Differentiation between contact and droplet stains on fabric is crucial in crime scene reconstruction. Karger and co-workers, compared three types of fabrics and distinguished between projected and contact bloodstains (Karger et al., 1998). Slemko, observed the effect of variation of droplet impact velocity on different types of fabrics (Slemko, 2003). As with any other bloodstain, the target surface must be considered prior to evaluating the stain. Research has been published indicating that both texture and composition of a fabric will affect the resulting shape of a bloodstain (Holbrook, 2010).

BPA specialists are interested in the resulting stain. They believe that as BPA is challenged through legal tests and legal counsel, understanding of all the dynamics of blood droplets is very important to fill the gap in research in this area (MacDonell, 2005; Bevel and Gardner, 2008; Shaler, 2011). "The field has been challenged in and out of court based on a lack of research into blood droplet dynamics (Bevel and Gardner, 2008)."

1.2 Blood rheology

An extensive literature on blood rheology has been published to date which reflects its significance. Blood is a liquid connective tissue that is critical to human survival. Blood transports nutrients, oxygen, and removes waste to support the cells. It facilitates the regulation of

body temperature and combats infection. Blood consists of fluid plasma (55%) and cells (45%) (Elert, 1998). A major component of fluid plasma is water (92%) and the remaining (8%) consists of proteins, metabolites and ions (Elert, 1998). Blood cells (45% by volume) are composed of Erythrocytes (Red Blood Cells, RBCs), Leukocytes (White Blood Cells, WBCs) and Thrombocytes (platelets). In a cubic millimeter of blood there are typically five million RBCs, five to 10 thousand WBCs and two-three hundred thousand platelets (Elert, 1998). About 8-9% of the average person's body mass is blood or 4.5 to 5 litres (James et al., 2005).

Blood rheology depends upon several factors: temperature, blood cell concentration, blood cell aggregability, blood cell deformability, protein concentration, etc (Thiriet, 2008). The rheological behavior of blood is governed largely by Erythrocytes, due to their abundance and overall size. It can be rightly said that blood is approximately a concentrated RBC suspension in plasma. Erythrocyte count is quite variable in the human body and depend largely upon age, sex, build, and health of a person.

The behavior of blood outside the body and the arrangement of stains in different patterns depend upon fluid properties such as surface tension (Elert, 1998). The viscosity of a fluid is the resistance to deformation caused by applying external stress. Blood is about four times more viscous than water (James et al., 2005). The viscosity of blood is affected by the ratio of red blood cell volume to whole blood known as the Hematocrit Value, which varies from person to person and can also depend on medical conditions. The higher Hematocrit Value, the higher the viscosity (Raymond et al., 1996; Thiriet, 2008).

Understanding blood flow properties has been of prime interest. Earliest records suggest blood to be a Newtonian fluid (Young, 1809). (Denning et al., 1906) and (Fåhræus and Lindqvist, 1931) were able to confirm the apparent viscosity of blood was dependent on the diameter of the tube used to measure it. Later researchers confirmed that blood behaves as a non-Newtonian fluid (Zhang and Kuang, 2000; Drochon, 2003).

Blood starts to coagulate as soon as it flows out of the human body (Attinger et al., 2013). It behaves differently from Newtonian fluids. Viscosity varies with shear rate in non-Newtonian

fluids rather than remaining constant for Newtonian liquids. Blood's viscosity depends on the size of the blood vessel it is flowing through. This property allows the blood to flow easily through capillaries and arteries which have different cross-sectional diameters in various organs within the body.

The viscosity of blood varies with shear rate (Yeleswarapu, 1996). Blood exhibits higher viscosity at low shear rate due to RBC aggregation and a lower viscosity at high shear rate due to deformability of the RBCs (Chien et al., 1967; Stoiber et al., 2005; Baskurt and Meiselman, 2003). Viscoelasticity is a material property of fluid which exhibits both viscous and elastic behavior under deformation. In addition, to blood being shear thinning fluid it also behaves viscoelastically. In an unsteady flow the viscosity of blood is dependent upon frequency (Thurston, 1979). Other properties that affect viscoelastic behavior of blood are the plasma composition and the shear rate (Thurston and Henderson, 2006). Blood behaves as a viscoelastic fluid only slightly, its shear-thinning behavior is more significant (Merrill, 1969).

Many rheological models have been used to model blood rheology, but none of them is universally acceptable. Szeri has discussed in much detail the rheology of blood and rheological models that have been used in the past to model blood rheology (Szeri, 2010). These can be divided into phenomenological and micro-structural models . In phenomenological models, the relationship between the stress and strain is derived from the observed trends, without taking into account micro-structures, thus making it simple to be implemented using Computational Fluid Dynamics (CFD). On the other hand, micro-structural rheological models consider the properties and structure of the microscopic particles (Szeri, 2010).

Phenomenological rheological models are either empirical based or continuum based. Empirical based models are usually one-dimensional, derived from fitting a suitable mathematical function to the observed experimental data. Continuum based models are three-dimensional and obey continuum physics rules. Empirical based models include the following: different Power-law models, Section 1.3.3.1.1, Ellis model (derived from power-law), Section 1.3.3.1.2, Carreau model, Section 1.3.3.1.3, etc. Continuum based models are too complex to apply using CFD as they are based on the theory of structured continua and micro-polar fluids (Szeri, 2010).

1.3 Phenomena involved in bloodstain formation

The deformation of the droplet after impact and its spreading on the substrate are governed primarily by the inertia it has gained before impact, viscous forces between the fluid and the substrate, capillary forces, and surface forces present at the contact-line (Rein, 1993; Frohn and Roth, 2000). A droplet spreads until these forces are balanced and the three phase system liquid, solid and vapor comes into equilibrium. When allowed to spread on a substrate, a droplet spreads out to form a thin film on the substrate, depending upon the fluid wetting properties of the surface. The spreading of a droplet or a thin fluid film on a substrate is a phenomenon where physics, chemistry and engineering overlap. Spreading is a challenging phenomenon to understand and model since classical hydrodynamics is not able to completely describe the motion of the contact line. Details of contact line motion are discussed in Section 1.3.1.

Besides blood spatter, the spreading of a fluid occurs in nature as well as in different industrial processes. For example, natural phenomena include, rain droplets on the ground and in the human body spreading of a fluid occurs as tears form thin films (Oron et al., 1997). Industrial processes include spray coating paints on automobiles, spraying pesticides on plant leaves (Bonn et al., 2009), spray coating of paper in printing applications (Grant, 2001), coating of microchips and deposition of inks in printing applications (Sellier, 2003). Frequently, in industrial applications there are different layers of films that are deposited. These layers are dried and surface finished to leave a thin film over the substrate. The purpose of these layers may be for decoration, insulation or storage of data.

Homogeneity is vital in the spreading dynamics of a fluid. Substrates are not always homogeneous and may have topographical imperfections or unwanted particles e.g. dust particles present in the environment which directly influence the spreading of a fluid. These particles may have hydrophobic or hydrophilic properties causing the droplet to spread in a preferred direction. These may cause the formation and spread of micro-droplets (Chen et al., 2008), thus disrupting the spread dynamics altogether. Beside these particles, the surface may be affected by the surrounding atmosphere, i.e. humidity, which has an immediate impact on the wetting properties.

It is important to understand the influence of physical heterogeneities, at the microscopic (roughness) and macroscopic (topography) scale, and chemical heterogeneities on the spreading dynamics of the fluid droplets. The experimental data available on droplet spreading dynamics suggests that micro-scale characteristics of the substrate can greatly influence the spreading dynamics (Cazabat and Stuart, 1986). For example, an experimental study (Chung et al., 2008) on blood and water showed that surface ablation caused an increase in equilibrium contact angles. Savva and co-workers, suggested appropriate statistical methods to study the effect of spatial heterogeneities on spreading dynamics (Savva et al., 2010). Vellingiri and co-workers employed the slip model to investigate two-dimensional droplet spreading on chemically heterogeneous surfaces (Vellingiri et al., 2011). Slip model is one of the methods to resolve contact line singularity. Slip model is described in Section 1.3.2.2. Schwartz and Eley studied droplet spreading on a substrate made of two chemically different materials, incorporating the variation of substrate wettability (Schwartz and Eley, 1998). Thus, the authors were able to model droplet motion on chemically varying surfaces.

Spreading dynamics of the droplet is greatly influenced by other factors like thermocapillary motion and evaporation/drying of droplets. Temperature fluctuations greatly impact the spreading dynamics because in a liquid/vapor phase system the surface tension of the fluid and phase transition largely depends on the surrounding temperature. Surface tension has a strong dependence on the temperature fluctuations which directly affects the motion of phase interfaces also known as the thermocapillary fluid motion. This phenomenon for thin droplet spreading dynamics has been studied by (Ehrhard and Davis, 1991).

Drying of droplets or thin films on solid substrates can be observed frequently in every day life. To understand the dynamics of this phenomenon is a challenge in itself. Blood droplets deposited on a substrate consist of a non-volatile solute and volatile solvent. The spreading dynamics of the droplet is considerably influenced by the rate of evaporation of the volatile solvent (Okuzono et al., 2009). Evaporation of the solvent accounts for an increase in drop viscosity, eventually leaving behind a solid non-volatile solute. If the rate of evaporation of the solvent is high, the concentration of the solute near the surface increases quickly, resulting in a gel-like surface known as the skin (De Gennes, 2001). The final shape of the dried droplet

is dependent on the formation of skin in this case.

Alternatively, if the rate of evaporation of the solvent is low the final shape is influenced by internal flow in the liquid phase. At the start of evaporation, the solute stops and sticks to the substrate causing a halt to the motion of the contact line, also known as contact line pinning. This is usually observed in the drying of a coffee droplet where a brown ring is left. The reason behind the formation of this ring is the capillary flow caused by the slow evaporation of the solvent; this forces the solute to move towards the contact line interface creating ring-like pattern also known as the contact line deposit of evaporating droplets (Deegan et al., 1997, 2000). Drying in BPA is highly significant since the observed droplets are always dry.

Spreading dynamics of droplets is to a considerable extent dependent on the absorptive property of the substrate. A substrate may be permeable. Spreading of a droplet after impact is at a faster time scale in comparison to the fluid absorption. After the spreading has completed, the volume of the droplet lost to the permeable substrate occurs in a relatively slow time scale (Davis and Hocking, 1999). There are a number of authors who have studied the penetration of fluid in a porous substrate. Denesuk and co-workers, investigated penetration of small droplets into a porous substrate driven by the action of capillarity (Denesuk et al., 1993). This work was based on two dewetting properties of the absorbing droplets: "Constant Drawing Area" (CDA) in which the contact line was assumed to be fixed during the absorption process and secondly "Decreasing Drawing Area" (DDA) in which the contact angle was assumed to be fixed with the moving contact line (Alleborn and Raszillier, 2004a). Experimental investigations (Desie et al., 2002; Holman et al., 2002) have shown that after the droplet impingement stage, capillarity drives the spreading and absorption of the droplet. The shape of the droplet can be considered similar to a spherical cap.

1.3.1 Wettability

A sessile droplet on a solid substrate in ambient air involves the consideration of three phases, liquid, solid and vapor. The point where all the three phases come into contact with each other, in the case of a two-dimensional cross-sectional view of a droplet, is known as the contact point. A collection of these contact points around a droplet forms the contact line. The

presence of three phases at the contact line points to the presence of three surface tensions, at the solid-vapor interface, at the solid-liquid interface, and at the liquid-vapor interface, which collectively govern the shape of the droplet on the solid substrate. The contact angle is defined as the angle between the liquid-vapor and solid-liquid interfaces. Factors affecting the contact angle include surface cleanliness and roughness, temperature, humidity, porosity, etc.

Young's equation (Young, 1805) addresses the relationship between the equilibrium contact angle, θ_e and the three surface tensions present at the contact line,

$$\sigma_{SV} = \sigma_{SL} + \sigma_{LV} \cos\theta_e \quad \rightarrow \quad \cos\theta_e = \frac{\sigma_{SV} - \sigma_{SL}}{\sigma_{LV}}, \tag{1.1}$$

where σ_{SV}, σ_{SL} and σ_{LV} denotes the solid-vapor, solid-liquid and liquid-vapor surface tensions.

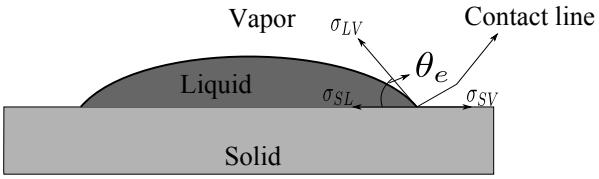

Figure 1.2: Demonstration of the equilibrium contact angle of a sessile droplet on a solid substrate (Bonn et al., 2009)

When a droplet is placed on a flat solid substrate, in general it will be far from an equilibrium state hence it starts to spread until the equilibrium contact angle, θ_e, is reached, see Figure 1.2. Equilibrium contact angle is not a universal entity for a specific liquid/solid/vapor phase system. For example, consider rain droplets on a glass window. The water droplets of different volumes and different shapes remain stuck on the surface demonstrating that, although at an equilibrium state, a liquid/solid/vapor system can have different equilibrium contact angles. Larger angles are at the bottom (advancing contact angle, θ_a) and smaller angles are towards the top (receding contact angle, θ_r) due to gravitational pull. θ_a is always greater than θ_r. The degree of difference between the two on a specific substrate is greatly influenced by the droplet sliding velocity. The difference between advancing and receding contact angles is known as contact angle hysteresis, θ_{hys}. Contact angle hysteresis is discussed in detail in Chapter 4.

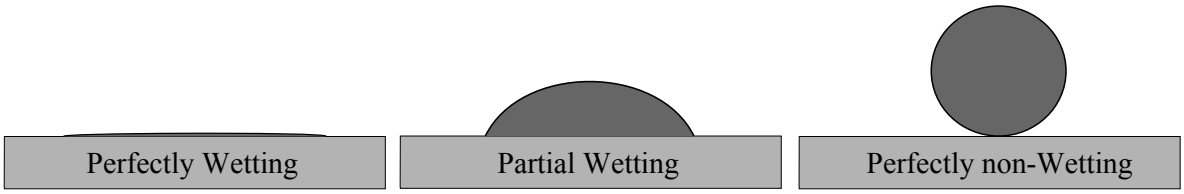

Figure 1.3: Different wetting states (Bonn et al., 2009)

Wetting is the property of the liquid to spread out and to remain in contact with the solid substrate. Different wetting states are shown in the Figure 1.3. For perfect/complete wetting surface $\theta_e = 0^o$, a droplet spreads almost indefinitely. Highly wettable surfaces have an equilibrium contact angle in the range of $0^o < \theta_e < 90^o$. Low wettability is characterized by an equilibrium contact angle in the range of $90^o < \theta_e < 180^o$. A perfectly non-wetting surface has $\theta_e = 180^o$. The spread factor or wettability, S, is defined as the degree of wetting,

$$S = \sigma_{SV} - (\sigma_{SL} + \sigma_{LV}) \tag{1.2}$$

S is the energy difference between the wet and dry substrate. When $S \geq 0$, signifying total wettability, the droplet spreads on the surface to form a thin film, $\theta_e = 0^o$. When $S \leq 0$, signifying partial wettability, the droplet spreads to an extent and after that comes into equilibrium at a finite value of θ_e.

1.3.2 Contact line singularity in fluid mechanics

Contact line motion has a complex dynamics which is still poorly understood. Consider a moving droplet on a surface. Due to friction the velocity at the contact interface should be zero (no-slip condition), but the droplet is in motion which gives birth to a singularity. Various methods are present to circumvent the singularity at the contact line. Computational performance depends strongly on the chosen method.

1.3.2.1 Coupled Van der Waals interface model and fluid mechanics equations

It is possible to resolve this singularity by coupling the Van der Waals interface model with the fluid mechanics equations (Seppecher, 1996). This model avoids singularity if the interface between the liquid/vapor phases is not sharp and combines easily with Laplace-Young equilibrium theory at zero velocity (Pomeau, 2002). Contact line motion can be modelled with this coupled Van der Waals-Stokes system in the evaporation/condensation phenomenon,

because in this phenomenon the interface is displaced without the motion of the fluid. Evaporation/condensation requires a thermodynamic force to measure the extent of the system being out of equilibrium. The velocity, u', of the contact line is defined as,

$$u' = kF(\theta, \theta_e) \tag{1.3}$$

where F is a dimensionless function which depends on equilibrium contact angle and the actual value of the contact angle and k is the mobility factor having the dimensions of velocity and of the order of molecular speed.

1.3.2.2 Introduction of slip

Another way of resolving the singularity is to introduce a small amount of slip between the fluid and substrate instead of considering the no-slip boundary condition at the substrate, see Figure 1.4. This means that at $z' = 0$, the velocity does not vanish and is defined as,

$$u' = \lambda_s \frac{\partial u'}{\partial z'} \tag{1.4}$$

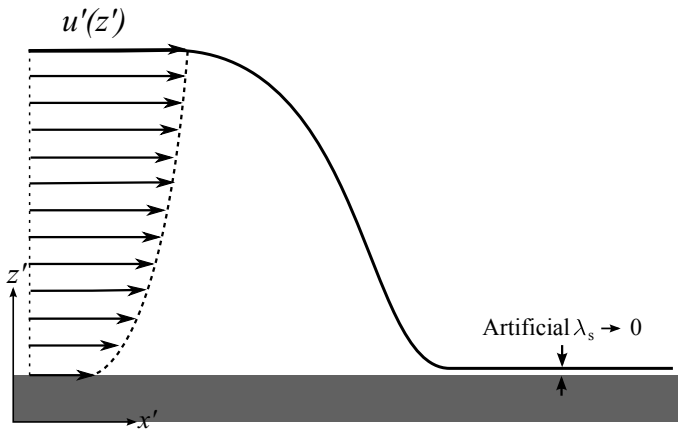

Figure 1.4: Slipping model (Diez et al., 2001)

where, u' is the velocity component parallel to the substrate, z' is the normal direction to the plane, and λ_s is the slipping length. λ_s is small so that the slip is minute away from the contact line region. In the contact line region, slip is high due to $\frac{\partial u'}{\partial z'}$ being large (Oron et al., 1997; Diez et al., 2001).

1.3.2.3 Introduction of a thin precursor film

This method assumes the presence of a thin precursor film ahead of the moving contact line. This means that the droplet slides on this thin film, see Figure 1.5. Considering this method gives birth to additional forces, i.e. Van der Waals forces which have to be taken into account for computations. A disjoining pressure term is introduced which exactly balances other driving forces when the static/equilibrium contact angle is reached. Details on precursor film and disjoining pressure are discussed later. A shortcoming for this approach is that the choice of the precursor film thickness, h'^*, is arbitrary and the spreading dynamics depends on it. Spaid and Homsy, showed that the approximation for the free surface is independent of the choice of model used to avoid contact line singularity (Spaid and Homsy, 1996). Both models produce comparable results if the slip length, λ_s, and precursor film thickness, h'^*, are numerically equivalent. The advantage of the disjoining pressure approach is that larger time steps can be used without compromising the results (Diez et al., 2001), hence the computational time may be reduced. In the present work, computational time motivates the selection of the thin precursor film model.

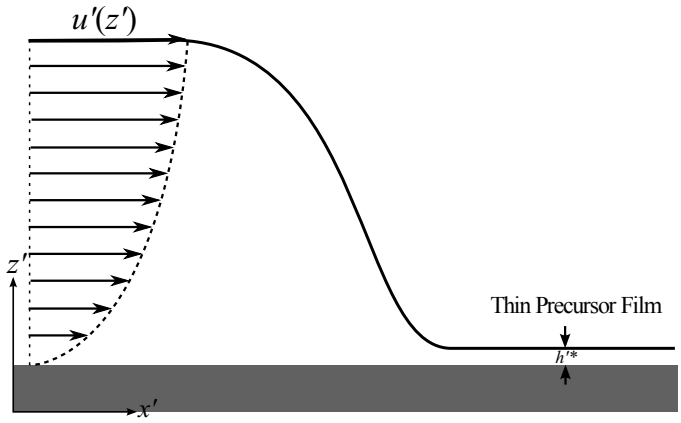

Figure 1.5: Thin precursor film model (Diez et al., 2001)

1.3.3 Fluid rheology

Newtonian fluids are fluids that exhibit a directly proportional relationship between the stress, τ, and strain rate, $\dot{\gamma}$, i.e.,

$$\tau = \mu\dot{\gamma} \tag{1.5}$$

where the viscosity, μ, is independent of the strain rate, $\dot{\gamma}$, but it can be affected by physical properties i.e. temperature and pressure. The stress versus strain rate graph for a New-

tonian fluid is a straight line through the origin (Chhabra and Richardson, 1999; Skelland, 1967). Fluids which do not exhibit the linearity between stress and strain rate are known as non-Newtonian fluids. Non-Newtonian fluids exhibit strain and time dependence of viscosity, yield-stress, and stress relaxation. The behavior of non-Newtonian fluids can be broadly divided into three categories: time-independent, viscoelastic and time-dependent (Skelland, 1967; Chhabra and Richardson, 1999).

Time-independent fluids are defined as those fluids in which the strain rate at a particular point is entirely dependent upon the instantaneous stress at that specific point. Viscoelastic fluids are those which upon removal of deforming stress have partial elastic recovery. These fluids possess the material properties of both viscous fluids and elastic solids, (Sochi, 2010). Time-dependent fluids are those for which the strain rate depends upon both the magnitude and the duration of stress and possibly of the time duration between consecutive applications of stress (Sochi, 2010). Fluids which exhibit a combination of the above mentioned classifications are known as complex fluids. Figure 1.6 shows the behavior of time-independent fluids on variation of strain rate and stress.

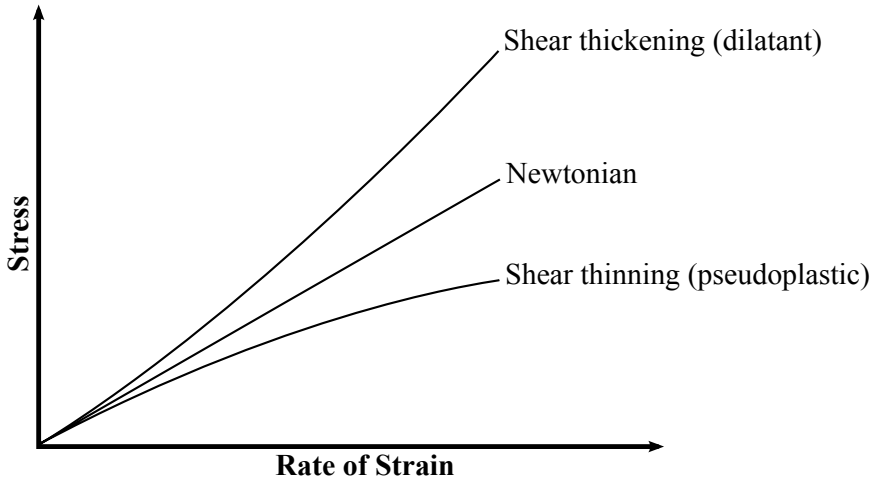

Figure 1.6: Stress against strain rate for time-independent fluids (Sochi, 2010)

1.3.3.1 Time-independent fluids

When non-Newtonian fluids undergo a shear flow, they behave as a Newtonian fluid at low shear rates. This Newtonian behavior disappears as the shear rate is increased. If the viscosity increases with increasing shear rate the fluid is a shear-thickening or dilatant fluid and if the viscosity decreases with increasing shear rate, the fluid is described as shear-thinning or

pseudo-plastic fluid. At a higher shear rate, this shear dependent behavior reaches a constant value of viscosity. Three fluid models of the time-independent category are described: Power-law, Ellis and Carreau.

1.3.3.1.1 Power-law model The power-law model, also known as the Ostwald de Waele model, is one of the simplest models having only two variables,

$$\mu = K\dot{\gamma}^{\frac{(n-1)}{2}} \tag{1.6}$$

where, μ is the viscosity, K is the consistency factor, $\dot{\gamma}$ is the strain rate and n is the flow behavior index. If $n < 1$, the fluid is shear-thinning or pseudo-plastic, see Figure 1.7. If $n > 1$, the fluid is shear-thickening or dilatant. For $n = 1$, the fluid behavior is Newtonian. This model is more often used to model shear-thinning behavior, but it can also be used to model the shear-thickening behavior. The major drawback of this model is its inability to model the Newtonian regimes at very low and very high shear rates.

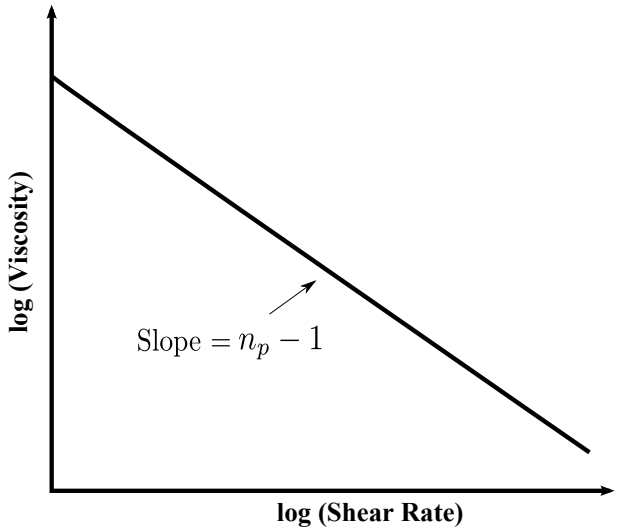

Figure 1.7: Viscosity against shear rate for a power-law fluid on logarithmic scales (Sochi, 2010)

1.3.3.1.2 Ellis model The Ellis model is a three variable model. It is usually described by a relationship in terms of the shear stress,

$$\mu = \frac{\mu_0}{1 + \left(\frac{\tau}{\tau_{1/2}}\right)^{\alpha_e - 1}} \tag{1.7}$$

where, μ is the viscosity, μ_0 is the low shear viscosity, τ is the shear stress, $\tau_{1/2}$ is the shear

stress at which the viscosity $\mu = \mu_0/2$, and α_e is an indicial parameter related to power-law index by $\alpha_e = 1/n$. The edge that the Ellis model has over the power-law model is its ability to model the Newtonian regime at very low shear rates, see Figure 1.8.

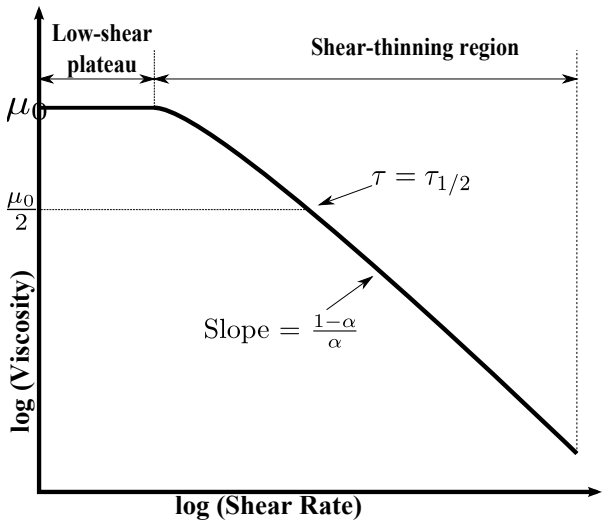

Figure 1.8: Viscosity against shear rate for an Ellis fluid on logarithmic scales (Sochi, 2010)

1.3.3.1.3 Carreau model The Carreau model is a four variable model. It describes the viscosity of the fluid as,

$$\mu = \mu_\infty + \frac{\mu_0 - \mu_\infty}{\left[1 + (\dot{\gamma} t_c)^2\right]^{\frac{n_c - 1}{2}}} \tag{1.8}$$

where, μ is the viscosity, μ_∞ is the viscosity at infinite shear rate, μ_0 is the viscosity at zero shear rate, t_c is the characteristic time, $\dot{\gamma}$ is shear rate and n_c describes the behavior of the flow. $n_c < 1$, corresponds to shear-thinning, see Figure 1.9. The main advantage of this model over others is the ability to model Newtonian behavior at very low and high shear rates.

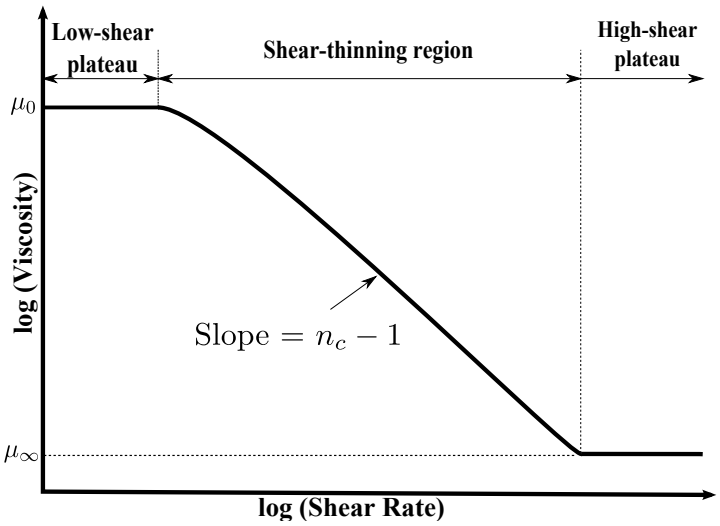

Figure 1.9: Viscosity against shear rate for a Carreau fluid on logarithmic scales (Sochi, 2010)

1.4 Aims and scope of the thesis

Forensic scientists have extensively relied upon experience and empirical knowledge in the past. Controversies in recent court cases have motivated an increased emphasis on the underlying physics involved in forensic science in general and BPA in particular. This work is a first step towards understanding the role of fluid mechanics in bloodstain formation. The generation of bloodstain is a very complex fluid mechanics problem involving a complex fluid (blood), a free interface between the blood and the air, and a wetting front. These are, in themselves, complex challenges to overcome in the broad field of fluid mechanics.

The impetus for the current research has come from the successful collaborative research to date between Environmental Science and Research (ESR) and the Mechanical Engineering Department at the University of Canterbury (UoC). Blood droplet impact was investigated recently (Sellier et al., 2010). The focus was on the use of Computational Fluid Dynamics (CFD) to solve the problem of the dynamics of blood droplets impacting on flat solid surfaces. Two aspects emerged from this project: firstly there was a need to dedicate significantly longer research time to the calculations required to fully elucidate the droplet collapse problem and secondly the potential for CFD to contribute to other bloodstain pattern analysis problems. A conclusion from the literature review was that a holistic model which describes the entire dynamics of blood during a crime scene is beyond the scope of present work. In this

research work, my contribution is to understand the spreading phase after the droplet has impacted on the surface and the influence of contact angle hysteresis, rheology, and substrate absorption on the spreading.

The mathematical explanation of the spreading is not straightforward, due to the fact that the contact interface is a free surface and the configuration for this free surface needs to be determined as a part of the solution to the governing equations. This makes the problem more difficult, because of the presence of too many variables. One method of solving the complexity of the problem is by analyzing long-scale phenomenon, which assumes that the variations along the fluid flow are much more gradual than the variations normal to the flow. The spreading phase essentially occurs at a time scale much slower than the impact phase. Based on this observation, lubrication approximation theory is a good approximation for the flow of thin viscous films. The lubrication approximation considerably reduces the complexity of the governing equations, forming a single non-linear partial differential equation in terms of film thickness. Another fluid parameter such as velocity is deduced from the solution of this single equation thus removing the complexity due to free boundary. The lubrication approximation, discussed in detail in Section 1.5 and Chapter 2, frames the fluid dynamics model of the spreading droplet.

1.5 Methodology

Due to the vast number of applications, over the years an intensive investigation has taken place to give a good insight into the behavior of the spreading of slow moving thin film flows or droplets. The numerical investigation of droplet flows is at a relatively early stage, because the computational requirements to solve the relevant system of Navier-Stokes equations to an acceptable level of accuracy in three-dimensions are huge. As a result, numerical investigations to date have applied legitimate assumptions to simplify the equations and make them computationally manageable.

When considering the problem of blood spreading after impacting the substrate, there are two assumptions that will be used: one is that the ratio of the typical blood droplet thickness to the characteristic radius of the droplet is small and the other is that inertia is negligi-

ble. These assumptions form the foundation of lubrication approximation (Oron et al., 1997; Bonn et al., 2009). The application of this assumption to the Navier-Stokes equations and analysis of the leading order terms can describe the evolution of the film by a coupled set of second order partial differential equations in terms of the film thickness and pressure across the film, or correspondingly by a single fourth order partial differential equation in terms of the film thickness alone (Myers, 1998). The backbone of the lubrication approximation was established by (Reynolds, 1886). He calculated the pressure in lubricated slipper bearings using the hydrodynamics of slow viscous flow.

The lubrication approximation, also known as the long-wave approximation, reduces significantly the difficulty of the free surface problem. In the Navier-Stokes equations, the pressure and velocity in a three-dimensional fluid domain are unknown variables whereas in the lubrication approximation the unknown variables are the film thickness and depth-averaged pressure depending on the substrate location only. For blood droplet spreading applications, this approximation is convenient because the overall height of the spreading droplet is small and the shape of the final footprint is usually the key factor to assess the flight path and origin of the droplet.

Although the lubrication approximation equations are much more tractable than the Navier-Stokes equations, they are still considerably difficult to solve either analytically or numerically. Lubrication equations are highly non-linear and can only be linearized for a few specific cases. In addition, the coefficient of the highest derivative of these equations tends to zero as the film thickness approaches zero (Myers, 1998). This issue is a matter of concern when a dynamic contact line is present since the film thickness is reduced to zero as the contact line is reached; this is also known as the contact line singularity, discussed in detail before, Section 1.3.2. Consequently, the lubrication approximation is able to model the dynamics of the free surface but is not able to relieve the contact line singularity.

The lubrication approximation has been employed to successfully model a range of droplet flows (Brien, 2002; Schwartz, 1998; Schwartz and Eley, 1998; Lee et al., 2011) and a variety of numerical techniques have been suggested to solve the underlying equations. The challenges involved in experimentation, theoretical knowledge, and computational restric-

tions have resulted in far less attention to numerically solving fully three-dimensional droplet flows. Several authors have used a time-splitting technique (Weidner et al., 1996; Schwartz, 1998; Schwartz and Eley, 1998; Eres et al., 1999). The most popular way of solving the 4^{th} order partial differential lubrication approximation equation is the use of a semi-implicit time splitting technique (Christov et al., 1997) with the use of an Alternating-Direction Implicit (ADI) technique (Schwartz and Eley, 1998). The motivation behind the use of this approach is to utilize the stability aspects of implicit techniques and the cost efficiency of the explicit techniques. Daniels and co-workers used the same approach on the flow of droplet down an inclined substrate using fully implicit multigrid lubrication flow solver (Daniels et al., 2001). The authors showed an improvement in the rate of convergence and the requirement of lower mesh refinements for an acceptable accuracy with the help of a multigrid technique. Gaskell and co-researchers made use of these to apply it to problems involving droplets spreading on surfaces having topographical and chemical heterogeneities by integrating multigrid technique with adaptive time-stepping (Sellier, 2003; Gaskell et al., 2004).

FILMPAR (Lee et al., 2009), a portable parallel multigrid thin film flow solver was developed, having an improved rate of convergence compared to ADI schemes (Christov et al., 1997), with automatic error-controlled automatic adaptive time-stepping (Sellier, 2003; Gaskell et al., 2004) and having adaptive mesh refinement (Lee et al., 2007). FILMPAR can be modified for the investigation of droplet spreading on chemical and topographical heterogeneous substrates (Lee et al., 2011). It efficiently solves the fluid dynamics of the problem by providing access to discretization technique, mesh refinement and time adaptivity. This flow solver forms the basis of this research and it is modified according to the specific requirements.

This research explores the effects of rheology, contact line hysteresis, and substrate permeability on the footprint of the fluid droplet. The lubrication approximation will form the basis of the mathematical model. Lubrication approximation will be expanded to account for the phenomena mentioned. Experiments have been performed to explore the effects of contact angle hysteresis and to compare the experimental results with the numerical results. Experimental studies have included the physical testing, i.e. major to minor axis expansion of the spreading droplet, speed of the spreading droplet and its dependence on inclination and factors affecting the final footprint as a function of time.

This research is valuable in assessing the fluid (blood) behavior as it spreads over the substrate. Non-Newtonian fluids, polymers and chemicals spreading have been extensively investigated using the lubrication approximation to explain the spreading dynamics in different applications, but studies related to blood spreading and consequent footprints are quite limited. This tool will illustrate the difference between the Newtonian and non-Newtonian dynamics of the fluid with inclusion of substrate properties like absorption.

Chapter 2

General modelling framework

Contents

In this chapter, the three dimensional time-dependent lubrication approximation governing equations for droplet spreading are derived.

2.1 Governing equations and appropriate scalings

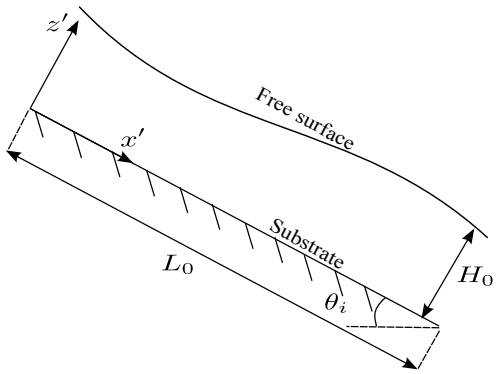

Figure 2.1: Sketch of the geometry of thin fluid film flowing down an inclined substrate

Consider a thin layer of viscous fluid flowing down an inclined substrate, see Figure 2.1. In the cartesian coordinate system (x', y', z') attached to the substrate, x' denotes the coordinate in-flow direction, y' denotes the coordinate in cross-flow direction and z' denotes the coordinate normal to the substrate. H_0 is the characteristic height of the thin film, and θ_i is the substrate inclination. The mass and momentum balance equations for an incompressible, isothermal Newtonian fluid with constant viscosity, μ, are given as,

$$\frac{\partial u'}{\partial x'} + \frac{\partial v'}{\partial y'} + \frac{\partial w'}{\partial z'} = 0, \tag{2.1}$$

$$\rho\left(\frac{\partial u'}{\partial t'} + u'\frac{\partial u'}{\partial x'} + v'\frac{\partial u'}{\partial y'} + w'\frac{\partial u'}{\partial z'}\right) = \rho g \sin\theta_i - \frac{\partial p'}{\partial x'} + \mu\left(\frac{\partial^2 u'}{\partial x'^2} + \frac{\partial^2 u'}{\partial y'^2} + \frac{\partial^2 u'}{\partial z'^2}\right), \tag{2.2}$$

$$\rho\left(\frac{\partial v'}{\partial t'} + u'\frac{\partial v'}{\partial x'} + v'\frac{\partial v'}{\partial y'} + w'\frac{\partial v'}{\partial z'}\right) = -\frac{\partial p'}{\partial y'} + \mu\left(\frac{\partial^2 v'}{\partial x'^2} + \frac{\partial^2 v'}{\partial y'^2} + \frac{\partial^2 v'}{\partial z'^2}\right), \tag{2.3}$$

$$\rho\left(\frac{\partial w'}{\partial t'} + u'\frac{\partial w'}{\partial x'} + v'\frac{\partial w'}{\partial y'} + w'\frac{\partial w'}{\partial z'}\right) = -\rho g \cos\theta_i - \frac{\partial p'}{\partial z'} + \mu\left(\frac{\partial^2 w'}{\partial x'^2} + \frac{\partial^2 w'}{\partial y'^2} + \frac{\partial^2 w'}{\partial z'^2}\right). \tag{2.4}$$

where, u', v' and w' represent the dimensional velocities in the x', y' and z' coordinate directions, p' is the pressure in the thin film and g represents the acceleration due to gravity.

On the substrate, the fluid is subject to the no-slip boundary condition,

$$u' = v' = w' = 0 \quad \text{at} \quad \text{z}' = 0. \tag{2.5}$$

At the top of the fluid layer of height, $h'(x', y', t')$, is a free surface the location of which is unknown until the problem is solved. Therefore, it is important to specify a kinematic boundary condition concerning the motion of the free surface and the dynamic boundary condition concerning the stresses in the free surface.

The free surface at $z' = h'$, is a material surface and should always be composed of the same particles. The fluid velocity is also tangent to the moving surface. Let $F(x', y', z', t')$ describe the free surface,

$$F(x', y', z', t') = h'(x', y', t') - z' = 0, \tag{2.6}$$

The material derivative, $\frac{D}{Dt} = \frac{\partial}{\partial t} + \text{u}.\nabla$, of an implicit formulation of the free surface is zero. Using equation (2.6),

$$0 = \frac{DF}{Dt'} = \frac{\partial F}{\partial t'} + u'\frac{\partial F}{\partial x'} \mid_{z'=h'} + v'\frac{\partial F}{\partial y'} \mid_{z'=h'} + w'\frac{\partial F}{\partial z'} \mid_{z'=h'}, \tag{2.7}$$

$$\frac{\partial h'}{\partial t'} + u'\frac{\partial h'}{\partial x'} + v'\frac{\partial h'}{\partial y'} + w'(-1) = 0, \tag{2.8}$$

$$\frac{\partial h'}{\partial t'} + u'\frac{\partial h'}{\partial x'} + v'\frac{\partial h'}{\partial y'} = w' \quad at \quad z' = h'(x', y', t'), \tag{2.9}$$

which is the kinematic boundary condition. Using equation (2.1) and Liebnitz's rule, equation (2.9) may be rewritten as,

$$\frac{\partial h'}{\partial t'} + \frac{\partial}{\partial x'}\left(\int_0^{h'} u' dz'\right) + \frac{\partial}{\partial y'}\left(\int_0^{h'} v' dz'\right) = 0, \tag{2.10}$$

where $Q_x = \int_0^{h'} u' dz'$ and $Q_y = \int_0^{h'} v' dz'$ are the rate of flow in the x and y respectively. So equation (2.10) becomes,

$$\frac{\partial h'}{\partial t'} + \frac{\partial Q_{x'}}{\partial x'} + \frac{\partial Q_{y'}}{\partial y'} = 0, \tag{2.11}$$

which is the three-dimensional basic form of lubrication approximation equation in dimensional form. The free surface has additional normal and tangential stresses giving rise to the

dynamic boundary conditions. The stress tensor components of a Newtonian fluid are,

$$\tau_{ij} = -p'\delta_{ij} + \mu D_{ij}, \tag{2.12}$$

where,

$$D_{ij} = \left(\frac{\partial u_i}{\partial x_j} + \frac{\partial u_j}{\partial x_i} \right). \tag{2.13}$$

Assuming the air exerts negligible shear stress on the free surface, the dynamic boundary condition at the free surface reads in tensor notation,

$$\vec{n}.\vec{\tau}_N = \sigma\kappa + \Pi(h') \;\; at \;\; z' = h', \tag{2.14}$$

$$\vec{n}.\vec{\tau}_T = 0 \;\; at \;\; z' = h', \tag{2.15}$$

where, $\vec{\tau}_N$ is the normal stress equals to $-p'\delta_{ij}$, $\vec{\tau}_T$ is the tangential stress equals to μD_{ij}, $\vec{n}$ is the outward normal vector to the free surface equals to $\frac{-\frac{\partial h'}{\partial x'}, -\frac{\partial h'}{\partial y'}, 1}{\sqrt{1+\left(\frac{\partial h'}{\partial x'}\right)^2+\left(\frac{\partial h'}{\partial y'}\right)^2}}$, and κ is the free surface curvature. Normal stress is the sum of capillary pressure from the surface tension σ and the disjoining pressure $\Pi(h')$ due to long-range intermolecular forces.

The kinematic and dynamic boundary conditions are highly non-linear and the exact position where to apply these conditions is not known. An important part of the analytical approximation is the introduction of scalings in the problem. There is no single method of scaling the problem. It depends upon the type of flow under consideration.

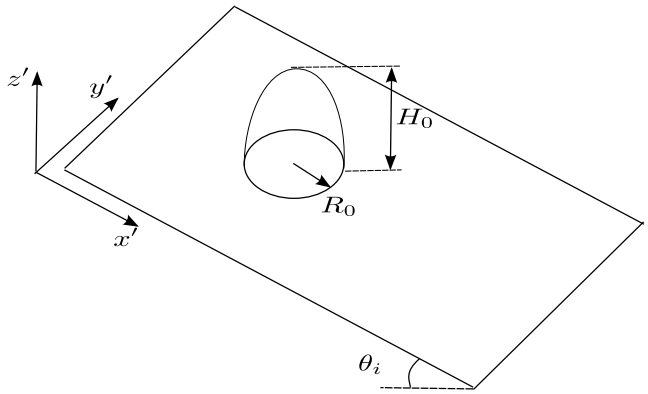

Figure 2.2: Sketch of the droplet geometry

In the present work, the spreading and sliding of a droplet is investigated. The problem is schematically illustrated in Figure 2.2. A three-dimensional problem is considered, where the

mass and momentum balance equations are (2.1), (2.2), (2.3), and (2.4).

These dimensional variables are first converted into non-dimensional ones (without primes). Let H_0 be the characteristic droplet thickness at rest on a horizontal substrate and $L_0 = R_0$ be the corresponding radius in case of a droplet. The lubrication approximation is based on the assumption that: $\epsilon = \frac{H_0}{L_0} \ll 1$. The scalings used here are usual and have been used extensively in the past for Newtonian rheology, i.e. $U_0 = \frac{L_0}{T_0},\ P_0 = \frac{\sigma\epsilon}{L_0}$ (Schwartz and Eley, 1998; Sellier, 2003). Orchard derived the characteristic time scale T_0 for the leveling of Newtonian viscous fluids (Orchard, 1963). A similar characteristic time scale has been used by others in the past for the dynamics of Newtonian fluids (Sellier, 2003; Lee et al., 2009). The characteristic time scale is given by $T_0 = \left(\frac{L_0\mu}{\sigma\epsilon^3}\right)$. The velocity, pressure and the space coordinates are made dimensionless using $u' = U_0 u,\ v' = U_0 v,\ w' = \epsilon U_0 w,\ p' = P_0 p,\ x' = L_0 x,\ y' = L_0 y,\ z' = H_0 z$ where U_0 is the velocity scale in the x direction. Neglecting terms of order $\epsilon^2 = \frac{H_0^2}{L_0^2} \ll 1$ or higher, equations (2.1), (2.2), (2.3), (2.4), can be written in dimensionless form as,

$$\frac{\partial}{\partial z}\left(\frac{\partial u}{\partial z}\right) = \frac{\partial p}{\partial x} - \frac{Bo\sin\theta_i}{\epsilon}, \tag{2.16}$$

$$\frac{\partial}{\partial z}\left(\frac{\partial v}{\partial z}\right) = \frac{\partial p}{\partial y}, \tag{2.17}$$

$$\frac{\partial p}{\partial z} = -Bo\cos\theta_i, \tag{2.18}$$

and the boundary conditions,

$$u = v = w = 0 \ \ at \ \ z = 0, \tag{2.19}$$

$$\frac{\partial u}{\partial z} = \frac{\partial v}{\partial z} = 0 \ \ at \ \ z = h, \tag{2.20}$$

$$p = -\nabla^2 h - \Pi(h) \ \ at \ \ z = h, \tag{2.21}$$

where, θ_i, is the inclination of substrate with the horizontal, and $Bo = \frac{\rho g L_0^2}{\sigma}$ is the Bond number representative of the ratio between the gravitational and surface tension forces. A thin precursor film ahead of the contact line is assumed to be present in order to alleviate the singularity at the dynamic contact line. In order to prescribe equilibrium contact angle,

a disjoining pressure term of the form,

$$\Pi(h) = \frac{(1-\cos\theta_e)(n_d-1)(m_d-1)}{h^*\varepsilon^2(n_d-m_d)}\left[\left(\frac{h^*}{h_{ij}}\right)^{n_d} - \left(\frac{h^*}{h_{ij}}\right)^{m_d}\right], \tag{2.22}$$

is used (Schwartz and Eley, 1998), where n_d and m_d are constants and h^* is the precursor film thickness. Details of disjoining pressure term are discussed in Section 2.2. The mesh resolution is dictated by the value of the precursor film thickness. Equations (2.16) and (2.17) are integrated twice with respect to z over the film or droplet thickness ($0 \leq z \leq h$) to give,

$$u = \left(\frac{Bo\sin\theta_i}{\epsilon} - \frac{\partial p}{\partial x}\right)\left(\frac{1}{2}\right)\left[h^2 - (h-z)^2\right], \tag{2.23}$$

$$v = \left(-\frac{\partial p}{\partial y}\right)\left(\frac{1}{2}\right)\left[h^2 - (h-z)^2\right]. \tag{2.24}$$

The time-dependent lubrication equations are obtained by substituting equations (2.23) and (2.24) in the dimensionless form of equation (2.11),

$$\frac{\partial h}{\partial t} = -\left[\frac{\partial}{\partial x}\left(\frac{h^3}{3}\left(C_1 - \frac{\partial p}{\partial x}\right)\right) + \frac{\partial}{\partial y}\left(\frac{h^3}{3}\left(-\frac{\partial p}{\partial y}\right)\right)\right], \tag{2.25}$$

where $C_1 = \frac{Bo\sin\theta_i}{\epsilon}$. Integrating equation (2.18) with respect to z and substituting equation (2.21), gives the pressure throughout the droplet profile,

$$p = -\nabla^2 h - \Pi(h) + Bo\cos\theta_i(h-z). \tag{2.26}$$

A detailed derivation is reported in Appendix A. Equations (2.25) and (2.26) form the second order coupled non-linear differential equations for h and p. Previous investigations reviewed in (Oron et al., 1997) have substituted equation (2.26) into (2.25) to form a fourth order time-dependent differential equation purely in h. Later studies (Sellier, 2003; Lee et al., 2009, 2007, 2011; Sellier et al., 2011) have shown that the two coupled second order non-linear form lubrication equations are easier to discretize and their implementation in the Full Approximation Storage (FAS) algorithm together with Full Multigrid (FMG), (Brandt, 1982), technique is more straightforward.

2.2 Disjoining pressure

For thin films having a thickness less than $1\mu m$, intermolecular forces become significant. This is essentially taken into account via the disjoining pressure (De Gennes, 2001; Oron et al., 1997; Schwartz, 1999). In close proximity to the substrate, the thickness of the film at the contact line becomes very small. Intermolecular forces therefore play an important role at this location and govern the wettability of a fluid on the substrate. The disjoining pressure term, $\Pi(h')$, is important in the case of droplet spreading as it relieves the stress singularity present at the contact line, i.e. liquid/solid/vapor phase system. The disjoining pressure approach assumes that a very thin precursor film, Section 1.3.2.3, is present ahead of the contact line so that the droplet spreads effectively on a prewetted surface (De Gennes, 2001; Schwartz and Eley, 1998; Warner et al., 2002). The thickness of the precursor film, h'^*, ranges between 1 to 100 nm (Schwartz and Eley, 1998). The existence of this precursor film has been experimentally shown to exist for smooth substrates (De Gennes, 2001). The introduction of a thin precursor film, facilitates the numerical treatment of the lubrication approximation equations by defining the position of the moving contact line, which is otherwise more difficult to handle. A good approximation for the wetting and dewetting phenomenon using thin precursor film requires fine mesh resolution in space and a finer time stepping (Diez et al., 2001; Schwartz, 1999).

Deryagin first suggested that the existence of a disjoining pressure term is responsible for the the contact line motion (Deryagin, 1955). Schwartz and Eley adopted a disjoining term of the form (Schwartz and Eley, 1998),

$$\Pi(h') = B\left[\left(\frac{h'^*}{h'}\right)^{n_d} - \left(\frac{h'^*}{h'}\right)^{m_d}\right], \tag{2.27}$$

where, B, n_d, and m_d are all positive constants with $n_d > m_d > 1$. The first term on the right hand side portrays the liquid-solid attraction and the second term constitutes the liquid-solid repulsion. Various values of n_d and m_d are used in the literature to identify the intermolecular forces. The values $n_d = 3$ and $m_d = 2$ have been popular for having a stable energy minimum at precursor film thickness, h'^*. These values of n_d and m_d are used in the thesis. Schwartz and Eley obtained the constant B by a force balance at the contact line at

equilibrium (Schwartz and Eley, 1998),

$$B = \frac{(n_d-1)(m_d-1)}{h'^*(n_d-m_d)}\sigma(1-\cos\theta_e) \approx \frac{(n_d-1)(m_d-1)}{2h'^*(n_d-m_d)}\sigma\theta_e^2. \tag{2.28}$$

In the present study, $B = \frac{(n_d-1)(m_d-1)}{h'^*(n_d-m_d)}\sigma(1-\cos\theta_e)$ has been used. The disjoining pressure term, equation (2.27), may be written in dimensionless form,

$$\Pi(h) = \frac{(n_d-1)(m_d-1)(1-\cos\theta_e)}{h^*(n_d-m_d)\epsilon^2}\left[\left(\frac{h^*}{h}\right)^{n_d} - \left(\frac{h^*}{h}\right)^{m_d}\right], \tag{2.29}$$

where h^* has a value of 0.01 throughout the thesis unless specified. The equilibrium configuration of the droplet is defined, where V_0, is the volume of the droplet lying on the substrate, R_0, is the characteristic radius of the droplet, H_0, is the maximum height, and θ_e, the equilibrium contact angle (in radians), see Figure 2.3a. The equilibrium droplet shape is assumed to be a paraboloid of revolution, for which simple formulae can be found for $V_0 = \frac{\pi}{2}H_0R_0^2$, $\epsilon = \frac{H_0}{R_0}$, and the equilibrium contact angle, $\theta_e = \arctan\left(\frac{2H_0}{R_0}\right) \approx \frac{2H_0}{R_0}$. The reference scales, $R_0 = \left(\frac{4V_0}{\pi\theta_e}\right)^{1/3}$and $H_0 = \frac{\theta_e R_0}{2}$ are calculated from values for V_0 and θ_e, because these are easily observable quantities. In numerical results, initial droplet profiles are paraboloids with central height H_i and radius R_i. The volume of the initial paraboloidal droplet V_0 satisfies $V_0 = \frac{\pi}{2}H_iR_i^2$, and its conservation imposes that,

$$\frac{\pi}{2}H_0R_0^2 = \frac{\pi}{2}H_iR_i^2, \tag{2.30}$$

where $R_i = rR_0$ and $H_i = hH_0$. h and r are the height and radius of the droplet in dimensionless terms, see Figure 2.3b. When $h = r = 1$, see on the right of Figure 2.3b, then the droplet is in equilibrium/stationary state.

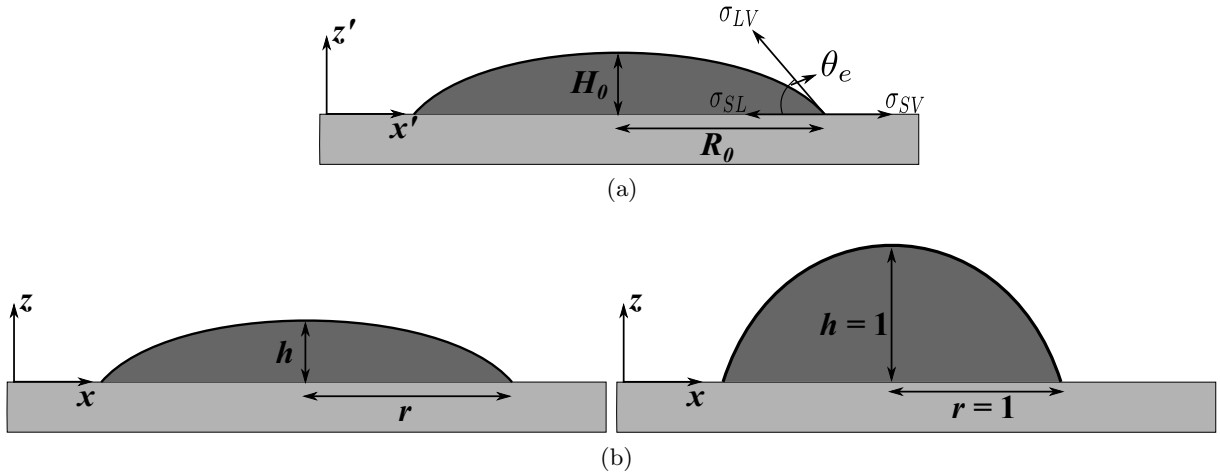

Figure 2.3: Side view of a reference droplet on the substrate in physical (Figure 2.3a) and dimensionless (Figure 2.3b) coordinate systems

2.3 Discretization

The spatial discretization of the lubrication approximation equations (2.25), and (2.26) uses the central Finite-Differencing scheme with uniform mesh spacing in the x and y direction, leading to values of h and p at mesh points (i, j) in the computational grid. To simplify the presentation of the derivations above, let the right-hand-side of equation (2.31) be represented by $\mathcal{F}_h^{n_t}$, i.e. $\frac{\partial h_{ij}}{\partial t} = \mathcal{F}_h^{n_t}$ the subscript represents the corresponding equation,

$$\frac{\partial h_{ij}}{\partial t} = \underbrace{-\frac{1}{\Delta x}\left\{\left(\frac{h_{i+1j}^3 + h_{ij}^3}{2(3)}\right)\left(C_1 - \frac{p_{i+1j} - p_{ij}}{\Delta x}\right) - \left(\frac{h_{i-1j}^3 + h_{ij}^3}{2(3)}\right)\left(C_1 - \frac{p_{ij} - p_{i-1j}}{\Delta x}\right)\right\}}_{-\frac{1}{\Delta y}\left\{\left(\frac{h_{ij+1}^3 + h_{ij}^3}{2(3)}\right)\left(\frac{p_{ij} - p_{ij+1}}{\Delta y}\right) - \left(\frac{h_{ij-1+}^3 h_{ij}^3}{2(3)}\right)\left(\frac{p_{ij-1} - p_{ij}}{\Delta y}\right)\right\}}, \quad \mathcal{F}_h^{n_t} \tag{2.31}$$

$$p_{ij} + \left(\frac{h_{i+1j} + h_{i-1j} - 2h_{ij}}{\triangle x^2}\right) + \left(\frac{h_{ij+1} + h_{ij-1} - 2h_{ij}}{\triangle y^2}\right) + \frac{(1 - cos\theta_e)\,(n-1)\,(m-1)}{\epsilon^2 h^*(n-m)}\left[\left(\frac{h^*}{h_{ij}}\right)^n - \left(\frac{h^*}{h_{ij}}\right)^m\right] - Bo\cos\theta_i(h_{ij}) = 0. \tag{2.32}$$

Time discretization of the equation (2.31) is achieved with the Crank-Nicolson method:

$$\frac{h_{ij}^{n_t+1} - h_{ij}^{n_t}}{\triangle t} = \frac{1}{2}\left(\mathcal{F}_h^{n_t+1} + \mathcal{F}_h^{n_t}\right), \tag{2.33}$$

where $\triangle t = \left(t^{n_t+1} - t^{n_t}\right)$. Equation (2.33) can be re-arranged such that the new time step variables are arranged to the left to give:

$$h_{ij}^{n_t+1} - \frac{\triangle t}{2}\mathcal{F}_h^{n_t+1} = h_{ij}^{n_t} + \frac{\triangle t}{2}\mathcal{F}_h^{n_t}. \tag{2.34}$$

Let $h_{ij}^{n_t+1} - \frac{\triangle t}{2}\mathcal{F}_h^{n_t+1} = \mathcal{L}_k^h$. The left hand side of equation (2.32) is equal to $\mathcal{L}_k^p$. The temporal error control described in (Gaskell et al., 2004) is used to enable the automatic adaptive time stepping (Lee et al., 2007). The time integration above is implemented in a Multigrid solver (Lee et al., 2009). Multigrid is a numerical technique used to solve the differential equations using a hierarchy of discretizations. The basic idea behind this numerical method is to accelerate the convergence by solving on coarser grid. This technique provides a fast and efficient approach to solve the highly non-linear equations (2.31) and (2.32). The convergence is achieved via the use of a hierarchical set of grid levels where residuals are effectively reduced on successive coarse grid levels and corrections to the solutions transferred back on to fine grid levels. Equations (2.31), and (2.32) can be rewritten at a particular grid level, k, as,

$$\mathcal{L}_k^h\left(h_k^{n_t+1}, p_k^{n_t+1}\right) = f_k^h\left(h_k^{n_t}, p_k^{n_t}\right), \tag{2.35}$$

$$\mathcal{L}_k^p\left(h_k^{n_t+1}, p_k^{n_t+1}\right) = f_k^p\left(h_k^{n_t}, p_k^{n_t}\right), \tag{2.36}$$

where, $f_k^h(h_k^{n_t}, p_k^{n_t})$, and $f_k^p\left(h_k^{n_t}, p_k^{n_t}\right)$ are the RHS of equations (2.34), and (2.32). Let $(h_{0k}^{n_t+1}, p_{0k}^{n_t+1})$ be the initial guess to the solution of equations (2.35), and (2.36). Equations (2.32) and (2.34) are solved using the full approximation storage (FAS) and Full Multigrid (FMG) Technique, described in (Lee et al., 2007) with Red-Black Gauss-Seidel Newton iteration scheme to perform relaxation. The linearized form of equations (2.35), and (2.36) is obtained by computing the local Jacobian, so that the relaxation goes forward by solving:

$$\frac{\partial \mathcal{L}_k^h}{\partial h_{ij}}\Delta h + \frac{\partial \mathcal{L}_k^h}{\partial p_{ij}}\Delta p = f_k^h - \mathcal{L}_k^h\left(h_k^{n_t}, p_k^{n_t}\right), \tag{2.37}$$

$$\frac{\partial \mathcal{L}_k^p}{\partial h_{ij}}\Delta h + \frac{\partial \mathcal{L}_k^p}{\partial p_{ij}}\Delta p = f_k^p - \mathcal{L}_k^p\left(h_k^{n_t}, p_k^{n_t}\right), \tag{2.38}$$

where the local Jacobian matrix, J, which is given for a particular grid level, k, as,

$$J = \frac{\partial \left(\mathcal{L}_k^h, \mathcal{L}_k^p\right)}{\partial \left(h_k^{n_t+1}, p_k^{n_t+1}\right)}, \tag{2.39}$$

$$J \begin{pmatrix} \Delta h \\ \Delta p \end{pmatrix} = \begin{pmatrix} f_k^h - \mathcal{L}_k^h(h_{0k}^{n_t+1}, p_{0k}^{n_t+1}) \\ f_k^p - \mathcal{L}_k^p(h_{0k}^{n_t+1}, p_{0k}^{n_t+1}) \end{pmatrix}, \tag{2.40}$$

for Δh and Δp at grid level k. A new approximate solution is obtained by simultaneously solving equations (2.37), and (2.38) and the initial estimates are updated accordingly via

$$\tilde{h}_{0k}^{n_t+1} = h_{0k}^{n_t+1} + \Delta h, \tag{2.41}$$

$$\tilde{p}_{0k}^{n_t+1} = p_{0k}^{n_t+1} + \Delta p. \tag{2.42}$$

A detailed derivation is described in Appendix A.

Chapter 3

Passive bloodstain formation: a preliminary numerical study

Contents

3.1 Validation of implementation in FILMPAR

The implementation of the governing equations in FILMPAR and the results may contain modelling errors. Therefore a validation procedure is required to be sure about the accuracy of the implementation. So COMSOL which is a commercially available finite-element analysis software is used to help validate the numerics. COMSOL is widely used to model and simulate many physics-based systems. COMSOL has a partial differential equation solver. Coupled partial differential equations derived in Chapter 2 have been applied in COMSOL. COMSOL is used here in order to verify the results from FILMPAR.

The simple case of a droplet spreading is solved numerically. The same parameters are chosen for both solvers (COMSOL and FILMPAR). The initial droplet shape is assumed to be paraboloid of revolution with blood fluid properties, Table 3.1 (Sellier et al., 2010). A 4µl droplet is allowed to spread over a 30^o inclined surface. Figure 3.1, shows the position of the centre of gravity of the droplet as a function of time. The final bloodstain shape is a consequence of the sliding and spreading of the blood droplet down the surface. Therefore, the numerical results are presented in terms of the position of the centre of gravity of the droplet and the maximum spread radius in the flow direction as a function of time. The purpose of measuring the position of centre of gravity of the droplet throughout the simulation is to have an idea about the rate at which the droplet spreads and moves down the inclined plane. The position of the center of gravity is computed according to,

$$x_{cg} = \frac{\int_\Omega (h - h^*) x d\omega}{\int_\Omega (h - h^*) d\omega}, \tag{3.1}$$

$$y_{cg} = \frac{\int_\Omega (h - h^*) y d\omega}{\int_\Omega (h - h^*) d\omega}, \tag{3.2}$$

where $\Omega = [0, 15] \times [0, 4]$ is the computational domain. h^*, the precursor film thickness is equal to 0.01 (i.e. 1% of the characteristic droplet thickness). Later in the thesis, the effect of a change in the value of h^* is also considered, see Figure 4.17. $h^* = 0.01$ is used throughout the thesis when droplet spreading is considered, because the solution requires comparatively less time to compute and without a very significant effect on the results. It can be deduced from Figure 3.1 that at the beginning of the simulation, the rate of change of the position of the center of gravity of the droplet is greater. After the droplet achieves its equilibrium

shape, it moves down the incline with a constant velocity and almost constant profile.

Physical Property	**Value**
Density, kg/m^3	1062
Viscosity, Pa.s	0.00475
Surface Tension, N/m	0.0555
Equilibrium contact angle, θ_{eq},^{o}	42, 45, 53
Inclination angle, θ_i, ^{o}	30 - 90
Volume of droplet, V_0, μl	2×10^{-9}-16×10^{-9}
Initial position of centre of gravity	(2,2)

Table 3.1: Newtonian properties of blood on vinyl, perspex and glass substrates (Sellier et al., 2010)

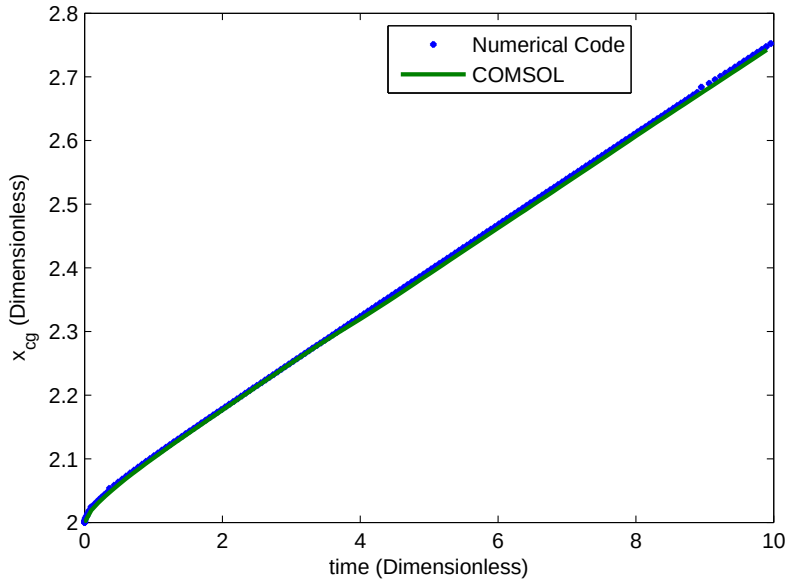

Figure 3.1: Comparison of the results from the numerical code with COMSOL

Both solvers are in excellent agreement, see Figure 3.1. This confirms the correct implementation of the governing equations in the solver FILMPAR and gives the required confidence that this solver can be used to include more complex physics such as: contact angle hysteresis, non-Newtonian rheology and absorption effects. COMSOL has some shortcomings since it does not allow access to the discretization technique or solver parameters. Consequently, convergence issues sometimes arise and it can be hard to overcome them or tailor the software to the specific requirements. This is the main reason COMSOL was disregarded in the following chapters as a modelling tool.

3.2 Influence of volume and substrate properties on blood droplet footprint

Numerical simulations have been performed using FILMPAR to understand how the blood footprint depends on key parameters such as droplet volume, surface inclination angle relative to the horizontal, and wetting properties of the underlying surface. The volume of the droplet is varied from 2µl to 16µl. Surface inclination angle is varied from 30° to 90° with an increase of 15°. For contact surfaces, vinyl, perspex and glass with equilibrium contact angles of 42°, 45° and 53° are selected as reported in (Sellier et al., 2010).

Figure 3.2 depicts the effect of increasing the inclination angle on the maximum spread in the major axis along the flow direction or the X-spread. For 75° and 90° inclination, a cusp forms at the trailing edge of the droplet. The formation of cusp is the reason for the sudden increase in the X-spread at higher inclinations with time. This cusp is only seen to form when the equilibrium contact angle is lower, i.e. for vinyl and perspex substrates. Figure 3.3, illustrates the formation of the cusp of a droplet spreading on a vertical vinyl surface at t = 0.024s.

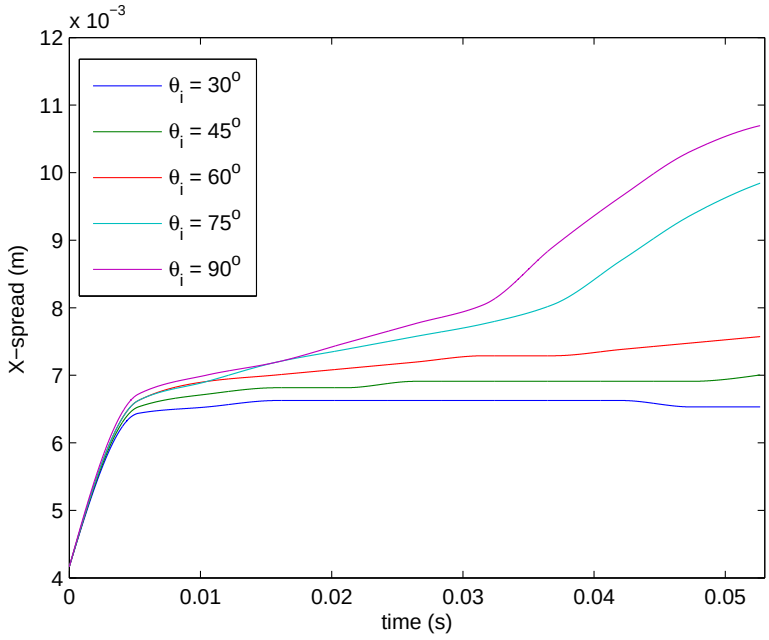

Figure 3.2: Influence of varying inclination angle on the spread in flow direction as a function of time - 16 µl on a vinyl substrate

This cusp/corner formation has been reported in the literature (Podgorski et al., 2001).

Conical similarity solutions near the tip of the drop cause the corner/cusp formation in the drops moving down an inclined surface (Podgorski et al., 2001).

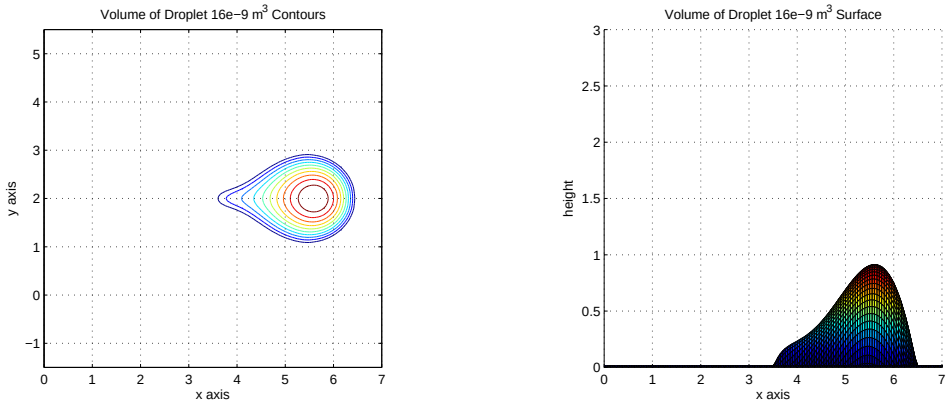

Figure 3.3: Top and side view of the cusp formation after 10 dimensionless time units of a droplet on a Vinyl substrate with a surface inclination of 90°

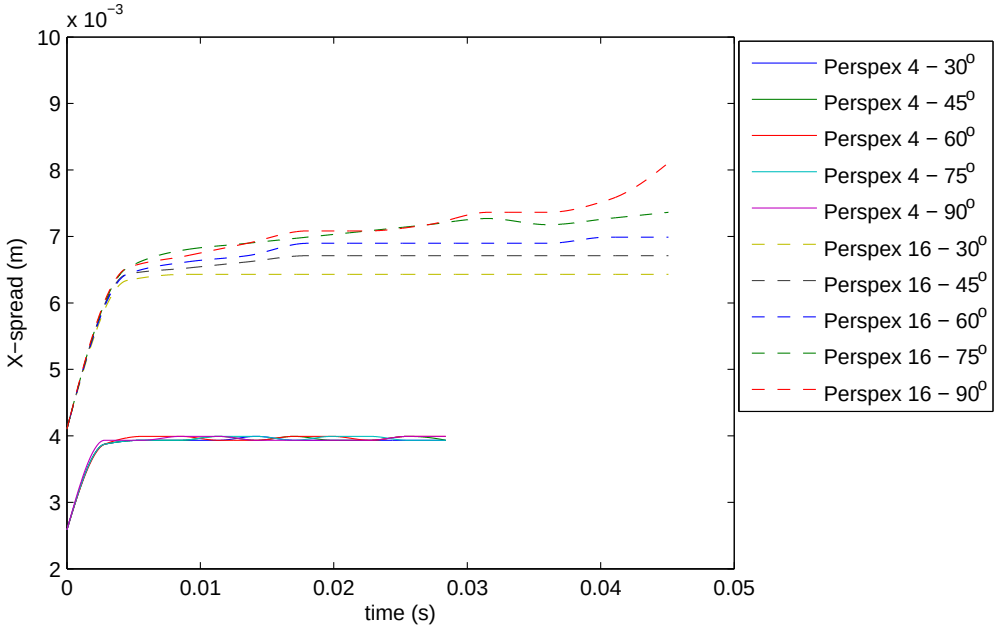

Figure 3.4: Influence of varying droplet volume on the spread in flow direction as a function of time - 4µl and 16µl droplets on perspex surface

The volume of the droplet plays a vital role in the final footprint, as shown in Figure 3.4. Increasing the volume increases the spread in the flow direction and consequently reduces the spread in cross-flow direction. For inclination angle greater than 75° and greater droplet volume, cusp formation occurs at the trailing edge as the droplet runs down the inclined surface. The cusp/corner formation at the trailing edge becomes sharper as the inclination angle is increased. This cusp formation is the reason for the steep rise in the curves for higher

inclinations when spread in flow direction for 16µl droplet is plotted against time, see Figure 3.4.

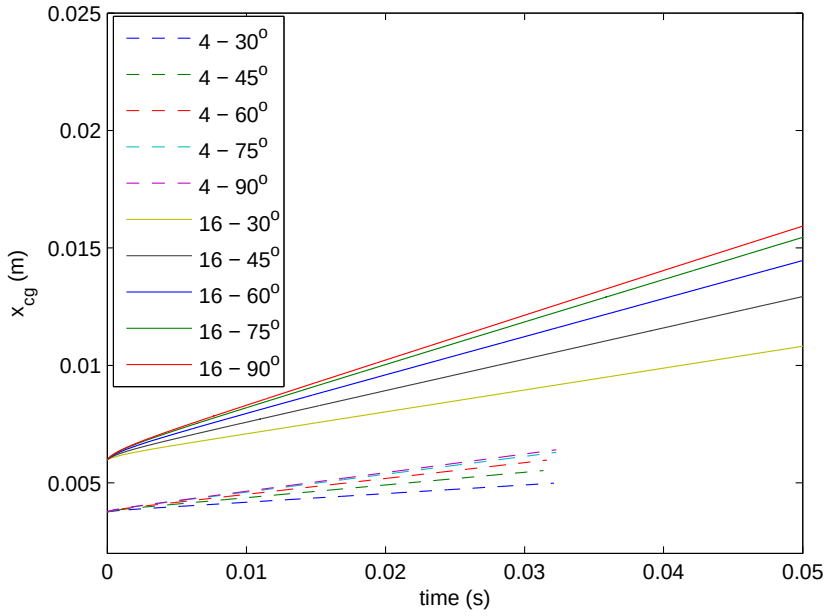

Figure 3.5: Influence of varying droplet volume on the position of the center of gravity of the droplet as a function of time - 4µl and 16µl droplets on perspex surface

The position of the center of gravity is plotted with time for the droplets having different volumes on perspex substrate, see Figure 3.5. As the droplet starts spreading, due to the potential energy and the effect of the inclination angle, for the first few milliseconds the droplet velocity (gradient of x_{cg} vs time) increases to a near constant velocity, see Figure 3.5. This near constant velocity (terminal velocity) increases with an increase in the inclination angle and an increase in volume of the droplet, see Figures 3.5 and 3.6.

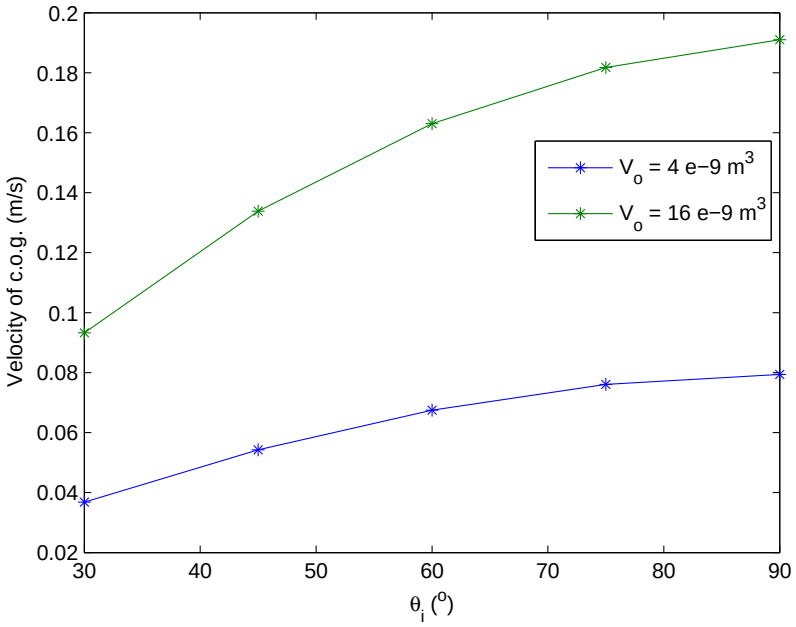

Figure 3.6: Travel velocity against inclination angle, from Figure 3.5

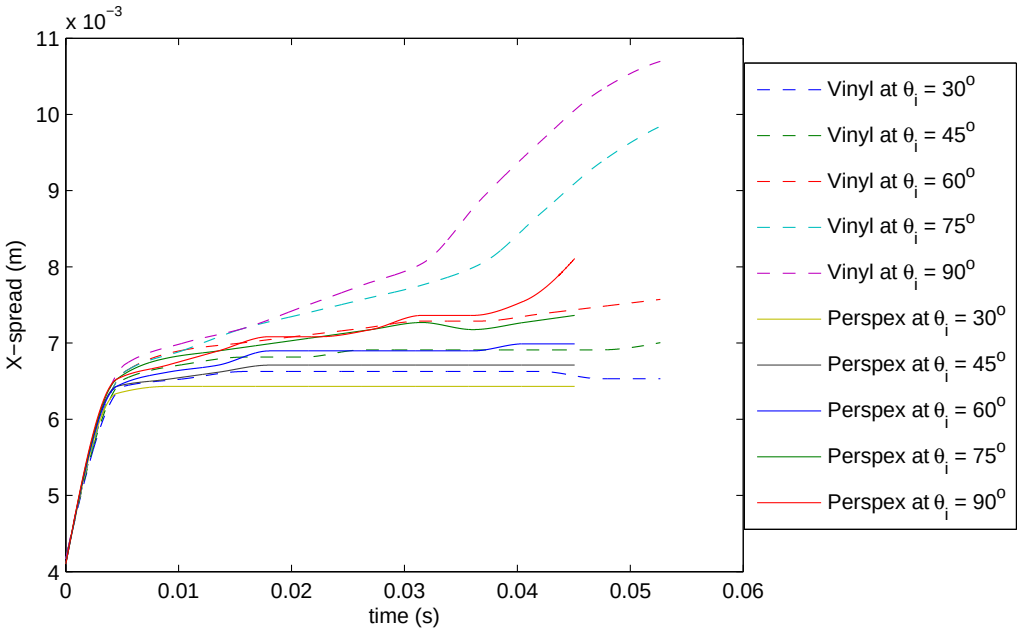

Figure 3.7: Influence of varying contact surface on the spread in flow direction as a function of time - 16µl droplets on perspex and vinyl surface

The wetting surface variation addresses the change in equilibrium contact angle. Among the surfaces considered, vinyl has the smallest equilibrium contact angle. A smaller contact angle means that the fluid is more wetting on the surface. As can be seen from Figure 3.7, the contact angle decrease results in an increase in major axis spread for the same inclination angle. Figure 3.8 shows that an increase in the equilibrium contact angle increases the slope

(sliding speed) of the plot between the position of center of gravity of the droplet with time for a particular inclination angle. The sliding speed also increases with an increase in inclination angle for a particular equilibrium contact angle.

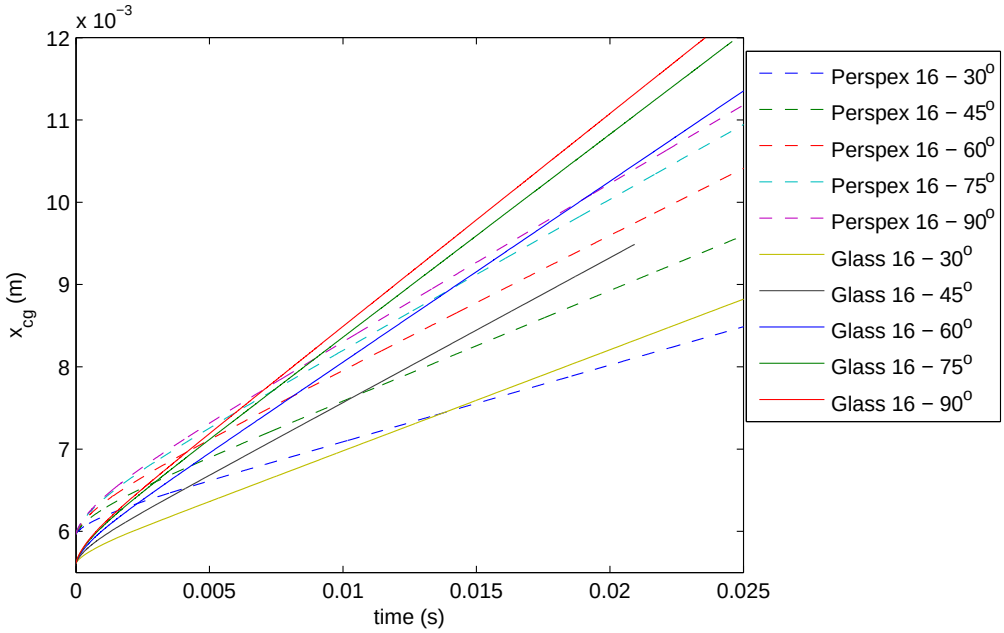

Figure 3.8: Influence of varying contact surface on the position of the center of gravity of the droplet as a function of time - 16µl droplets on perspex and glass surface

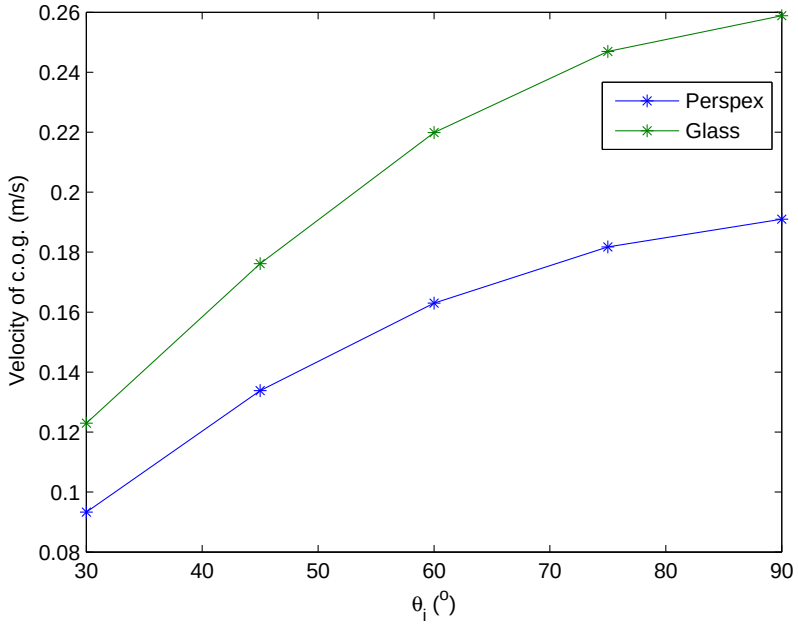

Figure 3.9: Travel velocity against inclination angle, from Figure 3.8

For partial wetting, the droplet slides down the substrate with an approximately constant

profile and with a near constant velocity. The droplet velocity (as it slides down the surface) increases with the inclination angle and droplet volume. As would be expected from a simple force balance, the major axis length increases with increasing droplet volume and droplet inclination, but decreases with increasing contact angle. The minor axis length decreases with an increase in substrate inclination and a decrease in contact angle. This is very important, because it dictates the final shape of the bloodstain. A cusp is observed at the rear of the droplet for large inclination angles and small contact angle.

Chapter 4

Effects of the contact angle hysteresis on the terminal velocity of droplets

Contents

Most of Chapter 4 has already been submitted as a paper titled, "Modelling the effects of contact angle hysteresis on sliding of droplets on inclined surfaces." for peer review in The European Journal of Mechanics - B/Fluids. This work was co-authored with Dr. Mathieu Sellier, Dr. Mark Jermy and Dr. Michael Taylor.

4.1 Introduction

Spreading/sliding droplets feature a very important phenomenon which is crucial to their dynamics, i.e. contact angle hysteresis, θ_{hys}. It is always present in natural as well as most industrial processes. This phenomenon is best understood by considering a droplet resting on an inclined substrate, like raindrops on a car windscreen. Gravitational pull favors the sliding of the droplet downslope while hysteresis resists it in static conditions. Therefore the droplet shape is asymmetric in comparison to the symmetric shape on a horizontal substrate. The droplet becomes thin with a lower contact angle at the back, known as the receding contact angle, θ_r, and becomes thick with a higher contact angle at the front, known as the advancing contact angle, θ_a. When the gravitational forces on the droplet exceed the substrate resistive forces, the droplet starts to slide down the incline maintaining its asymmetric shape with θ_a in the front and θ_r at the back, see Figure 4.1.

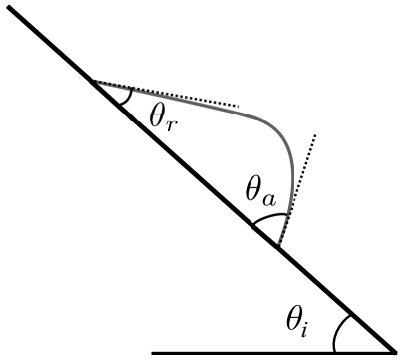

Figure 4.1: Sliding droplet with advancing, θ_a, and receding, θ_r contact angle

The difference between the advancing and receding contact angles is known as contact angle hysteresis. The presence of this hysteresis means that the system is in a metastable state. There are three major sources of hysteresis: chemical composition of the fluid, surface roughness, and chemical heterogeneities (De Gennes, 1985). Fluids such as polymers or surfactants may leave behind a film on the substrate; the presence or absence of this film will directly influence hysteresis. Hysteresis is greatly influenced by substrate roughness. Dettre

and Johnson investigated the change in hysteresis as the roughness is varied (Dettre and Johnson, 1964). They detected an unusual change in the θ_r as the roughness is decreased. Chemical heterogeneities in the substrate may also play a vital role. Differences in substrate wettability may cause unexpected sliding dynamics (Schwartz and Eley, 1998).

Contact angle hysteresis is also present in coating procedures, digital micro-fluidics, droplet evaporation, inkjet printing, and pesticides spraying applications. Hysteresis is problematic in a few industrial applications (immersion lithography), but is crucial in others (coating and spray painting) (Eral et al., 2013). Controlling the extent of hysteresis has a significant importance in most industrial operations.

The prominence of contact angle hysteresis, has led many scientists to study its origin and its effect on the motion of the droplets. Adam and Jessop first appreciated the existence of contact angle hysteresis due to the frictional resistance of the substrate (Adam and Jessop, 1925). De Gennes reviewed the early experiments that explain the phenomenon (De Gennes, 1985). Furmidge investigated spray (droplet) retention in the agricultural sector. Droplet retention is one of the sources and effects of contact angle hysteresis. Furmidge suggested a simple technique to describe the retention of the droplets sliding down the inclined substrates (Furmidge, 1962). Dussan and co-workers studied water droplets sliding at a constant velocity down the inclined substrates of different levels of roughness (Dussan V. and Chow, 1983; Dussan V., 1985, 1987). In these studies, the authors demonstrated a theoretical explanation of the retention forces responsible for the sticking of droplets on solid substrates. Various authors have analyzed contact angle hysteresis for variable substrate properties, such as surface roughness and surface heterogeneity, both computationally and experimentally (Timmons and Zisman, 1966; Lomas, 1970; Zografi and Johnson, 1984; Extrand and Kumagai, 1995). Hysteresis of one or two degrees may essentially be due to the uncertainty in measurement and can be neglected (Timmons and Zisman, 1966). In most practical droplet sliding applications, the hysteresis is around 10^o (De Gennes, 1985). Topographical heterogeneities such as peaks or ridges may cause the hysteresis to increase up to 50^o (Johnson and Dettre, 1963).

Contact angle hysteresis affects the sliding velocity of the droplet sliding down an inclined substrate. Various authors in the past have developed scaling laws to estimate the sliding

velocity of droplets using the small contact angle assumption to apply the lubrication approximation (Dussan V. and Chow, 1983; Hocking, 1981). Kim and co-workers performed experiments to measure the sliding velocity of partially wetting viscous droplets on a smooth surface. They constructed a scaling law which does not assume a small contact angle and demonstrates the dependence of sliding velocity on various parameters (Kim et al., 2002). As the droplet slides down with a particular hysteresis, there exists a no-slip boundary condition at the liquid-solid interface. A moving contact line is a clear violation of the no-slip boundary condition so it is necessary to use a model which can solve the singularity which arises from the contact line motion.

The presence of contact angle hysteresis in the advancing and the receding region and the formation of a sharp corner at the tail of the spreading droplet above a critical speed is observed experimentally (Podgorski et al., 2001; Le Grand et al., 2005). Podgorski and co-workers recorded the shape of a droplet from above and analyzed the velocity with which it runs down an inclined solid substrate (Podgorski et al., 2001). Le Grand and co-workers suggested a few improvements in the experimental setup of Podgorski and co-workers (Le Grand et al., 2005). Droplets start to develop a corner at the rear which changes to a cusp at a greater velocity. At an even higher velocity a satellite droplet at the tail separates and the pearling phenomenon occurs (Le Grand et al., 2005). Similar shape patterns are observed when solving the same problem numerically (Schwartz et al., 2005; Thiele et al., 2002). Schwartz and Eley investigated the hysteretic behavior of droplet motion using the lubrication approximation on a chemically heterogeneous surface (Schwartz and Eley, 1998). The introduction of disjoining pressure in the lubrication formulation can alleviate the contact line singularity. A hysteretic effect was demonstrated by applying different equilibrium contact angles at different positions on the substrate to measure the contact line velocity. The work of Gaskell and co-workers who implemented a hysteresis model in the context of the lubrication approximation is expanded here (Gaskell et al., 2009).

Nature demonstrates contact angle hysteresis phenomena in our daily surroundings. The approach to include this physical aspect in models is far from settled. The work presented in this thesis explores a new way of modelling contact angle hysteresis based on the geometry of the sliding droplet to predict the advancing and receding fronts of a sliding droplet and its

subsequent effect on the droplet terminal velocity.

The objective of this chapter is to present a way to introduce contact angle hysteresis and to study its effect on the motion of droplets as they spread/slide down inclined substrates. Section 4.2 provides details of the experimental setup and physical properties of the fluids and substrates. Section 4.3 describes the mathematical model, the governing equations, and the numerical technique employed to solve the governing equations. Lastly, Section 4.4 presents the results from the numerical simulations for fluid droplets spreading/sliding on inclined substrates under the influence of contact angle hysteresis. Numerical results are first compared with the experiments present in the literature, see Section 4.4.1 and then with the performed experiments, see Section 4.4.2. A simple analytical model is also proposed and compared with the numerical results for droplets moving down the incline with near circular footprints.

4.2 Experimental methodology

4.2.1 Experimental setup

Experimental studies such as (Podgorski et al., 2001; Le Grand et al., 2005) are very accurate and describe the dynamics of droplets sliding down the incline. Podgorski and co-workers have calculated the velocity of the droplet as the mean velocity of the fluid and Le Grand and fellow researchers have measured the velocity of the contact line. Both approaches are legitimate, but as we shall show later, using the center of gravity as a reference point for the droplet location appears to be more intuitively correct. In this proposed model, the velocity of the sliding droplet is determined by the position of its center of gravity as it slides.

Different experimental setups are described in the literature and the choice largely depends on the aspects of the spreading that is of interest. In the present study, the interest lies in the terminal speed of the droplet on the inclined surface and the shape it acquires as it spreads to form the footprint. The experimental setup proposed by Le Grand and co-workers makes the basis of experimentation for the present work, see Figure 4.2.

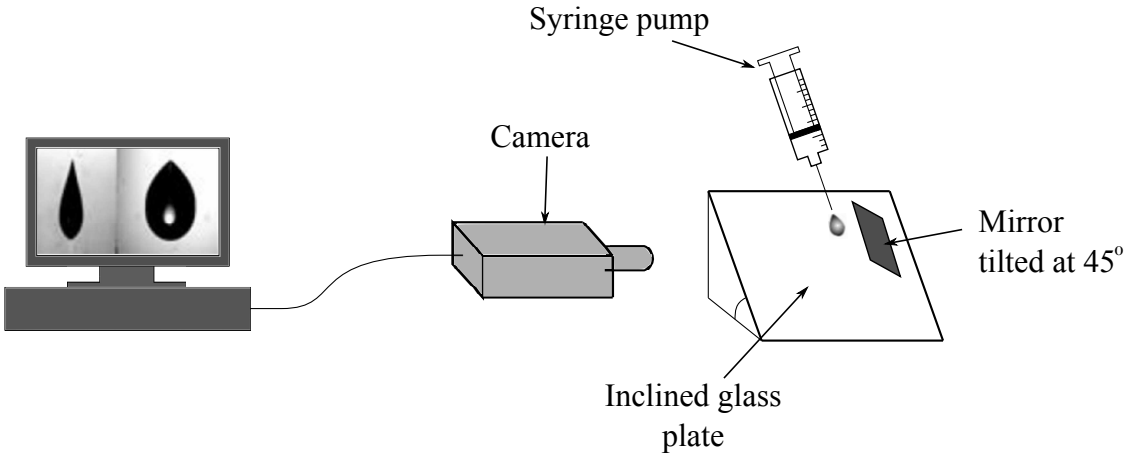

Figure 4.2: Experimental setup (Le Grand et al., 2005)

A solid substrate (smooth transparent glass) is placed on a custom-built angle variation device made of stainless steel. The dimensions of the base of this device are 30×19.3 cm. The base can rotate about a horizontal axis to vary the inclination angle from 0^o up to 90^o. Precise measurement of the angle of the inclination is made using the magnetic protractor/angle locator. The dimension of the glass plate used in the experiments is 30×20 cm. For consistency, all experiments are repeated on the same glass substrate. The 10×10 cm mirror, is attached to the substrate using a hinge at the back and a 45^o hollow wedge attached to the top corner of the mirror. The purpose of placing this mirror at 45^o is to capture simultaneously the droplet from the side and from above. The experimental setup is side and back lit by a Kaiser Halogen video light 2000W. The position of the light is far from the experimental rig so that the influence of heat from the light is negligible. The base and the substrate are placed at right angles to each other so that the substrate is not covered by the base so that the substrate can be illuminated from beneath in order to have a strong contrast for the top image. To avoid direct exposure to backlight a diffusing screen made of sand-blasted glass is placed in between the base and the substrate. At least nine identical trials are performed for each fluid droplet at a particular inclination angle to ensure data reproducibility.

Droplets are released from a syringe, which is connected to a syringe pump. The rate at which the fluid is dispensed is fixed to 0.235 ml per min for all the experimental runs. The syringe pump is used to dispense 10 droplets into the empty flask at the above specified rate. Mass of these 10 droplets is measured. With the help of the density of fluid the average volume of a single droplet is calculated. At this rate the approximate volume of the water

droplet released from the needle is $27.17 \pm 0.2\,\mu$l and for the glycerine solution a droplet is $24.16 \pm 0.2\,\mu$l. After dispensing a single droplet, the syringe pump is stopped and the droplet spreading dynamics on the inclined substrate is recorded. The recorded data which is of interest is when the droplet has achieved a stationary profile after impacting the substrate and there are no perturbations due to the impact. The experiments are performed at room temperature and pressure. Figure 4.3 shows the actual experimental setup.

Figure 4.3: Actual experimental setup

Before the start of the experiment, the substrate (glass) is first cleaned with Virkon 1% solution and ethanol to kill micro-organisms on the substrate. After treating the surface with Virkon and ethanol, the substrate is cleaned with isopropanol. The substrate is then rinsed with distilled water so that the substrate is free from the disinfectants mentioned above and then dried in hot air to remove any water residue.

Heat from the light is very important. The light was only turned on for the duration of the recording, i.e. for 3 to 4 seconds. It was kept far from the substrate to avoid as much as possible the influence of heat from the light source. After each set of experiment, there was a delay of approximately 10 minutes so that the substrate is at room temperature.

Figure 4.4: Water droplet spreading/sliding on a 60° inclined glass substrate and postprocessing in Image J

Water droplets are transparent, which makes them hard to observe without adequate lighting. Food color is added in water to increase the contrast. The motion of the droplet is recorded by a Photron FASTCAM SA 1.1 camera at a frame rate of 1000 fps. The captured images are processed using the Photron FASTCAM Viewer Version 3.0 and Image J software. Figure 4.4 shows the top and side view of the water droplet sliding down a 60° inclined glass substrate.

4.2.2 Fluid property measurement

The surface tension and contact angle of the fluids are measured using the contact angle and surface tension meter with FireWire CCD camera CAM 200 and provided software CAM 2008. These measurements are made using a 1.25 mm diameter hypodermic needle and a plastic syringe are used to produce fifteen pendant blood drops with fully developed (elongated) neck. The needle is cleaned with 1% Virkon solution to avoid any organic residue, rinsed thoroughly with ethanol and distilled water. Droplet images were captured and analyzed using curve/profile fitting procedure. A mean value of surface tension and standard deviation of the mean are calculated.

Viscosity of glycerine is measured at shear rate of 1000 s^{-1} with a rotational rheometer HAAKE RotoVisco RV 20 with NV coaxial cylinders sensor system. The rheometer heating bath thermocontroller HAAKE F3 maintains glycerine at room temperature. Two verification runs are made for each sample. Shear stress correction factors and instrumental error based on the device calibration with standard oil N10 are applied to the obtain good data.

The density of the fluid is measured by a weighting syringe method using analytical balance. For this ten independent measurements are taken and averaged. Corrections of order 1% based on validation runs (calibrations) with distilled water are applied. The mean values of the measured fluid properties have been reported in Tables 4.1 and 4.2.

Physical Property	**Value**	**Published values range (Sikalo et al., 2005)**
Density at 22°C, kg/m^3	998.6 ± 2	1000
Viscosity at 22°C, Pa.s		0.001
Surface Tension at 22°C, N/m	0.072 ± 0.003	0.072
Contact Angle on clean glass, ^{o}	11 ± 1	8.1
Volume of droplet, V_0, μl	27.17 ± 0.2	

Table 4.1: Measured physical properties of water

Physical Property	**Value**	**Published values range (Sikalo et al., 2005)**
Density at 25°C, kg/m^3	1122.6 ± 1	1123.8
Viscosity at 25°C, Pa.s	0.0051 ± 0.0002	$0.0050 - 0.0053$
Surface Tension at 25°C, N/m	0.0666 ± 0.0011	$0.066 - 0.068$
Contact Angle on clean glass, ^{o}	14.3 ± 2.00	$13 - 17$
Volume of droplet, V_0, μl	24.16 ± 0.2	

Table 4.2: Measured physical properties of glycerine 50% by weight solution

Hysteresis range for these fluids was not precisely measured. The values stated in Tables 4.1 and 4.2 are the values that are for equilibrium contact angle and the uncertainty mentioned in these values is in the measurement of the equilibrium contact angle.

4.2.3 Experimental results

Water and 50% by weight glycerine solution droplets are deposited on 30°, 45° and 60° inclined glass substrates. With the help of the Image J software, the side view is used to calculate the position of the centroid of the spreading droplet along the inclined axis. The

error calculated with this method in the measurement of the location of centroid is below 0.1 mm. This error is calculated by free hand drawing the shape of the sliding droplet while post-processing the experimental results in Image J software. The speed of the droplet is estimated by drawing a trendline through different plots for centroid position variation with time. In the plots of centroid position with time, data # shows the number of trials of the experiment and the average (dotted line) in the plots represents the mean position of the centroid estimated from the trendlines. The slope of these trendlines give an estimate of the terminal speed with which the droplet is sliding on the inclined substrate. The variation in the result of the experiments, apparent in the error bars, can be attributed to the uncertainty in the profile of the droplet as it slides down the incline, see Figures 4.31, 4.32, 4.34 and 4.35.

The experimental results for water droplets sliding on inclined glass substrate are shown in Figures 4.5, 4.6, 4.7 and 4.8. The plot in the figure shows the movement of the position of the centroid of the spreading droplet with time. The data set shown in the plots are from the time when the droplet has just started to slide on the inclined substrate. As the droplet impacts the substrate, for a micro-second it is not in a definite shape and it oscillates. So the data shown here is when it has come into equilibrium shape and is not oscillating.

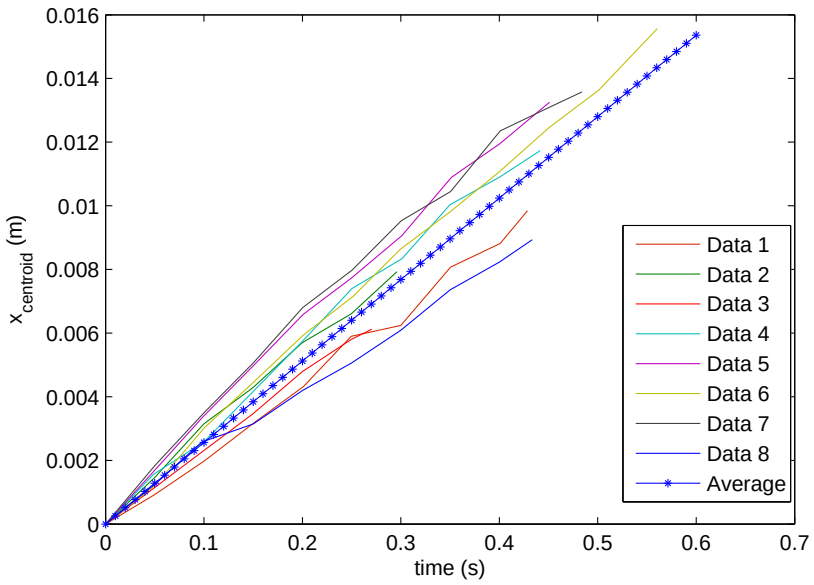

Figure 4.5: Water droplets spreading at 30° inclination

Figure 4.5 shows the position of the centroid as the droplet slides down the substrate inclined

at 30°. The average velocity of the centroid of the droplet is 0.0256 m/s with a standard deviation of 0.0032 m/s.

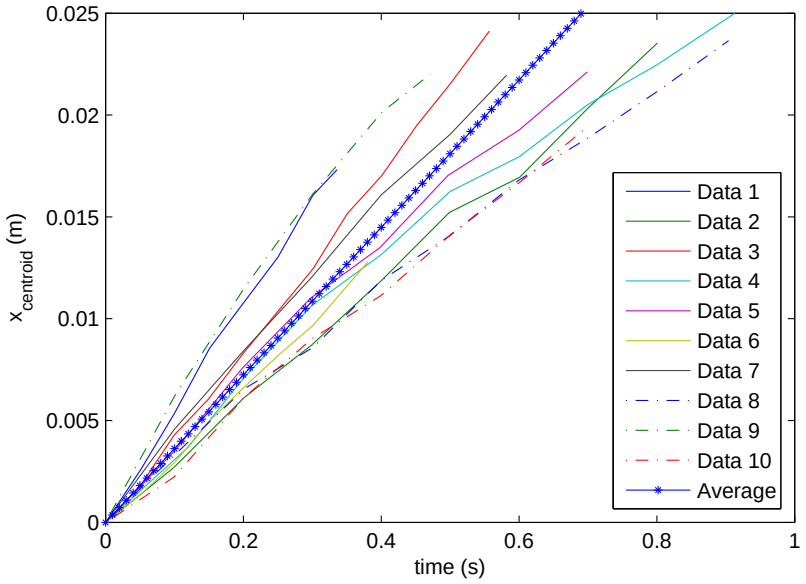

Figure 4.6: Water droplets spreading at 45° inclination

As the angle of inclination of the substrate is increased to 45° see Figures 4.6 and 4.7, there is a larger variation in the results for the position of the centroid of the droplet. The reason for this variation is that for some data trials the total spread increases and for others the total spread is reduced compared to total spread with $\theta_i = 30°$, where total spread is the length measured from the rear to the front of the droplet. This means that the fluid as it spreads on a 45° inclined substrate sometimes remains in contact/sticks with the substrate as it spreads, i.e. leaves a thin film behind it or sometimes flows down the incline. The phenomenon is commonly known as the contact angle hysteresis discussed earlier. Therefore two data sets were generated for 45° inclined glass substrate. The average velocity of the centroid from Figures 4.6 and 4.7 is 0.0342 m/s with a standard deviation of 0.0087 m/s.

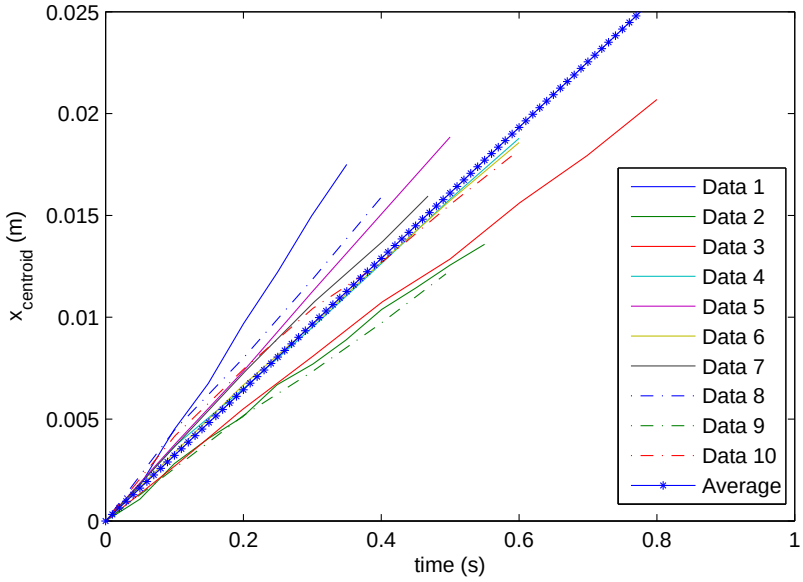

Figure 4.7: Water droplets spreading at 45° inclination (another try)

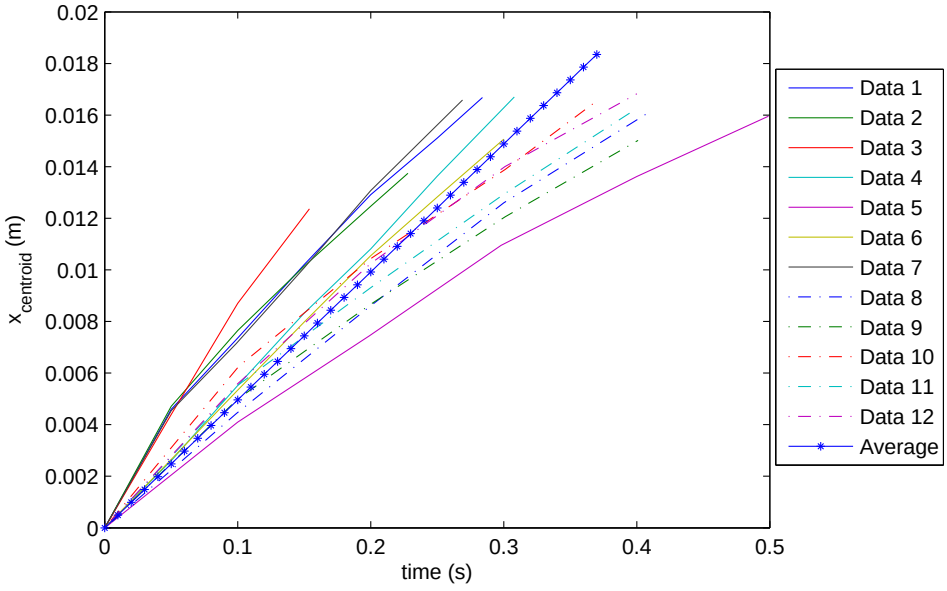

Figure 4.8: Water droplets spreading at 60° inclination

As the substrate inclination is increased to 60°, the average velocity of the centroid also increases due to high gravitational forces.The average velocity of the centroid of the droplet is 0.0496 m/s with a standard deviation of 0.0134 m/s. It is clear from the Figures 4.5, 4.6, 4.7 and 4.8 that the velocity of the centroid of the spreading/sliding droplet increases with an increase in the inclination angle.

The experimental results for glycerol solution droplets sliding on inclined glass substrate are shown in Figures 4.9, 4.10, and 4.11. The plot in the figure shows the movement of the position of the centroid of the spreading droplet with time.

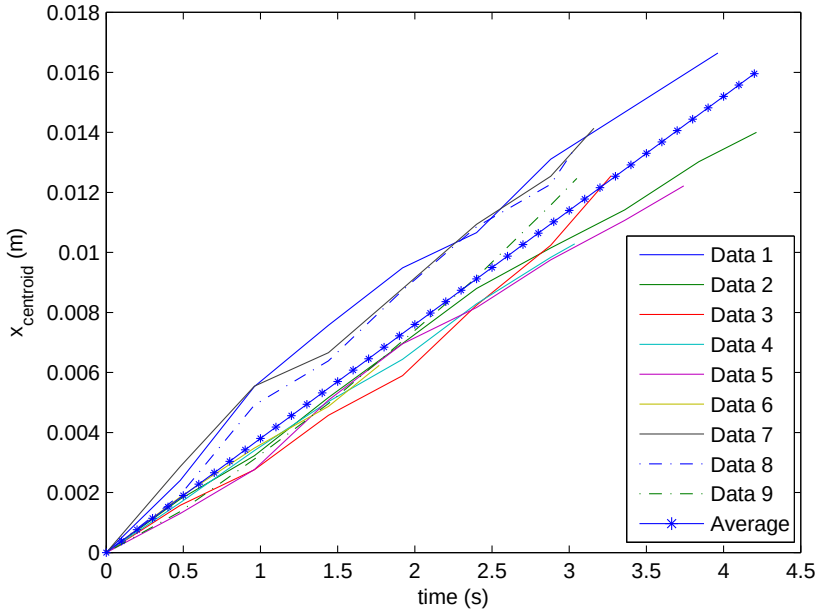

Figure 4.9: Glycerol solution droplets spreading at 30° inclination

Figure 4.9 shows the position of the centroid as the droplet slides down the substrate inclined at 30°. The average velocity of the centroid of the droplet is 0.0038 m/s with a standard deviation of 0.0004 m/s.

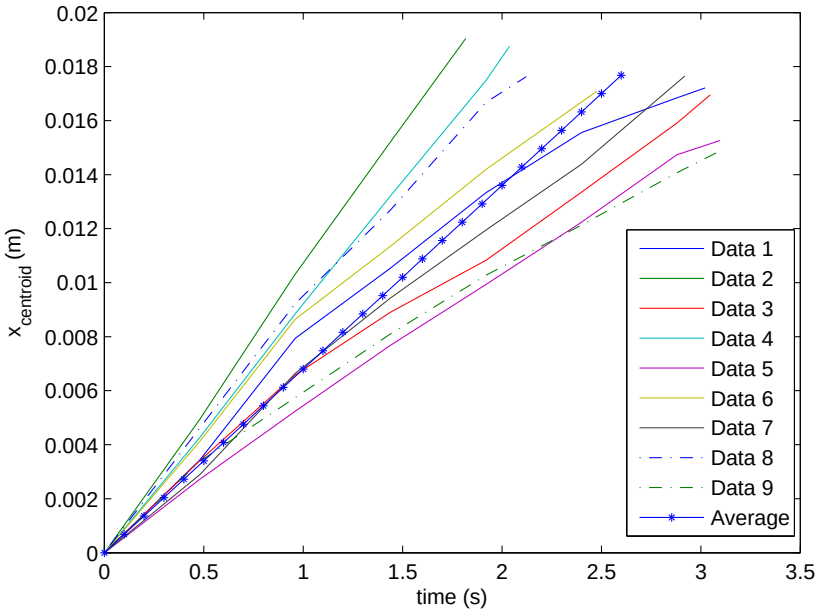

Figure 4.10: Glycerol solution droplets spreading at 45^{o} inclination

As the angle of inclination of the substrate is increased to 45^{o} see Figure 4.10, there is increase in the gravitational forces which in turn causes the position of the centroid of the glycerol solution droplet to slide quickly in comparison to the one for 30^{o}. The average velocity of the centroid from Figure 4.10 is 0.0068 m/s with a standard deviation of 0.0021 m/s.

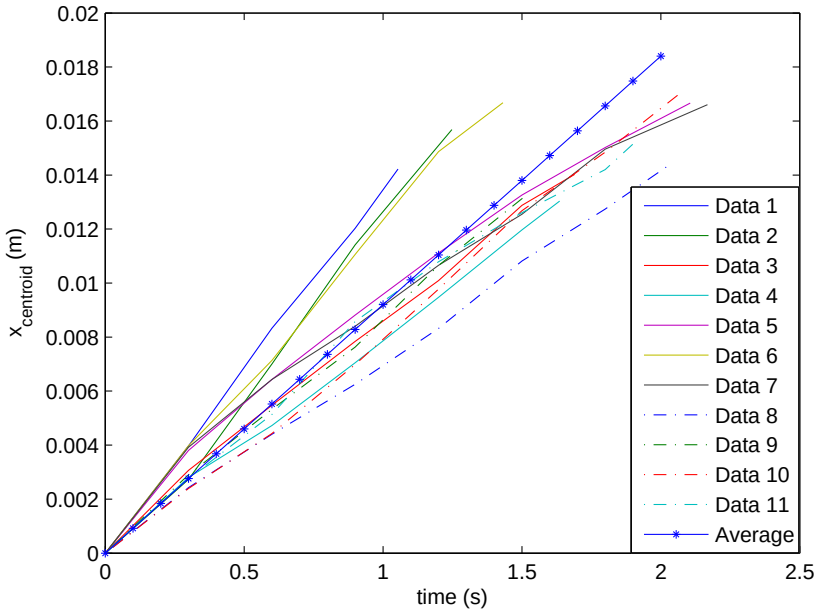

Figure 4.11: Glycerol solution droplets spreading at 60^{0} inclination

As the substrate inclination is increased to 60^o, the average velocity of the centroid also increases due to high gravitational forces. The average velocity of the centroid of the droplet is 0.0092 m/s with a standard deviation of 0.0023 m/s. It is clear from the Figures 4.9, 4.10, and 4.11 that the velocity of the centroid of the spreading/sliding droplet increases with increase in the inclination angle. Now the direction of thesis is turned to the numerics to try to see if the underlying phenomena involved can be replicated.

4.3 Problem specification and mathematical formulation

The Numerical and mathematical formulation has been described in detail in Chapter 2. The same mathematical formulation is used here with inclusion of contact angle hysteresis model described in the next Section 4.3.1.

4.3.1 Implementation of contact angle hysteresis model

Gaskell and co-researchers assigned the contact angle hysteresis with reference to the motion of the droplet (Gaskell et al., 2009). In other words, the assignment of contact angle during the simulation is based on the droplet motion history. A static advancing contact angle is assigned if the droplet height on the current time step is higher than the droplet height obtained in the previous time step. Similarly, a static receding contact angle is assigned if the droplet height is less than the previous value, or an equilibrium contact angle is assigned if no change in the droplet height is recorded. Hence for the new time step, a new set of contact angles are assigned to the model for the iteration (Gaskell et al., 2009).

Here in this work, contact angle hysteresis is introduced into the numerical code. The first step towards approximating the point which separates the advancing contact line from the receding contact line in a droplet sliding scenario is to assume that the droplet is symmetric about the $x-z$ plane. Let $l(x)$ be a length defined as a function of x which is parallel to the y-axis in the plane $z = 0$, and is from the centerline of the spreading droplet to the contact line. Then the point x_{hys}, where $l(x)$ is maximum, delineates the advancing and receding regions. $x > x_{hys}$ is the advancing part and $x < x_{hys}$ is the receding part in the droplet profile. At every time step the location of point of hysteresis is determined and the hysteresis

is applied by introducing static values of θ_a and θ_r to the disjoining pressure term. The model is schematically described in Figure 4.12.

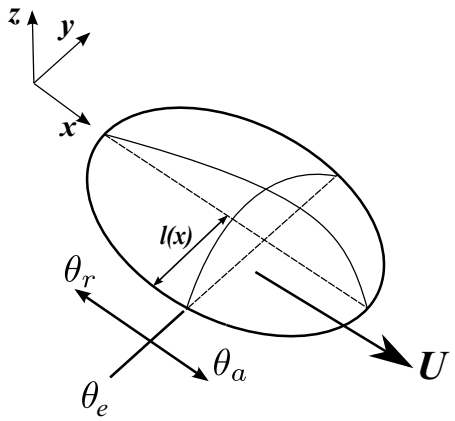

Figure 4.12: Contact angle hysteresis model

4.3.2 Analytical model

A number of analytical models are present in the literature to predict the velocity of the sliding/moving droplets (Kim et al., 2002; Fan et al., 2011; Sellier et al., 2013). In this section, a simple model is used to describe the constant terminal velocity achieved by the droplet as it slides down the inclined substrate. This motion is the result of a force balance between the gravitational force, capillary force present in the vicinity of the contact line, F_{cl}, and the viscous resistive force, F_r. According to Newton second law,

$$m\frac{dU'}{dt} = mg\sin\theta_i - F_{cl} - F_r, \tag{4.1}$$

where U' is the velocity with which the droplet slides down the incline. The left-hand side is equal to zero when the droplet reaches constant terminal velocity, i.e.

$$mg\sin\theta_i - F_{cl} - F_r = 0. \tag{4.2}$$

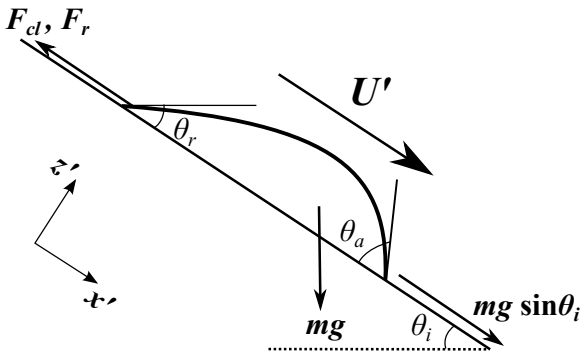

Figure 4.13: Schematic of the forces on the droplet as it slides down the inclined substrate

Figure 4.13 shows the force distribution on the droplet as it slides down the incline. If the droplet has a circular footprint during the sliding motion (Fan et al., 2011; Kim et al., 2002), then

$$F_{cl} = 2\sigma R_0 \int_0^{\pi} \cos\theta_c \cos\alpha d\alpha, \tag{4.3}$$

where σ denotes the surface tension of the fluid, α denotes the angular position, θ_c is the contact angle the droplet makes around the contact line. $\theta_c = \theta_a$ at the front of the droplet and $\theta_c = \theta_r$ at the rear of the droplet. Figure 4.14 shows the schematic of the contact angle, θ_c, as a function of the angular position.

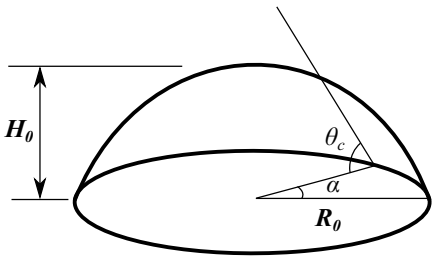

Figure 4.14: Illustration of the contact angle θ_c as a function of the angular position α

If the footprint of the droplet is assumed to be circular, then F_{cl} is given by,

$$F_{cl} = 2\sigma R_0 \left(\cos\theta_r - \cos\theta_a\right). \tag{4.4}$$

Wall shear stress is found to be (Sellier et al., 2013),

$$\tau_w = \frac{3\mu U'}{h}. \tag{4.5}$$

The resistive force is found by integrating the wall shear stress over the entire footprint of

the droplet,

$$F_r = \int_0^{R_0-\epsilon_c} \tau_w \left(2\pi r\right) dr, \tag{4.6}$$

where ϵ_c is the cut-off length to prevent the singularity at the contact line, h is the thickness of the droplet and is dependent on the radius, r. The profile of the droplet is approximated by a paraboloid,

$$h\left(r\right) = H_0 \left(1 - \frac{r^2}{R_0^2}\right), \tag{4.7}$$

where H_0 is the characteristic central height and R_0 is the characteristic base radius. Equation (4.2) can be written as,

$$mg\sin\theta_i - 2\sigma R_0 \left(\cos\theta_r - \cos\theta_a\right) - \int_0^{R_0-\epsilon_c} \frac{3\mu U'}{h} \left(2\pi r\right) dr = 0. \tag{4.8}$$

Equation (4.8) can be solved for the constant terminal sliding velocity, U'. Equation (4.1) can be written as,

$$mg\sin\theta_i - 2\sigma R_0 \left(\cos\theta_r - \cos\theta_a\right) - \int_0^{R_0-\epsilon_c} \frac{3\mu U'}{h} \left(2\pi r\right) dr = m\frac{dU'}{dt}. \tag{4.9}$$

Equation (4.9) can be solved to get the rate of change of velocity of the sliding droplet in case of variation of substrate inclination with time. Further extending this, it is possible to find the threshold inclination angle, $\theta_{threshold}$ after which the droplet starts to move. If the droplet is immobile, equation (4.9) can be simplified to,

$$mg\sin\theta_{threshold} = 2\sigma R_0 \left(\cos\theta_r - \cos\theta_a\right). \tag{4.10}$$

This model applies best when the footprint of the sliding droplet is close to a circle. If the equilibrium contact angle is lower, as in the case of water and glycerine solution droplets sliding on the glass substrate, the footprints formed by the droplets are not circular. These droplets form a large tail and a footprint which is complex and difficult to define mathematically. Podgorski and co-workers used silicone oil droplets on fluoro-polymer coated substrate having a θ_e of 45°. In the next section, the analytical model is used alongside numerical results and compared with experimental results.

4.4 Results and discussion

The numerical results are presented in terms of the position of the centre of gravity of the droplet as a function of time, see equations (3.1) and (3.2).

4.4.1 Comparison with the experimental literature

Podgorski and co-workers reported experiments about the change in shape of the spreading silicone oil droplet along an inclined fluoro-polymer (FC725 from 3M) coated substrate (Podgorski et al., 2001). At higher inclination angle, the speed attained by the spreading droplet increases. At a critical speed, the droplet shape is no longer rounded and develops a corner at the trailing edge. The shape of the corner becomes sharper up to 60^o of inclination, where it starts to shed smaller droplets behind (Podgorski et al., 2001). In the study of Podgorski et al., the capillary number, $Ca = \frac{\mu U'}{\sigma}$, is plotted against $Bo \sin\theta_i = \frac{\rho g V_0^{2/3}}{\sigma} \sin\theta_i$.

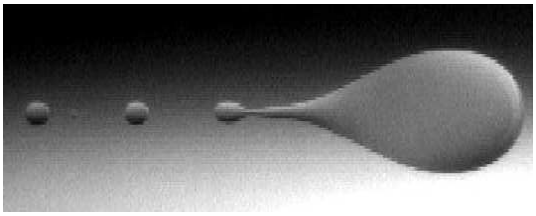

Figure 4.15: Satellite droplets (Podgorski et al., 2001)

Physical Property	**Silicone Oil (Podgorski et al., 2001)**
Density, kg/m^3	924
Viscosity, μ, Pa.s	0.00915
Surface Tension, N/m	0.0205
Equilibrium contact angle, θ_e, ^{o}	45
Advancing contact angle, θ_a, ^{o}	50
Receding contact angle, θ_r, ^{o}	40
Substrate inclination, θ_i, ^{o}	10-75
Volume of droplet, V_0, μl	8.3
Initial position of centre of gravity	(2,2)

Table 4.3: Properties of the silicone oil droplet spreading on inclined glass substrate

The physical properties of silicone oil on glass substrate are reported in Table 4.3, (Podgorski et al., 2001). In this section, experimental results from Podgorski et al. are introduced for comparison with the numerical model.

A mesh convergence study for precursor film thickness, h^* equal to 0.01 is performed, see Figure 4.16. Initially, the mesh is 960×128 which is then doubled to 1920×256 to investigate the effect of mesh refinement. Figure 4.16 shows that increasing the mesh density increases the accuracy at the expense of the computational resources. Above 1920×256 mesh resolution the results are very weakly affected. A noteworthy difference between the results of Podgorski et al. and the numerical results is the change of slope observed experimentally beyond $Bo \sin\theta_i = 1.3$ but not apparent in the simulation. It is thought to be an artefact of the way the position of the droplet is recorded: the present study uses the centre of gravity as the reference point while the reference point used by Podgorski et al. is not as clearly defined. Note that beyond $Bo \sin\theta_i = 1.3$, a cusp starts to develop at the rear of the droplets which is the likely cause for this change of slope.

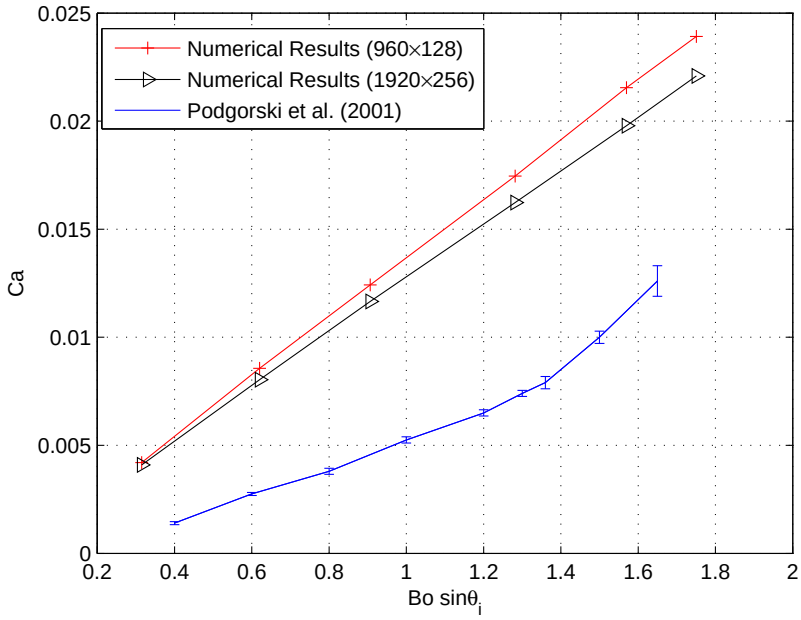

Figure 4.16: Mesh convergence without including contact angle hysteresis model: a comparison with experimental results from Podgorski et al. (Podgorski et al., 2001)

Figure 4.19a demonstrates the shape of the droplet at t=10 for different substrate inclination angles. As the inclination of the substrate is increased, the speed with which it slides increases. For lower inclination angles, the distance travelled by the droplet is small and the droplet approximately maintains its spherical cap shape. As the substrate inclination increases, the droplet forms a teardrop shape. At higher inclinations, the tail of the droplet thins further.

Another way to improve the numerical results is to decrease the precursor film thickness. The thickness of the precursor film, h'^*, is thought to range between 1 to 100 nm (Schwartz and Eley, 1998). Because this is very thin, it is not feasible to use realistic h^* in the numerical computations. For example, if the thickness of the droplet under consideration is 1mm, and a precursor film of 100 nm is used, this means the spatial mesh resolution must be of a very small order for two-dimensional simulations. If h^* is decreased by one order of magnitude, mesh must be refined by one order of magnitude in either direction i.e. 100 times more nodes subsequently increasing the computational time by 100 times. This does not take into account the fact that time step needs to be reduced too. For three-dimensional simulations it is out of computational reach in the near future. Related issues have been discussed in (Bertozzi and Brenner, 1997). Thicker precursor films tend to over predict the spreading rate. A good approximation for the wetting and dewetting phenomenon using thin precursor films requires fine mesh resolution in space and a finer time stepping (Diez et al., 2001; Schwartz, 1999). Thinner precursor films slow the motion of the contact line down because of the increasing viscous dissipation. Figure 4.17 shows the effect of reducing the precursor film thickness by 50% (i.e. $h^* = 0.005$). The mesh resolution of the mesh was doubled to maintain the accuracy (i.e. 3840×512). The results show that the prediction comes close to the experiment, but the computational time increases exponentially.

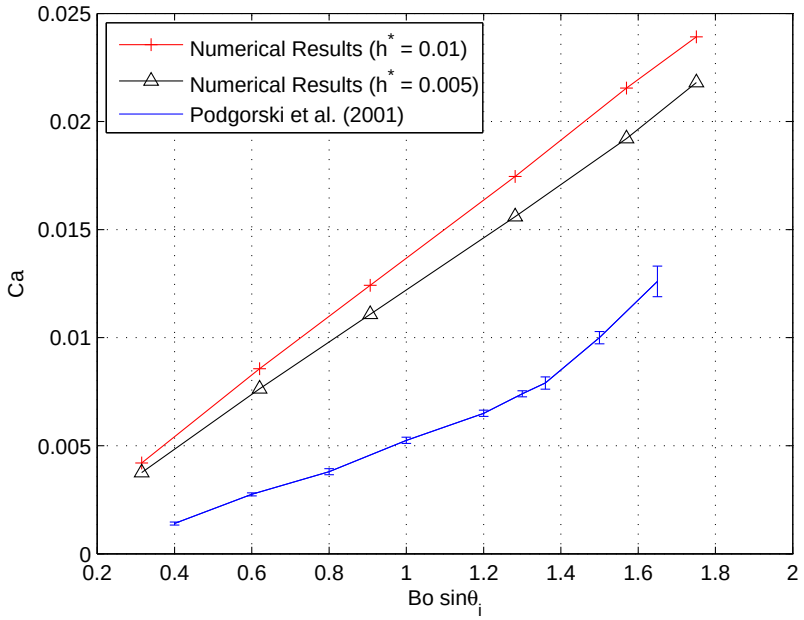

Figure 4.17: Effect of decrease in precursor film thickness, h^*, on the numerical results while comparing with experimental results from Podgorski et al. (Podgorski et al., 2001)

Later in the simulations, the value of h^* is equal to 0.01 and the mesh resolution of 1920×256 is used. In the results above, contact angle hysteresis is not included. The motion of the sliding droplet is affected by the inclusion of hysteresis. In the next instance, contact angle hysteresis, θ_{hys}, of 10^o is imposed, i.e. $\theta_a = \theta_e + (\theta_{hys}/2)$ and $\theta_r = \theta_e - (\theta_{hys}/2)$, where $\theta_e = 45^o$.

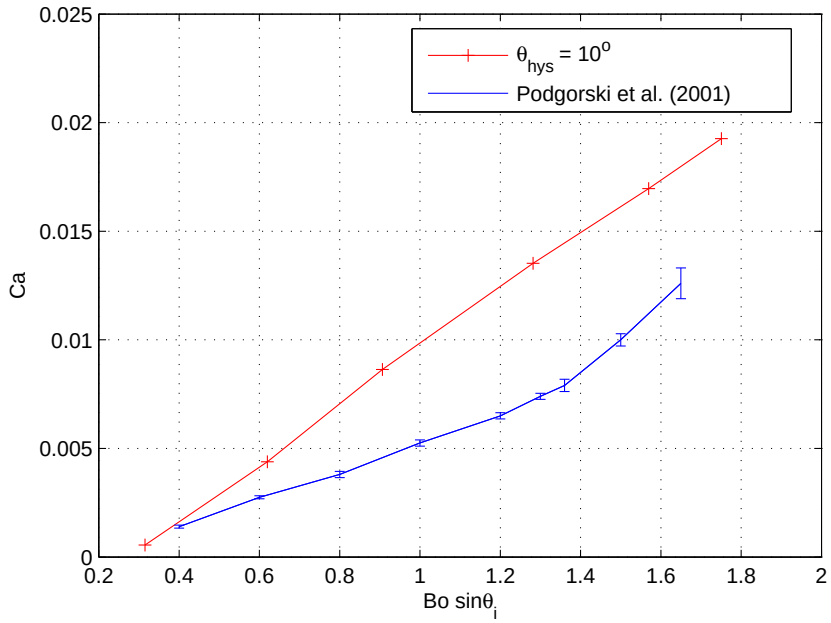

Figure 4.18: Comparison of experimental results (Podgorski et al., 2001) and numerical ones with a contact angle hysteresis of 10^o

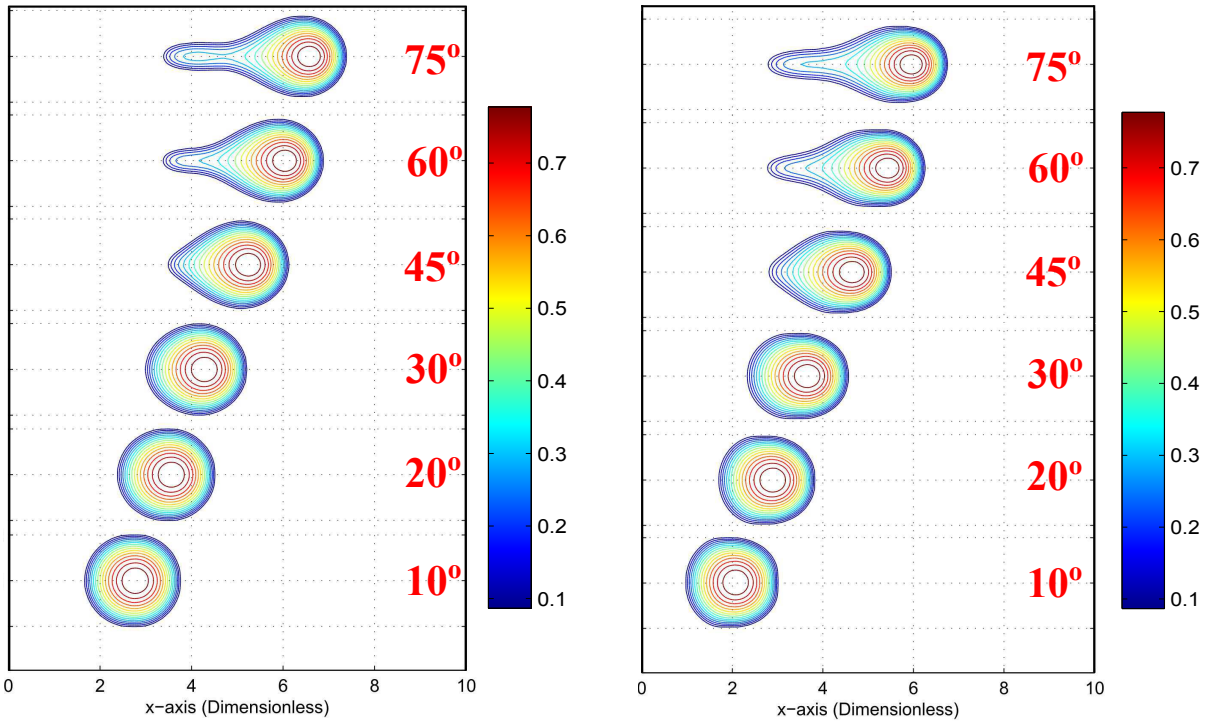

(a) $\theta_{hys} = 0^o$ (b) $\theta_{hys} = 10^o$

Figure 4.19: Thickness contours of the silicone oil droplets sliding down the incline (a) without hysteresis and (b) with hysteresis of 10°, for t=10 for different substrate inclinations

Figure 4.18 demonstrates that the application of contact angle hysteresis reduces the speed of the sliding droplet and it comes closer to experimental observations. It is generally observed that the advancing contact angle increases and receding contact angle reduces with increase in speed of the sliding droplet (Blake, 2006). The assumption of a uniform contact angle hysteresis of 10° for the entire range of substrate inclinations is only an approximation. This is well demonstrated from the plot in Figure 4.18. At lower inclination angles the droplet has a low velocity and a hysteresis of 10° which causes the droplet to slow down more than the experimental observations.

Figure 4.19b shows the droplet thickness contours of the droplets sliding with $\theta_{hys} = 10^o$ at t=10 for different substrate inclination angles. Figures 4.19a and 4.19b clearly show that the hysteresis reduces the speed with which the droplet slides down. This additional dissipative force explains why the numerical and experimental results are in better agreement, see Figure 4.18. For large inclination angles, the droplet forms a teardrop shape, but the tail formed is not as narrow as in the without hysteresis case.

Using the physical properties mentioned in Table 4.3, equation (4.8) is used to calculate the velocity using the analytical model. Analytical results are dependent on the value of the cut-off length, ϵ_c.

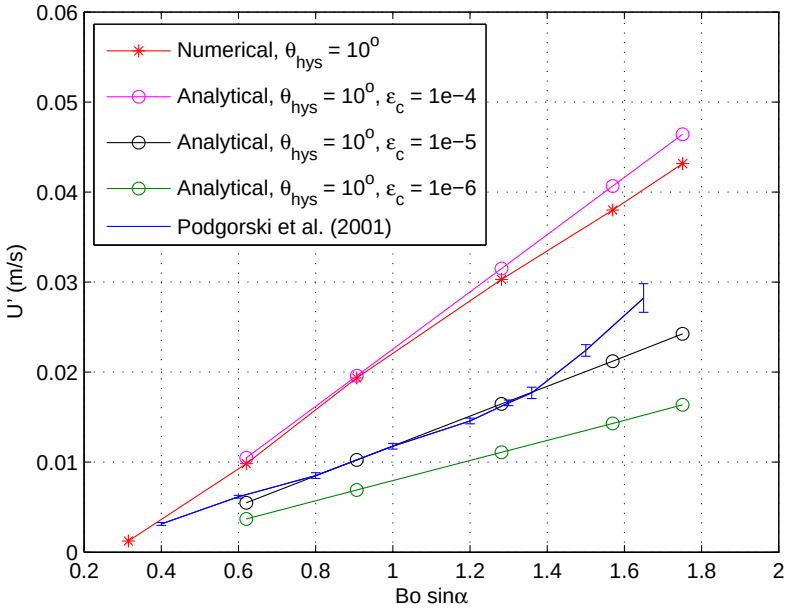

Figure 4.20: Comparison between experimental, numerical and analytical results

Figure 4.20 shows a comparison of the experimental, analytical and numerical results. It is clearly depicted that ϵ_c has an impact on the analytical results. For ϵ_c equal to 1×10^{-5}m, the analytical solution has an excellent agreement with the experimental results when the droplet has a near constant circular footprint. At higher inclination angles, the footprint of the droplet develops a cusp. As soon as this cusp is developed, the analytical model is a weaker approximation. When ϵ_c is increased to 1×10^{-4}m, the analytical solution has come closer to the numerical results where the inclination angles are lower and the droplet footprint is close to a circle. Analytical and numerical results deviate due to cusp formation at higher inclination angles. It is clear from these results, that the cut-off length ϵ_c plays a critical role in the prediction of the terminal velocity for the system considered. It appears that the optimal value of ϵ_c for this particular system is 10^{-5}m.

As a further test of the correct modelling of contact angle hysteresis, it is checked that the motion of the droplet stops when a varying substrate inclination reaches a threshold value. Increasing inclination angles beyond this threshold inclination angle should start the sliding

droplet motion at a particular contact angle hysteresis. Therefore as a final illustrative example, silicone oil droplets for the physical properties stated in Table 4.3 are allowed to flow down an inclined glass substrate with a variable inclination. Starting from an initial inclination of 10^o the inclination is ramped up in increments of 10^o every 2 dimensionless time units up to an inclination angle of 70^o in Case 1. Case 2 is the reverse cycle. This can be described with the help of Figure 4.21.

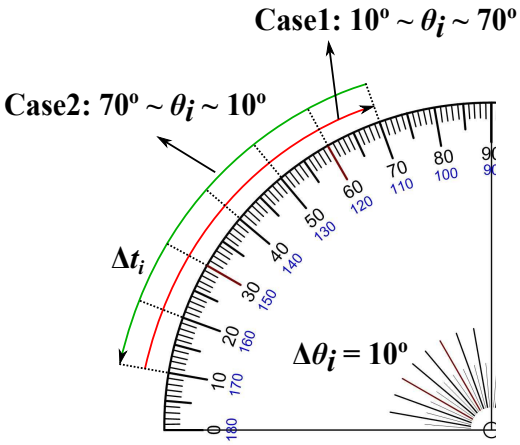

Figure 4.21: Protractor to show the variation of inclination angle, θ_i

The silicone oil droplet is released from a stationary equilibrium position. There are three different situations that are reported here. Firstly, the droplet slides down the incline without hysteresis ($\theta_{hys} = 0$). In the second and third cases θ_{hys} is introduced using the model defined in Section (4.3.1) to investigate its effects on the motion and shape of the droplet. An hysteresis of 10^o and 20^o is introduced for Cases 1 and 2, such that $\theta_a = \theta_e + (\theta_{hys}/2)$ and $\theta_r = \theta_e - (\theta_{hys}/2)$. The optimum cut-off length, ϵ_c is 1.4×10^{-4} m for these particular cases. This value of ϵ_c is used because, it gives the best closest match with the numerical results.

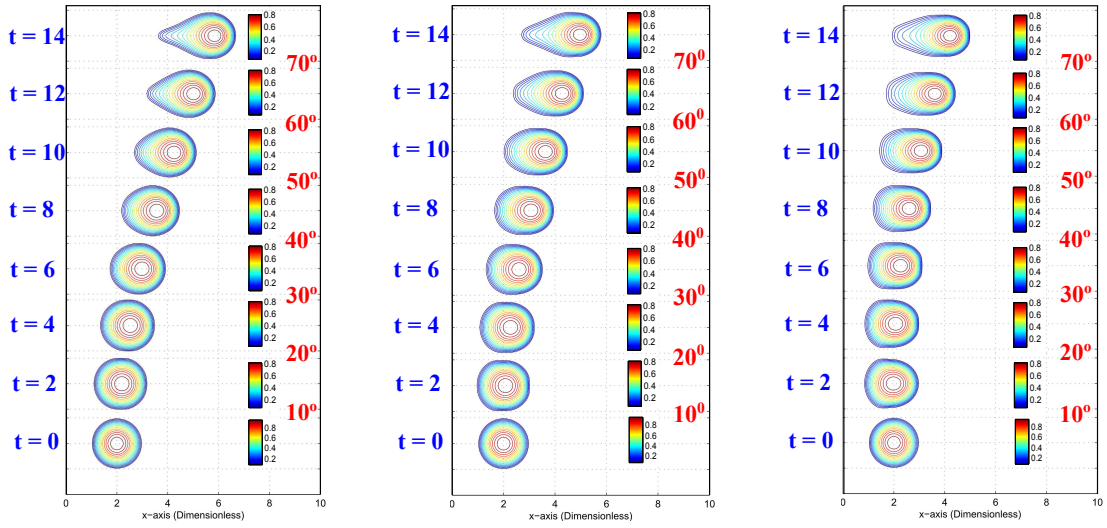

(a) $\theta_{hys} = 0^o$ (b) $\theta_{hys} = 10^o$ (c) $\theta_{hys} = 20^o$

Figure 4.22: Effect of contact angle hysteresis on the shape and displacement of silicone oil droplets for Case 1 scenario and $\Delta t_i = 2$

Figure 4.22 shows the three hysteresis situations for Case 1. It displays the contours of the droplet thickness. With no hysteresis, see Figure 4.22a, the droplet starts to move on the substrate at very small inclination angles around 10^o. As the inclination is increased, the speed gained by the droplet increases due to an increase in gravitational pull. It is visible from the contours that the shape of the droplet changes to an oval shape and then to a more conical shape. Figure 4.22b describes the effects of a 10^o hysteresis on the motion and shape of the droplet. In the start, the droplet moves very slightly but the equilibrium shape of the droplet changes. Contact angle hysteresis restricts the motion of the droplet. An interesting point to note is that the conical shape of the contours starts to appear when the inclination angle is large. Figure 4.22c demonstrates the effect of $\theta_{hys} = 20^o$ on the shape of the sliding droplet. An interesting point to note here is that the conical shape is not developed and the sliding velocity is reduced further.

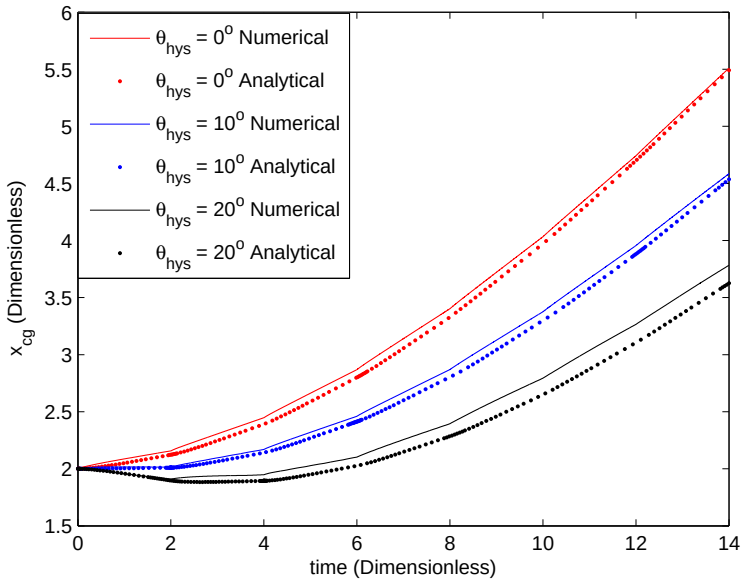

Figure 4.23: Position of center of gravity for contact angle hysteresis, $\theta_{hys} = 0^o$, 10^o, 20^o for Case 1 scenario for 14 non-dimensional time units

Figure 4.23 shows the position of the center of gravity of the droplet against time for the three situations. Initially at t=0, $x_{cg} = 2$. The position of the center of gravity is calculated with the help of equations (3.1) and (3.2). Results from the analytical model are also plotted. Forces due to hysteresis are greater than the gravitational forces due to inclined substrate. At greater hysteresis, the rear of the droplet spreads due to smaller contact angle causing the x_{cg} to shift backward. This is visible from the Figure 4.23 and the shape of the contours $\theta_{hys} = 20^o$ in Figure 4.22c. Both results show the same trend. There is an offset developing between both sets of results as the substrate inclination increases. This is primarily due to the change in footprint shape from a circle to a more oval shape, refer to Figure 4.22.

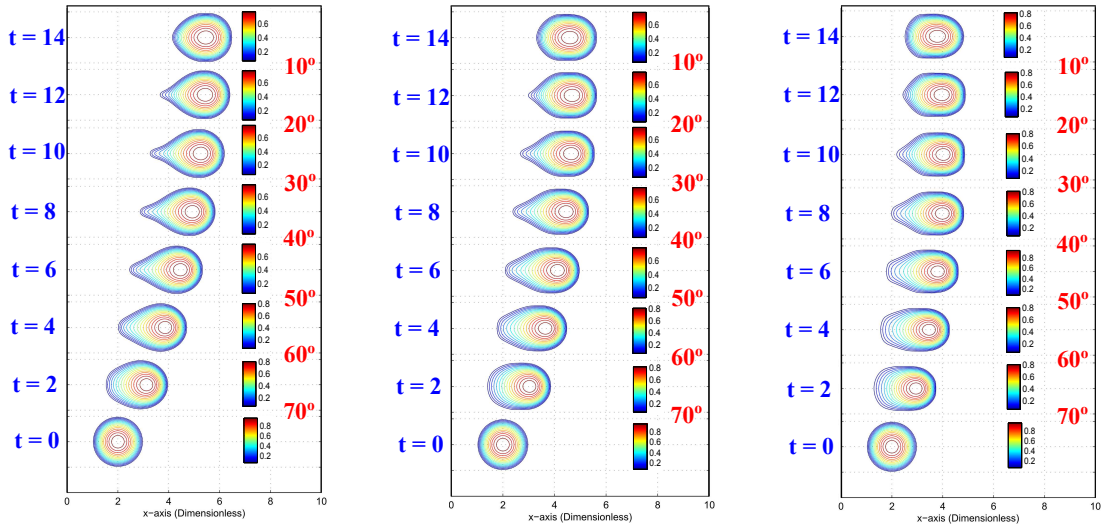

(a) $\theta_{hys} = 0^{o}$ (b) $\theta_{hys} = 10^{o}$ (c) $\theta_{hys} = 20^{o}$

Figure 4.24: Effect of contact angle hysteresis on the shape and displacement of silicone oil droplets for Case 2 scenario and $\Delta t_i = 2$

Figure 4.24 shows the three situations in Case 2. The Case 2 scenario is important in the sense that in Case 1, the droplet was accelerated gradually with time. In Case 2, the droplet is first accelerated due to high inclination angles then its speed is reduced due to the reduction in inclination angle. Figure 4.24a illustrates the motion of the droplet as it slides down the incline without hysteresis. In the start, the droplet slides down quickly forming a conical shape, but as the inclination is reduced the sliding speed is reduced. This happens due to reduction in gravitational forces with reduction in the tilt angle. An important point to note here is that the droplet shape changes from conical to a more oval shape. Reduction in speed does not cause the droplet to stop entirely for the case without hysteresis, it slides very slightly. Figures 4.24b and 4.24c represents the droplet shapes as it slides down with θ_{hys} of 10^{o} and 20^{o}. It clearly shows that as the hysteresis is increased the sliding velocity is reduced and the corresponding shape of the droplet is more oval. An important feature to note here is that the droplet stops to move at very low inclinations and the part of the droplet that expanded previously due to high inclinations starts to collect and form an oval shape, a well-known and observed consequence of contact angle hysteresis. This is in line with the theory that the hysteresis tends to stop the moving droplet until there is a change in physical condition.

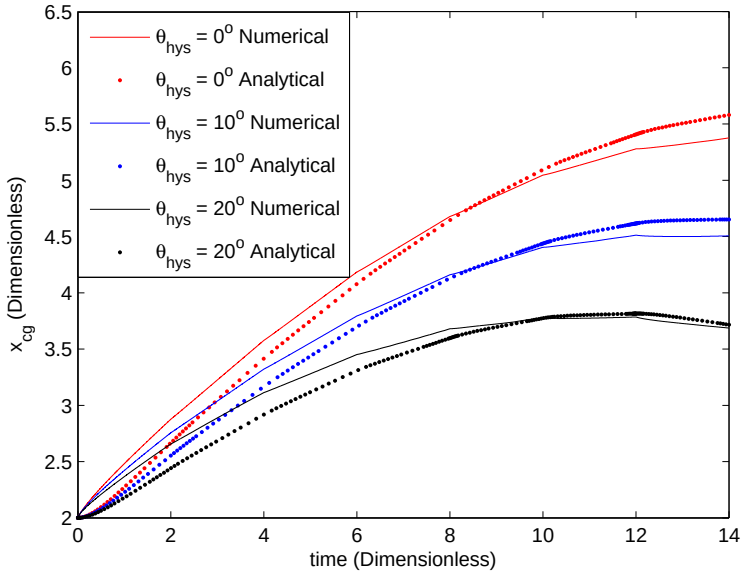

Figure 4.25: Position of center of gravity for contact angle hysteresis, $\theta_{hys} = 0^o$, 10^o, 20^o for Case 2 scenario for 14 non-dimensional time units

Figure 4.25 represents the position of the center of gravity of the droplet with time for the three situations for Case 2 scenario. Initially the droplet sliding velocity increases for all the three situations, but contact angle hysteresis plays a significant role in decelerating the droplet. Results from the analytical model are close to numerical results, but they are different in the start. In the start, the inclination angles are high, causing the droplet footprint to change instantaneously to an oval shape, whereas the analytical model assumes the droplet footprint to be circular, see Figure 4.24.

Up to this point, we have presented the effects of hysteresis has on two different scenarios in which the inclination angle is changing after 2 dimensionless time units for three different hysteresis situations. Δt_i is doubled next to investigate the influence on the shape and speed of the sliding droplet.

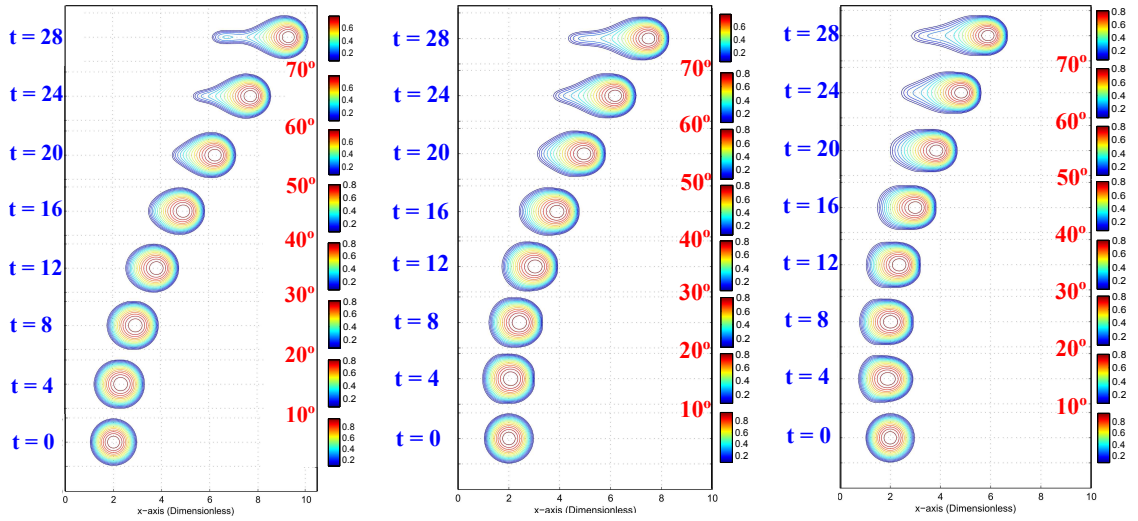

(a) $\theta_{hys} = 0^o$ (b) $\theta_{hys} = 10^o$ (c) $\theta_{hys} = 20^o$

Figure 4.26: Effect of contact angle hysteresis on the shape and displacement of silicone oil droplets for Case 1 scenario and $\Delta t_i = 4$

Figure 4.26 illustrates the shape of the droplet as it slides down the incline for Case 1 scenario. Figure 4.26a, shows that the droplet slides faster as the inclination angle is increased. At higher inclination angles, the droplet takes the form of a teardrop with a very narrow tail which elongates with time. Figures 4.26b and 4.26c describe the effects of increasing the contact angle hysteresis on the shape of the sliding droplet. As the hysteresis is increased, one of the direct effects is that the sliding velocity decreases; the other effect is that the teardrop shape formed at higher inclinations becomes less narrow.

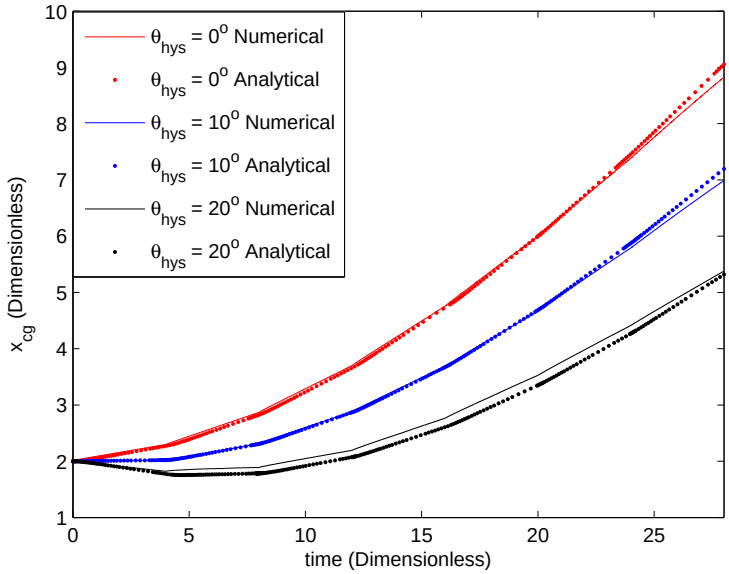

Figure 4.27: Position of center of gravity for contact angle hysteresis, $\theta_{hys} = 0^o$, 10^o, 20^o for Case 1 scenario for 28 non-dimensional time units with a $\Delta t_i = 4$

Figure 4.27 represents the position of the center of gravity of the droplet. It shows that the droplet moves slowly at the start, but as the gravitational force increases due to the increase in inclination, it moves down more rapidly. The increase in contact angle hysteresis reduces the pace of the sliding droplet. Results from the analytical model are close to the numerical results. There is an increase in backward shift of the center of gravity when Figures 4.23 and 4.27 are compared. The reason for this increase is due to increase in the time duration for the substrate to remain at 10°. Small discrepancies in these results arise when the shape of the footprint is far from a circular shape i.e. oval or a tear drop shape, refer to Figure 4.26.

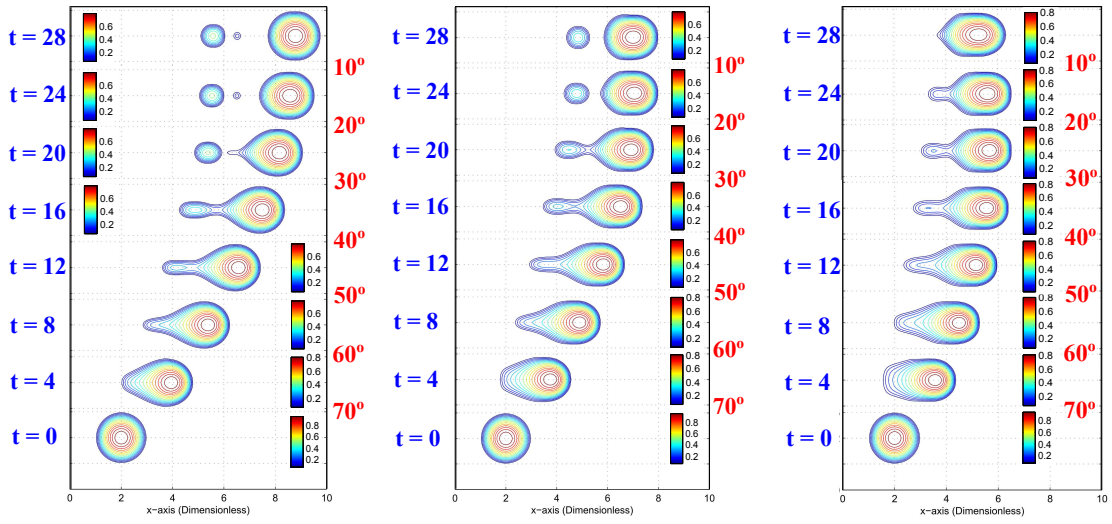

(a) $\theta_{hys} = 0^{o}$ (b) $\theta_{hys} = 10^{o}$ (c) $\theta_{hys} = 20^{o}$

Figure 4.28: Effect of contact angle hysteresis on the shape and displacement of silicone oil droplets for Case 2 scenario and $\Delta t_i = 4$

Figure 4.28 illustrates the shape of the droplet as it slides down the incline for Case 2. Figure 4.28a presents the situation in which the droplet slides down the incline without hysteresis. At the start the droplet gains velocity due to high inclination angles which causes it to expand initially to form a teardrop shape. As the inclination angle is reduced, the tail of the teardrop shape becomes narrow to the extent that the sliding droplet breaks up leaving behind satellite droplets. An important feature to observe here is that the major drop volume slides quickly in comparison to the satellite droplets. Figure 4.28b shows the results for $\theta_{hys} = 10^{o}$. The speed with which the droplet slides down is decreased in comparison to the one achieved without hysteresis. Droplet breakup is delayed due to reduction in the overall speed of the droplet, but the droplet eventually breaks up. In the last 4 dimensionless time units of the simulation, the droplet is almost stationary on a 10° inclination. Figure 4.28c demonstrates the effects of $\theta_{hys} = 20^{o}$. As it slides down the incline, the droplet first changes its shape to

a teardrop then develops a narrow tail. This tail does not gets separated due to low sliding speeds at lower inclination angles. In the last few seconds, the droplet is seen to retract, which results in the center of gravity shifting up slope as can be seen in the Figure 4.29.

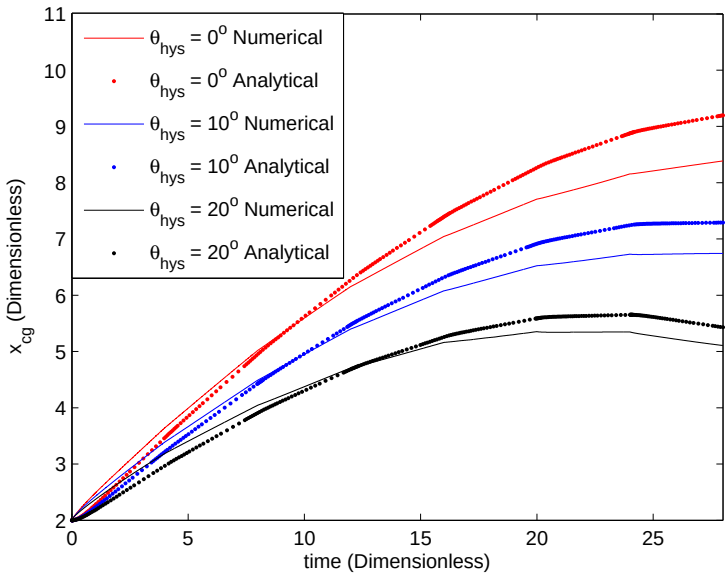

Figure 4.29: Position of center of gravity for contact angle hysteresis, $\theta_{hys} = 0^o$, 10^o, 20^o for Case 2 scenario for 28 non-dimensional time units

Figure 4.29 represents the position of the center of gravity of the droplet with which it slides down for Case 2. It shows that the droplet moves rapidly in the start, but as the gravitational forces decrease due to decrease in inclinations, it moves down slowly. Increase in hysteresis progressively reduces the pace of the sliding droplet. The apparent upslope motion of the droplet for θ_{hys} of 20^o is due to stationary contraction of the droplet at low inclination.

Making use of equation (4.10), the threshold inclination angle, $\theta_{threshold}$ can be calculated to further analyze the results from the numerical simulations. Evaluating $\theta_{threshold}$ for different contact angle hysteresis gives,

Contact angle hysteresis, θ_{hys}, ^{o}	**Threshold inclination angle, $\theta_{threshold}$, ^{o}**
0	0.00
10	9.21
20	18.56

Table 4.4: Threshold inclination angle calculations using equation (4.10)

It is clear from the Table 4.4 that for greater θ_{hys} the threshold inclination angle becomes bigger. This is also supported from the plots for center of gravity with time, see Figures

4.23, 4.25, 4.27 and 4.29. It is clearly shown that for a hysteresis of 10°, the position of the center of gravity of the droplet does not change with time for an inclination of 10°. As the hysteresis is increased to 20°, the droplet is stationary (center of gravity not changing with time) for inclination of 20° and if the inclination is less that 20° the droplet starts to retract.

4.4.2 Comparison with experiments

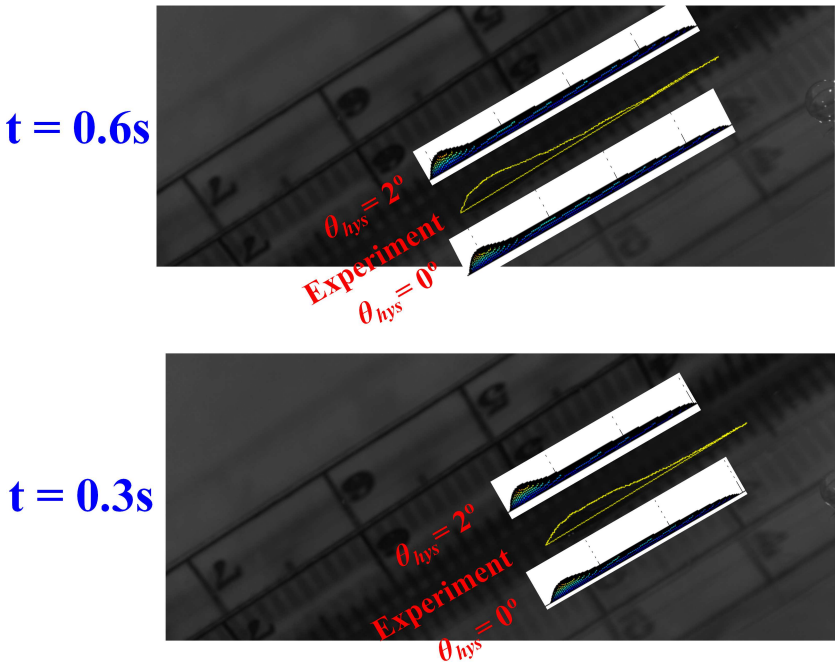

Figure 4.30: Comparison of the side-view of glycerine solution droplet profiles with the numerics at $\theta_i = 30^o$ sliding with and without hysteresis on glass substrate

Physical properties of the fluids used in the simulations are stated in Tables 4.1 and 4.2. Figure 4.30 shows the side-view of the glycerine solution droplets sliding down a 30° inclined glass substrate. In this figure, the position (along x) and the scale of the numerical droplet match the experimental case. The experimental droplet profiles are compared with the numerical results. With and without hysteresis, it is clear that as time passes the droplet elongates because of smaller equilibrium contact angle. As seen from the Figure 4.30, hysteresis results are close to the experimental results, but are not precisely matched.

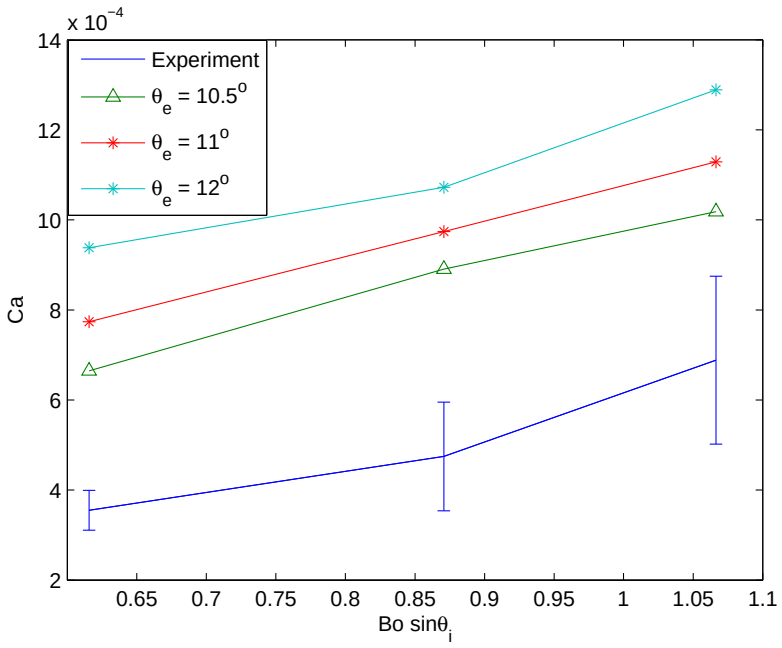

Figure 4.31: Ca versus $Bo \sin\theta_i$ for water

Figure 4.31 represents Ca versus $Bo \sin\theta_i$ for water, where θ_i is the angle of inclination of the substrate with the horizontal plane. The equilibrium contact angle of the water varies between 10.5° to 12° for the glass substrate, see Table 4.1. For different equilibrium contact angles and zero hysteresis, the numerical results are plotted. The results from the numerical code tend to over-estimate the sliding speed relative to experimental results. The numerical results can be improved by introducing contact angle hysteresis. The advancing contact line is well defined which is not the case for the receding contact line, because the droplet leaves a thin film as it slides down the inclined substrate causing errors in the accurate estimation of the location of the centroid with time.

In the above numerical results, a constant equilibrium contact angle is applied but actually the water droplet slides down the glass substrate with an advancing and receding contact angle which is different from the equilibrium contact angle. The equilibrium contact angle for water is quite low so a contact angle hysteresis, $\theta_a - \theta_r$, of 2° and 4° is applied in the simulation for equilibrium contact angles of 10.5° and 11°, i.e. $\theta_a = \theta_e + (1^o, 2^o)$ and $\theta_r = \theta_e - (1^o, 2^o)$.

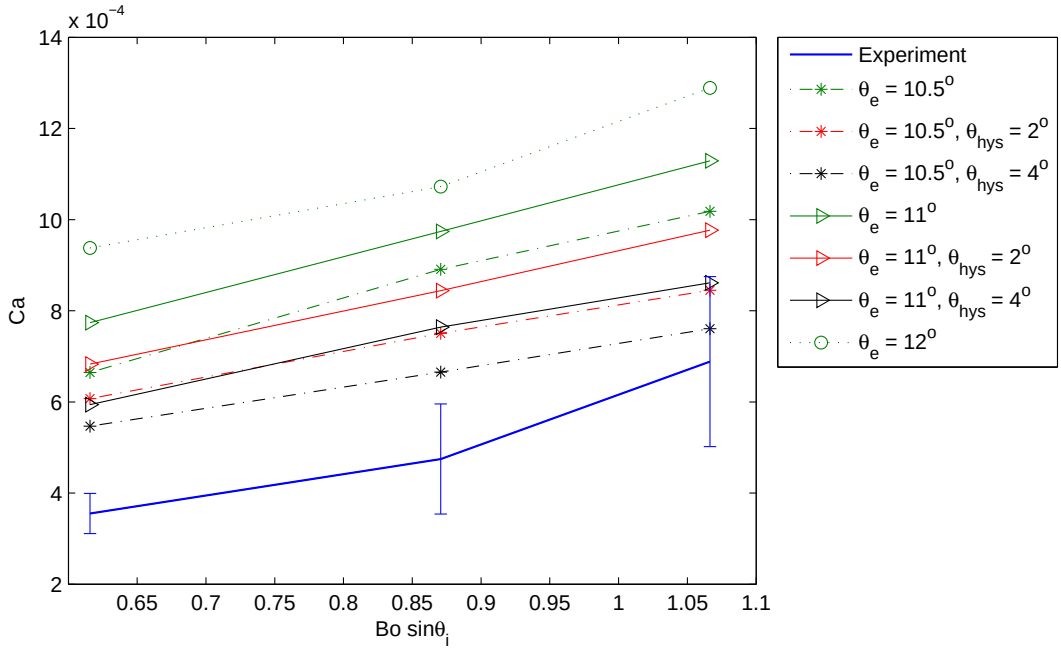

Figure 4.32: Effect of contact angle hysteresis on spreading of water droplets for equilibrium contact angles of 10.5° and 11°

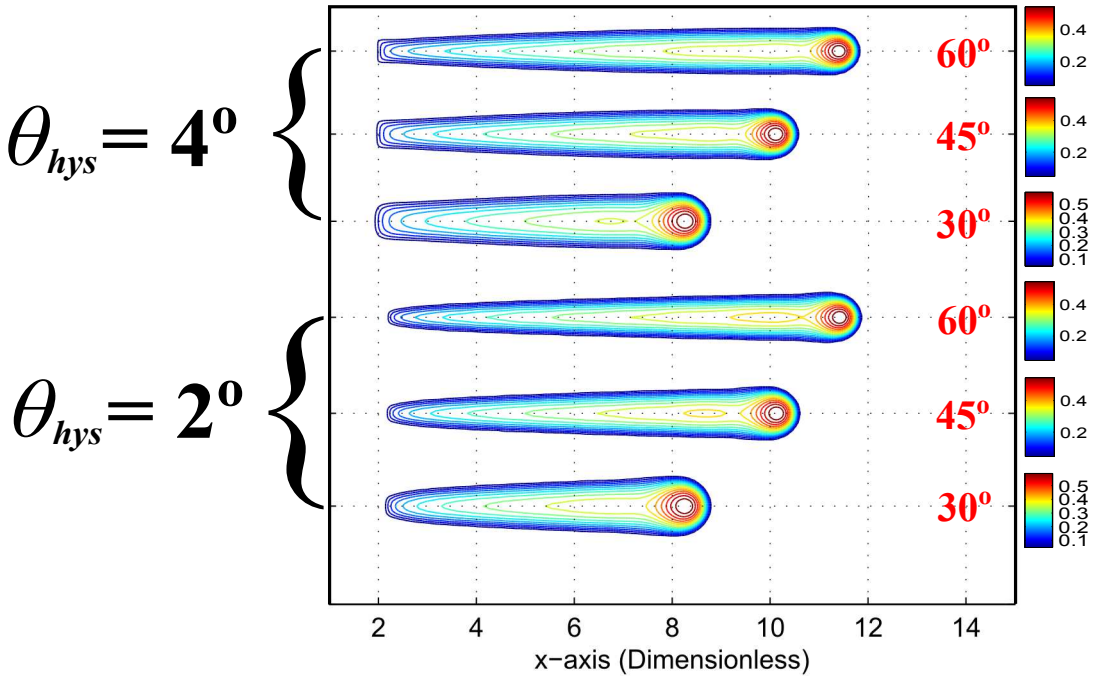

Figure 4.33: Effect of hysteresis on the shapes of water droplets after 4 dimensionless time units sliding on inclined substrates having, $\theta_e = 11^o$

Figure 4.32 demonstrates that with the increase in hysteresis the results produced come into much closer agreement with the experimental ones. Figure 4.32 indicates that if a lower equilibrium contact angle for water is used for the hysteresis analysis, it will produce results in reasonable agreement to the experimental investigation.

Figure 4.33 shows the effect of hysteresis on the contours of height for water droplet at different inclinations and after 4 dimensionless time units. It can clearly be deduced from the figure that the shape of the droplets under hysteresis is quite different. For a lower hysteresis, the shape of the tail is thinner in comparison to the droplets with larger θ_{hys}. This wider tail in case of large hysteresis causes the motion of the center of gravity of the droplet to slow down. In the experiments, rounded tail was observed, but as shown in Figure 4.30 the tail was not an exact match of the sliding droplets. In nature the tail formed by water and glycerine droplets on glass substrate is not uniform as that observed numerically.

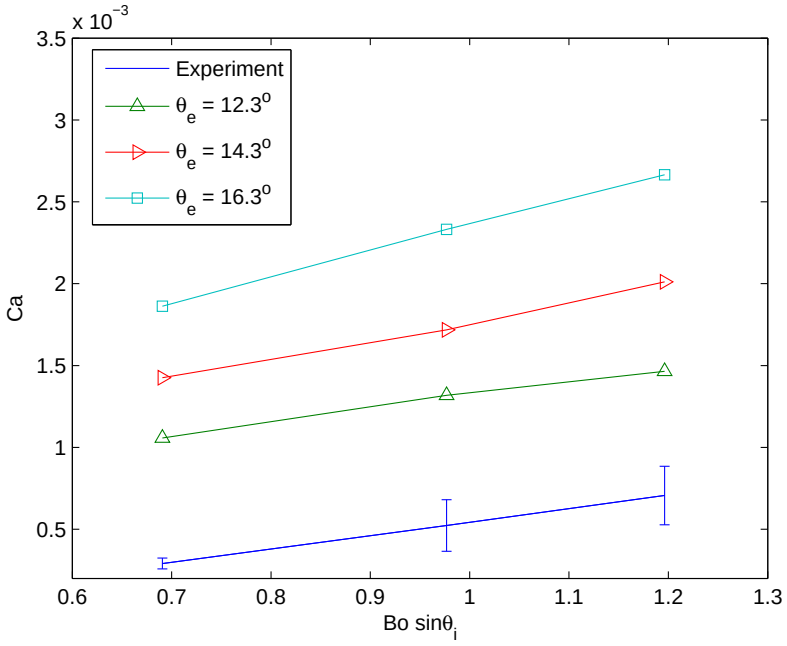

Figure 4.34: Ca versus $Bo \sin\theta_i$ for glycerine 50% by weight solution

Figure 4.34 represents Ca versus $Bo \sin\theta_i$ for glycerine 50% by weight solution. The equilibrium contact angle of this solution is $14.3^o \pm 2^o$ for the glass substrate, see Table 4.2. Computationally, three equilibrium contact angles are used. The reason for this choice is due to the uncertainty on the equilibrium contact angle when estimated with the help of the procedure stated earlier in the experimentation section. The trend of experimental spreading of glycerine solution droplets is similar to the one from the numerical code. The numerical results may be improved by introducing contact angle hysteresis.

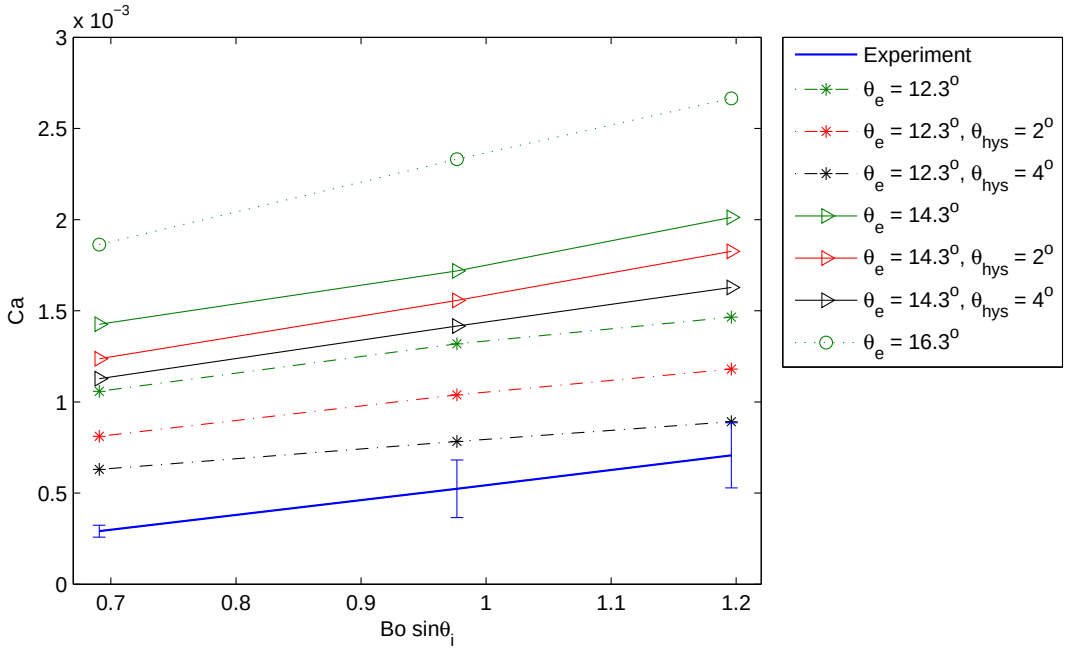

Figure 4.35: Effect of contact angle hysteresis on spreading of glycerine solution droplets for equilibrium contact angles of 12.3° and 14.3°

Figure 4.35 considers a hysteresis of up to 4° in the advancing and receding contact angles for the 12.3° and 14.3° equilibrium contact angle. It is clear from this figure that the introduction of hysteresis causes the results to converge towards the experimentation. Analyzing the lower bound of the estimated equilibrium contact angle, i.e. 12.3°, with a hysteresis, $\theta_a - \theta_r$, of 4° demonstrates a further reduction in the speed with which the droplet spreads on an inclined substrate, see Figure 4.35. Thus, increasing the hysteresis in the simulations improves the agreement with experimentation.

4.5 Concluding remarks

In this work, a mathematical model based on the lubrication approximation which describes the spreading/sliding motion of gravity driven fluid droplets under the influence of contact angle hysteresis is presented. This mathematical model consists of highly non-linear PDEs which are solved numerically via the Multigrid technique. A model to incorporate the contact angle hysteresis is proposed and implemented to investigate the effect of contact angle hysteresis on the motion of the droplets as they slide down the incline. A simple analytical model is also suggested to predict the dynamics of the sliding motion of the droplet. The results from the analytical and numerical implementation are compared with the experimental

results available in the literature and a new set of data obtained in this study. The shape of the droplets observed in the numerical simulations tends to agree with the shapes of the droplet described in the literature. Based on this, special cases are discussed in which the droplets tend to break up leaving satellite droplets behind. Droplets stick to the substrate in a few cases where the forces due to hysteresis overcome the forces present due to gravitational pull. An important effect of equilibrium contact angle is observed, i.e. the droplets having small θ_e are likely to form long tails as they slide down the incline substrates and the droplets with large θ_e are more likely to have shapes closer to teardrops. It has been shown here that our numerical simulations are able to capture the main effect of contact angle hysteresis.

Chapter 5

Leveling dynamics of thin non-Newtonian fluid films and verification of the numerical implementation

Contents

Most of Chapter 5 will appear in the paper titled, "Rheological effects on the leveling dynamics of thin fluid films." which has already been accepted for publication in the International Journal of Numerical Methods for Heat and Fluid Flow. This work was co-authored with Dr. Mathieu Sellier, Dr. Yeaw Chu Lee, Dr. Mark Jermy and Dr. Michael Taylor.

This chapter describes the numerical implementation of the non-Newtonian rheology in the FILMPAR framework. This chapter starts with by discussing the leveling dynamics of thin non-Newtonian films. The leveling dynamics of thin films is investigated because of the relative simplicity of the problem due to the absence of a contact line reducing the computational requirements. Keeping this advantage in mind, the non-Newtonian rheology described by a power-law is implemented in the numerical code. This implementation is verified through using approximate results obtained using the Method of Manufactured Solutions. In the next Chapter 6, the verified implementation of the leveling of thin films is used to explore the spreading and sliding dynamics of non-Newtonian fluid droplets on inclined substrates.

5.1 Introduction

During a coating application, the uniformity of the coated film is of prime significance. The coated film is allowed to level/flatten significantly before drying. At a microscopic level, leveling may influence the smoothness of coated film. The process of leveling is important to many physical phenomena such as coating applications, polymer films used in lithography, painting, electronic displays and in solar panel technology. In general, polymers, paints, and coatings exhibit non-Newtonian rheology, in which the viscosity is dependent on the variation of shear rates. When non-Newtonian fluids undergo a shear flow, they behave as a Newtonian fluid at low shear rates. This Newtonian behavior disappears as the shear rate is increased. If the viscosity increases with increasing shear rate the fluid is a shear-thickening or dilatant fluid and if the viscosity decreases with increasing shear rate, the fluid is described as shear-thinning or pseudo-plastic fluid. At higher shear rates this shear dependent behavior reaches a constant value of viscosity. Fluid rheology is discussed in detail in Section 1.3.3. Mostly in coating applications a uniform thin film thickness is desired, but this is not achieved due to the solidification of thin film before it levels completely. Therefore understanding the underlying factors which impact the leveling dynamics of thin films is very important.

The leveling of thin fluid films has been studied extensively, primarily due to its importance in coating processes. Orchard (Orchard, 1963) was the first to study the leveling problem theoretically where the leveling of sinusoidal perturbations at low Reynolds numbers are solved using the two-dimensional Stokes equations. The proposed linear theory predicted the time taken for the amplitude of the free surface perturbation to evolve and level. Based on two key assumptions, that the fluid is Newtonian and evaporation is negligible, good agreements between the derived linear theory and the non-linear film thickness governing equations for both thick and thin films are obtained. Later Kheshgi and Scriven (Kheshgi, 1988) used the long wave expansion and finite element method to derive the governing equations for the leveling of Newtonian fluids.

A main driving force behind the leveling of Newtonian fluids is surface tension. Overdiep (Overdiep, 1986) considered the leveling of a two component fluid containing a resin and a solvent where only the solvent is able to evaporate. This study demonstrated that evaporation of the fluid causes spatial surface tension gradients which directly impact on the leveling dynamics. Wilson et al. (Wilson, 1993; Howison et al., 1997) investigated the above model and the numerical results showed good agreement with experimental data.

The leveling of fluid films with different rheologies has also been explored. Keunings and Bousfield (Keunings and Bousfield, 1987) studied the leveling of viscoelastic fluids. They found that the surface tension influenced leveling of viscoelastic fluids using Orchard's asymptotic analysis provides a good measure for the leveling rate. Leveling of shear-thinning fluids is of prime importance when dealing with coatings but it had not received significant attention prior to Iyer and Bousfield's work (Iyer and Bousfield, 1996). They used the lubrication approximation thereby reducing the transient two-dimensional problem to a one-dimensional problem with the Carreau model for the employed fluid in their formulation. Leveling experiments of the non-Newtonian fluid that were performed demonstrate a reasonable agreement with their suggested Finite-Difference model. Investigations using the lubrication approximation with various non-Newtonian fluids were performed by Tsai et al. (Tsai et al., 2010) who investigated the leveling of colloidal suspensions while Livescu et al. (Livescu et al., 2011) investigated the leveling of thixotropic liquids which have a shear-thinning property.

Murphy (Murphy, 1968) derived the governing equations for a power-law fluid using Orchard's formulation and was extended by Ganguly et al. (Ganguly et al., 2012) for films flowing down an inclined plane using the lubrication approximation. Following the above approach, the author and others have derived the governing equations using a power-law fluid for droplets spreading and sliding on smooth inclined substrates (Ahmed et al., 2013) via the use of the disjoining pressure term (De Gennes, 1985; Schwartz and Eley, 1998).

This chapter presents a thorough numerical study of the leveling of a fluid having power-law rheology. Section 5.2 provides the details of the governing power-law equations and the numerical formulation of the proposed model. Section 5.3 is devoted primarily to the validation of the numerical scheme with the help of the Method of Manufactured Solutions (MMS). Lastly, Section 5.4 presents the results from the numerical simulations for thin fluid films of different rheologies leveling on horizontal substrates. This section also highlights key differences between the leveling of two-dimensional and three-dimensional film thickness perturbations. Conclusions are drawn in Section 5.5.

5.2 Mathematical model and numerical implementation

The non-Newtonian rheology is implemented using a simple power-law model. In this section, the model described earlier in Chapter 2 is extended to account for the non-Newtonian rheology. It is a model with two parameters: the consistency factor K, and the flow behavior index, n. The consistency factor, K, is always greater than zero and is known as the viscosity coefficient. It has units Pa.s$^{\mathrm{n}}$ to achieve dimensional consistency. The flow behavior index is also known as the power-law exponent which dictates the rheology of the fluid. The stress tensor τ_{ij} for an incompressible power-law fluid is defined by,

$$\tau_{ij} = 2K \left(4D_{kl}D_{lk}\right)^{(n-1)/2} D_{ij}, \tag{5.1}$$

$$n \begin{cases} < 1 & \text{Shear thinning,} \\ = 1 & \text{Newtonian,} \\ > 1 & \text{Shear thickening.} \end{cases}$$

where

$$D_{ij} = \frac{1}{2}\left(\frac{\partial u_i'}{\partial x_j'} + \frac{\partial u_j'}{\partial x_i'}\right) \tag{5.2}$$

D_{ij} is the strain-rate tensor with the spatial components as x_i' and velocity components as u_i'. Making use of equation (5.2), the second invariant, $D_{kl}D_{lk}$ (which is the summation with respect to k and l) of the strain-rate tensor D_{ij} is given by,

$$D_{kl}D_{lk} = \frac{1}{4}\left[\left(\frac{\partial u'}{\partial z'} + \frac{\partial w'}{\partial x'}\right)^2 + \left(\frac{\partial v'}{\partial z'} + \frac{\partial w'}{\partial y'}\right)^2 + \left(\frac{\partial u'}{\partial y'} + \frac{\partial v'}{\partial x'}\right)^2\right] - \left[\left(\frac{\partial u'}{\partial x'}\frac{\partial v'}{\partial y'}\right) + \left(\frac{\partial u'}{\partial x'}\frac{\partial w'}{\partial z'}\right) + \left(\frac{\partial w'}{\partial z'}\frac{\partial v'}{\partial y'}\right)\right] \tag{5.3}$$

A film on a flat horizontal substrate, $z = 0$ is considered. The mass and momentum balance equations for the thin films on horizontal substrates are given by,

$$\frac{\partial u'}{\partial x'} + \frac{\partial v'}{\partial y'} + \frac{\partial w'}{\partial z'} = 0, \tag{5.4}$$

$$\rho\left(\frac{\partial u'}{\partial t'} + u'\frac{\partial u'}{\partial x'} + v'\frac{\partial u'}{\partial y'} + w'\frac{\partial u'}{\partial z'}\right) = \rho g \sin\theta_i - \frac{\partial p'}{\partial x'} + \frac{\partial \tau_{x'x'}}{\partial x'} + \frac{\partial \tau_{x'y'}}{\partial y'} + \frac{\partial \tau_{x'z'}}{\partial z'}, \tag{5.5}$$

$$\rho\left(\frac{\partial v'}{\partial t'} + u'\frac{\partial v'}{\partial x'} + v'\frac{\partial v'}{\partial y'} + w'\frac{\partial v'}{\partial z'}\right) = -\frac{\partial p'}{\partial y'} + \frac{\partial \tau_{y'x'}}{\partial x'} + \frac{\partial \tau_{y'y'}}{\partial y'} + \frac{\partial \tau_{y'z'}}{\partial z'}, \tag{5.6}$$

$$\rho\left(\frac{\partial w'}{\partial t'} + u'\frac{\partial w'}{\partial x'} + v'\frac{\partial w'}{\partial y'} + w'\frac{\partial w'}{\partial z'}\right) = -\rho g \cos\theta_i - \frac{\partial p'}{\partial z'} + \frac{\partial \tau_{z'x'}}{\partial x'} + \frac{\partial \tau_{z'y'}}{\partial y'} + \frac{\partial \tau_{z'z'}}{\partial z'}, \tag{5.7}$$

where the primes denote dimensional variables and $\theta_i = 0^{\text{o}}$ in this chapter (only horizontal leveling is considered). The dimensional variables are converted into non-dimensional ones (without primes) by using a set of dimensional scaling variables. Let H_0 be the characteristic depth of the thin film and L_0 be the length of the substrate. The lubrication approximation is based on the assumption that

$$\epsilon = \frac{H_0}{L_0} \ll 1. \tag{5.8}$$

The scalings used here have been used extensively in the past for Newtonian rheology (Schwartz and Eley, 1998; Gaskell et al., 2010; Schwartz, 1998; Sellier, 2003; Gaskell et al.,

2009),

$$U_0 = \frac{L_0}{T_0},\ P_0 = \frac{\sigma\epsilon}{L_0}. \tag{5.9}$$

Where σ is the surface tension of the fluid and P_0 is the characteristic pressure scale. The characteristic time scale for power-law rheology can be derived using a similar derivation as in the leveling of Newtonian viscous fluids and is given by,

$$T_0 = \left(\frac{L_0 K}{\sigma\epsilon^{n+2}}\right)^{\frac{1}{n}}, \tag{5.10}$$

The velocity and other physical coordinates are made dimensionless in the following manner,

$$u' = U_0 u,\ v' = U_0 v,\ w' = \epsilon U_0 w,\ x' = L_0 x,\ y' = L_0 y,\ z' = H_0 z,,\ t' = T_0 t,\ p' = P_0 p, \tag{5.11}$$

where U_0 is the velocity scale in the x direction. As ϵ is much less than 1, equations (5.5)-(5.7) are reduced to the following set of equations (refer to Appendix B for details):

$$\frac{\partial}{\partial z}\left(\frac{\partial u}{\partial z}\right)^n = \frac{\partial p}{\partial x}, \tag{5.12}$$

$$\frac{\partial}{\partial z}\left(\frac{\partial v}{\partial z}\right)^n = \frac{\partial p}{\partial y}, \tag{5.13}$$

$$\frac{\partial p}{\partial z} = -Bo, \tag{5.14}$$

with no-slip boundary condition given as,

$$u = v = w = 0 \ \text{ on } \ z = 0, \tag{5.15}$$

and the boundary conditions on the thin film are given as,

$$\frac{\partial u}{\partial z} = \frac{\partial v}{\partial z} = 0 \ \text{ on } \ z = h, \tag{5.16}$$

$$p = -\nabla^2 h \ \text{ on } \ z = h. \tag{5.17}$$

where $Bo = \frac{\rho g L_0^2}{\sigma}$ is the Bond number, which is the ratio between the gravitational and surface tension forces. Details are given in Appendix B. Equations (5.12) and (5.13) are integrated

twice with respect to z over the film thickness ($0 \leq z \leq h$) to give,

$$u = \left(-\frac{\partial p}{\partial x}\right)^{\frac{1}{n}} \left(\frac{n}{n+1}\right) \left[h^{\left(\frac{n+1}{n}\right)} - (h-z)^{\left(\frac{n+1}{n}\right)}\right], \tag{5.18}$$

$$v = \left(-\frac{\partial p}{\partial y}\right)^{\frac{1}{n}} \left(\frac{n}{n+1}\right) \left[h^{\left(\frac{n+1}{n}\right)} - (h-z)^{\left(\frac{n+1}{n}\right)}\right]. \tag{5.19}$$

Assuming $\lambda = \frac{1}{n}$, the time dependent lubrication approximation for the thickness in a non-Newtonian fluid is given by,

$$\frac{\partial h}{\partial t} = -\frac{1}{\lambda+2}\left[\frac{\partial}{\partial x}\left(h^{(\lambda+2)}\left(-\frac{\partial p}{\partial x}\right)^{\lambda}\right) + \frac{\partial}{\partial y}\left(h^{(\lambda+2)}\left(-\frac{\partial p}{\partial y}\right)^{\lambda}\right)\right], \tag{5.20}$$

Integrating equation (5.14) with respect to z and setting the integration constant using equation (5.17) yields the pressure field throughout the film,

$$p = -\nabla^2 h + Bo(h-z). \tag{5.21}$$

Note that when $\lambda = 1$, the standard equations for a Newtonian fluid are recovered. In comparison to the standard Newtonian formulation, solving the equations above presents a significant challenge. The problem resides in equation (5.20) where the terms $\left(-\frac{\partial p}{\partial x}\right)^{\lambda}$ and $\left(-\frac{\partial p}{\partial y}\right)^{\lambda}$ may become complex-valued for certain values of λ when $-\frac{\partial p}{\partial x}$ and $-\frac{\partial p}{\partial y}$ are negative. Several authors have discussed this problem in the past and have used the signum function to overcome the restrictions (Perazzo and Gratton, 2003; Wang et al., 2007a). Using this approach in the governing equations changes equation (5.20) to,

$$\begin{aligned}\frac{\partial h}{\partial t} = &-\frac{1}{\lambda+2}\left\{\frac{\partial}{\partial x}\left(h^{(\lambda+2)}\text{sign}\left(-\frac{\partial p}{\partial x}\right)\left|\frac{\partial p}{\partial x}\right|^{\lambda}\right)\right\} \\ &-\frac{1}{\lambda+2}\left\{\frac{\partial}{\partial y}\left(h^{(\lambda+2)}\text{sign}\left(-\frac{\partial p}{\partial y}\right)\left|\frac{\partial p}{\partial y}\right|^{\lambda}\right)\right\},\end{aligned} \tag{5.22}$$

where,

$$\text{sign}\left(-\frac{\partial p}{\partial x}\right) = \begin{cases} -1 & \text{if } \left(-\frac{\partial p}{\partial x}\right) < 0, \\ 0 & \text{if } \left(-\frac{\partial p}{\partial x}\right) = 0, \\ 1 & \text{if } \left(-\frac{\partial p}{\partial x}\right) > 0. \end{cases}$$

with analogous expressions for sign $\left(-\frac{\partial p}{\partial y}\right)$. The spatial discretization of the lubrication

approximation equations (5.21) and (5.22) uses the central Finite-Differencing scheme with uniform mesh spacing in the x and y direction, leading to values of h and p at mesh points (i, j) in the computational grid:

$$\frac{\partial h_{ij}}{\partial t} = -\frac{1}{\Delta x}\left\{\left(\frac{h_{i+1j}^{\lambda+2}+h_{ij}^{\lambda+2}}{2(\lambda+2)}\right)\mathrm{sign_E}\left|\frac{p_{ij}-p_{i+1j}}{\Delta x}\right|^{\lambda}-\left(\frac{h_{i-1j}^{\lambda+2}+h_{ij}^{\lambda+2}}{2(\lambda+2)}\right)\mathrm{sign_W}\left|\frac{p_{i-1j}-p_{ij}}{\Delta x}\right|^{\lambda}\right\}$$
$$-\frac{1}{\Delta y}\left\{\left(\frac{h_{ij+1}^{\lambda+2}+h_{ij}^{\lambda+2}}{2(\lambda+2)}\right)\mathrm{sign_N}\left|\frac{p_{ij}-p_{ij+1}}{\Delta y}\right|^{\lambda}-\left(\frac{h_{ij-1}^{\lambda+2}+h_{ij}^{\lambda+2}}{2(\lambda+2)}\right)\mathrm{sign_S}\left|\frac{p_{ij-1}-p_{ij}}{\Delta y}\right|^{\lambda}\right\}, \tag{5.23}$$

$$p_{ij}+\left[\frac{1}{(\Delta x)^2}\left(h_{i+1j}+h_{i-1j}-2h_{ij}\right)+\frac{1}{(\Delta y)^2}\left(h_{ij+1}+h_{ij-1}-2h_{ij}\right)\right]-Boh_{ij}=0, \tag{5.24}$$

and

$$\mathrm{sign_E}=\begin{cases}-1 & \text{if } \left(\frac{p_{ij}-p_{i+1j}}{\Delta x}\right)<0,\\ 0 & \text{if } \left(\frac{p_{ij}-p_{i+1j}}{\Delta x}\right)=0,\\ 1 & \text{if } \left(\frac{p_{ij}-p_{i+1j}}{\Delta x}\right)>0.\end{cases}$$

with analogous expressions for $\mathrm{sign_W}$, $\mathrm{sign_N}$, and $\mathrm{sign_S}$. Where E, W, N, and S, are directions east, west, north, and south. Spatial and temporal discretization are the same as in Section 2.3. A detailed description of the discretization and solution procedure is reported in Appendix B.

5.2.1 Comparison with the one-dimensional model

Based on the same governing equations a more general convergent solver has been developed by Gaskell and co-researchers (Gaskell et al., 2010). The main advantage of this numerical code is that the Jacobian is calculated numerically and the cumbersome derivation for the analytical expressions of the Jacobian is avoided. A comparison between the one-dimensional and the two-dimensional solvers is conducted to show that they both produce identical results. The properties of the sinusoidal wave considered are given below in Table 5.1. The sinusoidal wave is introduced in such a way that it is in the centre of the computational domain considered, see Figure 5.1. The region to the right and left side of the sinusoidal wave is considered to be at rest at the start of the numerical simulation. This stationary region is three times the wavelength of the perturbation on both sides. The purpose of this undisturbed region is to avoid any influence from the boundary. Dirichlet boundary conditions are

implemented on both sides.

Physical Property	Case 1	0.2wt% XG	Blood	Water	10wt% PPG+15 nm silica
Density, kg/m^3	1000	999	1062 (Attinger et al., 2013)	1000	1086.17
Flow behavior index, n	0.6-1.5	0.35	0.6-0.7 (Hussain et al., 1999; Myers, 2005)	1	1.728
Consistency factor, K, Pa.s^n	0.001	0.454	0.035 (Myers, 2005)	0.001	0.0705
Surface Tension, N/m	0.07	0.0725	0.062 (Attinger et al., 2013)	0.072	0.04699

Table 5.1: Physical properties of the leveling film

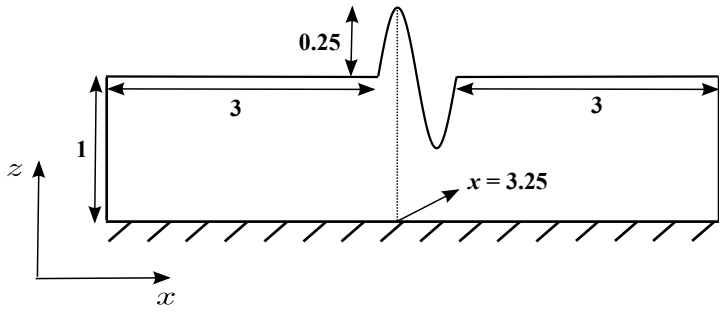

Figure 5.1: Sinusoidal thin film profile

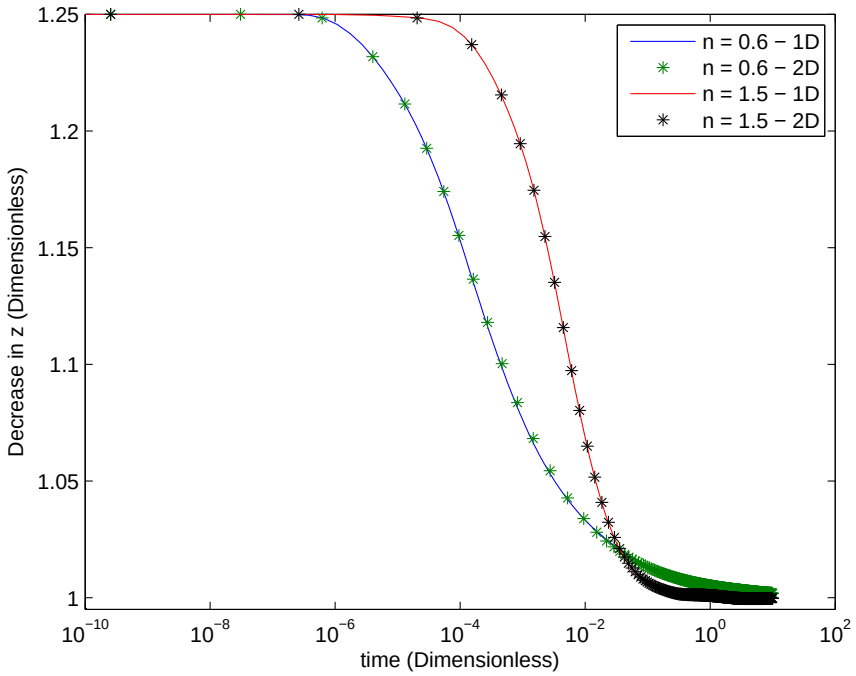

Figure 5.2: Comparison between the solvers in the literature, (Lee et al., 2009) and (Gaskell et al., 2010), for a Case 1 fluid with an initial amplitude of 0.25, initial wavelength of 1 and average film height of 1

The decrease in height of the leveling film at $x = 3.25$ is plotted against time, see Figure 5.2. Units are all dimensionless. For comparison, the flow behavior index, n, for both the solvers is set to 0.6 and 1.5, i.e, shear-thinning and shear-thickening behavior. The same

initial profile is introduced in both solvers. The plot shows that initially the leveling rate is high, but after some time it starts to decrease. Figure 5.2 shows that both the solvers are in excellent agreement with each other hence providing some confidence in the implementation of the power-law rheology.

5.3 Verification of the numerical scheme

The results obtained have to be verified in order to be sure that the numerics performed and the results obtained can be relied on. It is usually stated in research articles that the accuracy of the verification of codes is difficult for complex problems. For example the solution of full Navier-Stokes equations is unattainable because the exact solutions only exist for a few simple problems with different assumptions and do not fully utilize the potential of the code. Many researchers approach this problem - accuracy of the verification of the numerical code - in a very haphazard manner, often comparing the results with a problem reduced in complexity. There is, however, a very general method of producing analytical solutions for accuracy verification of the numerical code. This is explored in the next Section 5.3.1.

5.3.1 Method of Manufactured Solutions (MMS)

The Method of Manufactured Solutions (MMS) is a procedure for obtaining analytical solution of PDEs to verify the accuracy of a numerical algorithm. This method was first used by Steinberg and Roache (Steinberg and Roache, 1985) and was later supported and expanded by Roache (Roache, 1998b,a). The fundamental concept behind this method is to manufacture an exact solution, without worrying about its physical authenticity. An arbitrary function is chosen and inserted in the PDE of interest which also includes the boundary conditions. If the solutions do not satisfy the PDE, the function will generate a residual. But because the function is analytical, this residual can be expressed explicitly. In order to verify the numerical algorithm one only needs to consider the PDE with the residual added as a source term which is denoted by $Q(x, y, t)$.

The solution selected for the MMS is non-trivial and it must be sufficiently differentiable. The selected function is then passed through all the governing PDEs to account for the source term, $Q(x, y, t)$ which builds the selected solution. The governing equations in our case are

the one-dimensional power-law lubrication approximation equations which read as follows:

$$\frac{\partial h}{\partial t} = -\frac{1}{\lambda+2}\left[\frac{\partial}{\partial x}\left(h^{(\lambda+2)}\left(-\frac{\partial p}{\partial x}\right)^{\lambda}\right)\right], \tag{5.25}$$

$$p = -\frac{\partial^2 h}{\partial x^2}. \tag{5.26}$$

These partial differential equations are combined together by substituting equation (5.26) into (5.25),

$$\frac{\partial h}{\partial t} = -\frac{1}{\lambda+2}\left[\frac{\partial}{\partial x}\left(h^{(\lambda+2)}\left(\frac{\partial^3 h}{\partial x^3}\right)^{\lambda}\right)\right]. \tag{5.27}$$

The resulting equation is a fourth-order highly non-linear partial differential equation for h only which is easier for the application of the MMS technique. Expanding equation (5.27) further and replacing h with h_m (the manufactured solution) just to remove any misconception, gives,

$$Q = \frac{\partial h_m}{\partial t} + h_m^{\lambda+1}\left(\frac{\partial^3 h_m}{\partial x^3}\right)^{\lambda-1}\left[\frac{\partial h_m}{\partial x}\left(\frac{\partial^3 h_m}{\partial x^3}\right) + \frac{\lambda h_m}{\lambda+2}\left(\frac{\partial^4 h_m}{\partial x^4}\right)\right], \tag{5.28}$$

where h_m signifies the initially selected function which is independent of the numerics. The profile chosen here is the Gaussian distribution function, also known as Normal distribution function. The mean, x_m, and the standard deviation, σ, define the curvature of this function. In this study, $\sigma = 1$ is chosen and the function selected is set as,

$$h_m = 1 + \frac{1}{4}e^{-t}e^{-2(x-x_m)^2}, \tag{5.29}$$

where x_m is the mean of the Gaussian distribution, then,

$$\frac{\partial h_m}{\partial t} = -\frac{1}{4}e^{-t}e^{-2(x-x_m)^2}, \tag{5.30}$$

$$\frac{\partial h_m}{\partial x} = e^{-t}e^{-2(x-x_m)^2}\left(x_m - x\right), \tag{5.31}$$

$$\frac{\partial^2 h_m}{\partial x^2} = e^{-t}e^{-2(x-x_m)^2}\left(4x_m^2 - 8x_m x + 4x^2 - 1\right), \tag{5.32}$$

$$\frac{\partial^3 h_m}{\partial x^3} = 4e^{-t}e^{-2(x-x_m)^2}\left[4x_m^3 - 12x_m^2 x + 3x_m\left(4x^2-1\right) - 4x^3 + 3x\right], \tag{5.33}$$

$$\frac{\partial^4 h_m}{\partial x^4} = 4e^{-t}e^{-2(x-x_m)^2}\left[16x_m^4 - 64x_m^3 x + 24x_m^2\left(4x^2-1\right) + x_m\left(48x - 64x^3\right) + 16x^4 - 24x^2 + 3\right]. \tag{5.34}$$

where equations (5.29)-(5.34) are substituted into equation (5.28) to produce the source term for the MMS solution of the Gaussian distribution. The source term, Q, is then added to the partial differential equation,

$$\frac{\partial h}{\partial t} + h^{\lambda+1}\left(\frac{\partial^3 h}{\partial x^3}\right)^{\lambda-1}\left[\frac{\partial h}{\partial x}\left(\frac{\partial^3 h}{\partial x^3}\right) + \frac{\lambda h}{\lambda+2}\left(\frac{\partial^4 h}{\partial x^4}\right)\right] = Q. \tag{5.35}$$

When equation (5.35) is solved with compatible initial and boundary conditions and the discretization described earlier, it should produce the solution $h_m = 1 + \frac{1}{4}e^{-t}e^{-2(x-x_m)^2}$. The initial condition at $t = 0$ is,

$$h\left(x,0\right) = 1 + \frac{1}{4}e^{-2(x-x_m)^2}. \tag{5.36}$$

The flow domain extends over 6 dimensionless units and the mean of the Gaussian distribution, x_m is equal to 3. At the boundaries, Neumann boundary conditions are applied,

$$\frac{\partial h\left(0,t\right)}{\partial x} = 0, \quad \frac{\partial h\left(6,t\right)}{\partial x} = 0. \tag{5.37}$$

The fluid properties correspond to case 1 in Table 5.1, where the flow behavior index is equal to 0.6.

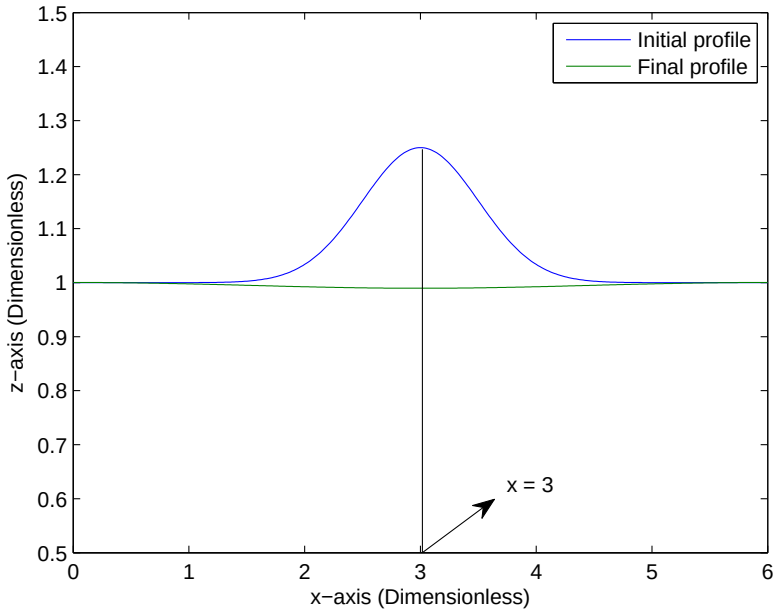

Figure 5.3: Initial and final profile after 10 dimensionless time units for Case 1 fluid with a mesh resolution of 416 and $n = 0.6$ nodes

The initial and final bell-shaped profile after running the simulation for 10 non-dimensional time units is shown in Figure 5.3. The initial maximum height is 1.25 at $x = 3$. In Figure 5.4a, the leveling height from the numerics and the actual solution, h_m, is plotted against time at $x = 3$.

Figure 5.4a shows that when an initial computational mesh of 416 nodes are used, both the MMS solution and the actual/exact solution, h_m, overlap each other most of the time. The error is defined as the maximum difference between the discrete solution and the actual/exact solution. If the error is plotted against time, it shows that the error increases and approaches a constant value after very few dimensionless time units.

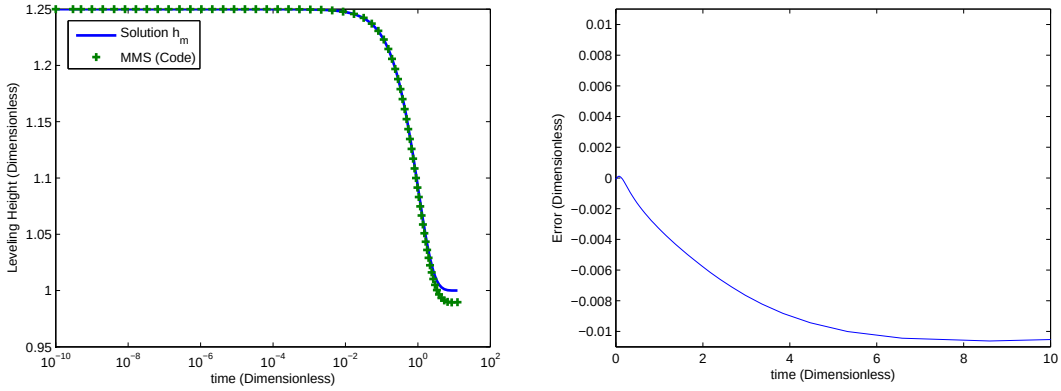

(a) Mesh resolution of 416 nodes

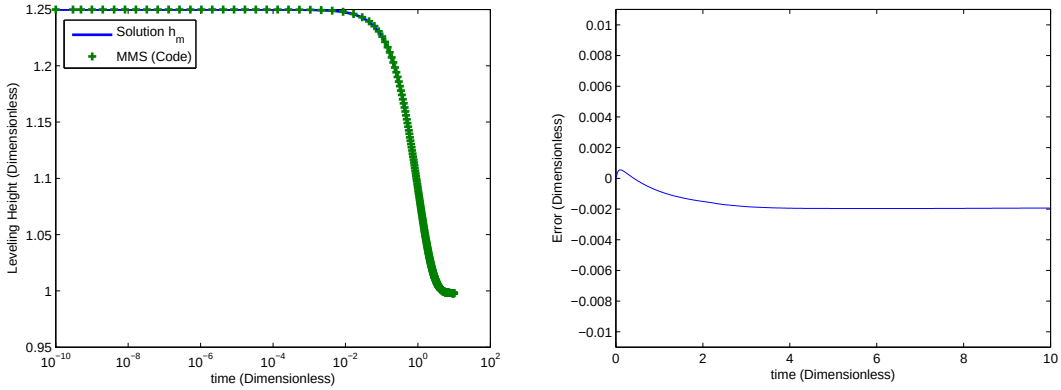

(b) Mesh resolution of 992 nodes

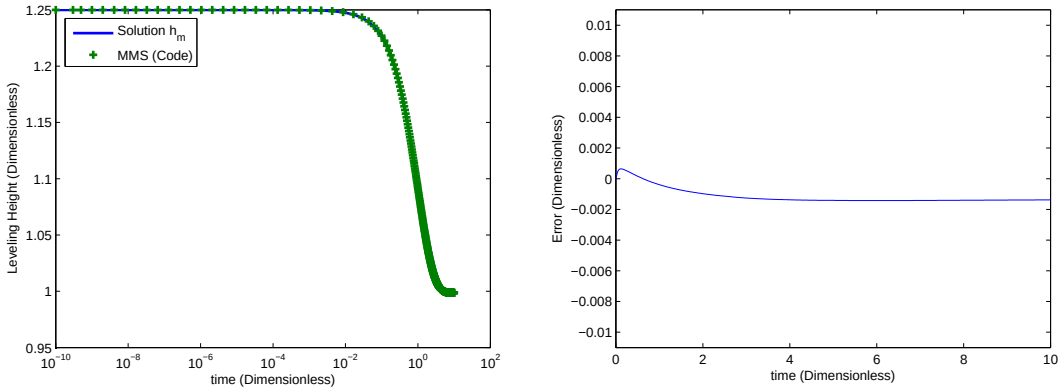

(c) Mesh resolution of 1376 nodes

Figure 5.4: Comparison between h_m and MMS showing the leveling height and the associated error with time and effect of mesh resolution on the comparison

The numerical solution should approach the exact solution with design-order accuracy as the mesh is refined. The mesh resolution is increased to 992 nodes and finally to 1376 nodes. Figures 5.4b and 5.4c show that with the increase in mesh resolution the numerical solution closely approaches the manufactured solution, h_m. This gives the required confidence in the accuracy of the numerical implementation.

5.4 Results and Discussion

The film is perturbed by a single sinusoidal perturbation of wavelength λ_w and amplitude A centered at x_0, the center of the computational domain. Accordingly, the perturbation is given by $\Delta h = A \sin\left({}^{2\pi(x-x_0)}/_{\lambda_w}\right)$ and is surrounded by an unperturbed uniform film thickness which spans three dimensionless space units on either side, see Figure 5.1. Dirichlet boundary condition is implemented on the left and right of the domain.

The decrease in height of the leveling film at the perturbation peak ($x = 3.25$) is plotted against time, see Figure 5.5. Case 1 fluid properties are used. The flow behavior index, n, is increased from 0.6 to 1.5, i.e, from shear-thinning to shear-thickening behavior but keeping all the other physical properties constant. An important observation is made on Figure 5.5 where it shows that the onset of leveling occurs much earlier for the fluid with the lower power-law exponent, i.e. the shear-thinning fluid. Because of this earlier leveling onset, the amplitude of the perturbation decays faster initially for shear-thinning fluids. However, this is compounded by the fact that the leveling rate of the shear thickening fluid is higher at later times since the magnitude of the slope of the curves in Figure 5.5a is highest for higher values of the power-law exponent. This results in a cross-over of the curves which suggests the definition of a "threshold" film thickness approximately equal to $h^\star \sim 1.02$ in the case shown in Figure 5.5a. The film thins to a level higher for smaller values of the power-law exponent in comparison to larger values of this exponent. This can be related to the level of shear rate which is highest during the earliest stages of the flow but decreases with time. During the early stages, the higher level of shear rate means that the viscosity of the shear-thinning fluid is comparatively lower than that of the shear-thickening one. The results show that at a higher shear rate the leveling rate is higher for the shear-thinning fluid. With the passage of time the shear rate becomes significantly less, and the opposite trend is observed for shear-thickening fluid which then levels at a much faster rate. This trend was also reported by Eley in (Eley, 2012).

It should be noted that the power-law exponent is the only parameter present in the governing equations and therefore the above observation is generally applicable but this is combined with the fact that the time scale is highly dependent on the power-law exponent. For example,

taking $L_0 = 0.001$ m, $K = 0.001$ Pa.s$^{\text{n}}$, $\sigma = 0.07$ N/m, and $\epsilon = 0.1$, the time scale T_0 grows by almost 2 orders of magnitude as the power-law exponent is increased from 0.6 to 1.5. This means that the time-axis should be considerably stretched as the power-law exponent increases from 0.6 to 1.5. This time scale disparity means that this curve overlap does not necessarily occur in practice. This is illustrated in Figure 5.5b where the film thickness is plotted against a dimensionless time $t = t^{T_0^n}/T_0^{0.6}$which is the same for all values of n where $T_0^{0.6}$ is the time scale computed by taking $n = 0.6$, $L_0 = 0.001$ m, $K = 0.001$ Pa.s$^{\text{n}}$, $\sigma = 0.07$ N/m, and $\epsilon = 0.1$ and T_0^n is the corresponding time scale for a power law exponent of n.

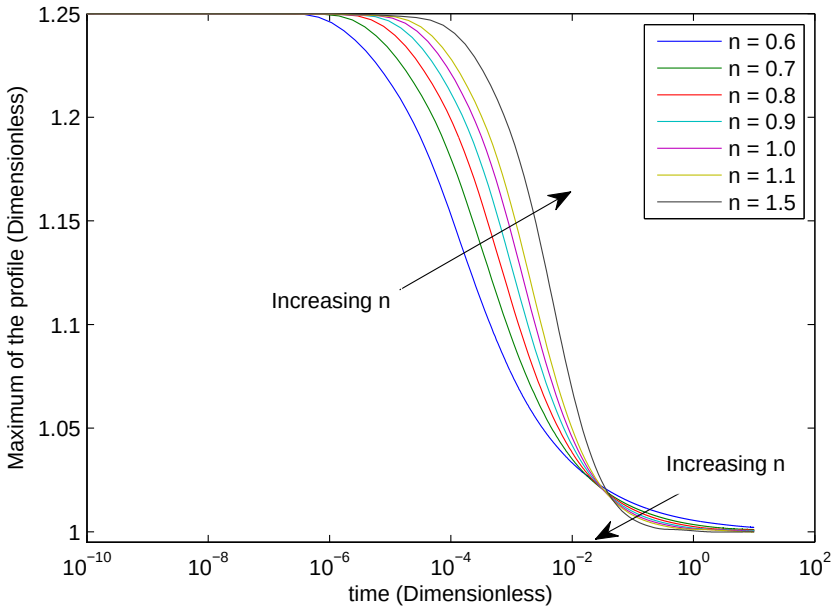

(a) Leveling height with time

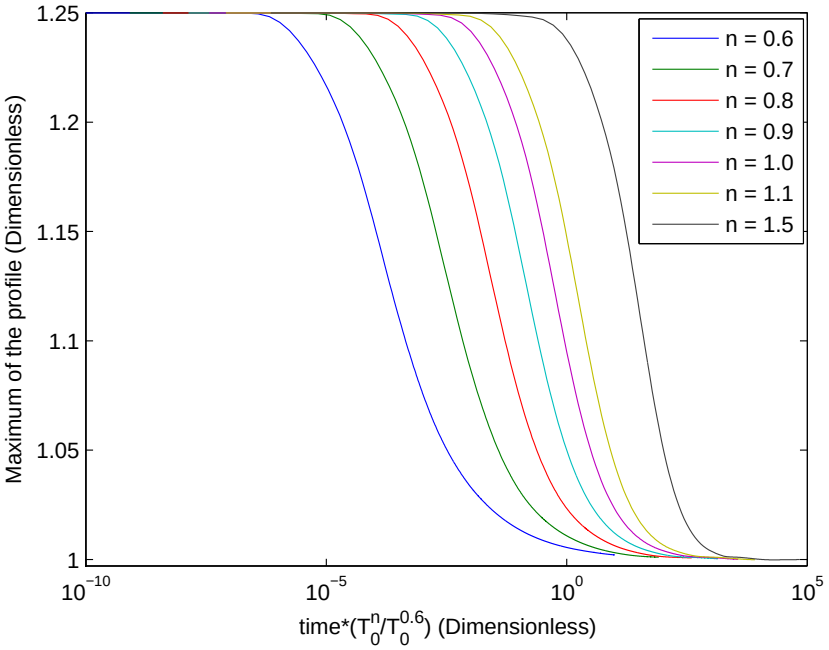

(b) Leveling height with time = $t^{T_0^n}/_{T_0^{0.6}}$

Figure 5.5: Effect of change in flow behavior index, n for Case 1 fluid

Next, the dependence of the leveling dynamics on the amplitude and wavelength of sinusoidal perturbation is studied. The wavelength λ_w is first varied from 0.5 to 2 keeping the amplitude A equal to 0.25. For each wavelength, two power-law exponent values are considered, i.e. shear-thinning ($n = 0.6$) and shear-thickening ($n = 1.5$) to compare the rheological effect. In Figure 5.6, the decrease in the maximum height of the leveling film ($x = 3$ for $\lambda_w = 2$, $x = 3.25$ for $\lambda_w = 1$, and $x = 3.375$ for $\lambda_w = 0.5$) is plotted against time. This figure shows

that as the wavelength is reduced, the time for the perturbation to level reduces. This is to be expected as for a given amplitude, reducing the wavelength increases the curvature of the free surface and therefore the driving capillary pressure. Interestingly, the effect of the power-law exponent appears to be more significant for shorter wavelengths, whereas shear-thinning rheology invariably leads to a faster leveling. The curve cross-over discussed above which defines the "threshold" film thickness increases with an increasing wavelength ($h^\star \sim 1$ for $\lambda_w = 0.5$, $h^\star \sim 1.02$ for $\lambda_w = 1$, $h^\star \sim 1.06$ for $\lambda_w = 2$). It is also interesting to note that for a given power-law exponent, the curves appear to be self-similar and merely shifted along the time-axis. Again, the magnitude of the slope of the curves is highest for the larger value of the power-law exponent i.e. in the shear-thickening rheology case.

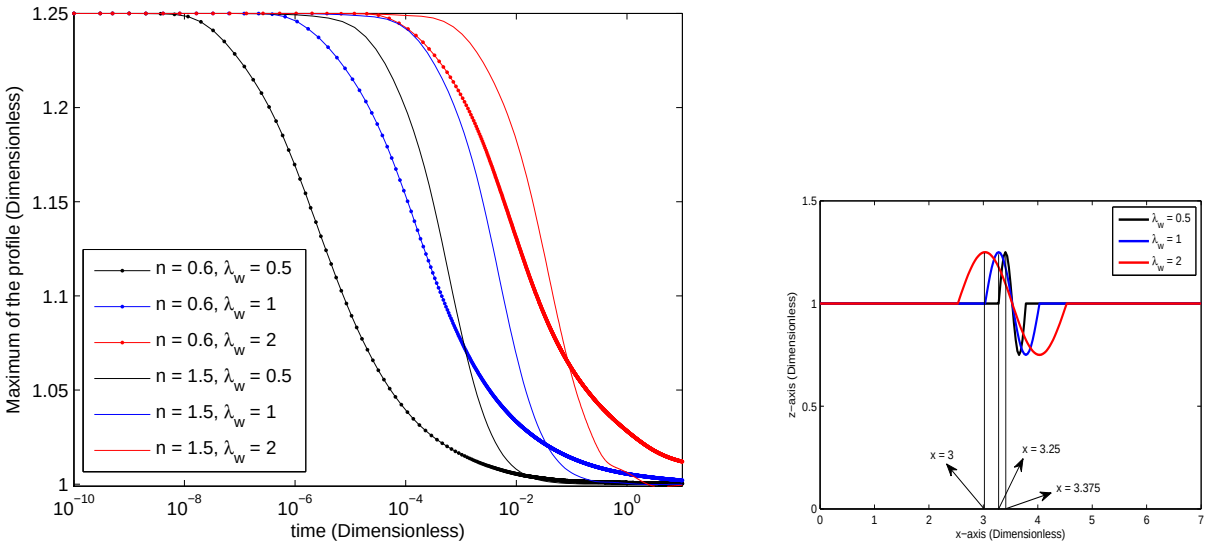

Figure 5.6: Varying wavelength of the sinusoidal perturbation of Case 1 fluid

The effect of the amplitude A is investigated next by varying its value from 0.125 to 0.5 while keeping the wavelength constant at $\lambda_w = 1$. Figure 5.7 shows the variation of the normalized film thickness perturbation $\frac{h-1}{A}$. For the shear-thinning case ($n = 0.6$), the thinning of higher amplitude perturbations is faster. The same reason as above is invoked here to justify this observation; a higher amplitude perturbation leads to a greater free surface curvature and therefore a higher driving potential. Interestingly, for the shear-thickening case ($n = 1.5$), the opposite trend is observed with the largest amplitude perturbation being the slowest to level. This counter-intuitive observation is attributed to the fact that a higher amplitude perturbation will induce greater shear rates in the fluid layer which will result in a higher apparent viscosity, hence more resistance to flow and therefore slower leveling rates.

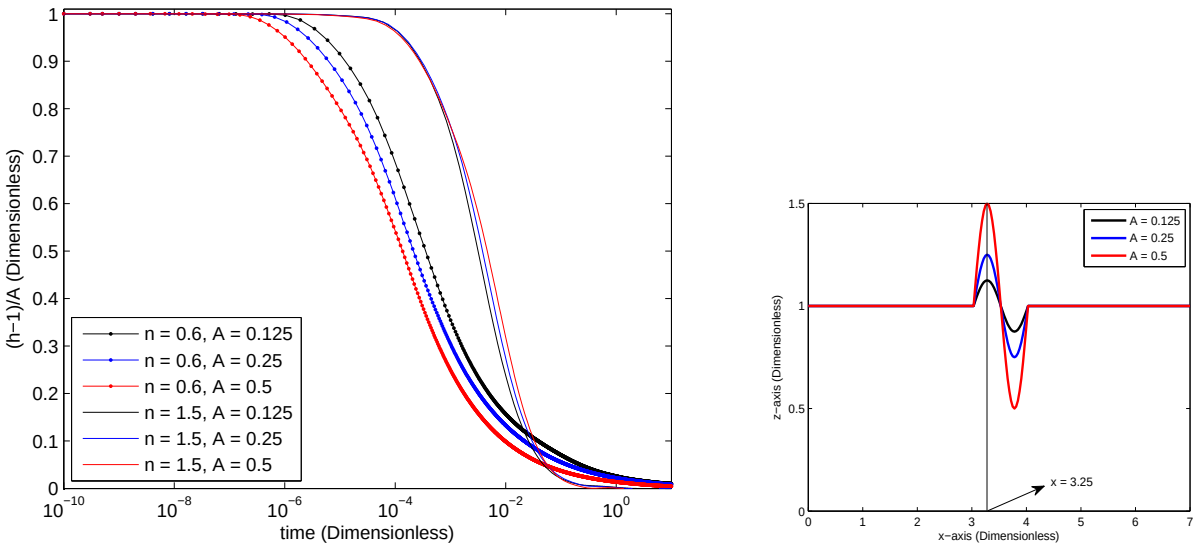

Figure 5.7: Varying amplitude of the sinusoidal perturbation of Case 1 fluid

Finally, the analysis above is extended to account for three-dimensional free surface perturbations effects. This contrasts with earlier studies which invariably consider only plane flows. The fluid physical properties used are the same as in Case 1 given in Table 5.1. The initial profiles considered are shown in Figure 5.8 and are both released from rest.

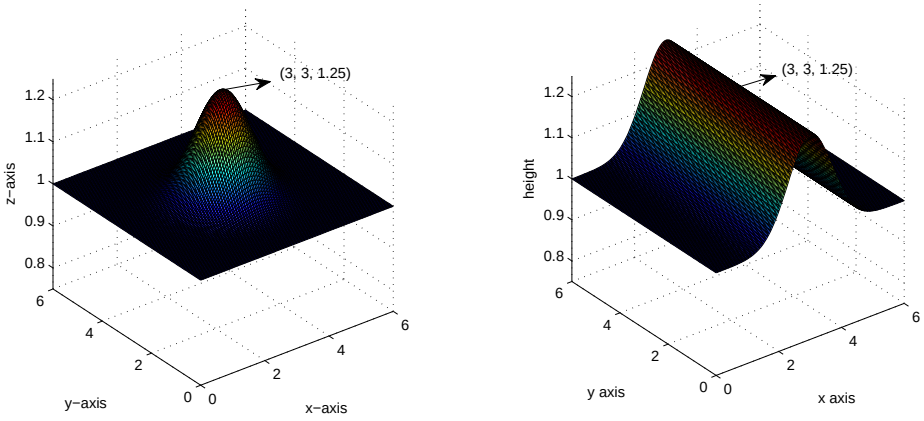

(a) Localized bell-shaped perturbation

(b) Plane bell-shaped perturbation

Figure 5.8: Profiles of the three dimensional localized and plane bell-shaped perturbations considered for comparison

The film height at the domain center (i.e. at point $(3, 3)$) is plotted against time as shown in Figure 5.9. The dotted line represents the plane bell-shaped perturbation and the solid line represents the localized bell-shaped perturbation. This figure clearly shows the difference between the two leveling rates. This highlights the importance of 3D modeling. Clearly, the

leveling of the localized disturbance is faster than the plane one because of the increased curvature introduced in the y-direction which provides an increased driving capillary force. It is noted that the rate of leveling is higher for the shear-thinning fluid in comparison to the shear-thickening fluid.

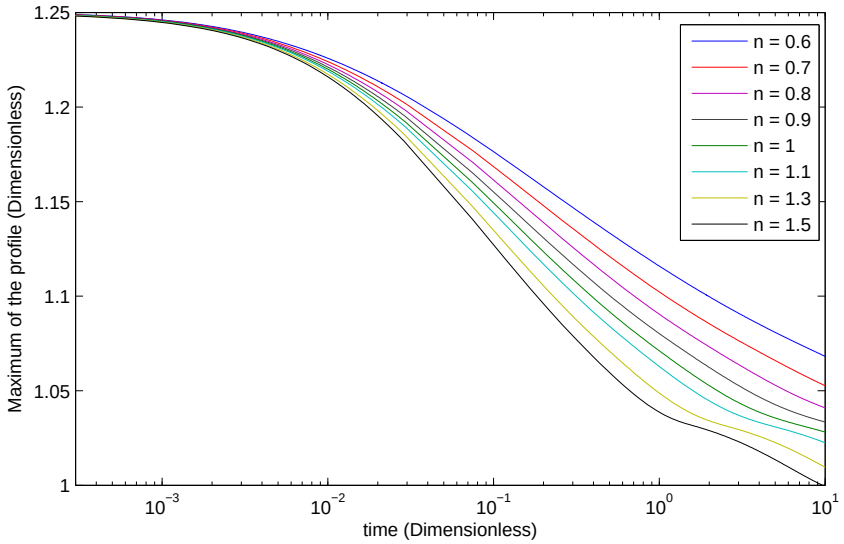

(a) Localized bell-shaped perturbation

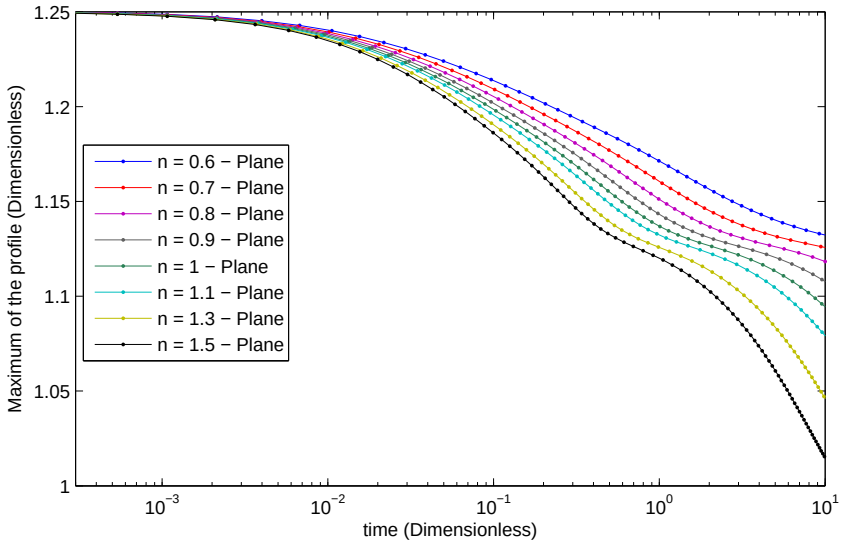

(b) Plane bell-shaped perturbation

Figure 5.9: Leveling dynamics of three dimensional profiles at the point (3, 3)

As a final illustrative example, Xanthan gum-water (0.2wt% XG) solutions (highly shear-thinning), blood (shear-thinning), water (Newtonian) and PPG silica (10wt% PPG + 15nm silica) solution (shear-thickening) sinusoidal perturbation leveling on a horizontal substrate are studied. The physical power-law properties of these fluids have been collected from the literature, see Table 5.1. The values for blood have been reported by various researchers

(Hussain et al., 1999; Myers, 2005). Wang and co-workers have reported the physical power-law properties of PPG Silica solution on glass substrates (Wang et al., 2007b). Dechelette and co-researchers have reported the physical power-law properties of Xanthan Gum-Water solution (Dechelette et al., 2010).

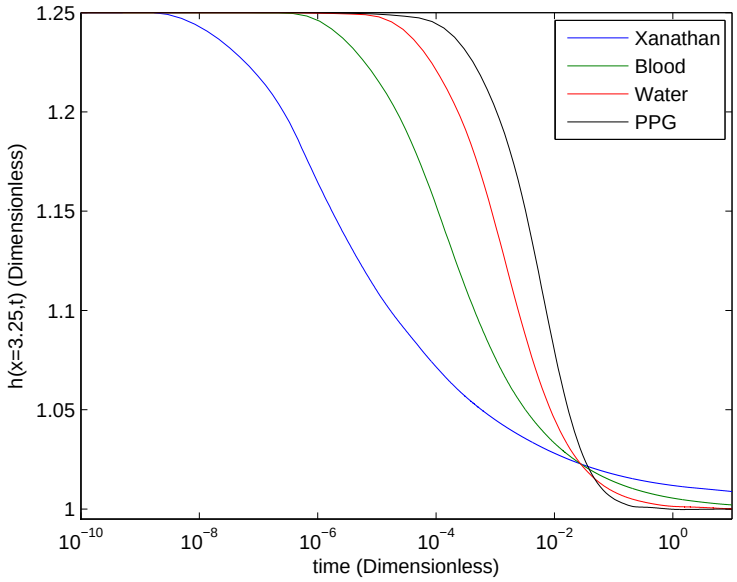

Figure 5.10: Leveling of sinusoidal perturbations of real fluids with different rheologies

Figure 5.10 illustrates the decrease in the height of the sinusoidal perturbation with time. It is apparent that, as noted previously, the time for onset of leveling increases with the power-law exponent from the Xanthan Gum-Water solution ($n = 0.35$) to the PPG/Silica solution ($n = 1.728$). However, once leveling is initiated, the rate at which the fluid layer thins is higher for increasing values of the flow behavior index. The effect of other fluid properties is encapsulated in the time scale, see equation (5.10). For example, increasing the consistency factor K by a factor two will stretch the time axis by a factor $2^{1/n}$ or increasing the surface tension σ by a factor 2 will stretch the time axis by a factor $(1/2)^{1/n}$.

5.5 Concluding remarks

In this work, a mathematical model based on the lubrication approximation which describes the leveling dynamics of thin power-law fluid films is presented. This mathematical model consists of highly non-linear PDEs which are solved numerically via the Multigrid technique. The proposed model was validated using the MMS technique which is implemented here for the first time for thin films where it verifies the power-law computations using the normal

distribution bell-shaped perturbation as a benchmark. The validation of the power-law fluid dynamics gives the required confidence that the model and discretization are accurate. Based on this validation, the problem of leveling of a sinusoidal perturbation on horizontal substrates having different fluid rheologies is investigated. The trends observed are in line with the literature (Eley, 2012). Specifically, numerical simulations revealed that the flow behavior index which differentiates the shear-thinning and shear-thickening fluids, plays a cardinal role in the leveling dynamics. It influences the time of onset and the rate at which the fluid layer levels. Other physical properties, such as surface tension and flow consistency constant, K, have a substantial impact on leveling dynamics through the time scale of the problem which stretches (or contracts) along the time-axis. An example with a three-dimensional perturbation is also discussed. The example highlights the importance of three-dimensional effects which are often ignored in the study of leveling in thin films.

Chapter 6

Spreading/sliding of non-Newtonian droplets

Contents

Most of Chapter 6 has already appeared in the paper, "Modeling the spreading and sliding of power-law droplets." published in the Colloids and Surfaces A: Physicochemical and Engineering Aspects (Ahmed et al., 2013). This work was co-authored with Dr. Mathieu Sellier, Dr. Yeaw Chu Lee, Dr. Mark Jermy and Dr. Michael Taylor.

6.1 Introduction

Droplets sliding down incline planes are ubiquitous in natural and industrial processes. A good illustration of this process, familiar to most, is a droplet flowing down a car windscreen on a rainy day. It is, of course, also relevant to many other applications such as in the deposition of pesticides, the coating of surfaces, or falling film evaporators to name a few. Its widespread applications have motivated numerous studies.

At a crime scene there are a wide range of surfaces having different properties, e.g. roughness, dust particles, prewetted, porosity, etc. After impacting the surface the drying process starts. How quickly this happens depends on the surface where the blood landed, how much blood is contained in the spatter, and the heat and humidity present at the crime scene. The outer edge dries first. A really dry blood spatter can skeletonize, flaking off and leaving a ring around the original diameter of the spatter. An analyst can help to pinpoint when the crime occurred based on the dryness of the blood (Dutelle, 2010). The drying of a droplet of human blood exhibits coupled physical mechanisms, such as Marangoni flow, evaporation and wettability (Brutin et al., 2010).

There has therefore been a recent drive to understand the validity of BPA (Council, 2009) from a more fundamental angle looking at the processes involved in bloodstain formation. The work presented here is an early step in that direction. It focuses on an apparently simple configuration that describes the spreading and/or sliding of a droplet on a surface and highlights the rheological effects. Blood has a shear-thinning behavior and it is therefore important to understand the non-Newtonian fluid mechanics to fully understand bloodstain formation.

In the past, a few experimental studies have analyzed the spreading of non-Newtonian fluids.

Carré and Eustache considered the spreading of shear-thinning fluids on a glass substrate (Carré and Eustache, 2000). More specifically, they investigated the spreading of PDMS-silica solution and acrylic typographic ink having different power-law exponents. Rafai and co-workers experimented with the spreading of shear-thinning fluid using xanthan solution and polyacrylamide solution on a mica surface (Rafaï et al., 2005). Wang and co-workers explored for the first time the spreading dynamics of partially wetting non-Newtonian fluids (Wang et al., 2007b). They considered both shear-thinning and shear-thickening fluids in their experimental study. They determined the effect that partially and fully-wetting power-law fluids have on the spreading radius.

Starov and co-workers considered the spreading of non-Newtonian droplets on solid substrates. They took into account the gravitational and the capillary regimes of spreading in their investigation (Starov et al., 2003). Neossia and Momoniat investigated the axisymmetric spreading of non-Newtonian fluid on a horizontal surface without considering surface tension effects (Nguetchue and Momoniat, 2008). They were able to predict the spreading rate with an analytical relationship. Dandapat and Singh used the energy approach to investigate the spreading of droplets with a power-law rheology (Dandapat and Singh, 2010). They used physical and geometrical reasoning to obtain a correlation for the rate of spreading of the droplet. They figured out that the spreading rate of a shear-thickening fluid is greater than a Newtonian fluid and for a shear-thinning fluid droplet the spreading rate is slower than a Newtonian fluid droplet. Dechelette and co-researchers recently investigated for the first time, the spreading of a power-law fluid droplet from the point of impact on a flat substrate to the recession phase (Dechelette et al., 2010).

Here, the power-law rheological model is chosen to study the spreading/sliding of a non-Newtonian fluid droplet. This model has been used extensively in the literature to capture non-Newtonian fluid properties. Biswas and Gupta were the first to investigate the flow of a thin free layer of power-law fluid over a horizontal plane by assuming a similarity solution (Biswas and Gupta, 1987). Betelu and Fontelos studied the spreading of a power-law fluid droplet on a horizontal plane without neglecting surface tension (Betelu and Fontelos, 2003). Gratton and co-researchers derived the governing equations for creeping gravity currents of fluids which satisfy a power-law rheology using the lubrication approximation (Gratton et al.,

1999). Perazzo and Gratton investigated theoretically the slow motion of a power-law liquid on an inclined plane (Perazzo and Gratton, 2003). In the above studies, plane flow was always assumed.

In the past, power-law thin films flowing down inclined substrates have received considerable attention but to the best of my knowledge, three-dimensional modeling of a power-law fluid droplet spreading/sliding using the lubrication approximation has not previously been reported. The objective of this chapter is to study the behavior of droplets of different rheologies as they spread/slide down inclined substrates. Section (6.2) provides details of the governing power-law equations and the numerical implementation of the proposed model. Lastly, Section (6.3) presents the results from the numerical simulations for fluid droplets of different rheologies spreading/sliding on inclined substrates.

6.2 Mathematical model and numerical solution

The non-Newtonian rheology is implemented using the simple power-law model which has been described in detail in Section 5.2. Let us consider a three-dimensional problem, where the mass and momentum balance equations (5.4)-(5.7) are used with disjoining pressure term in the pressure term where $\vec{g} = g\sin\theta_i\,\hat{\mathrm{i}} + g\cos\theta_i\,\hat{\mathrm{k}}$ as the substrate may be inclined. Where $\hat{\mathrm{i}}$ and $\hat{\mathrm{k}}$ are unit vectors in x and z direction. Let H_0 be the characteristic droplet thickness and $L_0 = R_0$, where R_0 is the radius of the droplet. The scalings used here are same as the ones used in the previous chapter, Section 5.2. Equations (5.4)-(5.7) can be written in dimensionless form as,

$$\frac{\partial}{\partial z}\left(\frac{\partial u}{\partial z}\right)^n = \frac{\partial p}{\partial x} - \frac{Bo\sin\theta_i}{\epsilon}, \tag{6.1}$$

$$\frac{\partial}{\partial z}\left(\frac{\partial v}{\partial z}\right)^n = \frac{\partial p}{\partial y}, \tag{6.2}$$

$$\frac{\partial p}{\partial z} = -Bo\cos\theta_i, \tag{6.3}$$

with boundary conditions mentioned in equations (2.19), (2.20) and (2.21). Equations (6.1) and (6.2) are integrated twice with respect to z over the film or droplet thickness ($0 \le z \le h$) to give,

$$u = \left(\frac{Bo\sin\theta_i}{\epsilon} - \frac{\partial p}{\partial x}\right)^{\frac{1}{n}} \left(\frac{n}{n+1}\right)\left[h^{\left(\frac{n+1}{n}\right)} - (h-z)^{\left(\frac{n+1}{n}\right)}\right], \tag{6.4}$$

$$v = \left(-\frac{\partial p}{\partial y}\right)^{\frac{1}{n}} \left(\frac{n}{n+1}\right) \left[h^{\left(\frac{n+1}{n}\right)} - (h-z)^{\left(\frac{n+1}{n}\right)}\right]. \tag{6.5}$$

Let $\lambda = \frac{1}{n}$, the time dependent lubrication approximation for non-Newtonian fluid is given by,

$$\frac{\partial h}{\partial t} = -\frac{1}{\lambda+2}\left[\frac{\partial}{\partial x}\left(h^{(\lambda+2)}\left(\frac{Bo\sin\theta_i}{\epsilon} - \frac{\partial p}{\partial x}\right)^{\lambda}\right) + \frac{\partial}{\partial y}\left(h^{(\lambda+2)}\left(-\frac{\partial p}{\partial y}\right)^{\lambda}\right)\right], \tag{6.6}$$

and the pressure field in the droplet,

$$p = -\nabla^2 h - \Pi(h) + Bo\cos\theta_i(h-z). \tag{6.7}$$

Note that for $\lambda = 1$, the standard equations for a Newtonian thin liquid film are recovered. In comparison to the standard Newtonian formulation, these equations present a significant challenge. The problem resides in equation (6.6) where the terms $\left(\frac{Bo\sin\theta_i}{\epsilon} - \frac{\partial p}{\partial x}\right)^{\lambda}$ and $\left(-\frac{\partial p}{\partial y}\right)^{\lambda}$ may become complex-valued for certain values of λ when $\left(\frac{Bo\sin\theta_i}{\epsilon} - \frac{\partial p}{\partial x}\right)$ and $-\frac{\partial p}{\partial y}$ are negative. Several authors have discussed this problem in the past and used the signum function was proposed to overcome this problem (Wang et al., 2007a; Perazzo and Gratton, 2003). Using this approach in the governing equations changes equation (6.6) to,

$$\begin{aligned}\frac{\partial h}{\partial t} = &-\frac{1}{\lambda+2}\left\{\frac{\partial}{\partial x}\left(h^{(\lambda+2)}\mathrm{sign}\left(\frac{Bo\sin\theta_i}{\epsilon} - \frac{\partial p}{\partial x}\right)\left|\frac{Bo\sin\theta_i}{\epsilon} - \frac{\partial p}{\partial x}\right|^{\lambda}\right)\right\} \\ &-\frac{1}{\lambda+2}\left\{\frac{\partial}{\partial y}\left(h^{(\lambda+2)}\mathrm{sign}\left(-\frac{\partial p}{\partial y}\right)\left|-\frac{\partial p}{\partial y}\right|^{\lambda}\right)\right\},\end{aligned} \tag{6.8}$$

where,

$$\mathrm{sign}\left(\frac{Bo\sin\theta_i}{\epsilon} - \frac{\partial p}{\partial x}\right) = \begin{cases} -1 & \text{if } \left(\frac{Bo\sin\theta_i}{\epsilon} - \frac{\partial p}{\partial x}\right) < 0, \\ 0 & \text{if } \left(\frac{Bo\sin\theta_i}{\epsilon} - \frac{\partial p}{\partial x}\right) = 0, \\ 1 & \text{if } \left(\frac{Bo\sin\theta_i}{\epsilon} - \frac{\partial p}{\partial x}\right) > 0. \end{cases} \quad \mathrm{sign}\left(-\frac{\partial p}{\partial y}\right) = \begin{cases} -1 & \text{if } \left(-\frac{\partial p}{\partial y}\right) < 0, \\ 0 & \text{if } \left(-\frac{\partial p}{\partial y}\right) = 0, \\ 1 & \text{if } \left(-\frac{\partial p}{\partial y}\right) > 0. \end{cases}$$

The spatial and temporal discretizations have been described in detail in Appendix B.

6.3 Droplet spreading

Having established the validity of the code in the previous chapter, the spreading of a droplet on a horizontal substrate is investigated. The physical properties of the fluid droplet (Case 1) are stated in Table 6.1. The equilibrium contact angle, $\theta_e = 0^o$, i.e. a fully-wetting fluid is considered for this first case. Figure 6.1 shows the changes in the spread radius of the droplet as a function of time when n is varied from 0.7 to 1.5. It can be seen that with an increasing flow behavior index, the fluid wets the substrates more rapidly at lower shear rates, i.e. after higher shear rates initially. The explanation of this behavior has been proposed by Dandapat and Singh (Dandapat and Singh, 2010).

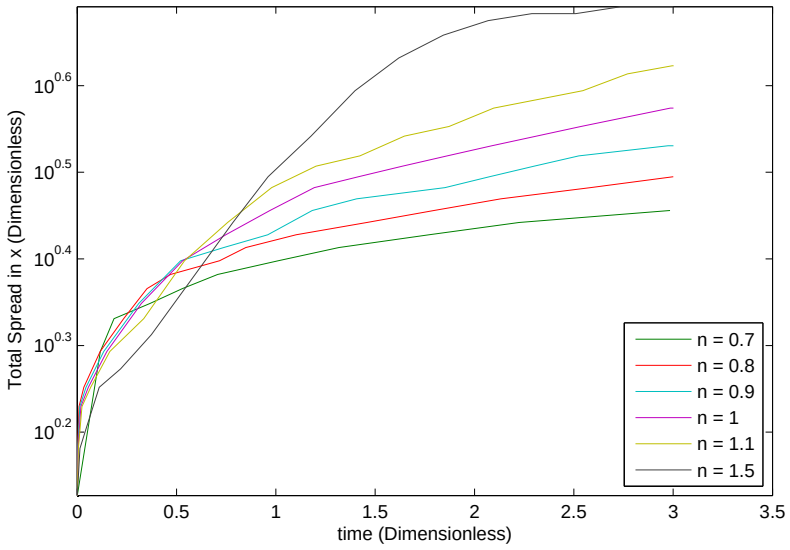

Figure 6.1: Droplet spreading on a horizontal substrate with change in flow behavior index, n

If the droplet is released from a non-equilibrium state, it takes time to reach an equilibrium state. In the early stages, the shear rate is higher but as the spreading proceeds the shear rate reduces causing the viscosity to increase in the shear thinning case. In other words, the fluid exhibiting more shear-thinning behavior becomes more viscous at lower shear rates and therefore resists spreading more.

Droplets spreading on an inclined plane can demonstrate a range of complex phenomena such as droplet splitting or breakup. As illustrated in Chapter 4, this is greatly influenced by the wetting property of the solid substrate. Next, the spreading of shear-thinning, Newtonian,

or shear thickening partially wetting droplets on an inclined substrate is investigated. In particular, the sliding velocities of the spreading/sliding droplets of different rheologies are compared. The numerical results are presented in terms of the position of the center of gravity of the droplet as a function of time. The position of the center of gravity is computed according to equations (3.1) and (3.2), where $\Omega = [0, 15] \times [0, 4]$ is the computational domain.

Physical Property	**Case 1**	**Blood**	**Water**	**10wt% PPG+15nm silica**
Density, kg/m^3	1000	1062 (Attinger et al., 2013)	1000	1086.17 (Wang et al., 2007b)
Flow behavior index, n	0.7-1.5	0.6-0.7 (Hussain et al., 1999; Myers, 2005)	1	1.728 (Wang et al., 2007b)
Consistency factor, K, Pa.s^n	0.001	0.035 (Myers, 2005)	0.001	0.0705 (Wang et al., 2007b)
Surface Tension, N/m	0.07	0.062 (Attinger et al., 2013)	0.072	0.04699(Wang et al., 2007b)
Equilibrium contact angle, θ_e^o	45	27.66	11	26.2 (Wang et al., 2007b)
Substrate inclination, θ_i^o	30, 45, 60	30, 45, 60	30, 45, 60	30, 45, 60
Volume of droplet, μl	8.3	8.3	8.3	8.3
Initial position of center of gravity	(2,2)	(2,2)	(2,2)	(2,2)

Table 6.1: Properties of the droplet spreading on inclined substrate

Table 6.1 reports the physical properties used in the numerical study. For a given time, Figure 6.2 shows that as the inclination angle is increased from 30^o to 60^o, the position of the center of gravity is shifted further downstream, as intuitively expected. It should also be noted that after an initial settling stage, the slope of the curves becomes constant, indicating that the droplet has reached its terminal velocity which results from a balance between gravity, the driving force, and the viscous dissipative force. Inclusion of contact angle hysteresis in the non-Newtonian rheology would definitely have an impact on the motion as well as the shape of the footprint of the sliding droplet, but this has not been implemented at this stage and is left as future work. Clearly, this slope increases with increasing inclination angle indicating an increase of the terminal velocity with inclination angle. The terminal velocity of the droplet is also affected by the flow behavior index, n. Initially shear-thinning fluids tend to spread/slide more rapidly due to the initially higher shear rates, but this trend is inverted later in the simulation as the shear rate becomes lower leading to a comparative decrease of the viscosity for the shear thickening fluid, $n > 1$.

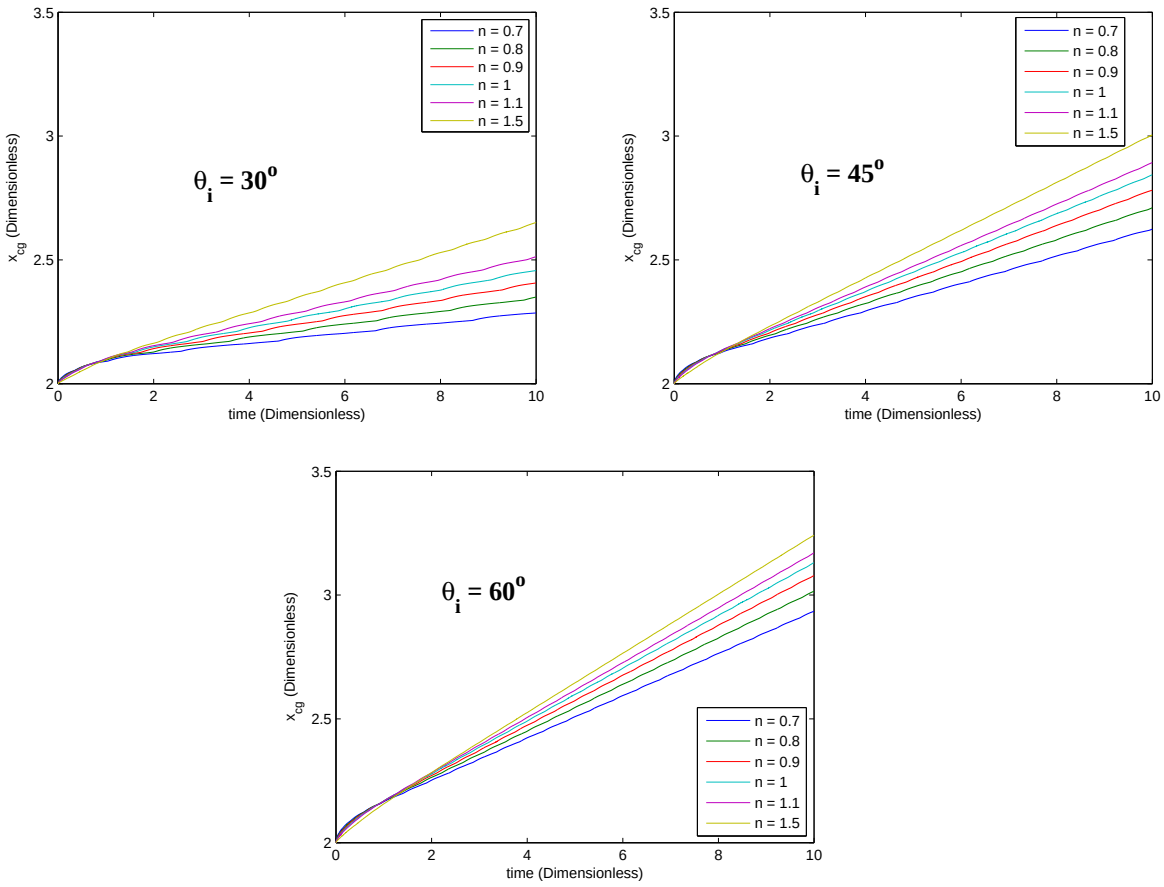

Figure 6.2: Position of center of gravity for Case 1 fluid at 30°, 45° and 60° substrate inclination

As a final illustrative example, blood (shear-thinning), water (Newtonian) and PPG/silica solution (shear-thickening) droplets are allowed to flow down an inclined glass substrate. The physical properties of these fluids are tabulated in Table 6.1. The physical properties of blood and water are measured at room temperature and pressure (RTP). For fluid property measurements for blood and water, techiques described in Section 4.2.2 are used. A mean value for the contact angle and surface tension are calculated and are reported in Table 6.1. Wang and co-researchers have reported the physical properties of PPG/Silica solution on glass substrate (Wang et al., 2007b).

Figure 6.3 illustrates the change of position of the center of gravity of the droplets with time and Figure 6.4 shows droplet height contours for water, PPG/silica solution and blood. It can be seen that the water droplet slides quickly in comparison to blood and PPG/silica solution because of its higher wetting behavior (lower θ_e) on the glass substrate. The shear rates at the beginning are higher and decrease as the droplet spreads/slides down the incline. As the

shear rates are reduced the viscosity increases for the shear-thinning fluids and decreases for shear-thickening fluids. It can be seen in Figure 6.3 that at 30° a blood droplet's motion is slower than the PPG/silica solution. On the other hand, as the inclination increases to 45° and 60°, the blood droplet "overtakes" the PPG/silica solution droplet because of its lower surface tension and higher power-law consistency factor, K. The formation of the droplet tail as the PPG/silica solution droplet slides down the incline is also apparent and becomes prominent with an inclination increase, thus slowing down a shear-thickening fluid. It is interesting to see this shift in the behavior of shear-thinning and shear-thickening fluids having similar wetting properties.

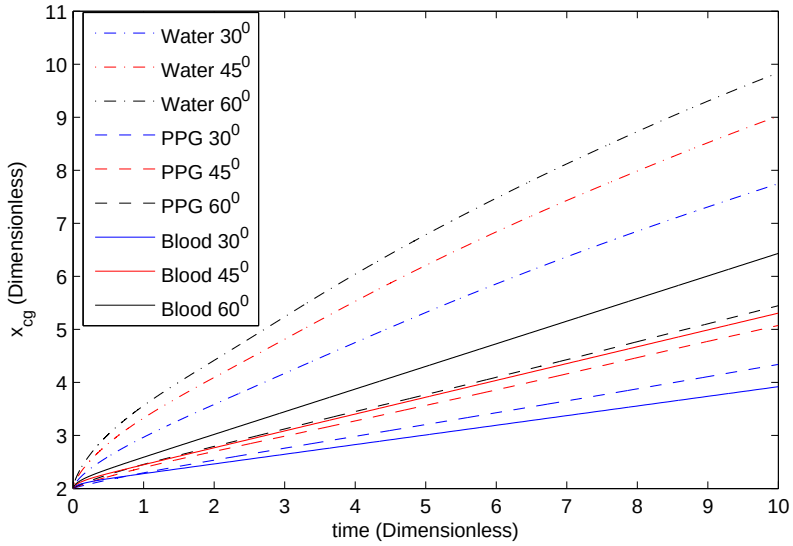

Figure 6.3: Position of center of gravity of different fluids at 30°, 45° and 60° inclinations on glass substrate

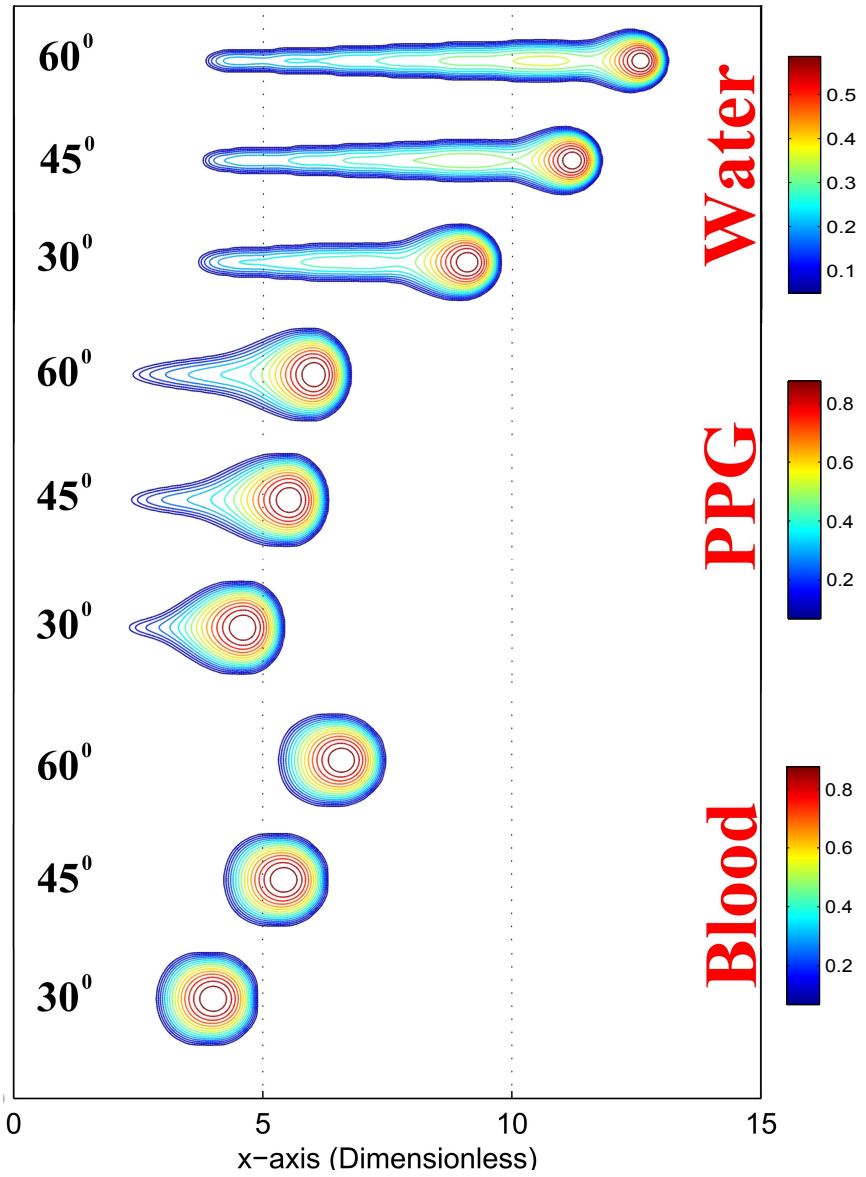

Figure 6.4: Droplet profiles after 10 non-dimensional time units

6.4 Concluding remarks

In this work, a mathematical model based on the lubrication approximation is presented which describes the spreading and sliding of droplets of a power-law fluid. These highly-nonlinear partial differential equations are solved for three-dimensional flows using a Multigrid approach. The validated numerical code first enables the investigation of the spreading of a perfectly wetting droplet of power-law fluid on a horizontal substrate. The numerical results confirm earlier observations that for all other quantities being equal, an increase of the flow index, n, leads to a more rapid wetting. The investigation is then focused on droplets spreading and sliding down an inclined plane. An interesting observation is that after an

initial transient stage, the droplets reach a constant terminal velocity and essentially travel down the inclined plane with a constant profile. It was noted, as intuitively expected, that the terminal velocity of the droplets increases with the slope of the inclined plane irrespective of the rheology but for a given inclination angle, the flow behavior index is found to have a major impact on this terminal velocity. The observed trend is that the terminal velocity decreases with the flow index, i.e. droplets of shear thinning fluid travel down slope more slowly. The trends observed are in line with the theory, and the decrease in viscosity is observed at higher shear rates for shear-thinning fluids; the opposite is true for shear-thickening fluids. The sliding dynamics of three different fluids having different rheologies are finally compared numerically. The Newtonian water droplet being a more wetting liquid spreads at a higher rate on a glass substrate and travels down slope faster than the other two fluids. Blood is a shear-thinning fluid, its viscosity therefore increases as the shear rates are reduced. For the smallest inclination angle (30^o) the blood droplet terminal velocity is higher than that of the PPG/Silica solution. This trend is then inverted for the higher inclination angles. Interestingly, the simulations revealed the formation of a tail at the rear of the sliding droplet for the shear-thickening fluid.

Chapter 7

Effect of absorption on the spreading dynamics

Contents

7.1 Introduction

The final footprint formed by the blood is not only dependent on the angle at which the droplet impacts the surface, but it is also influenced by the characteristics of the substrate it comes in contact with, i.e. substrate thickness, substrate texture and its absorptive properties (Shaler, 2011). Figure 7.1 shows bloodstains on a thin cotton t-shirt and a thick cotton towel. The impact conditions for both fabrics are the same. The material is cotton, but the texture of cotton in these two fabrics is very different. In the t-shirt, the stains observed have satellite stains and as the fabric is thin and less rough, the blood spreads inside the fabric. On the other hand, the thick towel stain has no satellite stains. This is due to the more absorptive/rough surface of the towel.

(a) Bloodstain on a thin cotton t-shirt

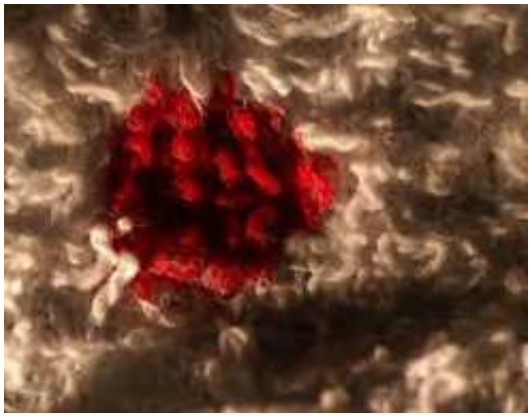

(b) Bloodstain on a thick cotton towel

Figure 7.1: Shape of the bloodstain on different porous substrates (Shaler, 2011)

The extent to which the blood droplet spreads on the porous substrate depends not only on the volume of the droplet, but also on the absorptive property of that material. If a porous substrate readily absorbs blood, the stain formed on such substrate will be compact and will express the ability of the material to absorb the fluid immediately in the porous medium before it can spread. The absorptive property plays a vital role in the shape of the bloodstains and modeling this will help forensic scientists to understand the effect of absorption on the footprints formed by blood on a porous medium.

There are two main physical processes that occur in the formation of bloodstain patterns on a porous substrate. One is the impact phase and the other is the absorption phase. In the second phase, the droplet forms a wetting front inside the porous medium and gets absorbed. The primary objective of this chapter is to investigate the droplet absorption dynamics after

its impact with the porous substrate. It is also of interest to see how the droplet absorption dynamics are affected by a change in the inclination of the porous substrate.

Droplet spreading and absorption in a porous medium is a process that has a wide range of industrial applications, for example spray painting, ink-jet printing, coating processes in pharmaceutical tablets and for protecting wood, textile processing, micro-fabrications in ceramic structures, and as discussed earlier, it has a major role in the formation of blood patterns. Due to its vast applications, absorption in porous medium has received significant attention in the past (Acton et al., 2001; Alleborn and Raszillier, 2004b; Aradian et al., 1999; Clarke et al., 2002; Davis and Hocking, 1999, 2000; Holman et al., 2002; Schwartz, 1999; Siregar et al., 2010; Starov et al., 2002; Zadrazil et al., 2006). Research related to droplet absorption in a porous medium is often based on Darcy's law to predict the rate of absorption, depth of penetration and spreading of the fluid in the porous substrate.

Davis and Hocking considered the absorption and spreading of two-dimensional droplets on horizontal porous substrates using the lubrication approximation framework (Davis and Hocking, 1999, 2000). In their model, they considered the substrate to be a cluster of vertical pores with constant depth. They performed an asymptotic analysis of the governing equations for the shape of the droplet and the fluid penetration in the porous substrate during absorption. The important result from their investigation was that for small porosity, the spreading of the droplet occurs at a fast time scale, during which the fluid penetration in the porous substrate is minimal. The absorption continues at a relatively slow rate, while the droplet spreads to come to an equilibrium state.

The industrial applications of coating and printing have been explored in depth by researchers and this research has contributed greatly to the field. Holman and co-researchers have investigated the application of a droplet on the porous substrate from the printing perspective and have come to the conclusion that the impact and the spread after impact occurs at a fast time scale (Holman et al., 2002). Alleborn and Raszillier also investigated the absorption of droplets on porous substrates, using Darcy's law for penetration into unsaturated and layered porous substrates (Alleborn and Raszillier, 2004a,b). They derived the lubrication equations for the droplet profile over and penetration depth inside the porous substrate.

The numerical model adopted here uses the physical properties of the fluid as well as physical properties of the porous substrate. This model is based on the lubrication approximation. The main assumption in this approximation is that droplet height to radius ratio is small and the inertial effects are negligible as well. The contact line singularity is overcome by introducing a thin precursor film ahead of the contact line. A disjoining pressure term is introduced to maintain the equilibrium contact angle of the droplet. The absorption model is based on Darcy's law (Alleborn and Raszillier, 2004a; Siregar et al., 2010).

This chapter presents a verified numerical study of the absorption of fluid droplets on horizontal and inclined porous substrates having different absorptive properties. Section 7.2 outlines different methodologies that are available to model the absorption of fluid in porous substrates and establishes the methodology adopted in this research. Section 7.3 provides the details of the governing equations and the numerical formulation of the proposed model. Section 7.4 is devoted to presenting the details of the validation of the numerical scheme with the help of a comparison with an analytical solution. Lastly, Section 7.5 presents the results from the numerical simulations for absorption of droplets on horizontal and inclined porous substrates. This section also highlights the importance of different parameters that influence the absorption dynamics. Conclusions are drawn in Section 7.6.

7.2 Methodology

A porous medium is a structure that contains interconnected cavities/gaps. These are distributed all across a porous medium. These cavities can be classified into two types; large and small ones. Large cavities are also known as pores. These have a major contribution towards the fluid flow in a porous medium. On the other hand, the size of small cavities is comparable to the size of molecules. These do not contribute towards bulk fluid motion in the porous medium, but they may contribute towards the diffusion process. The microscopic properties of the porous medium are very complex and are often ignored in the characterization of the physical properties of the porous medium. Macroscopic properties that are commonly used in describing the physical properties of the porous medium are the porosity and the permeability. Porosity defines the ratio of pore to total volume while permeability is the capability

of the porous medium to transmit fluid. There are a number of factors that affect permeability, e.g. textural properties, pore/grain size and their distribution, shape and packing (homogeneity) of grains, etc. Most natural and artificial porous media are inhomogeneous, because of their complex structure and are rarely uniform in cavity distribution. The porous medium can still be considered homogeneous if the microscopic properties have negligible effect on the overall macroscopic properties. A complete mathematical description of the porous medium is very hard due to the complex nature of its structure. Lattice Boltzmann models seem to do a good job of modelling the detail of the flow through a porous medium, the issue being the difficulty of modelling a sizeable chunk of material. The modelling of flow dynamics in a porous substrate using Lattice Boltzmann models for a reasonable size of material is not going to be possible in the foreseeable future (Pan et al., 2006). There are many methodologies that have been developed to understand and appreciate the mechanisms that drive the flow through a porous medium; however, these methodologies are based on assumptions and involve many approximations. The main methodologies are the capillary bundle models, numerical methods, pore-scale network modeling and continuum approaches (Sochi, 2010).

The continuum approach is a simplified macroscopic method in which the porous medium is considered to be a continuum. The complexities and minute details of the microscopic structure are incorporated in terms like permeability and porosity, which represent the average properties of the porous medium. Commonly used continuum models are Darcy's law, Blake-Kozeny-Carman and Ergun (Sochi, 2010). Darcy's law is one of the most straightforward continuum models widely used in the literature to solve the problem of fluid flow in a porous medium.

Capillary bundle models the porous medium as a bundle of tubes. These tubes can have different shapes. The simplest is identical parallel cylindrical tubes. The advantage this model has over other models is its simplicity. The main disadvantage of this model is the limitation to the definition of the tube structure. In practice, the cavity region is not well represented by uniform tubes and is very random and more complex than the simple shapes. Another drawback of this model which makes it an unsatisfactory choice is that it is a unidirectional model and can only solve one-dimensional fluid flow scenarios (Sochi, 2010).

A numerical technique requires a comprehensive representation of the porous medium at the pore-scale with relevant physical properties at that scale as well. Numerical methods utilize the finite difference or finite volume technique to solve the problem computationally. The main advantage of this approach is that it is the most explicit way to describe a physical phenomenon and is very close to the analytical solution (Sochi, 2010). The major drawback of this method is the detailed pore description that is necessary for this approach to produce practical results. Other difficulties with this technique are the high computational costs to implement it and convergence problems (Sochi, 2010).

Pore-scale network modelling is much too diverse and complicated. It is a combination of the continuum approach and numerical techniques. It partially uses the physical characteristics of the porous media with the details of the structure at the pore-scale. The advantage of this technique is the affordable computational cost. The cavities in the porous medium are described by a network of channels having regular geometries. This method is able to predict the average behavior, because it is the combination of the two strong methods. Complexity arises when combining the two methods (Sochi, 2010).

The continuum approach with Darcy's model to define the constitutive equations in the porous medium is the base method which is going to be utilized to solve the absorption dynamics problem of interest here. There are several reasons behind choosing this methodology. Firstly, that the actual pore structure is too diverse and is beyond the scope of this research. The logical explanation is that the pore structure is very inconsistent and varies from specimen to specimen; also it is challenging to determine correctly the porous structure experimentally. Secondly, the pore size is relatively smaller than the actual mesh resolution adopted. In order to get satisfactory results the mesh has to be very fine which increases computational costs. This approach utilizes average physical properties of the porous medium. This method will not be able to predict the results from one single experiment, but the results from the numerical simulations can be treated as average results for a series of experiments.

7.3 Mathematical and numerical formulation

In this section, the model described earlier is extended to account for the absorption dynamics. The fluid is assumed to be incompressible. Density, surface tension, and viscosity remain constant during absorption, i.e. the fluid is Newtonian. In the sliding absorption dynamics, contact angle hysteresis has been neglected and is left as future work. Figure 7.2 shows a two-dimensional sketch of the droplet and the absorbed fluid in $x - z$ plane. The porous substrate is described by porosity, ϕ, and permeability, k_p. The depth to which the fluid gets absorbed is denoted by $h_p\,(x, y, z, t)$. Capillary pressure, p_c has a vital role in porous medium. It is the force necessary to squeeze the droplet through the pore diameter. The droplet thickness is denoted by $h\,(x, y, z, t)$. The equilibrium contact angle of the droplet is denoted by θ_e. In order to avoid contact-line singularity, a thin precursor film, h^*, is introduced ahead of the contact line with a suitable disjoining pressure term (Schwartz and Eley, 1998). h^* is also introduced in the porous medium to avoid singularity as the fluid starts to get absorbed.

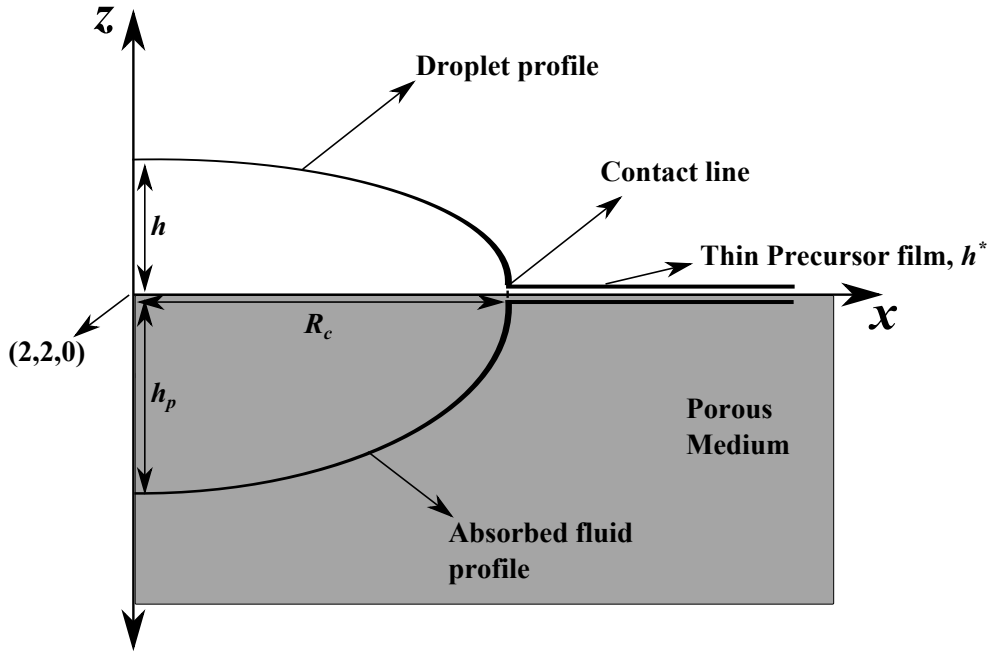

Figure 7.2: Profile of the droplet and the absorbed fluid

The droplet flow above the porous substrate is governed by continuity and the Navier-Stokes equations mentioned earlier, see equations (2.1), (2.2), (2.3), and (2.4). The porous medium flow equations are illustrated by the volume averaged velocity vector, $\vec{U_p'} = u_p'\,\hat{\mathrm{i}} + v_p'\,\hat{\mathrm{j}} + w_p'\,\hat{\mathrm{k}}$. Where $\hat{\mathrm{i}}$, $\hat{\mathrm{j}}$, and $\hat{\mathrm{k}}$ are unit vectors in x, y and z directions. The primes denote dimensional

variables. The continuity equation in the porous medium is,

$$\nabla.\vec{U_p'} = 0. \tag{7.1}$$

By Darcy's law, the velocity in the porous medium is given by,

$$\overrightarrow{U_p'} = -\frac{k_p}{\mu}\left(\nabla p_p' + \rho\overrightarrow{g}\right), \tag{7.2}$$

where p_p is the pressure in the porous medium. p_p follows a Laplacian relationship:

$$\triangle p_p' = 0. \tag{7.3}$$

p_p' is equal to the capillary pressure, $p_p' = -p_c$ at the fluid front. These dimensional variables are first converted into non-dimensional ones (without primes). Let H_0 be the characteristic droplet thickness at rest on a horizontal substrate and $L_0 = R_0$ be the characteristic radius of the droplet. The lubrication approximation is based on the assumption that: $\epsilon = \frac{H_0}{L_0} \ll 1$. The scalings used here are usual and have been used extensively in the past for Newtonian rheology, i.e. $U_0 = \frac{L_0}{T_0},\ P_0 = \frac{\sigma\epsilon}{L_0}$ (Schwartz and Eley, 1998; Sellier, 2003). The characteristic time scale used here is that proposed by Orchard, $T_0 = \frac{L_0\mu}{\sigma\epsilon^3}$, (Orchard, 1963). The velocity, pressure and the space coordinates are made dimensionless using,

$$u' = U_0 u,\ u_p' = U_0 u_p,\ v' = U_0 v,\ v_p' = U_0 v_p,\ w' = \epsilon U_0 w,\ w_p' = \epsilon U_0 w_p,$$
$$p_p' = P_0 p_p,\ x' = L_0 x,\ y' = L_0 y,\ z' = H_0 z,\ h' = H_0 h,\ h_p' = H_0 h_p, \tag{7.4}$$

where U_0 is velocity scale in the x direction. The no-slip boundary conditions on the substrate surface ($z = 0$) for the droplet lead to,

$$u(x, y, 0, t) = v(x, y, 0, t) = 0, \tag{7.5}$$

and there is no stress at the liquid-air interface,

$$\left.\frac{\partial u}{\partial z}\right|_{z=h} = \left.\frac{\partial v}{\partial z}\right|_{z=h} = 0, \tag{7.6}$$

Mass conservation and pressure continuity along the surface of the porous substrate suggests

that the vertical velocity of the droplet and penetrated fluid is given as,

$$w\left(x,y,0,t\right)=w_p\left(x,y,0,t\right), \tag{7.7}$$

and for the pressure,

$$p_p(x,y,0,t)=p(x,y,0,t), \tag{7.8}$$

The kinematic condition gives,

$$\phi\frac{\partial h_p}{\partial t}+u_p\frac{\partial h_p}{\partial x}+v_p\frac{\partial h_p}{\partial y}+w_p=0. \tag{7.9}$$

Capillary effects are taken into account with the change in pressure at the wet front, $z=-h_p$,

$$p_p(x,y,-h_p,t)=-p_c, \tag{7.10}$$

where p_c is the capillary pressure. The droplet spreads in the x and y coordinate. In the porous substrate, the fluid motion takes place mostly in the vertical direction and the radial motion in the x and y direction of the fluid is considered to be negligible,

$$\frac{\partial p_p}{\partial x},\frac{\partial p_p}{\partial y}\ll\frac{\partial p_p}{\partial z}, \tag{7.11}$$

Neglecting terms of order $\epsilon^2=\frac{H_0^2}{L_0^2}\ll 1$ or higher, mass and momentum balance equations along with boundary conditions reduce the governing equations to a partial differential equation for the height of the droplet which can be written in dimensionless form, h, as,

$$\frac{\partial h}{\partial t}=-\left[\frac{\partial}{\partial x}\left(\frac{h^3}{3}\left(\frac{Bo\sin\theta_i}{\epsilon}-\frac{\partial p}{\partial x}\right)\right)+\frac{\partial}{\partial y}\left(\frac{h^3}{3}\left(-\frac{\partial p}{\partial y}\right)\right)\right]+w_p, \tag{7.12}$$

which is dependent on the sink term, w_p, which describes the mass lost in the porous substrate due to capillary suction. The influence of gravity is characterized by the Bond number, Bo, which is dimensionless. The physical properties of the porous substrate are described by dimensionless numbers, i.e. the permeability number, Pm, the porosity, ϕ, and the suction number, Su,

$$Pm=\frac{k_pL_0^2}{H_0^4},\quad Su=\frac{p_cL_0^2}{\sigma H_0},\quad Bo=\frac{\rho gL_0^2}{\sigma}. \tag{7.13}$$

With the help of the above mentioned boundary conditions and scalings, the rate of change

of fluid penetration depth, h_p from equation (7.9) is given by,

$$\frac{\partial h_p}{\partial t} = -\frac{w_p}{\phi}, \tag{7.14}$$

and the vertical velocity of the absorbed fluid in dimensionless form is given by,

$$w_p = -Pm\left(\frac{Su + p}{h_p} + Bo\cos\theta_i\right). \tag{7.15}$$

For details, see Appendix (C). Combining equations (7.14) and (7.15) leads to:

$$\frac{\partial h_p}{\partial t} = \frac{Pm}{\phi}\left(\frac{Su + p}{h_p} + Bo\cos\theta_i\right), \tag{7.16}$$

and pressure in the droplet is given by,

$$p = -\nabla^2(h) - \Pi(h) + Bo\cos\theta_i\,(h - z)\,, \tag{7.17}$$

where, $\Pi(h)$ is the disjoining pressure term and θ_i is the substrate inclination angle. Equations (7.12), (7.16), and (7.17) form the governing equations for the fluid flow over and inside the porous substrate. A detailed derivation is in the Appendix C.

7.3.1 Numerical discretization

The spatial discretization of the lubrication approximation equations (7.12), (7.16), and (7.17) uses the central Finite-Differencing scheme with uniform mesh spacing in the x and y direction, leading to values of h and p at mesh points (i, j) in the computational grid. To simplify the presentation of the derivations below, let the right-hand-side of equations (7.18) and (7.19) be represented by $\mathcal{F}^{n_t}$, i.e. $\frac{\partial h_{ij}}{\partial t} = \mathcal{F}^{n_t}$, and with subsequent subscripts to represent

the relevant equations:

$$\frac{\partial h_{ij}}{\partial t} = -\frac{1}{\Delta x}\left\{\left(\frac{h_{i+1j}^3 + h_{ij}^3}{2(3)}\right)\left(C_1 - \frac{p_{i+1j} - p_{ij}}{\Delta x}\right) - \left(\frac{h_{i-1j}^3 + h_{ij}^3}{2(3)}\right)\left(C_1 - \frac{p_{ij} - p_{i-1j}}{\Delta x}\right)\right\}$$
$$- \frac{1}{\Delta y}\left\{\left(\frac{h_{ij+1}^3 + h_{ij}^3}{2(3)}\right)\left(\frac{p_{ij} - p_{ij+1}}{\Delta y}\right) - \left(\frac{h_{ij-1+}^3 h_{ij}^3}{2(3)}\right)\left(\frac{p_{ij-1} - p_{ij}}{\Delta y}\right)\right\}$$
$$\underbrace{-Pm\left(Bo\cos\theta_i + \frac{Su + pij}{h_{pij}}\right)}_{\mathcal{F}_h^{n_t}}, \tag{7.18}$$

$$\frac{\partial h_{p\,ij}}{\partial t} = \underbrace{\frac{Pm}{\phi}\left(Bo\cos\theta_i + \frac{Su + p_{ij}}{h_{p\,ij}}\right)}_{\mathcal{F}_{h_p}^{n_t}}, \tag{7.19}$$

$$p_{ij} + \left(\frac{h_{i+1j} + h_{i-1j} - 2h_{ij}}{\triangle x^2}\right) + \left(\frac{h_{ij+1} + h_{ij-1} - 2h_{ij}}{\triangle y^2}\right)$$
$$+ \frac{(1 - cos\theta_e)\,(n_d - 1)\,(m_d - 1)}{\epsilon^2 h^*(n_d - m_d)}\left[\left(\frac{h^*}{h_{ij}}\right)^{n_d} - \left(\frac{h^*}{h_{ij}}\right)^{m_d}\right] - Bo\cos\theta_i(h_{ij}) = 0. \tag{7.20}$$

Time discretization of the equation (7.18) is achieved with the help of the Crank-Nicolson method:

$$\frac{h_{ij}^{n_t+1} - h_{ij}^{n_t}}{\triangle t} = \frac{1}{2}\left(\mathcal{F}_h^{n_t+1} + \mathcal{F}_h^{n_t}\right), \tag{7.21}$$

where $\triangle t = \left(t^{n_t+1} - t^{n_t}\right)$. Equation (7.21) can be re-arranged such that the new time step variables are arranged to the left to give:

$$h_{ij}^{n_t+1} - \frac{\triangle t}{2}\mathcal{F}_h^{n_t+1} = h_{ij}^{n_t} + \frac{\triangle t}{2}\mathcal{F}_h^{n_t}, \tag{7.22}$$

with a similar expression for h_p,

$$h_{p\,ij}^{n_t+1} - \frac{\triangle t}{2}\mathcal{F}_{h_p}^{n_t+1} = h_{p\,ij}^{n_t} + \frac{\triangle t}{2}\mathcal{F}_{h_p}^{n_t}, \tag{7.23}$$

where $h_{ij}^{n_t+1} - \frac{\triangle t}{2}\mathcal{F}_h^{n_t+1} = \mathcal{L}_k^h$. The same notation is adopted for h_p where $h_{p\,ij}^{n_t+1} - \frac{\triangle t}{2}\mathcal{F}_{h_p}^{n_t+1} = \mathcal{L}_k^{h_p}$ and the left hand side of equation (7.20) is equal to $\mathcal{L}_k^p$. The temporal error control described in (Gaskell et al., 2004) is used to enable the automatic adaptive time stepping (Lee et al., 2007). The time integration above is implemented in a Multigrid solver to provide a fast and efficient approach to the solution of the non-linear equations (7.18), (7.19) and (7.20)

by accelerating convergence via the use of a hierarchical set of grid levels where residuals are effectively reduced on successive coarse grid levels and corrections to the solutions transferred back to fine grid levels. Equations (7.18), (7.19) and (7.20) can be re-written at a particular grid level, k, as,

$$\mathcal{L}_k^h\left(h_k^{n_t+1}, p_k^{n_t+1}, h_{p\,k}^{n_t+1}\right) = f_k^h\left(h_k^{n_t}, p_k^{n_t}, h_{p\,k}^{n_t}\right), \tag{7.24}$$

$$\mathcal{L}_k^{h_p}\left(p_k^{n_t+1}, h_{p\,k}^{n_t+1}\right) = f_k^{h_p}\left(p_k^{n_t}, h_{p\,k}^{n_t}\right), \tag{7.25}$$

$$\mathcal{L}_k^p\left(h_k^{n_t+1}, p_k^{n_t+1}\right) = f_k^p\left(h_k^{n_t}, p_k^{n_t}\right), \tag{7.26}$$

where, $f_k^h(h_k^{n_t}, p_k^{n_t}, h_{p\,k}^{n_t})$, $f_k^{h_p}(p_k^{n_t}, h_{p\,k}^{n_t})$ and $f_k^p\left(h_k^{n_t}, p_k^{n_t}\right)$ are the right-hand-sides of equations (7.22), (7.23), and (7.20). Let $(h_{0k}^{n_t+1}, p_{0k}^{n_t+1}, h_{0pk}^{n_t+1})$ be the initial estimate to the solution of equations (7.24), (7.25) and (7.26). Equations (7.20), (7.22), and (7.23) which are for h and similar equations for h_p are solved using the full approximation storage (FAS) and Full Multigrid (FMG) technique, described in (Lee et al., 2007) with Red-Black Gauss-Seidel Newton iteration scheme used with linearized Newton iterative steps to perform relaxation. The linearized form of equations (7.24), (7.25) and (7.26) is obtained by computing the local Jacobian, so that the relaxation goes forward by solving:

$$\frac{\partial \mathcal{L}_k^h}{\partial h_{ij}}\Delta h + \frac{\partial \mathcal{L}_k^h}{\partial p_{ij}}\Delta p + \frac{\partial \mathcal{L}_k^h}{\partial h_{p\,ij}}\Delta h_p = f_k^h - \mathcal{L}_k^h\left(h_k^{n_t}, p_k^{n_t}, h_{p\,k}^{n_t}\right), \tag{7.27}$$

$$\frac{\partial \mathcal{L}_k^{h_p}}{\partial h_{ij}}\Delta h + \frac{\partial \mathcal{L}_k^{h_p}}{\partial p_{ij}}\Delta p + \frac{\partial \mathcal{L}_k^{h_p}}{\partial h_{p\,ij}}\Delta h_p = f_k^{h_p} - \mathcal{L}_k^{h_p}\left(h_{p\,k}^{n_t}, p_k^{n_t}\right), \tag{7.28}$$

$$\frac{\partial \mathcal{L}_k^p}{\partial h_{ij}}\Delta h + \frac{\partial \mathcal{L}_k^p}{\partial p_{ij}}\Delta p + \frac{\partial \mathcal{L}_k^p}{\partial h_{p\,ij}}\Delta h_p = f_k^p - \mathcal{L}_k^p\left(h_k^{n_t}, p_k^{n_t}\right). \tag{7.29}$$

$$J = \frac{\partial\left(\mathcal{L}_k^h, \mathcal{L}_k^p, \mathcal{L}_k^{h_p}\right)}{\partial\left(h_k^{n_t+1}, p_k^{n_t+1}, h_{p\,k}^{n_t+1}\right)}. \tag{7.30}$$

where the local Jacobian, J, is given for a particular grid level, k. The Newton iteration proceeds by solving,

$$J\begin{pmatrix}\Delta h\\ \Delta p\\ \Delta h_p\end{pmatrix} = \begin{pmatrix} f_k^h - \mathcal{L}_k^h(h_{0k}^{n_t+1}, p_{0k}^{n_t+1}, h_{p0\,k}^{n_t+1}) \\ f_k^p - \mathcal{L}_k^p(h_{0k}^{n_t+1}, p_{0k}^{n_t+1}) \\ f_k^{h_p} - \mathcal{L}_k^{h_p}(p_{0k}^{n_t+1}, h_{p0\,k}^{n_t+1}) \end{pmatrix} \tag{7.31}$$

for Δh, Δh_p and Δp at grid level k. A new approximate solution is obtained by simultaneously solving equations (7.27), (7.28) and (7.29) and the initial estimates are updated accordingly via,

$$\tilde{h}_{0k}^{n_t+1} = h_{0k}^{n_t+1} + \Delta h, \tag{7.32}$$

$$\tilde{p}_{0k}^{n_t+1} = p_{0k}^{n_t+1} + \Delta p. \tag{7.33}$$

$$\tilde{h}_{p0k}^{n_t+1} = h_{p0k}^{n_t+1} + \Delta h_p, \tag{7.34}$$

A detailed derivation of the approach is described in Appendix C.

7.4 Validation

Thin film dynamics are easy to solve in comparison to the motion of droplets, because the singularity which arises due to contact-line motion is absent. This reduces the complexity of the problem. Therefore, the absorption of a uniform thickness film is used to validate the numerical scheme introduced in the previous section. Acton and co-researchers derived the analytical solution for the growth of the penetration depth inside the porous substrate and the reduction of the height of the thin film above the porous substrate for the motion of wetting the front in an unsaturated porous medium (Acton et al., 2001). Alleborn and co-researcher extended Acton's work by including the effect of capillary pressure in the analytical solution (Alleborn and Raszillier, 2004a). Neglecting the disjoining pressure term and the surface tension effects, the governing equations (7.12) and (7.16) are reduced to,

$$\frac{\partial h}{\partial t} = -Pm\left(\frac{Su}{h_p} + Bo\right), \tag{7.35}$$

$$\frac{\partial h_p}{\partial t} = \frac{Pm}{\phi}\left(\frac{Su}{h_p} + Bo\right), \tag{7.36}$$

and,

$$h + \phi h_p = h_0, \tag{7.37}$$

where, $h\,(t=0) = h_0$, i.e. the initial thickness of the thin film above the porous substrate.

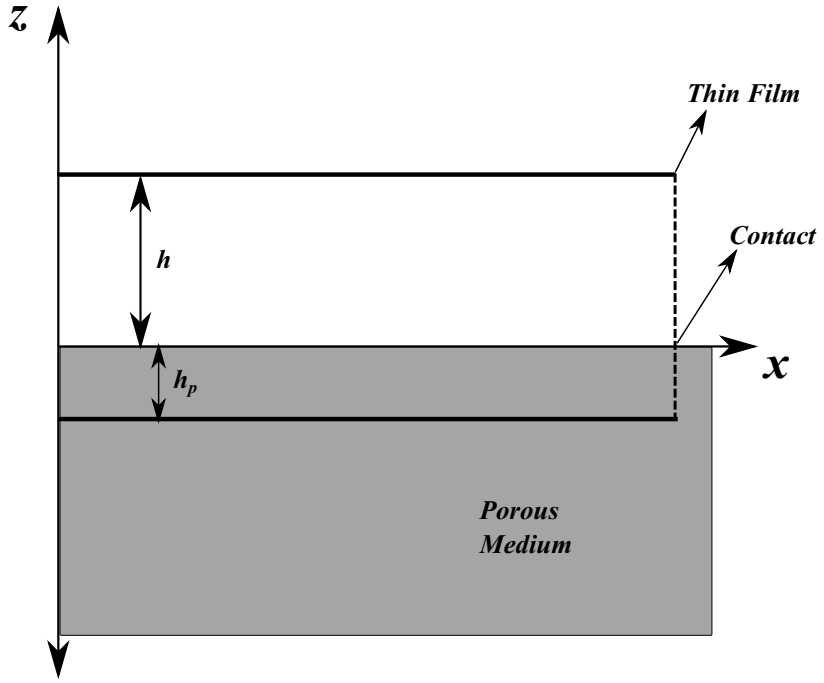

Figure 7.3: Sketch of the thin film absorption

Figure 7.3 shows the sketch of the thin film and of the absorbed fluid in the porous substrate. Consider equation (7.35) for the analytical solution. Substitute the value of h_p from equation (7.37) into (7.35) and rearrange to give,

$$\frac{\partial h}{\partial t} = -Pm\left(Bo - \frac{Su\,\phi}{h - h_0}\right), \tag{7.38}$$

where $h_0 = 1$ for the simulations. Divide both sides of equation (7.38) by $\left(Bo - \frac{Su\,\phi}{h-1}\right)$ and integrate with respect to time,

$$\int \frac{1}{\left(Bo - \frac{Su\,\phi}{h-1}\right)} \frac{\partial h}{\partial t} dt = \int -Pm\, dt, \tag{7.39}$$

This ordinary differential equation is integrated to solve for time,

$$t = \frac{Su\,\phi\,\log\left(Su\,\phi\right) - \mathrm{Su}\,\phi\,\log\left(Su\,\phi - Bo\,(h-1)\right)}{Pm\,Bo^2} - \frac{(h-1)}{Pm\,Bo}. \tag{7.40}$$

This is the analytical solution for the time taken for the height of the film to change as it gets absorbed in the porous medium. Using the relationship described in equation (7.37), a similar analytical expression can be calculated for the time for the change in fluid penetration depth inside the porous substrate.

In the following, computations are carried out with fixed properties given in Table (7.1),

Property	**Value**
Bond number, Bo	1
Permeability number, Pm	0.005
Suction number, Su	1
Porosity, ϕ	0.2

Table 7.1: Properties of fluid used in simulations of uniform thin film absorption

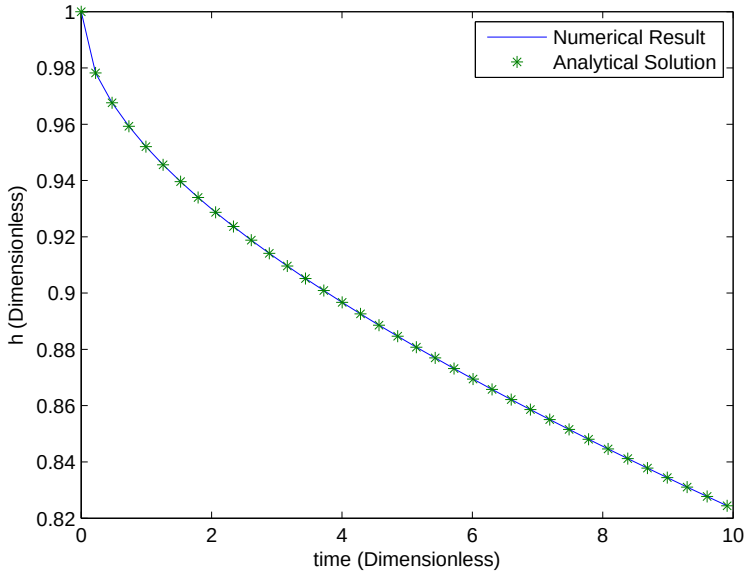

(a) Variation of thin film height with time

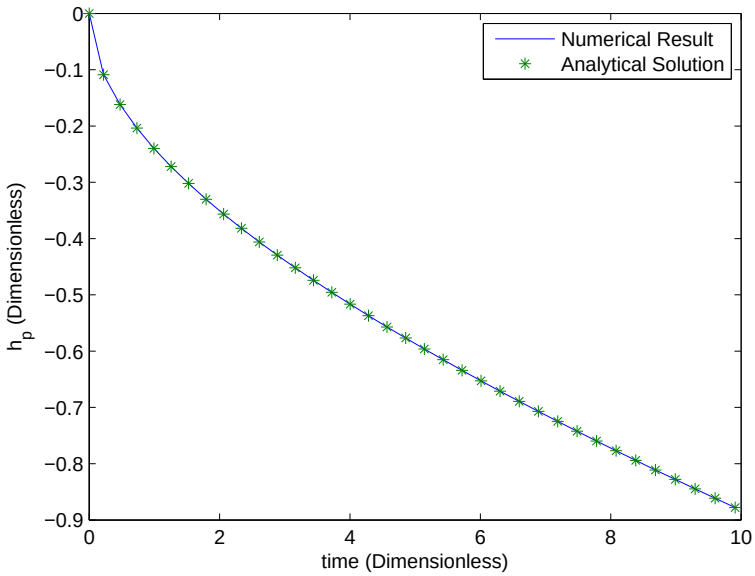

(b) Variation of penetration depth with time

Figure 7.4: Comparison of the analytical and numerical results to validate the absorption dynamics

Figure 7.4 shows that the numerical computation and analytical results have a good agreement for the height of the thin film above the porous substrate and the penetrated depth inside the porous substrate. This gives the required confidence in the accuracy of the numerical implementation.

7.5 Results and discussion

The absorption model described in the previous section is applied to the two different types of flow: absorption on horizontal and inclined porous substrates.

7.5.1 Horizontal Absorption

The physical properties of the fluid, i.e. surface tension, viscosity, density, etc., and the properties of the substrate, i.e. porosity, permeability, roughness, equilibrium contact angle, suction, etc., play a vital role in the dynamics of the droplet on a porous medium. There are principally four physical parameters which govern the motion of fluid in the porous medium, i.e. porosity, permeability, suction number, and equilibrium contact angle. In the present study, each parameter is varied keeping all the other parameters constant to see the temporal effect on the absorbed volume, droplet volume above the porous substrate, droplet profile and the profile of the absorbed fluid.

7.5.1.1 Effect of porosity, ϕ

Physical Property	**Case 1**
Density, kg/m^3	1000
Viscosity, μ, Pa.s	0.001
Surface Tension, N/m	0.07
Equilibrium Contact Angle, θ_e, $^{\circ}$	22.92
Porosity, ϕ	0.1-0.9
Suction number, Su	1×10^4
Permeability, Pm	5×10^{-5}
Volume of droplet, V_0, μl	10.42
Initial position of centre of gravity	(2,2)

Table 7.2: Physical properties for simulations of porosity variations on horizontal substrates

Figure 7.5 shows effect of porosity on the absorption dynamics of droplets on horizontal substrates. The first plot shows the variation of the maximum height of the droplet with time. As the porosity is decreased, the rate of change in height decreases i.e. the slope of the plot becomes less negative. The time taken for the droplet to get fully absorbed increases as the porosity is reduced, as shown in the plot of the variation of the volume of the droplet with time. The depth of absorption increases with a decrease in porosity. This is true because the porosity dictates the pore-to-bulk volume ratio. Lower porosity suggests that the pore size is

very small so the fluid will penetrate further into the porous substrate to achieve equilibrium, because all the other physical properties are constant. Figure 7.7 describes the shape of a droplet after 10 dimensionless units. The results clearly show the type of behavior observed in Figure 7.5. As the porosity of the material is reduced, the material will allow the fluid to penetrate more and vice-versa. So the porosity dictates the extent of absorption for the fluid. The total time of absorption, τ_{absorp} is calculated for different values of the porosity. In Figure 7.6, the numerically calculated τ_{absorp} is plotted against porosity. This figure shows clearly that the τ_{absorp} has a power-law dependence on the porosity, with an exponent of -0.7708.

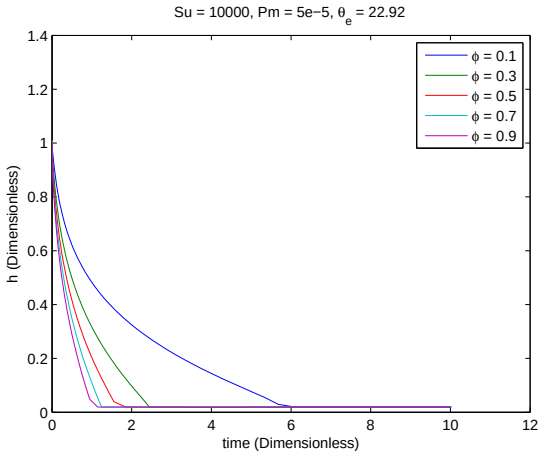

(a) Variation of the maximum height of the droplet

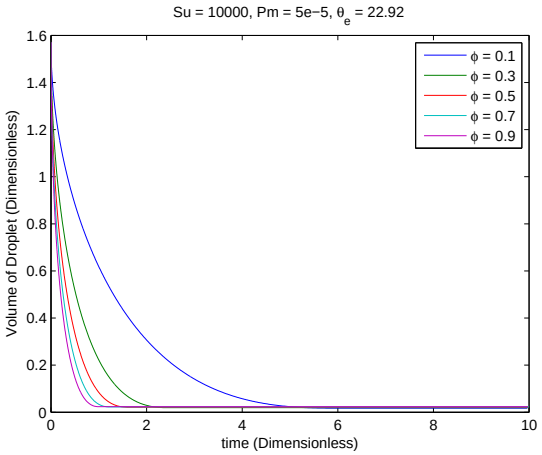

(b) Variation of volume of the droplet

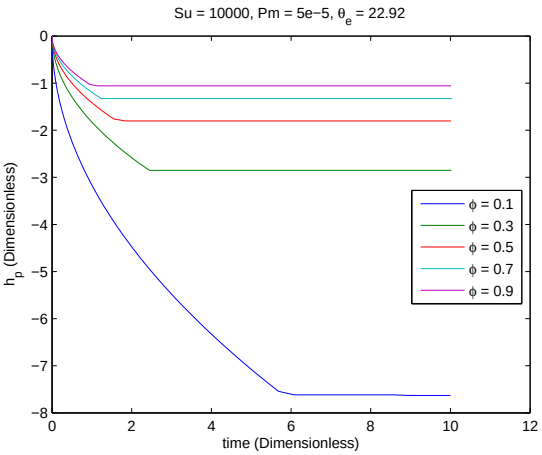

(c) Variation of the maximum depth of absorbed fluid

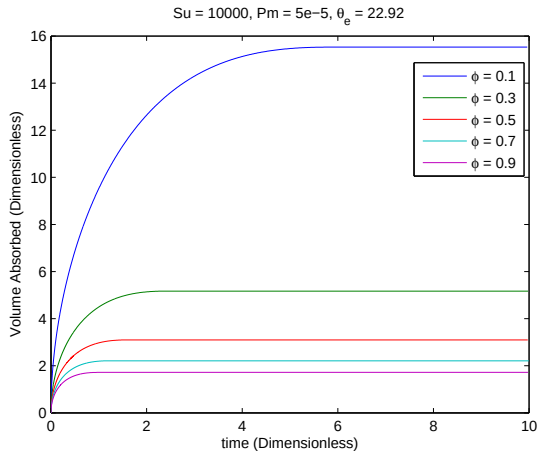

(d) Variation of absorbed volume

Figure 7.5: Effect of the variation of porosity on absorption of droplets on horizontal substrates

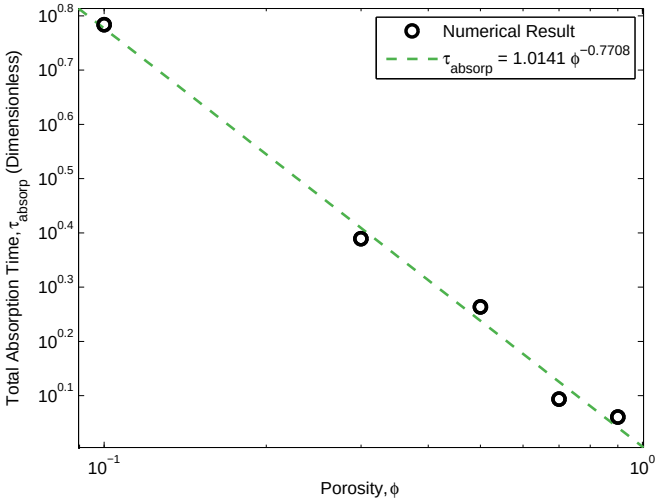

Figure 7.6: Dependence of total absorption time, τ_{absorp} on porosity

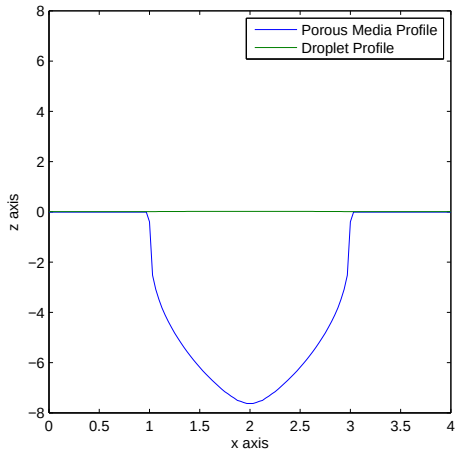

(a) $\phi = 0.1$

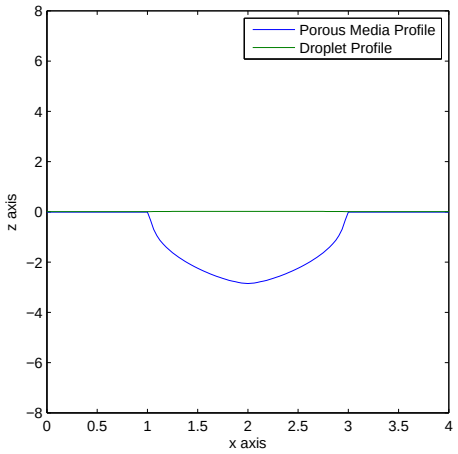

(b) $\phi = 0.3$

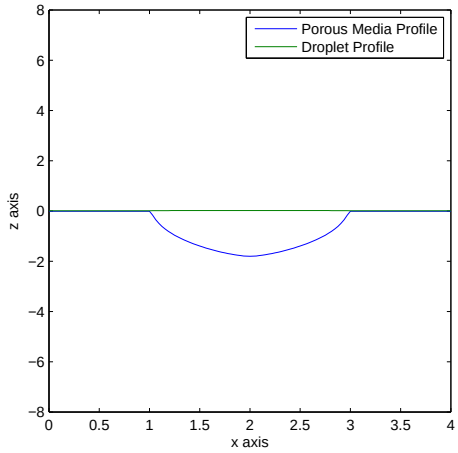

(c) $\phi = 0.5$

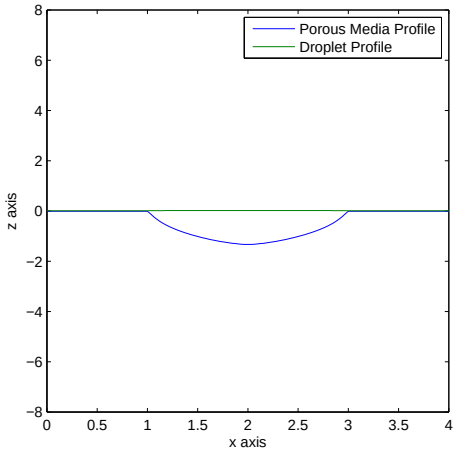

(d) $\phi = 0.7$

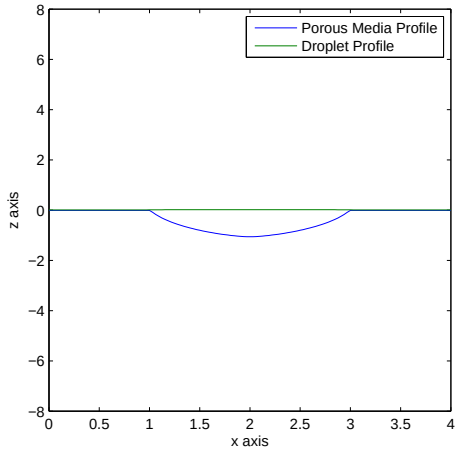

(e) $\phi = 0.9$

Figure 7.7: Effect of the porosity on the profile of the droplet and shape of the fluid in the porous medium after 10 dimensionless time units

7.5.1.2 Effect of permeability, Pm

Physical Property	**Case 1**
Density, kg/m^3	1000
Viscosity, μ, Pa.s	0.001
Surface Tension, N/m	0.07
Equilibrium Contact Angle, θ_e, $^{\circ}$	22.92
Porosity, ϕ	0.5
Suction number, Su	1×10^4
Permeability, Pm	5×10^{-4} to 5×10^{-7}
Volume of droplet, V_0, μl	10.42
Initial position of centre of gravity	(2,2)

Table 7.3: Physical properties for permeability variations on horizontal substrates

Figure 7.8 shows the effect of change of permeability on the absorption dynamics. Permeability is the ability of a material to transmit fluid. Keeping all the other properties constant, the reduction in permeability causes resistance in the absorption of the fluid. The rate of change in height of the droplet decreases which will directly cause the volume rate to change as well. The depth to which the fluid is absorbed also changes with a variation in permeability. The volume in the porous medium occupied by the fluid reduces as the permeability is reduced. Figure 7.10 shows the effect of a change in permeability on the shape of the droplet and its subsequent penetration in the porous medium after 10 dimensionless time units. Permeability dictates the resistance in absorption dynamics. Interestingly, these profiles show that as the permeability is reduced the droplet starts to spread from its equilibrium position of 1 due to the increased resistance from the porous media. This spread causes a significant change in the shape of the fluid in the porous medium, i.e. the starting absorption diameter becomes large. A range of values of permeability between the range of 5×10^{-4} to 5×10^{-7} is used to see the influence of permeability on the total absorption time, τ_{absorp}. Figure 7.9 shows that τ_{absorp} also has a power-law dependence on permeability, with an exponent of -0.7943. This power-law dependence has also been reported previously by Alleborn and Raszillier (Alleborn and Raszillier, 2004a). Their dependence analysis was only on permeability. Here all the major factors that can influence the rate of absorption are taken into account.

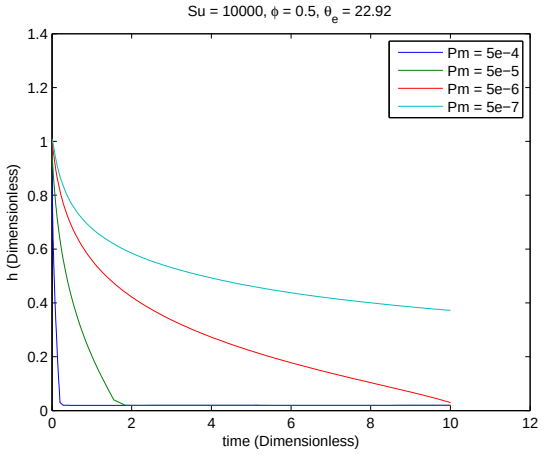

(a) Variation of the maximum height of the droplet

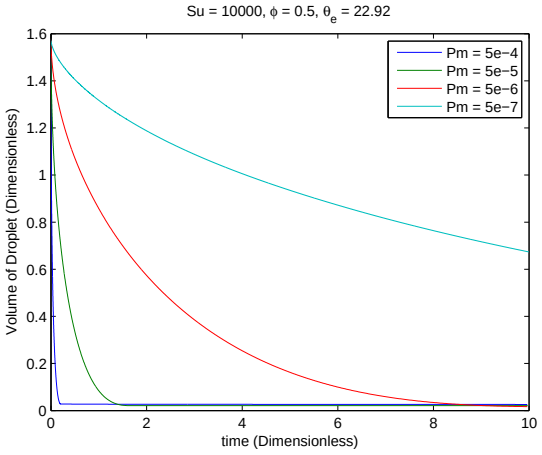

(b) Variation of volume of the droplet

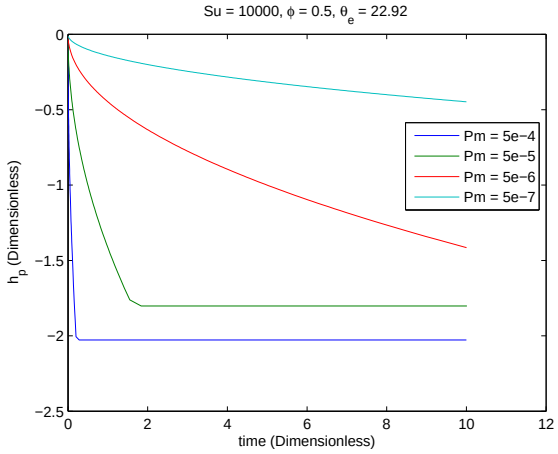

(c) Variation of the maximum depth of absorbed fluid

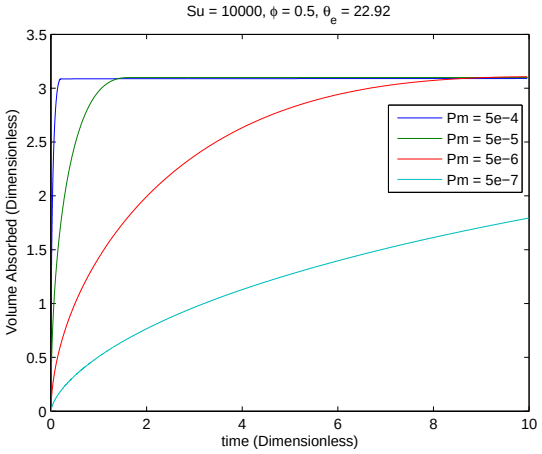

(d) Variation of absorbed volume

Figure 7.8: Effect of the variation of permeability on absorption

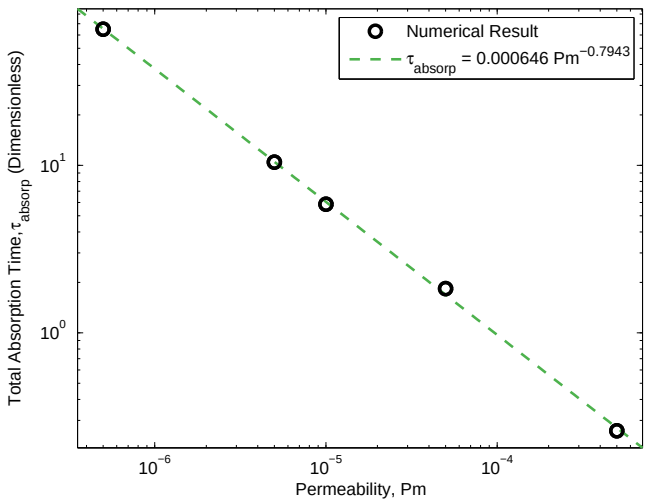

Figure 7.9: Dependence of total absorption time, τ_{absorp} on permeability

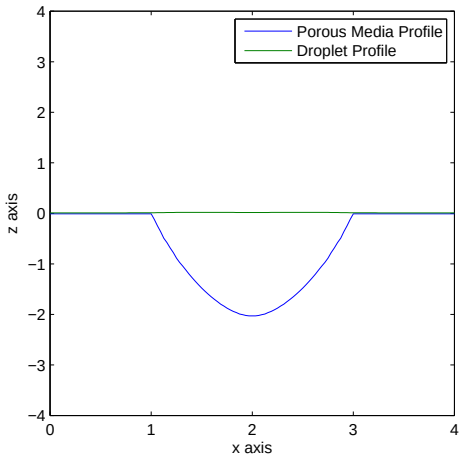

(a) $Pm = 5 \times 10^{-4}$

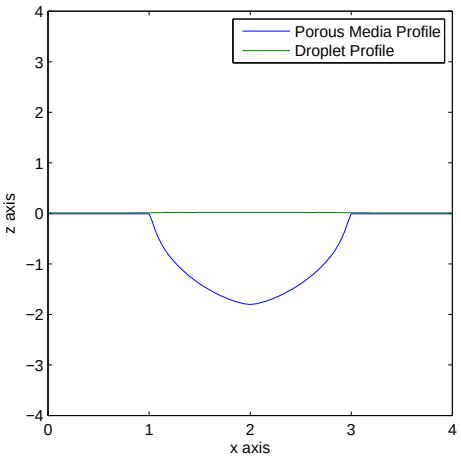

(b) $Pm = 5 \times 10^{-5}$

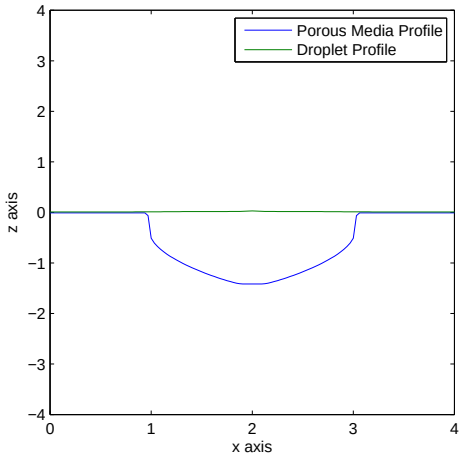

(c) $Pm = 5 \times 10^{-6}$

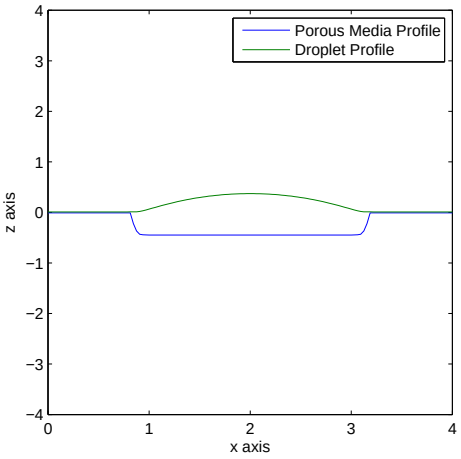

(d) $Pm = 5 \times 10^{-7}$

Figure 7.10: Effect of the permeability on the profile of the droplet and shape of the fluid in the porous medium after 10 dimensionless time units

7.5.1.3 Effect of suction number, Su

Physical Property	**Case 1**
Density, kg/m^3	1000
Viscosity, μ, Pa.s	0.001
Surface Tension, N/m	0.07
Equilibrium Contact Angle, θ_e, $^{\circ}$	22.92
Porosity, ϕ	0.5
Suction number, Su	10 to 10000
Permeability, Pm	5×10^{-5}
Volume of droplet, V_0, μl	10.42
Initial position of centre of gravity	(2,2)

Table 7.4: Physical properties for suction number variations on horizontal substrates

The suction number is a non-dimensional entity which depends on the capillary pressure. Figure 7.11 shows that as the capillary pressure is reduced, the rate at which the droplet height reduces has decreased. This directly affects the rate reduction of volume of the droplet due to absorption. The rate of change of volume occupied by the absorbed fluid also decreases as the capillary pressure is reduced. Figure 7.13 describes the effect of reduction in the capillary pressure on the droplet absorption after 10 dimensionless time units. The droplet tends to spread on the substrate prior to becoming absorbed at low suction numbers because the capillary force is quite low; this is essentially responsible for driving the fluid inside the porous medium. Figure 7.12 clearly shows that τ_{absorp} has a power-law dependence on the suction number with an exponent of -0.7894. The power-law exponents obtained from the variation of permeability and suction are analogous, but their overall magnitude is different.

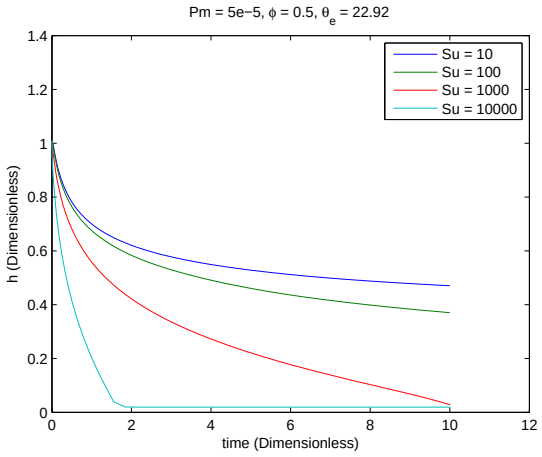

(a) Variation of the maximum height of the droplet

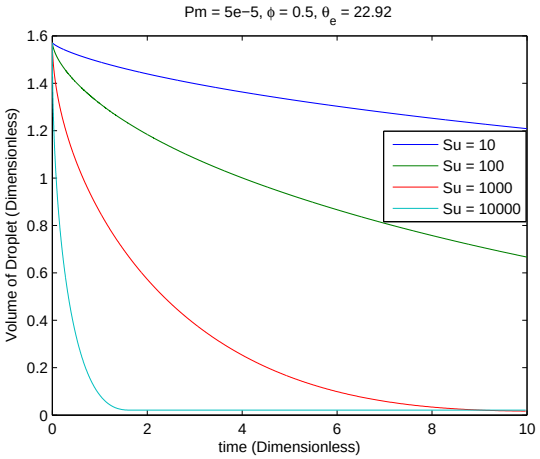

(b) Variation of volume of the droplet

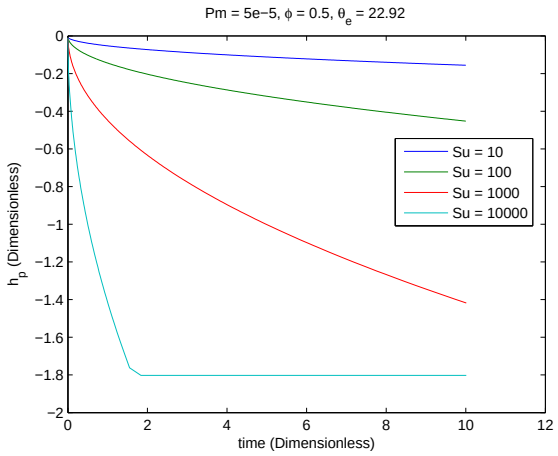

(c) Variation of the maximum depth of absorbed fluid

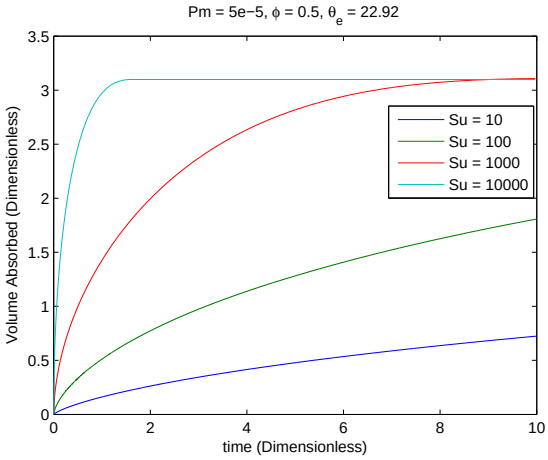

(d) Variation of absorbed volume

Figure 7.11: Effect of the variation of suction number on absorption

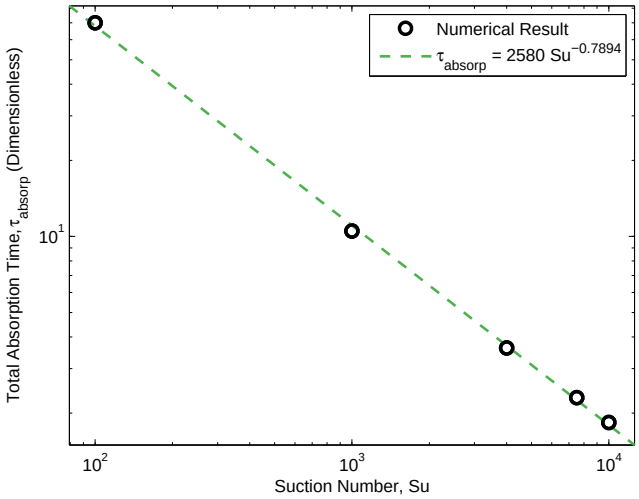

Figure 7.12: Dependence of total absorption time, τ_{absorp} on suction number

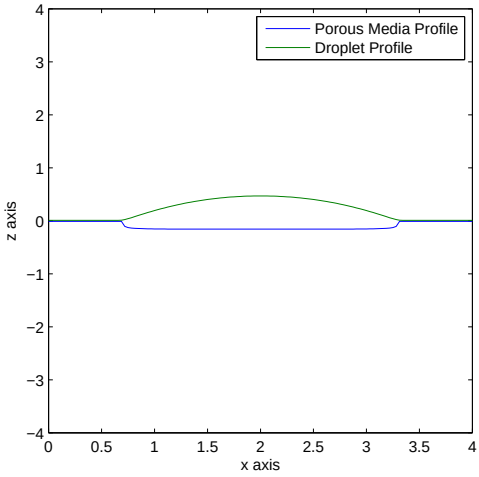

(a) $Su = 10$

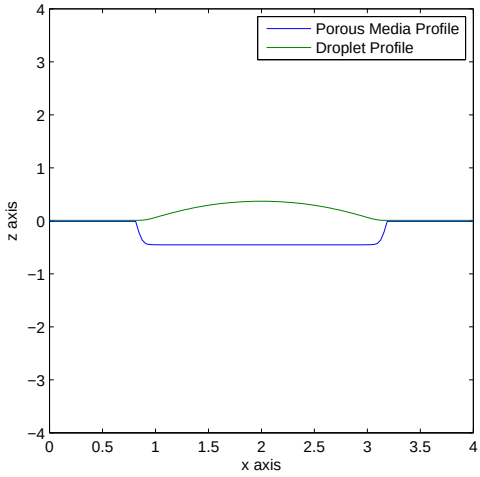

(b) $Su = 100$

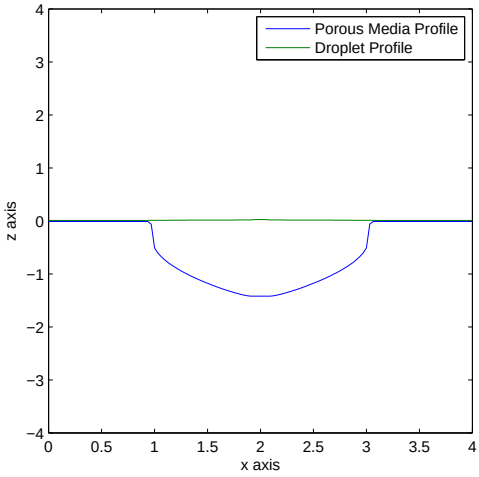

(c) $Su = 1000$

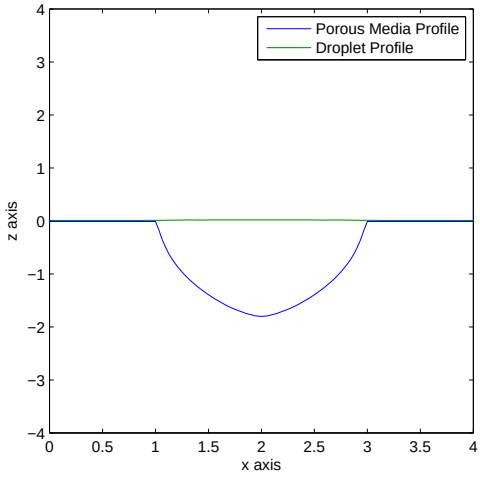

(d) $Su = 10000$

Figure 7.13: Effect of the suction number on the profile of the droplet and shape of the fluid in the porous medium after 10 dimensionless time units

7.5.1.4 Effect of equilibrium contact angle, θ_e

Physical Property	**Case 1**
Density, kg/m^3	1000
Viscosity, μ, Pa.s	0.001
Surface Tension, N/m	0.07
Equilibrium Contact Angle, θ_e, $^{\circ}$	10 - 60
Porosity, ϕ	0.5
Suction number, Su	10000
Permeability, Pm	5×10^{-5}
Volume of droplet, V_0, μl	10.42
Initial position of centre of gravity	(2,2)

Table 7.5: Physical properties for equilibrium contact angle variations on horizontal substrates

Figure 7.14 shows that the rate of decrease in the droplet height reduces as the equilibrium contact angle is increased. It also suggests that the final volume occupied by the absorbed fluid remains almost constant. The only significant difference is the depth to which the fluid penetrates. As the equilibrium contact angle is increased the depth of fluid penetration increases. This is best described by the plots in the Figure 7.16, where the absorbed fluid profile takes the shape of a cone as the equilibrium contact angle is increased. Figure 7.15 shows that the total absorption time, τ_{absorp} has an exponential dependence on the equilibrium contact angle.

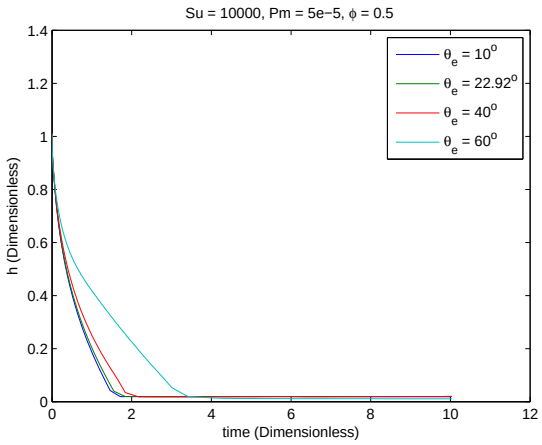

(a) Variation of the maximum height of the droplet

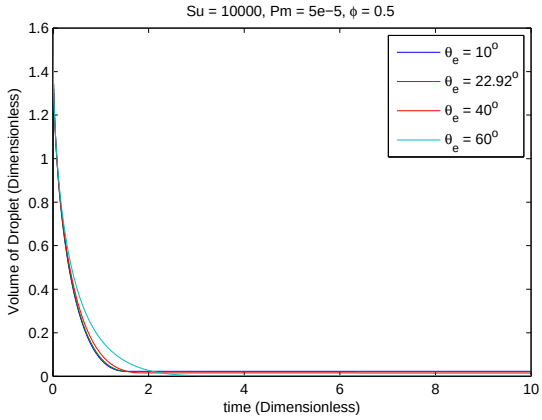

(b) Variation of volume of the droplet

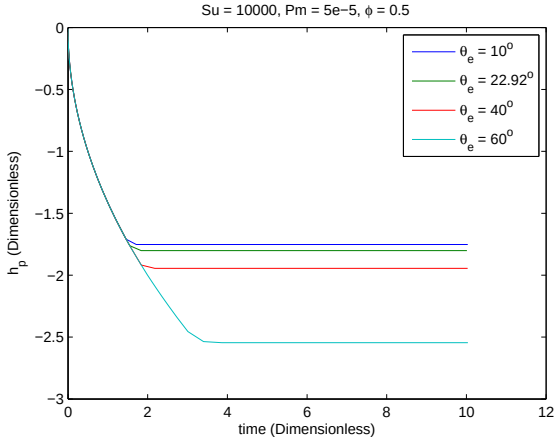

(c) Variation of the maximum depth of absorbed fluid

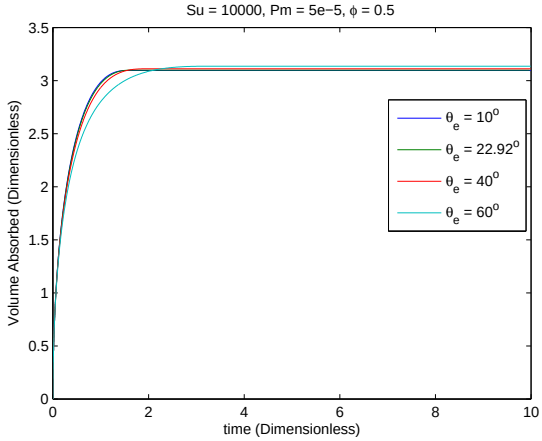

(d) Variation of absorbed volume

Figure 7.14: Effect of the variation of equilibrium contact angle on absorption

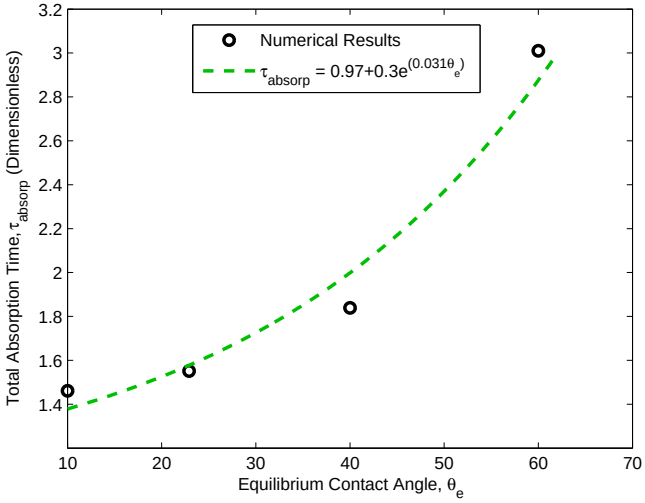

Figure 7.15: Dependence of total absorption time, τ_{absorp} on equilibrium contact angle

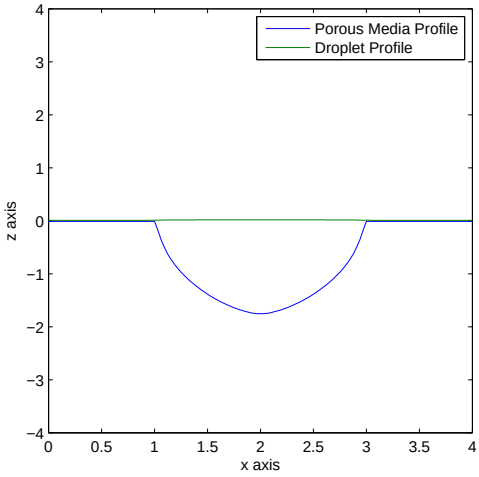

(a) $\theta_e = 10^o$

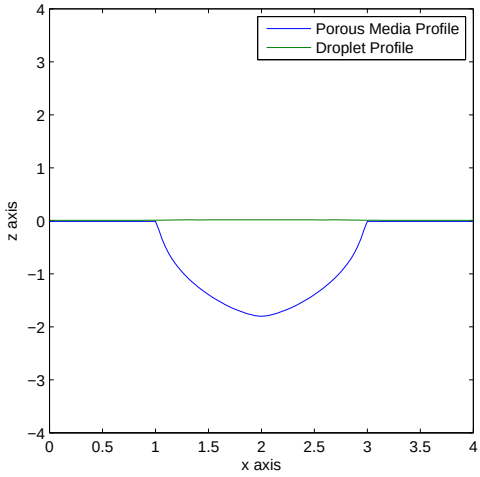

(b) $\theta_e = 22.92^o$

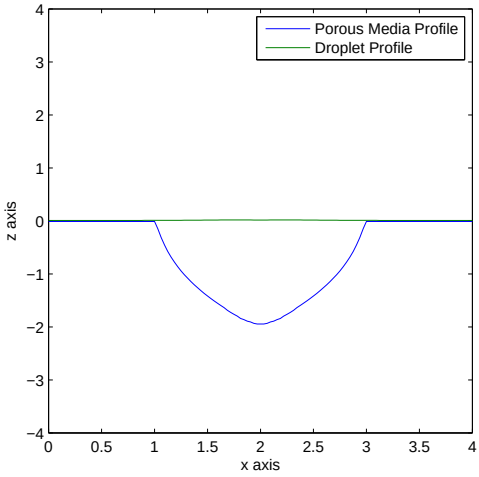

(c) $\theta_e = 40^o$

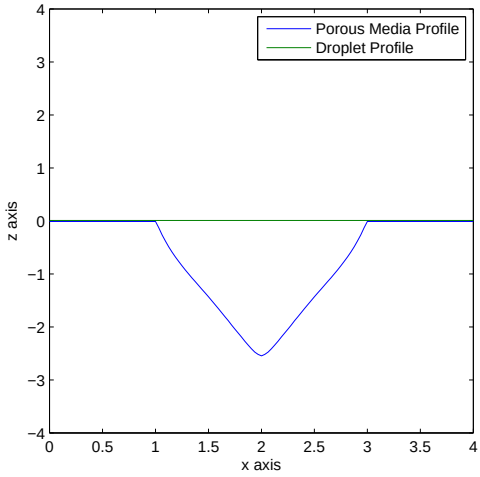

(d) $\theta_e = 60^o$

Figure 7.16: Effect of the equilibrium contact angle on the profile of the droplet and shape of the fluid in the porous medium after 10 dimensionless time units

7.5.2 Inclined Absorption

Surfaces are not always horizontal especially in the context of BPA. When inclination is included there is an extra phenomenon added, i.e. the sliding of droplets. Sliding and absorption play a vital role in the shape of the final footprint of the droplet on the outside and the absorbed fluid inside the porous substrate. Inclined porous substrates have received little attention in the past. In the next sections, the effect of substrate inclination on the absorption of droplets are examined. The physical properties, such as porosity, permeability, suction number, and equilibrium contact angle are varied and compared with the horizontal absorption results. The effect of the physical properties and orientation of the porous substrate on the sliding dynamics of the droplets are also discussed. The numerical results are also presented in terms of the position of the centre of gravity of the droplet and of the absorbed fluid as a function of time. The position of the center of gravity is computed according to,

$$x_{cg} = \frac{\int_\Omega (h - h^*) x d\omega}{\int_\Omega (h - h^*) d\omega} \quad \text{and} \quad y_{cg} = \frac{\int_\Omega (h - h^*) y d\omega}{\int_\Omega (h - h^*) d\omega} \tag{7.41}$$

$$x_{cg\ porous} = \frac{\int_\Omega (h_p - h^*) x d\omega}{\int_\Omega (h_p - h^*) d\omega} \quad \text{and} \quad y_{cg\ porous} = \frac{\int_\Omega (h_p - h^*) y d\omega}{\int_\Omega (h_p - h^*) d\omega} \tag{7.42}$$

where $\Omega = [0, 5] \times [0, 4]$ is the computational domain.

7.5.2.1 Effect of porosity, ϕ

Physical Property	**Case 1**
Density, kg/m^3	1000
Viscosity, μ, Pa.s	0.001
Surface Tension, N/m	0.07
Equilibrium Contact Angle, θ_e, ^{o}	22.92
Porosity, ϕ	0.1-0.9
Suction number, Su	1×10^4
Permeability, Pm	5×10^{-5}
Inclination angle, θ_i, ^{o}	$30 - 60$
Volume of droplet, V_0, μl	10.42
Initial position of centre of gravity	(2,2)

Table 7.6: Physical properties for porosity variations on inclined substrates

The droplet is released on an inclined porous substrate from an equilibrium state. This droplet slides as well as gets absorbed in the porous substrate. The physical properties of the fluid droplet are reported in Table 7.6. Figure 7.17 shows a similar trend as that ob-

served in the absorption of droplets on horizontal substrates. There is another phenomenon added to the absorption as the inclination angle is varied i.e. the sliding of the droplet down the incline. The physical properties of the porous substrate play a key role in determining the extent to which the sliding takes place, before the droplet gets fully absorbed. For the physical properties mentioned in Table 7.6, the rate of absorption of the droplet is high in comparison to the rate of sliding over the porous substrate. This causes the droplet to slide very slightly within the initial radius of the contact region. This is the source of hump-like behavior as seen in the Figure 7.18a, where the position of the center of gravity of the droplet is plotted against time. The droplet starts to slide due to gravitational pull, which causes the center of gravity of the droplet to move down the incline, however, at the same time, the absorption is also taking place. This causes the center of gravity to shift to its original/start position. For comparison, in the same figure the sliding behavior of a droplet with the same physical properties on a non-porous/solid substrate is also plotted. It clearly illustrates that the porous medium slows down the sliding motion. Figure 7.18a shows that the center of gravity of the droplet after it is fully absorbed in the porous medium is not at 2. Final center of gravity position must be at 2 after the absorption of the droplet. This is obviously not visible from the figure. The center of gravity predicted is around 1.9975 for the lowest line. And it does not remain at 1.9975 (as it seems in the plots). This value is slowly but gradually increasing to 2 as the simulations proceed. The change in the center of gravity of the droplet is very fast. Increasing and decreasing within 1-2 dimensionless time units. This may cause the numerical code to under estimate the value of the center of gravity.

On the other hand, the center of gravity of the absorbed fluid moves down the incline for the duration in which the droplet is being absorbed. As soon as the droplet absorption is finished, the center of gravity of the fluid stays constant, see Figure 7.18b. The extent of the movement of the center of gravity of the absorbed fluid increases with a decrease in porosity. Figure 7.19 shows the time contours of the droplet and the fluid as it gets absorbed during the first 10 non-dimensional time units and supports the above discussion.

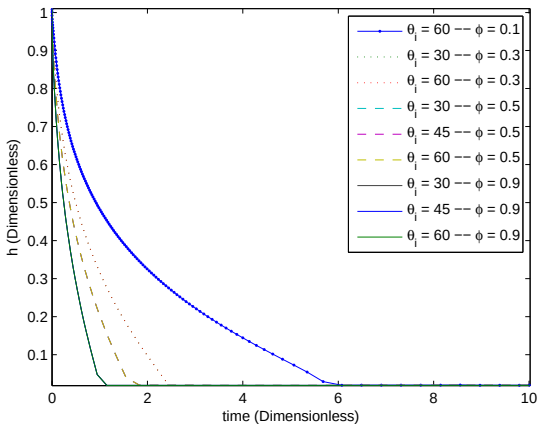

(a) Variation of the maximum height of the droplet

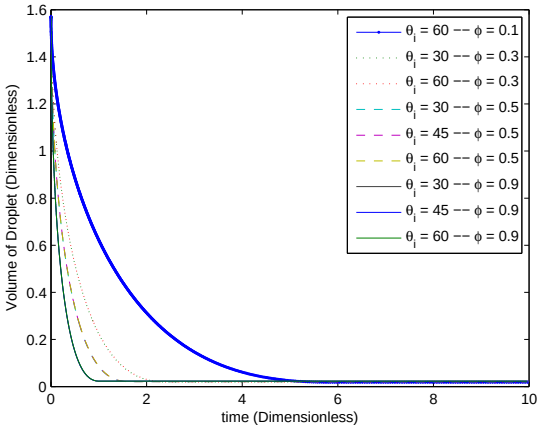

(b) Variation of volume of the droplet

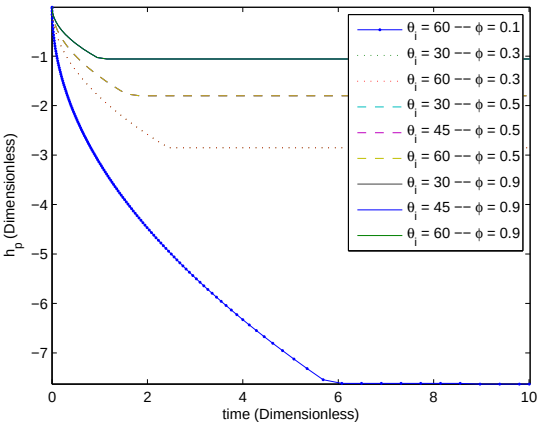

(c) Variation of the maximum depth of absorbed fluid

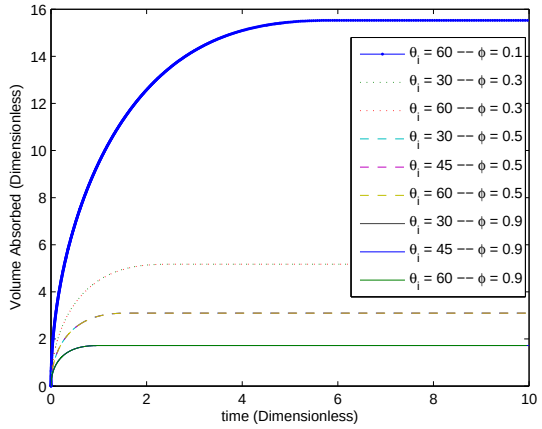

(d) Variation of absorbed volume

Figure 7.17: Effect of the variation of porosity on absorption of droplets on inclined porous substrates

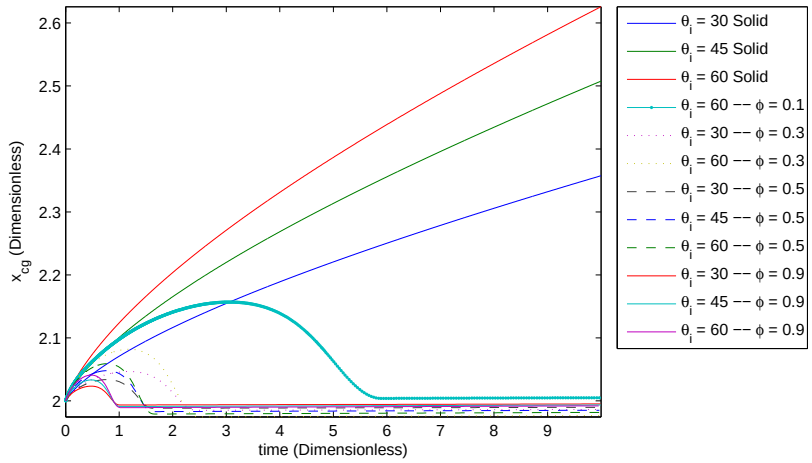

(a) Variation of center of gravity of the droplet

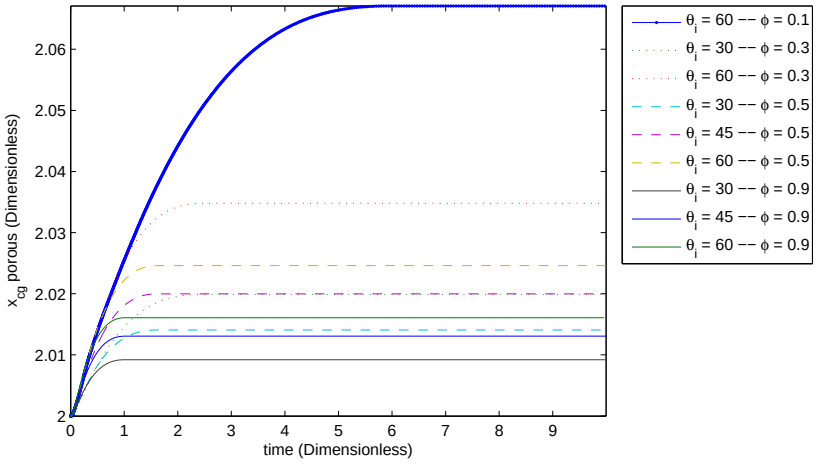

(b) Variation of center of gravity of the absorbed fluid

Figure 7.18: Effect of the porosity on the position of the center of gravity of the droplet and the absorbed fluid with time

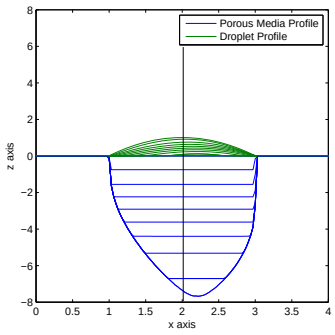

(a) $\phi = 0.1$ and $\theta_i = 60^o$

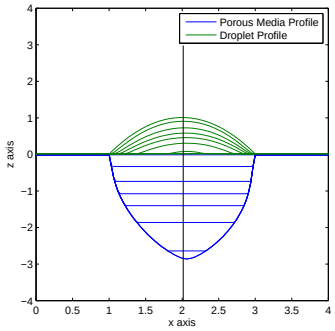

(b) $\phi = 0.3$ and $\theta_i = 30^o$

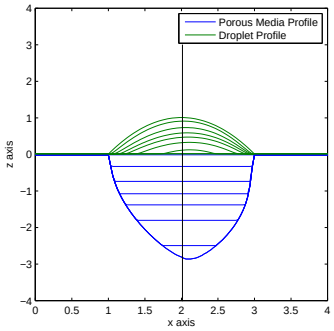

(c) $\phi = 0.3$ and $\theta_i = 60^0$

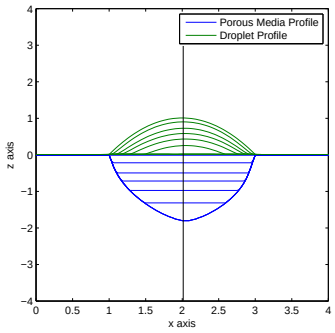

(d) $\phi = 0.5$ and $\theta_i = 30^o$

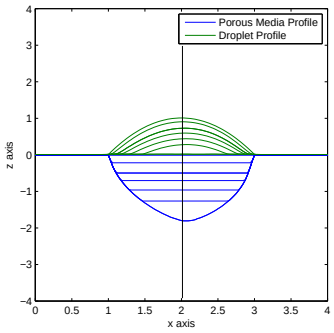

(e) $\phi = 0.5$ and $\theta_i = 45^o$

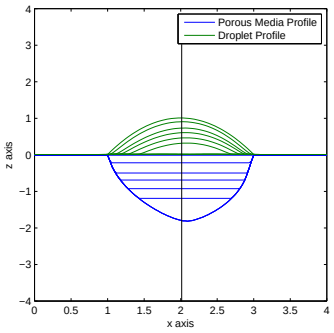

(f) $\phi = 0.5$ and $\theta_i = 60^o$

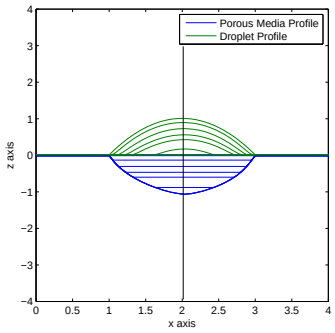

(g) $\phi = 0.9$ and $\theta_i = 30^o$

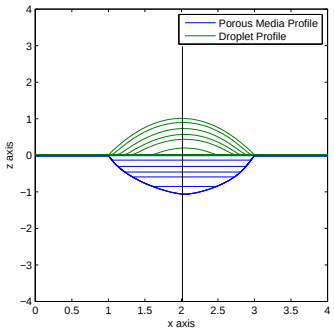

(h) $\phi = 0.9$ and $\theta_i = 45^o$

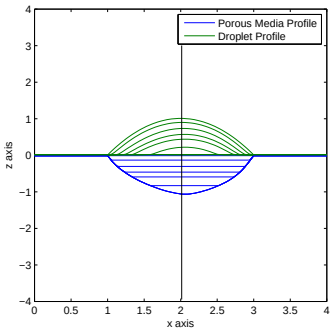

(i) $\phi = 0.9$ and $\theta_i = 60^o$

Figure 7.19: Effect of the porosity on the profile of the droplet and shape of the fluid in the inclined porous medium for the first 10 dimensionless time units

7.5.2.2 Effect of permeability, Pm

Physical Property	**Case 1**
Density, kg/m^3	1000
Viscosity, μ, Pa.s	0.001
Surface Tension, N/m	0.07
Equilibrium Contact Angle, θ_e, $^{\circ}$	22.92
Porosity, ϕ	0.5
Suction number, Su	1×10^4
Permeability, Pm	$5 \times 10^{-5} - 5 \times 10^{-7}$
Inclination angle, θ_i, $^{\circ}$	$30 - 60$
Volume of droplet, V_0, μl	10.42
Initial position of centre of gravity	(2,2)

Table 7.7: Physical properties for permeability variations on inclined substrates

In this section the permeability number, Pm and the inclination angle are varied. Figure 7.20 shows that the effect of a change of inclination with variation of Pm does not have any effect on the volume occupied by the fluid absorbed in the porous substrate and is comparable to the horizontal absorption results. The curves overlap each other. As the Pm is reduced, the rate of absorption of the fluid droplet reduces. This causes the droplet to slide on the substrate which causes a shift in the center of gravity of the droplet down the incline, see Figure 7.21a. Subsequently, this causes a shift in the center of gravity of the fluid absorbed in the porous substrate, see Figure 7.21b. A point to note here is that these rates of change are different primarily due to the fact that the rate of change of the volume of the droplet is different from the rate of change of the volume of the absorbed fluid. This is supported by the time contours plotted in the Figure 7.22. Another interesting outcome is that as the permeability is reduced, the motion of the sliding droplet approaches the motion of droplet spreading/sliding on a non-porous/solid substrate.

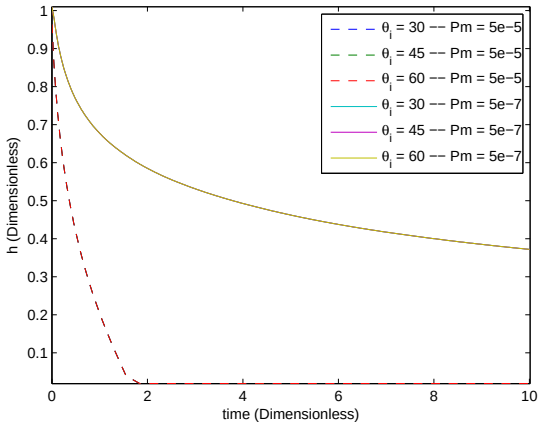

(a) Variation of the maximum height of the droplet

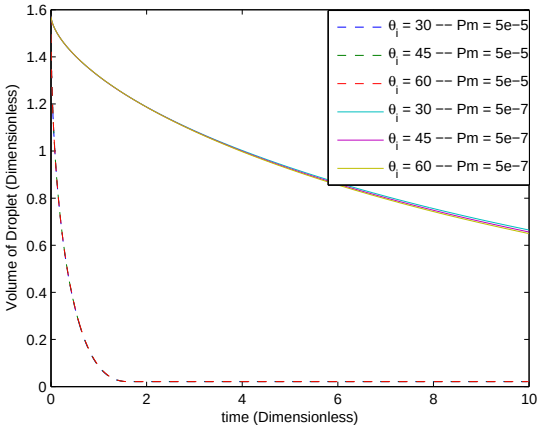

(b) Variation of volume of the droplet

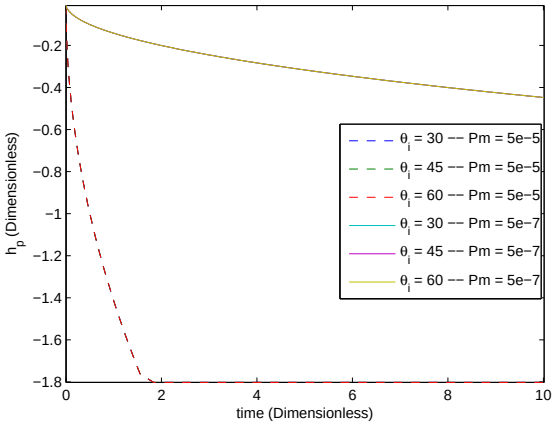

(c) Variation of the maximum depth of absorbed fluid

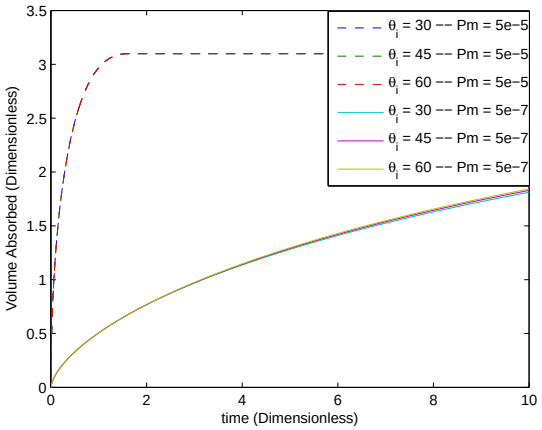

(d) Variation of absorbed volume

Figure 7.20: Effect of the variation of permeability on absorption of droplets on inclined porous substrates

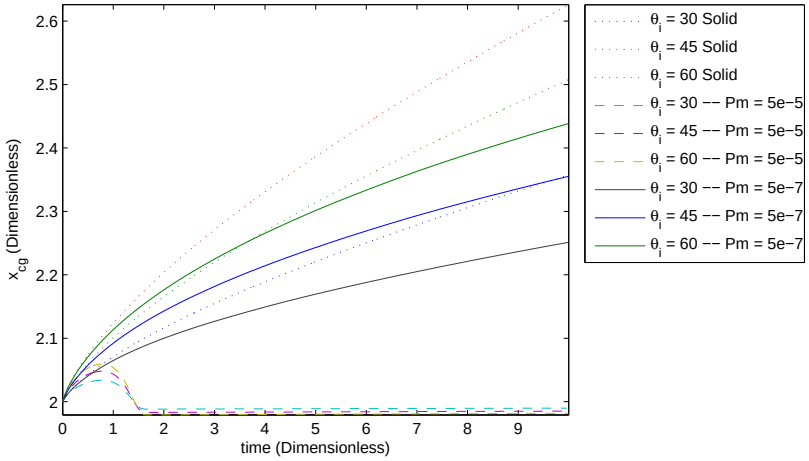

(a) Variation of center of gravity of the droplet

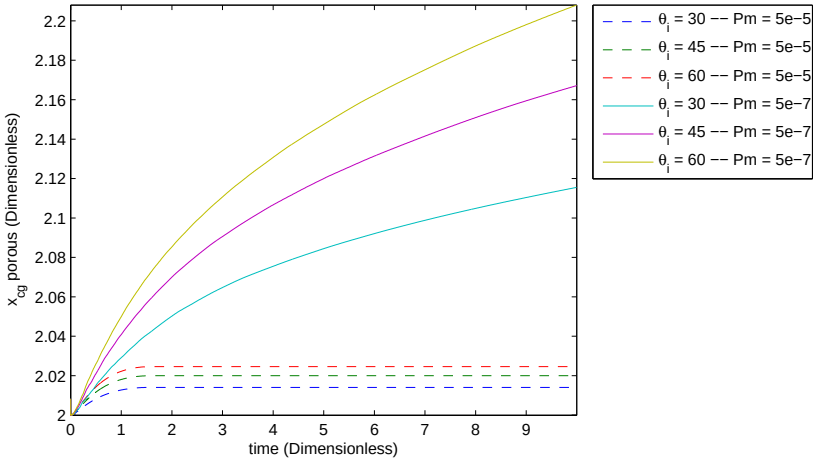

(b) Variation of center of gravity of the absorbed fluid

Figure 7.21: Effect of the permeability on the position of the center of gravity of the droplet and the absorbed fluid with time

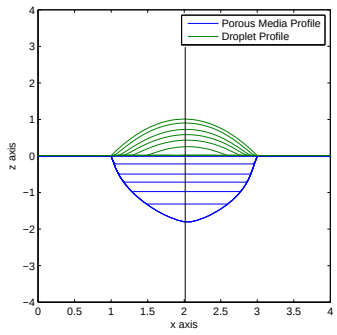

(a) $Pm = 5 \times 10^{-5}$ and $\theta_i = 30^o$

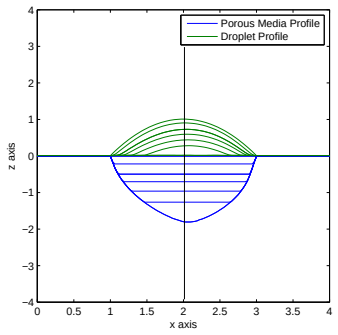

(b) $Pm = 5 \times 10^{-5}$ and $\theta_i = 45^o$

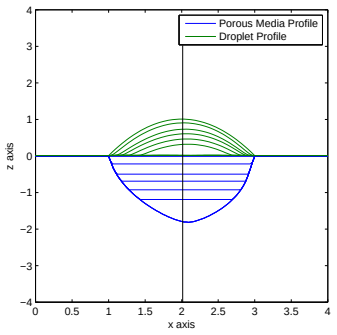

(c) $Pm = 5 \times 10^{-5}$ and $\theta_i = 60^o$

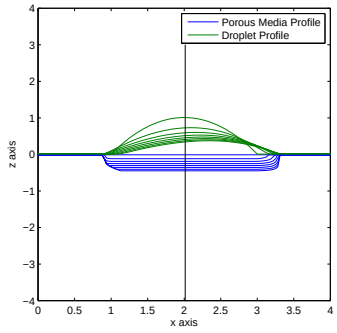

(d) $Pm = 5 \times 10^{-7}$ and $\theta_i = 30^o$

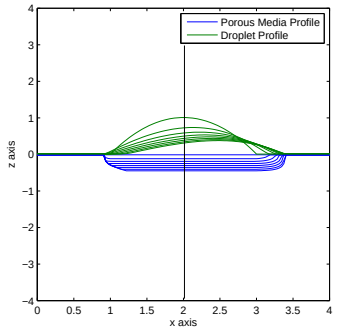

(e) $Pm = 5 \times 10^{-7}$ and $\theta_i = 45^o$

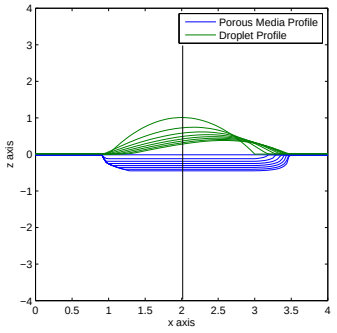

(f) $Pm = 5 \times 10^{-7}$ and $\theta_i = 60^o$

Figure 7.22: Effect of the permeability on the profile of the droplet and shape of the fluid in the inclined porous medium for the first 10 dimensionless time units

7.5.2.3 Effect of suction number, Su

Physical Property	**Case 1**
Density, kg/m^3	1000
Viscosity, μ, Pa.s	0.001
Surface Tension, N/m	0.07
Equilibrium Contact Angle, θ_e, ^{o}	22.92
Porosity, ϕ	0.5
Suction number, Su	$1 \times 10^1 - 1 \times 10^4$
Permeability, Pm	5×10^{-5}
Inclination angle, θ_i, ^{o}	$30 - 60$
Volume of droplet, V_0, μl	10.42
Initial position of centre of gravity	(2,2)

Table 7.8: Physical properties for suction number variations on inclined substrates

Figures 7.23 and 7.24 show that the change in suction number with increasing inclination very slightly changes the absorbed volume in comparison to the absorbed volume results for the horizontal substrates (for comparison see Figure 7.11). As the suction number is reduced,

the absorption rate decreases. The position of the center of gravity of the droplet and the fluid absorbed moves further down the incline with an increase in the inclination angle during the first 10 dimensionless time units, see Figures 7.25a and 7.25b. As the inclination angle is increased and the suction number is decreased, the droplet absorption rate decreases causing an increase in the rate of change of position of the center of gravity of the droplet. It can be further deduced from this observation that there is a set of physical properties of the porous substrate where the sliding dynamics surpass the absorption dynamics, i.e. the edge contact line of the droplet moves beyond the initial contact line. Also, the region of properties where this takes place is where the slide occurs beyond the initial contact radius of the droplet, R_c. Figure 7.26 shows the effect of change of suction number with increasing inclination angle on the profiles of the droplets above the surface and shape of the absorbed fluid.

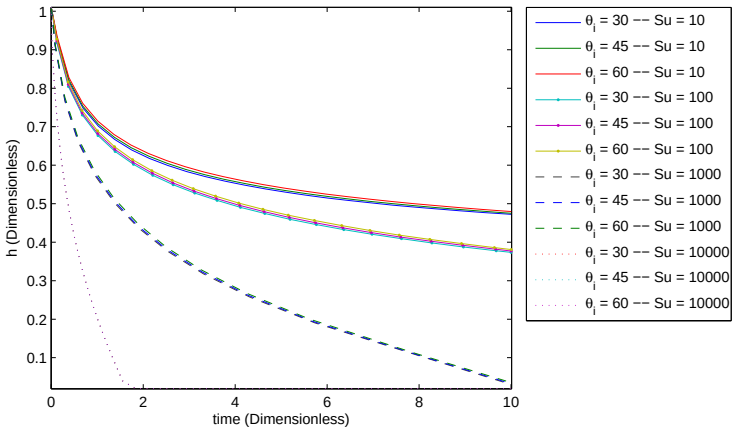

(a) Variation of the maximum height of the droplet

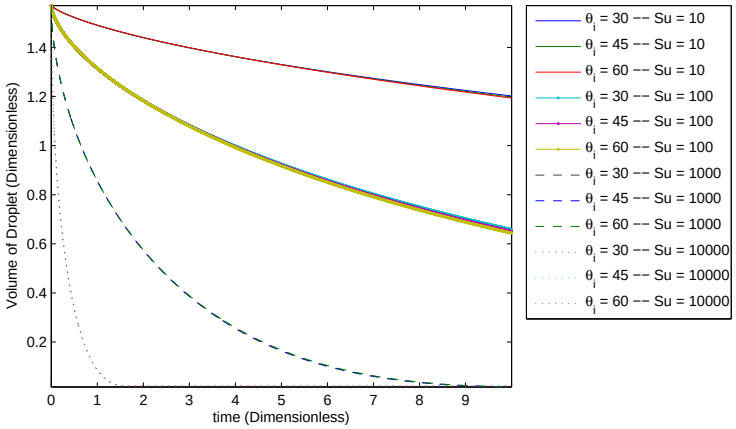

(b) Variation of volume of the droplet

Figure 7.23: Effect of the variation of suction number on the absorption of droplets on inclined porous substrates

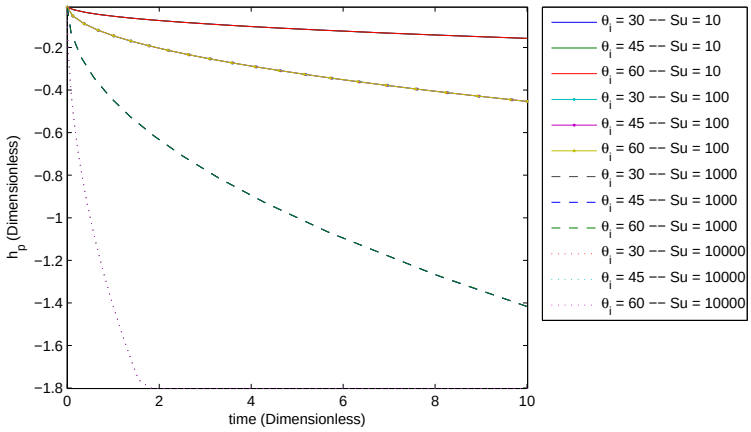

(a) Variation of the maximum depth of absorbed fluid

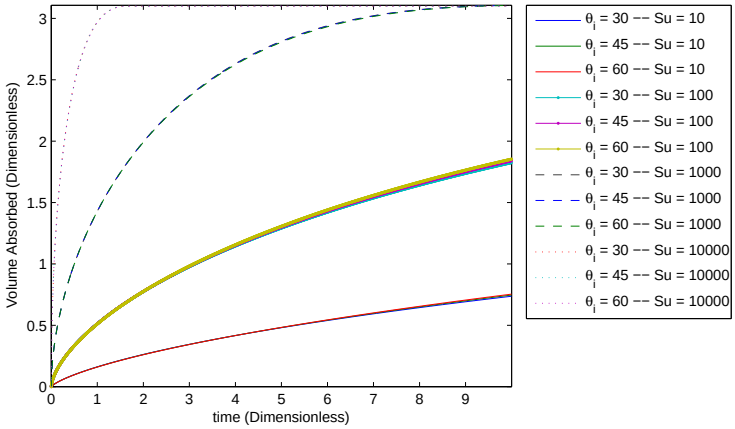

(b) Variation of absorbed volume

Figure 7.24: Effect of the variation of suction number on the absorption of droplets on inclined porous substrates

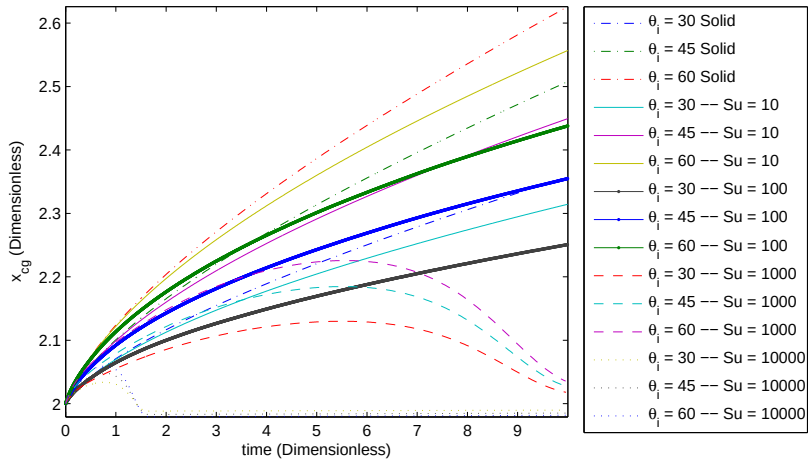

(a) Variation of center of gravity of the droplet

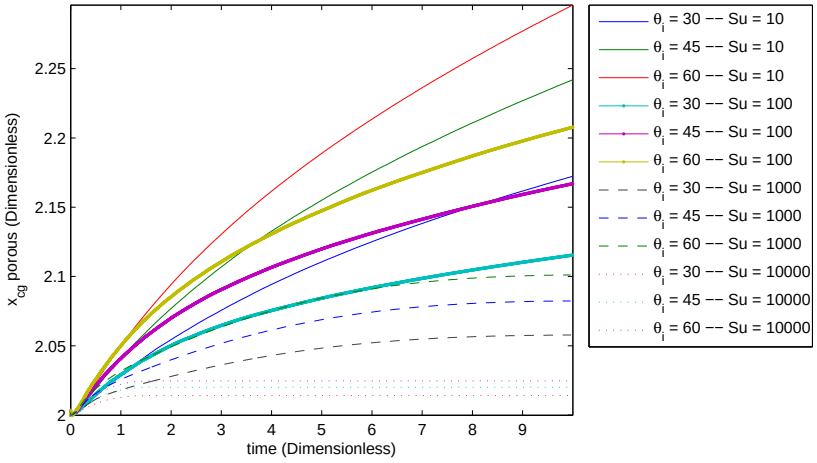

(b) Variation of center of gravity of the absorbed fluid

Figure 7.25: Effect of the suction number on the position of the center of gravity of the droplet and the absorbed fluid with time

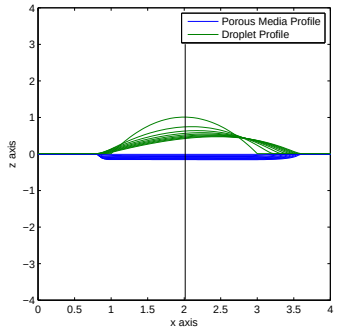

(a) $Su = 10$ and $\theta_i = 30^o$

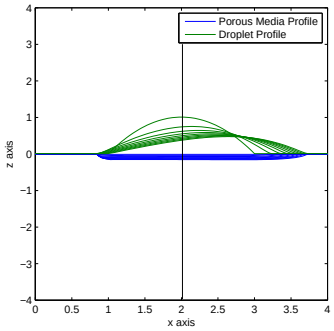

(b) $Su = 10$ and $\theta_i = 45^o$

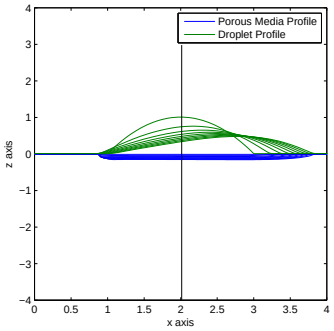

(c) $Su = 10$ and $\theta_i = 60^o$

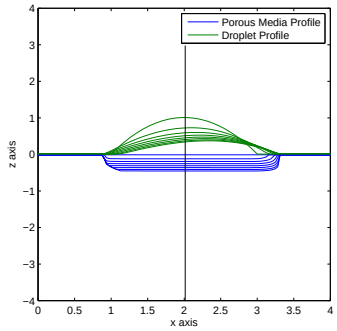

(d) $Su = 100$ and $\theta_i = 30^o$

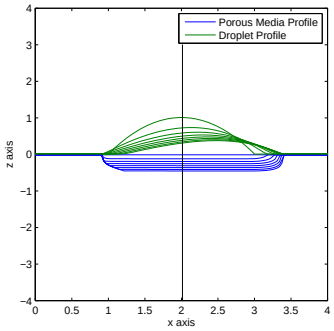

(e) $Su = 100$ and $\theta_i = 45^o$

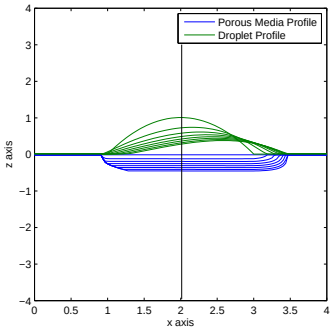

(f) $Su = 100$ and $\theta_i = 60^o$

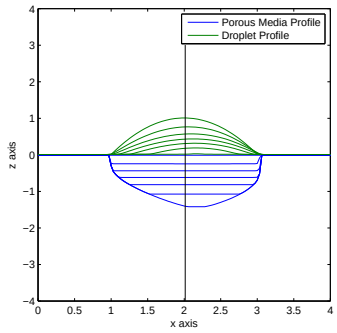

(g) $Su = 1000$ and $\theta_i = 30^o$

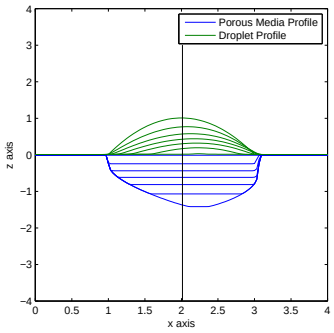

(h) $Su = 1000$ and $\theta_i = 45^o$

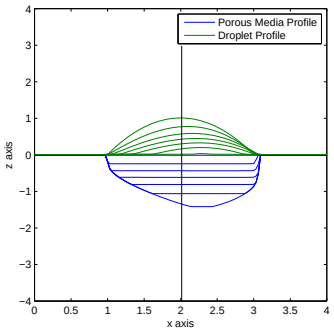

(i) $Su = 1000$ and $\theta_i = 60^o$

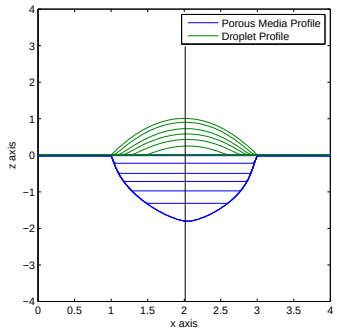

(j) $Su = 10000$ and $\theta_i = 30^o$

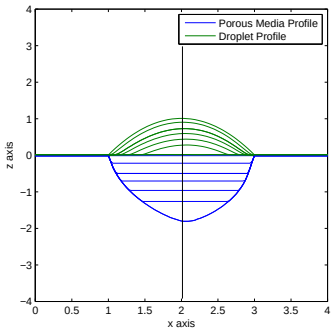

(k) $Su = 10000$ and $\theta_i = 45^o$

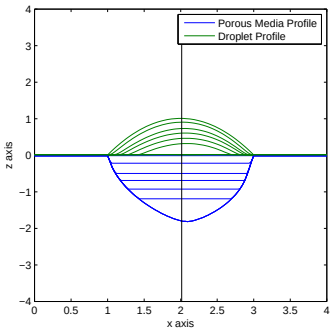

(l) $Su = 10000$ and $\theta_i = 60^o$

Figure 7.26: Effect of the suction number on the profile of the droplet and shape of the fluid in the inclined porous medium for the first 10 dimensionless time units

7.5.2.4 Effect of equilibrium contact angle, θ_e

Physical Property	**Case 1**
Density, kg/m^3	1000
Viscosity, μ, Pa.s	0.001
Surface Tension, N/m	0.07
Equilibrium Contact Angle, θ_e, ^{o}	10-60
Porosity, ϕ	0.5
Suction number, Su	10
Permeability, Pm	5×10^{-5}
Inclination angle, θ_i, ^{o}	$30 - 60$
Volume of droplet, V_0, μl	10.42
Initial position of centre of gravity	(2,2)

Table 7.9: Physical properties for equilibrium contact angle variations on inclined substrates

The equilibrium contact angle, θ_e, plays a vital role in the sliding dynamics of the droplet. Figures 7.27 and 7.28 show that for a particular θ_e with an increase in inclination angle, the volume of the fluid absorbed is slightly different. This means that out of all the physical properties, θ_e variation causes a small difference in the height of the droplet and the depth of the fluid absorbed. Figures 7.29a, 7.29b and 7.29c describe the change of position of the center of gravity of the droplet and the absorbed fluid as the inclination angle is varied. The wetting property is varied, i.e. the equilibrium contact angle is increased. As the equilibrium contact angle is increased, the rate of change of the position of the center of gravity of the droplet is also increased. In Figures 7.29a and 7.29b, the position of the center of gravity of the droplet on a porous substrate is also compared with a droplet sliding on a solid substrate having similar physical characteristics. It is clearly seen that the absorptive properties of the substrates decreases the rate of slide of the droplet because the droplet is being absorbed as it slides which causes a decrease in its momentum.

Figure 7.30 shows the time contours of the droplet and the absorbed fluid. An important aspect to notice here is that as θ_e is increased the droplet slides more on the substrate and maintains a constant shape. At smaller θ_e the droplet tends to flatten (a more fully wetting shape) as it slides down the incline. Note that the suction number is kept at 10 to see this effect because at smaller Su the rate of absorption of droplet is very low.

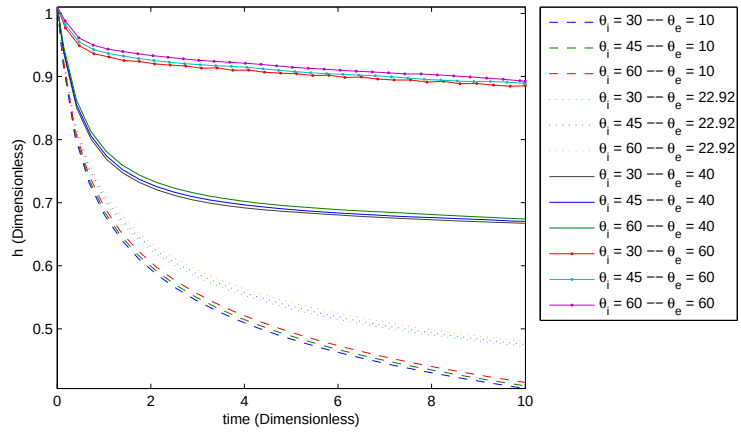

(a) Variation of the maximum height of the droplet

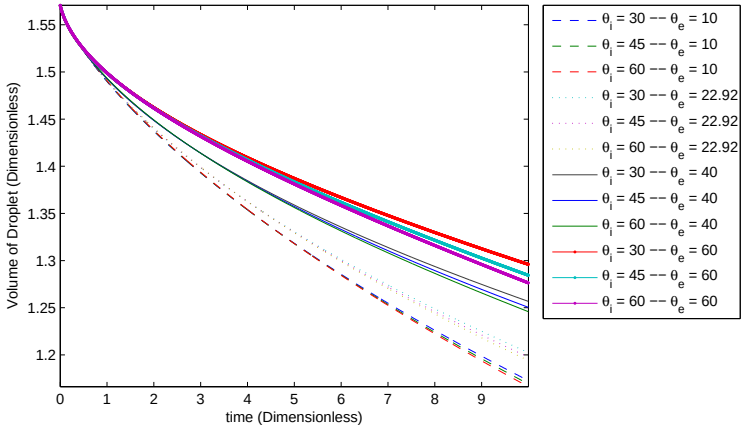

(b) Variation of the volume of the droplet

Figure 7.27: Effect of the variation of equilibrium contact angle on the absorption of droplets on inclined porous substrates

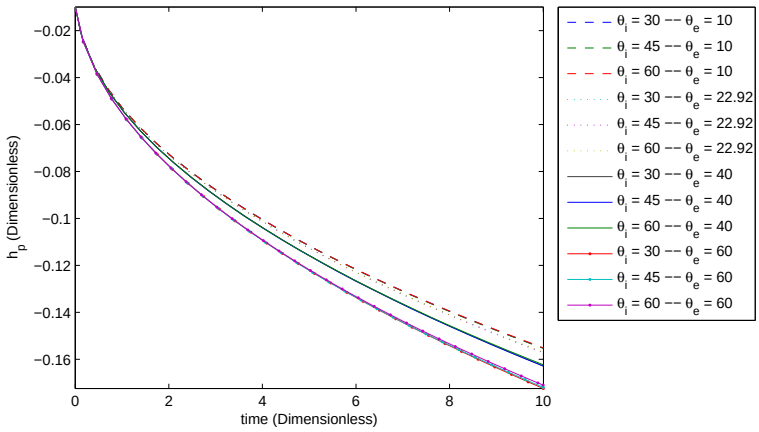

(a) Variation of the maximum depth of absorbed fluid

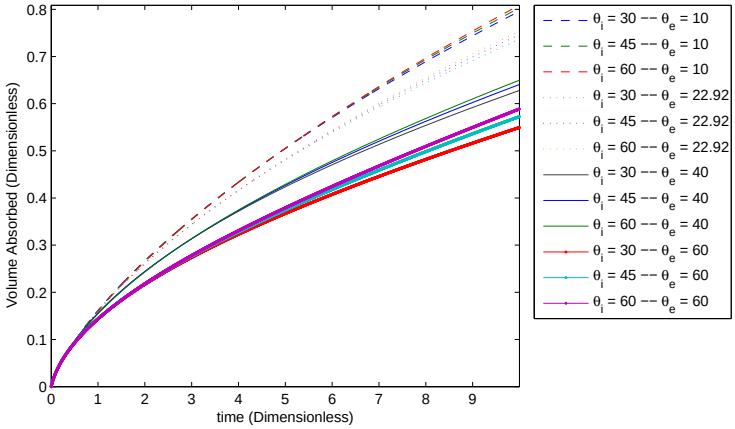

(b) Variation of absorbed volume

Figure 7.28: Effect of the variation of equilibrium contact angle on the absorption of droplets on inclined porous substrates

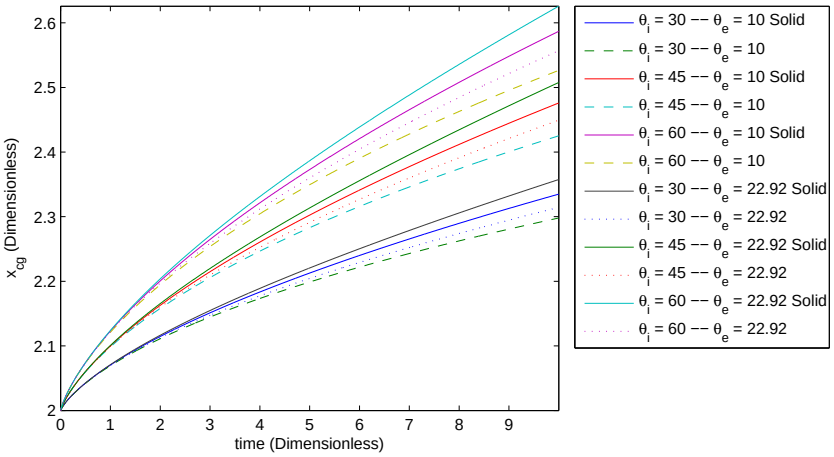

(a) Variation of center of gravity of the droplet for equilibrium contact angles of 10° and 22.92°

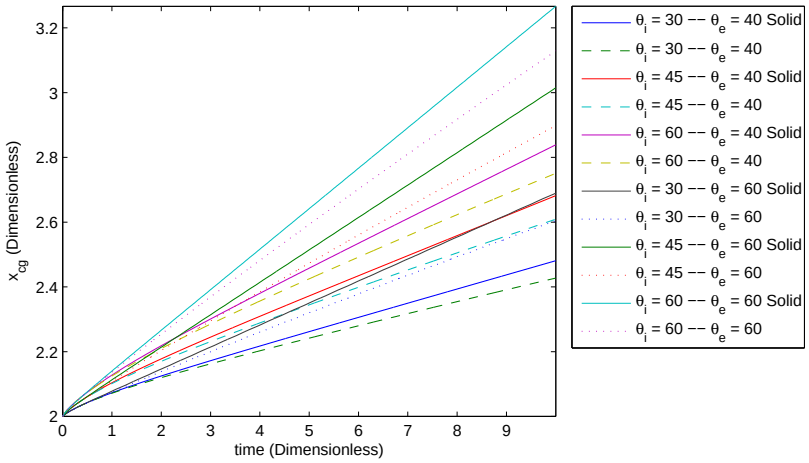

(b) Variation of center of gravity of the droplet for equilibrium contact angles of 40° and 60°

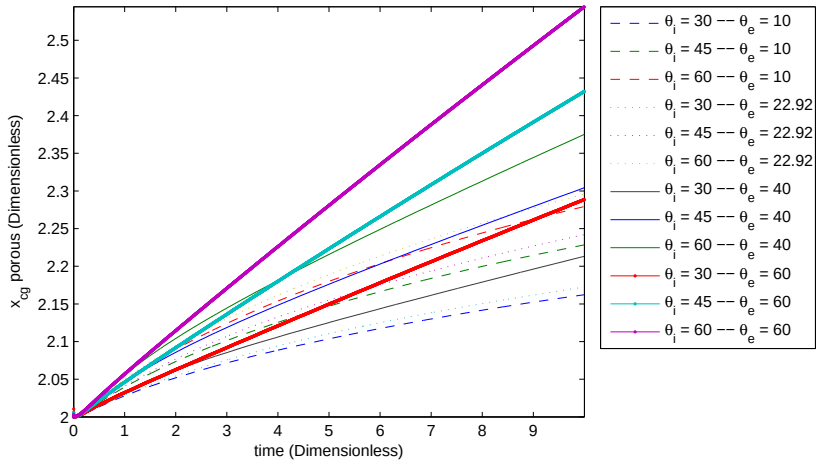

(c) Variation of center of gravity of the absorbed fluid

Figure 7.29: Effect of the equilibrium contact angle on the position of the center of gravity of the droplet and the absorbed fluid with time

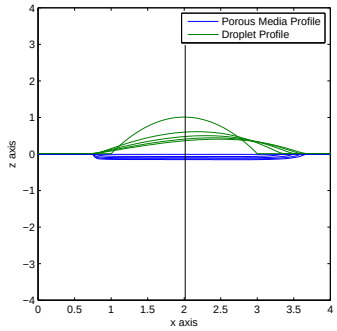

(a) $\theta_e = 10^o$ and $\theta_i = 30^o$

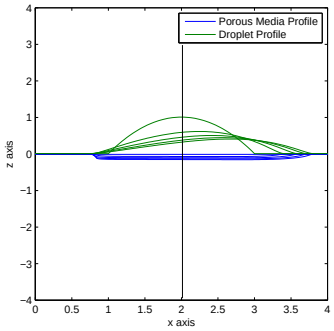

(b) $\theta_e = 10^o$ and $\theta_i = 45^o$

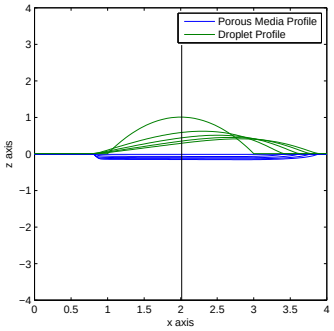

(c) $\theta_e = 10^o$ and $\theta_i = 60^o$

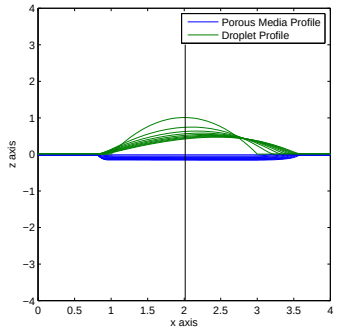

(d) $\theta_e = 22.92^o$ and $\theta_i = 30^o$

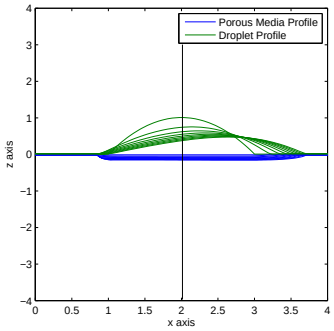

(e) $\theta_e = 22.92^o$ and $\theta_i = 45^o$

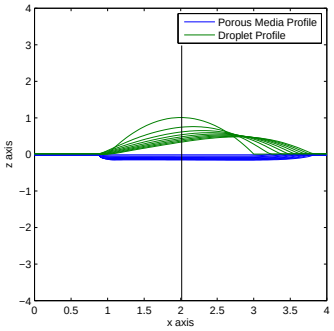

(f) $\theta_e = 22.92^o$ and $\theta_i = 60^o$

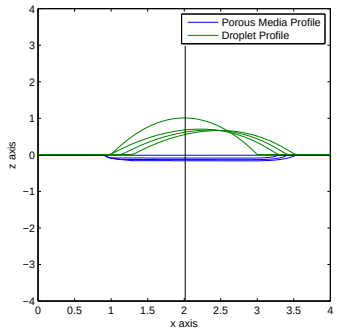

(g) $\theta_e = 40^o$ and $\theta_i = 30^o$

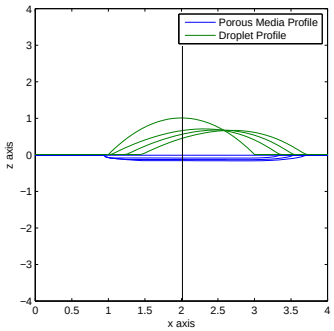

(h) $\theta_e = 40^o$ and $\theta_i = 45^o$

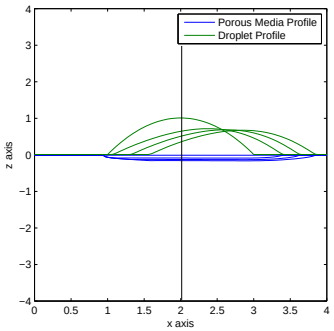

(i) $\theta_e = 40^o$ and $\theta_i = 60^o$

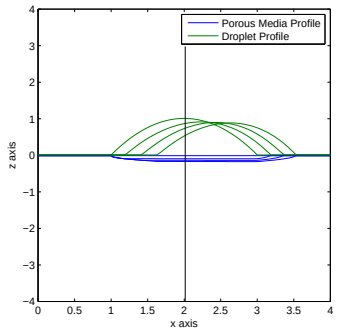

(j) $\theta_e = 60^o$ and $\theta_i = 30^o$

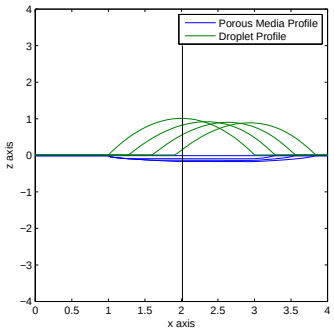

(k) $\theta_e = 60^o$ and $\theta_i = 45^o$

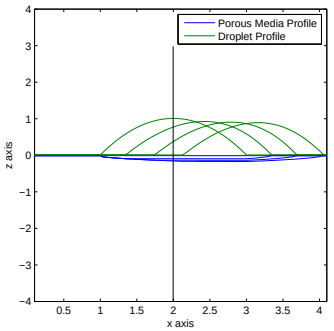

(l) $\theta_e = 60^o$ and $\theta_i = 60^o$

Figure 7.30: Effect of the equilibrium contact angle on the profile of the droplet and shape of the fluid in the inclined porous medium for the first 10 dimensionless time units

An important interpretation from the results obtained for the horizontal and inclined absorption while varying the equilibrium contact angle is that this primarily determines the shape of the absorbed fluid in the porous medium. Porosity variations mainly affect the extent of fluid penetration in the porous medium. Permeability and Suction number are the two physical properties that most affect the rate of absorption and the rate of slide. In the next Section 7.5.2.5, an analysis on these parameters is conducted so that a logical relationship between the physical properties of the porous substrate and the sliding/absorption is developed.

7.5.2.5 Analysis

In this section, further analysis was conducted based on the results from the inclined porous substrates section. On inclined porous substrates, droplets tend to slide as well as get absorbed at the same time. It is observed that for some physical properties of the porous substrates the droplet slides within the initial contact radius, R_c, and for other properties droplets tend to go beyond and move down the incline. In BPA interest lies in footprint of the droplet. The physical properties, permeability and suction number are varied to determine whether the droplet slides and gets absorbed beyond the initial footprint.

Physical Property	**Case 1**
Density, kg/m^3	1000
Viscosity, μ, Pa.s	0.001
Surface Tension, N/m	0.07
Equilibrium Contact Angle, θ_e, ^{o}	22.92
Porosity, ϕ	0.5
Suction number, Su	Varied
Permeability, Pm	Varied
Inclination angle, θ_i, ^{o}	$30 - 60$
Volume of droplet, V_0, μl	10.42
Initial position of centre of gravity	(2,2)

Table 7.10: Physical properties for analysis on inclined substrates

Based on insight from earlier results, the chosen physical properties of the substrate and fluid are shown in Table 7.10. Multiple simulations with different values of Pm and Su are used to define the regions where the droplet slide and absorption is confined within the R_c. Figure 7.31 shows a permeability against suction number plot on logarithmic scales for 30^0 inclination. It reports results from 25 simulations. The black points on the graph show the region where the sliding and absorption remain within the initial droplet footprint. The red

points show that the slide and absorption are not bounded by R_c. Each line represents three simulations. These lines on the plot approximately separate the two regions and they show that as the permeability is increased for any particular suction number, the absorption tends to take place within the initial droplet footprint. For example, line in the plot representing $R_c + 0.156$ shows three simulations with different Pm and Su values. In these simulations, the droplet slides beyond the initial contact radius on an 30^o inclined porous substrate as it gets absorbed. The extent to which the droplet goes beyond R_c is equal to 0.156. Similar explanation for other lines in the plot, where the extent is gradually decreased to 0.062. Upon increasing the inclination angle this region should shift upwards because higher inclination angles increase gravitational pull which causes the droplet to slide as it gets absorbed.

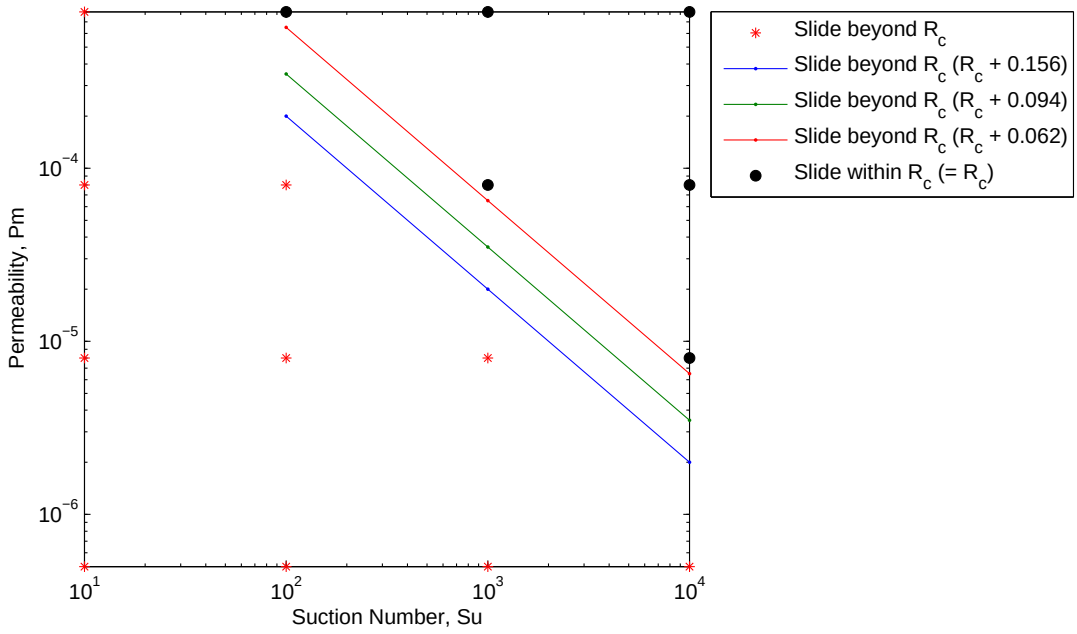

Figure 7.31: Variation of physical properties, Pm and Su, to determine whether the fluid gets absorbed within or outside the initial contact area on an inclined porous substrate (i.e. $\theta_i = 30^o$)

To complete the study, the same analysis is performed with an inclination angle of 60^o, see Figure 7.32. It clearly shows a small upward shift in the separation region. Therefore, it is deduced that for every fluid there exists a specific separation region for a range of absorptive substrates.

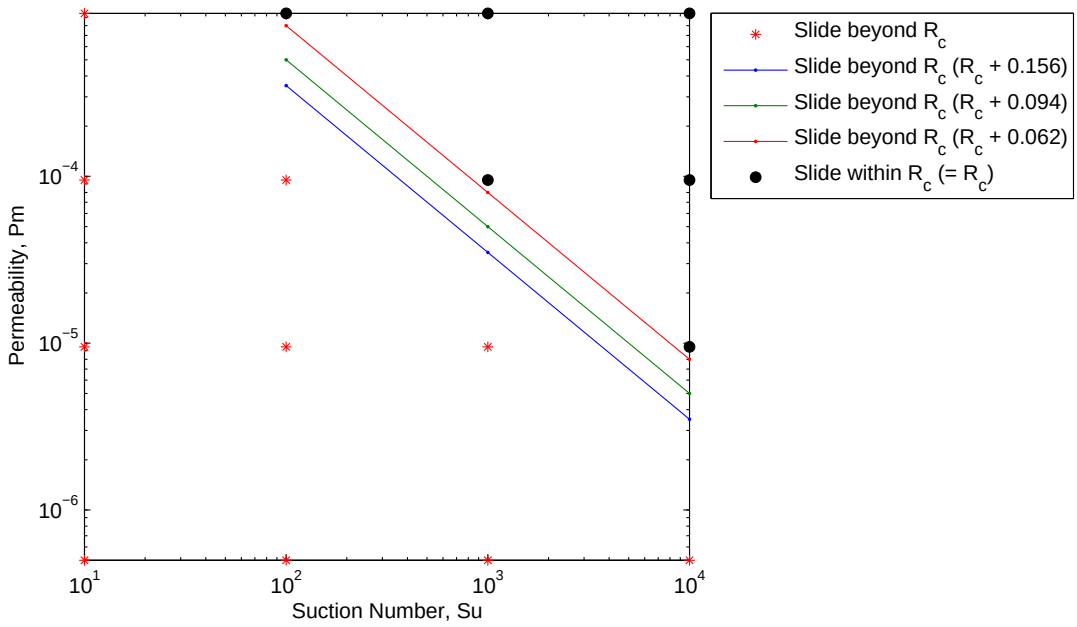

Figure 7.32: Variation of physical properties, Pm and Su, to determine whether the fluid gets absorbed within or outside the initial contact area on an inclined porous substrate (i.e. $\theta_i = 60^o$)

Based on insight from the earlier results, absorption of water droplets on three different porous substrates inclined at 60° to the horizontal having highly, partially and very low absorptive properties are discussed. Figure (7.33) shows the height contours formed by water droplets inside and outside the different porous substrates for the same time duration. As the absorptive property is increased, the rate of absorption is increased and the absorption occurs within the the initial contact radius. On the other hand, low absorptive property causes the droplets to slide on the substrate and increase the footprint area. The shape of the footprint inside the substrate is oval and the shape is primarily dependent on the inclination of the substrate. With an increase in inclination, the footprint becomes more elliptic on a low absorptive substrate.

This is a very important result from a BPA perspective as this forms the basis of looking at the fabrics from a whole new perspective. It can help in determining whether the blood will slide beyond the initial contact region. In addition to this, it is also interesting to see the depth of penetration of the blood on different porous substrates. This can help forensic scientists especially to determine the shape of the footprint and the fluid left on top due to saturation inside the porous substrate.

Physical Property	Low Absorption	Partial Absorption	Full Absorption
Density, kg/m^3	1000	1000	1000
Viscosity, μ, Pa.s	0.001	0.001	0.001
Surface Tension, N/m	0.07	0.07	0.07
Equilibrium Contact Angle, θ_e, ^{o}	22.92	22.92	22.92
Porosity, ϕ	0.5	0.5	0.5
Suction number, Su	10	100	1000
Permeability, Pm	5×10^{-5}	5×10^{-5}	5×10^{-5}
Inclination angle, θ_i, ^{o}	60	60	60
Volume of droplet, V_0, μl	10.42	10.42	10.42
Initial position of centre of gravity	(2,2)	(2,2)	(2,2)

Table 7.11: Physical properties of the fluid and porous medium which produced the footprints seen in Figure 7.33

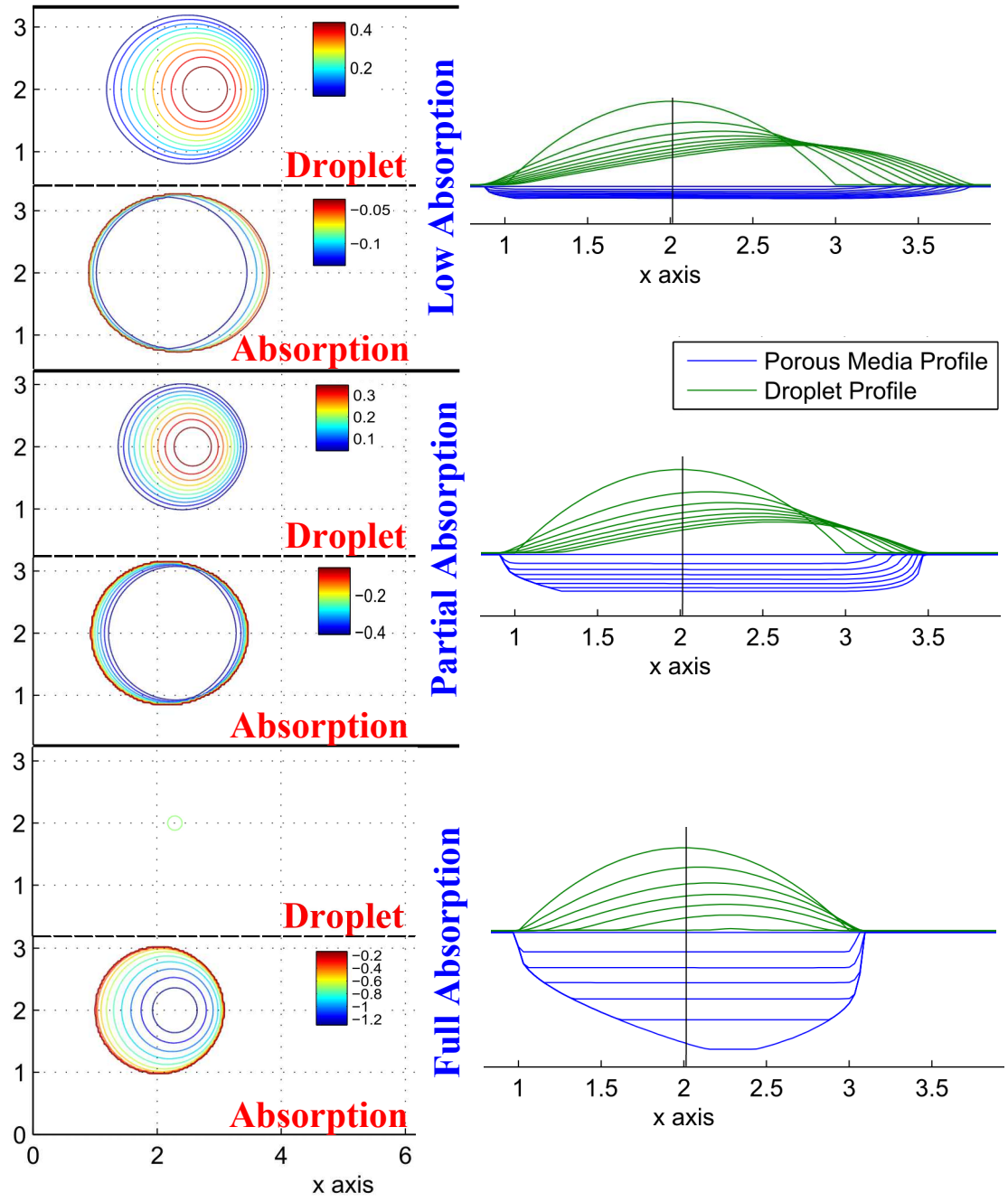

Figure 7.33: Footprints left by fluid on and inside the porous substrates inclined at 60° to the horizontal with different absorptive properties

7.6 Concluding remarks

There are principally four parameters which govern the motion of fluid in the porous medium i.e. porosity, permeability, suction number, and equilibrium contact angle. Darcy's law is used to incorporate the absorption dynamics in the numerical code. This implementation is compared with the analytical solution for the absorption of a thin film in a porous substrate. Analytical and numerical solutions are in good agreement with each other. Porosity dictates

primarily the extent to which the droplet gets absorbed. As the porosity of a substrate is reduced, the depth of penetration through the porous substrate increases and the time taken for the droplet to get fully absorbed also increases. Permeability essentially controls the transmission of fluid through the porous substrate. It has a direct relation with the rate of absorption of a fluid droplet i.e. reduction in permeability causes a decrease in the rate of absorption. Suction number or capillary pressure is vital in regulating the fluid distribution in pores of the porous substrate. Change in capillary pressure is also directly related to the rate of absorption of droplet i.e. as the capillary pressure is reduced the rate of absorption is reduced. The equilibrium contact angle mainly dictates the shape of the absorbed fluid in the porous media. Increasing the equilibrium contact angle causes the shape of the absorbed fluid to look more conical. An important conclusion from the results is that the time taken for the fluid droplet to get fully absorbed in the porous substrate, τ_{absorp} has a power-law dependence on permeability, suction number and porosity whereas it has an exponential dependence on the equilibrium contact angle. The results of inclined absorption show that permeability and suction number most affect the rate of absorption and rate of slide on an inclined porous substrate. Keeping the focus to these two properties, finally a region of properties i.e. suction number and permeability, is defined in which the droplet slides and gets absorbed within the initial contact radius.

Chapter 8

Conclusion

Contents

8.1 Summary

The aim of this research is to develop a model that can numerically solve the problem of spreading and sliding of fluid droplets on inclined solid and porous substrates. The purpose is to help forensic scientists understand the fluid mechanics behind the formation of bloodstain footprints. In this work, three properties which affect the spreading and sliding dynamics discussed in detail are the contact angle hysteresis, fluid rheology and fluid absorption in porous medium.

In Chapter 1, the thesis starts by introducing the bloodstain pattern analysis. Physical processes involved during the formation of blood footprints are discussed. It explores the interpretations used by forensic scientists while extracting valuable information from a crime scene. Physical properties of blood are described and the fundamentals of fluid mechanics involved in the spreading of droplets on surfaces are outlined first. Rheological models available in the literature to model blood properties are then discussed. A power-law model is selected to model the blood properties while it is spreading/sliding on substrates. The lubrication approximation is used to reduce the complexity of the Navier-Stokes equations. An existing parallel multigrid thin film solver, FILMPAR, is modified to incorporate the physical phenomena discussed above.

In the next Chapter 2, the governing equations for the three-dimensional time-dependent lubrication approximation for a droplet spreading are derived. A brief description of the solver, FILMPAR, is mentioned. The equations which are replaced in the solver to model the spreading and sliding of droplets are specified. This is followed by Chapter 3, which verifies the correct implementation of governing equations in FILMPAR by comparing the numerical results with the results from COMSOL, a commercially available finite-element solver.

After the verification of the numerical code, a preliminary study of blood droplets on different substrates is conducted. Newtonian properties of blood are assumed. In this analysis, the influence of the volume of the droplet and the substrate wetting properties on the spreading/sliding dynamics are discussed. Two key outcomes from this are that an increase in droplet volume increases the speed with which the droplet slides down the incline and sub-

strate wettability and inclination influences the extent of the spread of the footprints formed by the sliding droplets.

In Chapter 4, the influence of contact angle hysteresis is explored by suggesting a simple model to incorporate contact angle hysteresis in the sliding droplets. An analytical model based on the forces affecting the droplet slide motion is proposed. The limitation of this analytical model is that the footprint has to remain close to a circle during the sliding motion. This analytical model relates well with experimental and numerical results for the droplets having higher contact angles, i.e. greater than 45^{o} and lower inclinations i.e. where the droplet footprint is close to circle. The shape of the droplets observed in the numerical simulations tends to agree with the shapes of the droplet described in the literature. Based on this, special cases are discussed in which the droplets tend to break up leaving satellite droplets behind. Droplets stick to the substrate in a few cases where the force due to hysteresis overcomes the forces present due to gravitational pull. An important effect of equilibrium contact angle is observed, i.e. the droplets having small θ_e are likely to form long tails as they slide down the incline substrates and the droplets with large θ_e are more likely to have shapes closer to teardrops.

Next the effects of rheology on the fluid flow are discussed. Chapter 5 explores the leveling dynamics of thin non-Newtonian fluid films. This problem is first analyzed because of its simplicity due to absence of contact line reducing the computational requirements to solve the problem. A power-law model is used to define non-Newtonian rheology. The subsequent governing equations are derived and implemented in the numerical code. This implementation is then verified using Method of Manufactured Solutions (MMS) technique. This verification gives the required confidence for the accuracy of the model. Based on this validation, the problem of leveling of a sinusoidal perturbation on horizontal substrates having different fluid rheologies is investigated. The trends observed are in line with the literature (Eley, 2012). Outcomes of the leveling of the sinusoidal perturbations suggest that the rheology plays a cardinal role in the leveling dynamics. It determines the rate at which the fluid levels. Finally, the leveling of localized and plane bell-shaped perturbations are discussed. This example highlights the importance of three-dimensional effects which are often ignored in the study of leveling in thin films.

In Chapter 6, the verified non-Newtonian model is used to study the effects of rheology on droplet spreading. The numerical results confirm earlier observations that for all other quantities being equal, an increase of the flow index, n, leads to a more rapid wetting. An interesting observation is that after an initial transient stage, the droplets reach a constant terminal velocity and essentially travel down the inclined plane with a constant profile. It was observed as intuitively expected, that the terminal velocity of the droplets increases with the slope of the inclined plane irrespective of the rheology but for a given inclination angle, the flow behavior index is found to have a major impact on this terminal velocity. The droplets of shear-thinning fluid travel downslope more slowly. The trends observed are in line with the theory, and the decrease in viscosity is observed at higher shear rates for shear-thinning fluids; the opposite is true for shear-thickening fluids. The sliding dynamics of three different fluids having different rheologies are finally compared numerically. The Newtonian water droplet being a more wetting liquid spreads at a higher rate on a glass substrate and travels down the slope faster than the other two fluids. Blood is a shear-thinning fluid, its viscosity therefore increases as the shear rates are reduced. For the smallest inclination angle (30^o) the blood droplet terminal velocity is higher than that of the PPG/Silica solution. This trend is then inverted for the higher inclination angles. Interestingly, the simulations revealed the formation of a tail at the rear of the sliding droplet for the shear-thickening fluid.

Finally, the absorption of Newtonian droplets in porous substrates were considered in Chapter 7. This was achieved with the help of Darcy's law. There exists principally four physical parameters which controls the motion is porous medium: porosity, permeability, suction number, and equilibrium contact angle. The results show that porosity controls the extent of penetration of the droplet as it gets absorbed. As the porosity of the substrate is reduced, the depth to which it penetrates increases due to less free space in the porous medium. Subsequently the time taken by the droplet to get fully absorbed also increases. Permeability and suction number directly affect the rate of absorption. As these properties were reduced, the rate of absorption was reduced. The equilibrium contact angle influences the shape which the fluid attains in the porous medium. Increases in θ_e causes the shape to be more conical. An important outcome of this study was to figure out that the time taken for the fluid droplet to get fully absorbed had a power-law dependence on porosity, permeability and suction number

whereas an exponential dependence on the equilibrium contact angle. The rate of absorption and the rate of slide in case of absorption of droplets on inclined porous substrates were most affected by permeability and suction number. Keeping this in mind, a range of values of these two properties were tried to see the extent to which the droplet slides before it gets absorbed.

8.2 Suggestions for future work

Substrates are not always smooth and there might be heterogeneities on the substrates. The effects of the topographic features on the speed of the spreading/sliding droplets are important. A next step towards the development of the numerical code could be to incorporate appropriate changes in the numerical code to implement droplet spreading on topographically different substrates. The concept of adding a variable to define the topographic features in the z-direction has been used before in the simulations of thin films over topographical heterogeneities (Lee et al., 2007). Moreover, the effect of chemical heterogeneities on the spreading/sliding dynamics of fluid droplets could be explored as these have a potential to radically alter the spreading dynamics.

Bloodstain formation on solid substrates relies upon the following physical processes: wettability, drying/evaporation, viscous dissipation, and coagulation (Attinger et al., 2013). Understanding the drying process is of prime importance to the forensic investigators. It helps the investigators in reconstructing the events and to determine/predict the time elapsed after the crime. In this work, evaporation/drying processes were not explored. It would be insightful to study the effects of drying on the spreading dynamics.

The drying process has been extensively explored in the past. Eres and co-workers presented a three-dimensional drying model for coating films on horizontal surfaces (Eres et al., 1999). To extend this work, Gaskell and co-workers explored the evaporation of thin films under the lubrication approximation framework and well-mixed approximations (Gaskell et al., 2006). The fluid is assumed to be incompressible and Newtonian, having a volatile solvent and a non-volatile solute. Solvent concentration is important in the dynamics of the drying (Gaskell et al., 2006). Viscosity must be exponentially dependent upon solvent concentration (Eres et al., 1999; Schwartz et al., 2001; Gaskell et al., 2006). Evaporation rate can be added as a

source term to the governing equation. Another equation is required to describe the solvent concentration and incorporates the evaporation model. The choice of evaporation model depends on solvent diffusivity. If the solvent diffuses rapidly, it is assumed to be uniform across the fluid, well-mixed assumption. Howison and co-workers suggested the equation for solvent conservation under the well-mixed approximation (Howison et al., 1997; Gaskell et al., 2006). Drying process of blood may be explored with the assumption that the blood is well mixed with plasma (volatile solvent) and RBCs (non-volatile solute).

Absorption of fluid droplets on fabrics is of prime importance to forensic scientists. There still remains a lot to be done in the area of absorption of droplets on porous substrates. In Chapter 7, absorption in the vertical plane is investigated in detail. The next step would be to see the effects of lateral absorption on the overall absorption dynamics and the effects on the shape of the footprint. In this work, the absorption of Newtonian fluid is explored. It would be beneficial for forensic scientists to explore the absorption dynamics of non-Newtonian fluids because of blood's shear-thinning property. Darcy's law can be modified to accommodate this non-Newtonian behavior.

Appendix A

Derivation of the governing equations for Newtonian fluid

The mass and momentum balance equations are given as,

$$\frac{\partial u'}{\partial x'} + \frac{\partial v'}{\partial y'} + \frac{\partial w'}{\partial z'} = 0, \tag{A.1}$$

$$\rho\left(\frac{\partial u'}{\partial t'} + u'\frac{\partial u'}{\partial x'} + v'\frac{\partial u'}{\partial y'} + w'\frac{\partial u'}{\partial z'}\right) = \rho g \sin\theta_i - \frac{\partial p'}{\partial x'} + \mu\left(\frac{\partial^2 u'}{\partial x'^2} + \frac{\partial^2 u'}{\partial y'^2} + \frac{\partial^2 u'}{\partial z'^2}\right), \tag{A.2}$$

$$\rho\left(\frac{\partial v'}{\partial t'} + u'\frac{\partial v'}{\partial x'} + v'\frac{\partial v'}{\partial y'} + w'\frac{\partial v'}{\partial z'}\right) = -\frac{\partial p'}{\partial y'} + \mu\left(\frac{\partial^2 v'}{\partial x'^2} + \frac{\partial^2 v'}{\partial y'^2} + \frac{\partial^2 v'}{\partial z'^2}\right), \tag{A.3}$$

$$\rho\left(\frac{\partial w'}{\partial t'} + u'\frac{\partial w'}{\partial x'} + v'\frac{\partial w'}{\partial y'} + w'\frac{\partial w'}{\partial z'}\right) = -\rho g \cos\theta_i - \frac{\partial p'}{\partial z'} + \mu\left(\frac{\partial^2 w'}{\partial x'^2} + \frac{\partial^2 w'}{\partial y'^2} + \frac{\partial^2 w'}{\partial z'^2}\right). \tag{A.4}$$

Convert the dimensional variables into non-dimensional variables, where the scalings for the Newtonian fluid are given as,

$$\begin{gathered} U_0 = \frac{R_0}{T_0},\ P_0 = \frac{\sigma\epsilon}{R_0},\ T_0 = \left(\frac{\mu R_0}{\sigma\epsilon^3}\right),\ \epsilon = \frac{H_0}{R_0},\ \epsilon \ll 1, \\ u' = U_0 u,\ v' = U_0 v,\ w' = \epsilon U_0 w,\ x' = R_0 x,\ y' = R_0 y,\ z' = H_0 z. \end{gathered} \tag{A.5}$$

To avoid complexity, let us first consider the x-axis equation (A.2),

$$\rho\left[\frac{U_0}{T_0}\left(\frac{\partial u}{\partial t}\right)+\frac{U_0^2}{R_0}\left(u\frac{\partial u}{\partial x}+v\frac{\partial u}{\partial y}+w\frac{\partial u}{\partial z}\right)\right]=\rho g\sin\theta_i- \frac{P_0}{R_0}\frac{\partial p}{\partial x}+\mu\frac{U_0}{H_0^2}\left(\frac{H_0^2}{R_0^2}\frac{\partial^2 u}{\partial x^2}+\frac{H_0^2}{R_0^2}\frac{\partial^2 u}{\partial y^2}+\frac{\partial^2 u}{\partial z^2}\right). \tag{A.6}$$

It is known through lubrication approximation that $\epsilon^2=\frac{H_0^2}{L_0^2}$, $\epsilon^2\ll 1$, which the reduces the equation to,

$$\frac{\partial^2 u}{\partial z^2}=\frac{P_0H_0^2}{\mu U_0R_0}\frac{\partial p}{\partial x}-\frac{\rho gH_0^2}{\mu U_0}\sin\theta_i, \tag{A.7}$$

which can be re-written as,

$$\frac{\partial}{\partial z}\left(\frac{\partial u}{\partial z}\right)=\frac{H_0^2P_0}{U_0\mu L_0}\frac{\partial p}{\partial x}-\frac{\rho gH_0^2}{U_0\mu}\sin\theta_i, \tag{A.8}$$

where $U_0=\frac{R_0}{T_0}$,

$$\frac{\partial}{\partial z}\left(\frac{\partial u}{\partial z}\right)=\left[\frac{T_0H_0^2P_0}{\mu R_0^2}\frac{\partial p}{\partial x}-\frac{\rho gH_0^2T_0}{R_0\mu}\sin\theta_i\right], \tag{A.9}$$

and $T_0=\left(\frac{\mu R_0}{\sigma\epsilon^3}\right), P_0=\frac{\sigma\epsilon}{R_0}$, and $\epsilon=\frac{H_0}{L_0}$,

$$\frac{\partial}{\partial z}\left(\frac{\partial u}{\partial z}\right)=\frac{\partial p}{\partial x}-\frac{\rho gR_0^2}{\sigma\epsilon}\sin\theta_i. \tag{A.10}$$

The Bond number, Bo is defined as, $Bo=\frac{\rho gR_0^2}{\sigma}$, so,

$$\frac{\partial}{\partial z}\left(\frac{\partial u}{\partial z}\right)=\frac{\partial p}{\partial x}-\frac{Bo\sin\theta_i}{\epsilon}. \tag{A.11}$$

Integrate the above equation with respect to z,

$$\int\frac{\partial}{\partial z}\left(\frac{\partial u}{\partial z}\right)dz=\int\left(\frac{\partial p}{\partial x}-\frac{Bo\sin\theta_i}{\epsilon}\right)dz, \tag{A.12}$$

$$\left|\left(\frac{\partial u}{\partial z}\right)\right|=\left(\frac{\partial p}{\partial x}-\frac{Bo\sin\theta_i}{\epsilon}\right)|z+c_1|, \tag{A.13}$$

where c_1 is the constant of integration and at $z=h,\ c_1=-h$,

$$\left(\frac{\partial u}{\partial z}\right)=\left(\frac{Bo\sin\theta_i}{\epsilon}-\frac{\partial p}{\partial x}\right)(h-z). \tag{A.14}$$

Integrate again the above equation with respect to "z",

$$\int \frac{\partial u}{\partial z} dz = \left(\frac{Bo \sin \theta_i}{\epsilon} - \frac{\partial p}{\partial x} \right) \int (h - z) dz, \tag{A.15}$$

$$u| = \left(\frac{Bo \sin \theta_i}{\epsilon} - \frac{\partial p}{\partial x} \right) \left(\frac{1}{2} \right) \left| \left[-(h - z)^2 + c_2 \right] \right|, \tag{A.16}$$

where c_2 is the constant of integration and at $z = 0,\ u = 0$,

$$c_2 = (h)^2, \tag{A.17}$$

so the velocity, u in the x-direction is given as,

$$u = \left(\frac{Bo \sin \theta_i}{\epsilon} - \frac{\partial p}{\partial x} \right) \left(\frac{1}{2} \right) \left[h^2 - (h - z)^2 \right]. \tag{A.18}$$

The flux in x-direction is defined as,

$$Q_x = \int u dz. \tag{A.19}$$

Substitute u in the Q_x,

$$Q_x = \int \left(\frac{Bo \sin \theta_i}{\epsilon} - \frac{\partial p}{\partial x} \right) \left(\frac{1}{2} \right) \left[h^2 - (h - z)^2 \right] dz. \tag{A.20}$$

Performing the integration in the above equation gives,

$$Q_x = \left(\frac{Bo \sin \theta_i}{\epsilon} - \frac{\partial p}{\partial x} \right) \left(\frac{1}{2} \right) \left| \left[h^2 z + (\frac{1}{3})(h - z)^3 + c_3 \right] \right|, \tag{A.21}$$

where c_3 is the constant of integration and for $z = 0,\ Q_x = 0$,

$$c_3 = -\frac{1}{3}(h)^3, \tag{A.22}$$

Substitute c_3 back in the x-flux term,

$$Q_x = \left(\frac{Bo \sin \theta_i}{\epsilon} - \frac{\partial p}{\partial x} \right) \left(\frac{1}{2} \right) \left[h^2 z + \frac{1}{3}(h - z)^3 - \frac{1}{3}(h)^3 \right], \tag{A.23}$$

at $z = h$, the Q_x is given as,

$$Q_x = \left(\frac{Bo \sin\theta_i}{\epsilon} - \frac{\partial p}{\partial x}\right)\left(\frac{1}{3}\right) h^3, \tag{A.24}$$

Now consider the y-axis equation (A.3),

$$\rho\left(\frac{\partial v'}{\partial t'} + u'\frac{\partial v'}{\partial x'} + v'\frac{\partial v'}{\partial y'} + w'\frac{\partial v'}{\partial z'}\right) = -\frac{\partial p'}{\partial y'} + \mu\left(\frac{\partial^2 v'}{\partial x'^2} + \frac{\partial^2 v'}{\partial y'^2} + \frac{\partial^2 v'}{\partial z'^2}\right). \tag{A.25}$$

Applying the scalings and non-dimensionalization gives,

$$\begin{aligned}\rho\left[\frac{U_0}{T_0}\left(\frac{\partial v}{\partial t}\right) + \frac{U_0^2}{R_0}\left(u\frac{\partial v}{\partial x}\right) + \frac{U_0^2}{R_0}\left(v\frac{\partial v}{\partial y}\right) + \frac{\epsilon U_0^2}{H_0}\left(w\frac{\partial v}{\partial z}\right)\right] = \\ -\frac{P_0}{R_0}\frac{\partial p}{\partial y} + \mu\left(\frac{U_0}{R_0^2}\frac{\partial^2 v}{\partial x^2} + \frac{U_0}{R_0^2}\frac{\partial^2 v}{\partial y^2} + \frac{U_0}{H_0^2}\frac{\partial^2 v}{\partial z^2}\right),\end{aligned} \tag{A.26}$$

It is known through lubrication approximation that $\epsilon^2 = \frac{H_0^2}{L_0^2}$, $\epsilon^2 \ll 1$, which the reduces the equation to,

$$\frac{\partial^2 v}{\partial z^2} = \frac{P_0 H_0^2}{\mu R_0 U_0}\frac{\partial p}{\partial y}, \tag{A.27}$$

where $U_0 = \frac{R_0}{T_0}, T_0 = \left(\frac{\mu R_0}{\sigma\epsilon^3}\right)$ and $P_0 = \frac{\sigma\epsilon}{R_0}$,

$$\frac{\partial}{\partial z}\left(\frac{\partial v}{\partial z}\right) = \frac{\sigma\epsilon H_0^2 R_0 \mu}{\sigma\epsilon^3 \mu R_0^3}\frac{\partial p}{\partial y}, \tag{A.28}$$

$$\frac{\partial}{\partial z}\left(\frac{\partial v}{\partial z}\right) = \frac{\partial p}{\partial y}. \tag{A.29}$$

Integrate the above equation with respect to z,

$$\int \frac{\partial}{\partial z}\left(\frac{\partial v}{\partial z}\right) dz = \int \left(\frac{\partial p}{\partial y}\right) dz, \tag{A.30}$$

$$\left|\left(\frac{\partial v}{\partial z}\right)\right| = \left(\frac{\partial p}{\partial y}\right)|z + c_1|, \tag{A.31}$$

where c_1 is the constant of integration and at $z = h,\ c_1 = -h$,

$$\frac{\partial v}{\partial z} = \left(\left(-\frac{\partial p}{\partial y}\right)(h - z)\right). \tag{A.32}$$

Integrate again the above equation with respect to "z",

$$\int \frac{\partial v}{\partial z} dz = \left(-\frac{\partial p}{\partial y}\right) \int (h - z) dz, \tag{A.33}$$

$$v|_0^v = \left(-\frac{\partial p}{\partial y}\right) \left(\frac{1}{2}\right) \left|\left[-(h-z)^2 + c_2\right]\right|, \tag{A.34}$$

where c_2 is the constant of integration and at $z = 0,\ v = 0$,

$$c_2 = (h)^2, \tag{A.35}$$

Then the velocity, v, in the y-direction is given by,

$$v = \left(-\frac{\partial p}{\partial y}\right) \left(\frac{1}{2}\right) \left[h^2 - (h-z)^2\right]. \tag{A.36}$$

The flux in y-direction is given by,

$$Q_y = \int v dz, \tag{A.37}$$

Substituting v in the flux equation gives,

$$Q_y = \int \left(-\frac{\partial p}{\partial y}\right) \left(\frac{1}{2}\right) \left[h^2 - (h-z)^2\right] dz, \tag{A.38}$$

Performing the integration in the above equation gives,

$$Q_y = \left(-\frac{\partial p}{\partial y}\right) \left(\frac{1}{2}\right) \left|\left[h^2 z + \frac{1}{3}(h-z)^3 + c_3\right]\right|, \tag{A.39}$$

where c_3 is the constant of integration and for $z = 0,\ Q_y = 0$,

$$c_3 = -\frac{1}{3}(h)^3, \tag{A.40}$$

Then flux in y-direction is given as,

$$Q_y = \left(-\frac{\partial p}{\partial y}\right) \left(\frac{1}{2}\right) \left[h^2 z + \frac{1}{3}(h-z)^3 - \frac{1}{3}(h)^3\right]. \tag{A.41}$$

At $z = h$, the Q_y is given as,

$$Q_y = \left(-\frac{\partial p}{\partial y}\right) \left(\frac{1}{3}\right) h^3. \tag{A.42}$$

The basic lubrication equation in 3D is given by,

$$\frac{\partial h}{\partial t} + \frac{\partial Q_x}{\partial x} + \frac{\partial Q_y}{\partial y} = 0. \tag{A.43}$$

Let $C_1 = \frac{Bo \sin\theta}{\epsilon}$,

$$\frac{\partial h}{\partial t} = -\left[\frac{\partial}{\partial x}\left(\frac{h^3}{3}\left(C_1 - \frac{\partial p}{\partial x}\right)\right) + \frac{\partial}{\partial y}\left(\frac{h^3}{3}\left(-\frac{\partial p}{\partial y}\right)\right)\right], \tag{A.44}$$

Spatial discretization in the x-axis only is given as,

$$= \frac{1}{\Delta x}\left[\frac{h^3_{i+\frac{1}{2}}}{3}\left(C_1 - \frac{\partial p_{i+\frac{1}{2}}}{\partial x}\right) - \frac{h^3_{i-\frac{1}{2}}}{3}\left(C_1 - \frac{\partial p_{i-\frac{1}{2}}}{\partial x}\right)\right], \tag{A.45}$$

$\frac{\partial p_{i+\frac{1}{2}}}{\partial x}$ and $\frac{\partial p_{i-\frac{1}{2}}}{\partial x}$ after spatial discretization can be written as,

$$= \frac{1}{\Delta x}\left[\frac{h^3_{i+\frac{1}{2}}}{3}\left(C_1 - \frac{p_{i+1} - p_i}{\Delta x}\right) - \frac{h^3_{i-\frac{1}{2}}}{3}\left(C_1 - \frac{p_i - p_{i-1}}{\Delta x}\right)\right], \tag{A.46}$$

where by interpolation, $h^3_{i+\frac{1}{2}} = \frac{h^3_{i+1}+h^3_i}{2}$ and $h^3_{i-\frac{1}{2}} = \frac{h^3_{i-1}+h^3_i}{2}$,

$$= \frac{1}{\Delta x}\left[\left(\frac{h^3_{i+1} + h^3_i}{2(3)}\right)\left(C_1 - \frac{p_{i+1} - p_i}{\Delta x}\right) - \left(\frac{h^3_{i-1} + h^3_i}{2(3)}\right)\left(C_1 - \frac{p_i - p_{i-1}}{\Delta x}\right)\right]. \tag{A.47}$$

Spatial discretization in the y-axis only is given as,

$$= \frac{1}{\Delta y}\left[\frac{h^3_{j+\frac{1}{2}}}{3}\left(-\frac{\partial p_{j+\frac{1}{2}}}{\partial y}\right) - \frac{h^3_{j-\frac{1}{2}}}{3}\left(-\frac{\partial p_{j-\frac{1}{2}}}{\partial y}\right)\right], \tag{A.48}$$

$\frac{\partial p_{j+\frac{1}{2}}}{\partial y}$ and $\frac{\partial p_{j-\frac{1}{2}}}{\partial y}$ after spatial discretization can be written as,

$$= \frac{1}{\Delta y}\left[\frac{h^3_{j+\frac{1}{2}}}{3}\left(-\frac{p_{j+1} - p_j}{\Delta y}\right) - \frac{h^3_{j-\frac{1}{2}}}{3}\left(-\frac{p_j - p_{j-1}}{\Delta y}\right)\right], \tag{A.49}$$

where by interpolation, $h^3_{j+\frac{1}{2}} = \frac{h^3_{j+1}+h^3_j}{2}$ and $h^3_{j-\frac{1}{2}} = \frac{h^3_{j-1}+h^3_j}{2}$

$$= \frac{1}{\Delta y}\left[\left(\frac{h^3_{j+1} + h^3_j}{2(3)}\right)\left(\frac{p_j - p_{j+1}}{\Delta y}\right) - \left(\frac{h^3_{j-1} + h^3_j}{2(3)}\right)\left(\frac{p_{j-1} - p_j}{\Delta y}\right)\right], \tag{A.50}$$

Combining the x and y-axis spatial discretization,

$$\frac{\partial h_{ij}}{\partial t} = -\frac{1}{\Delta x}\left\{\left(\frac{h_{i+1j}^3 + h_{ij}^3}{2(3)}\right)\left(C_1 - \frac{p_{i+1j} - p_{ij}}{\Delta x}\right) - \left(\frac{h_{i-1j}^3 + h_{ij}^3}{2(3)}\right)\left(C_1 - \frac{p_{ij} - p_{i-1j}}{\Delta x}\right)\right\}$$
$$\underbrace{-\frac{1}{\Delta y}\left\{\left(\frac{h_{ij|+1}^3 + h_{ij}^3}{2(3)}\right)\left(\frac{p_{ij} - p_{ij+1}}{\Delta y}\right) - \left(\frac{h_{ij-1+}^3 h_{ij}^3}{2(3)}\right)\left(\frac{p_{ij-1} - p_{ij}}{\Delta y}\right)\right\}}_{\mathcal{F}_h^{n_t}}, \tag{A.51}$$

The right-hand side of the equation (A.51) may be represented as $\mathcal{F}_h^{n_t}$, i.e. $\frac{\partial h_{ij}}{\partial t} = \mathcal{F}_h^{n_t}$. Then using the Crank-Nicolson scheme yields,

$$\frac{h_{ij}^{n_t+1} - h_{ij}^{n_t}}{\triangle t} = \frac{1}{2}\left[\mathcal{F}_h^{n_t+1} + \mathcal{F}_h^{n_t}\right]. \tag{A.52}$$

Re-arranging equation (A.52) gives,

$$\underbrace{h_{ij}^{n_t+1} - \frac{\Delta t}{2}\left[\mathcal{F}_h^{n_t+1}\right]}_{\mathcal{L}_k^h} = h_{ij}^{n_t} + \frac{\Delta t}{2}\left[\mathcal{F}_h^{n_t}\right], \tag{A.53}$$

now, consider the z-axis equation (A.4),

$$\rho\left(\frac{\partial w'}{\partial t'} + u'\frac{\partial w'}{\partial x'} + v'\frac{\partial w'}{\partial y'} + w'\frac{\partial w'}{\partial z'}\right) = -\rho g\cos\theta_i - \frac{\partial p'}{\partial z'} + \mu\left(\frac{\partial^2 w'}{\partial x'^2} + \frac{\partial^2 w'}{\partial y'^2} + \frac{\partial^2 w'}{\partial z'^2}\right). \tag{A.54}$$

Applying the scalings and non-dimensionalization gives,

$$\rho\left(\frac{\epsilon U_0}{T_0}\frac{\partial w}{\partial t} + \frac{\epsilon U_0^2}{L_0}u\frac{\partial w}{\partial x} + \frac{\epsilon U_0^2}{L_0}v\frac{\partial w}{\partial y} + \frac{\epsilon^2 U_0^2}{H_0}w\frac{\partial w}{\partial z}\right) = -\rho g\cos\theta_i - \frac{P_0}{H_0}\frac{\partial p}{\partial z} + \mu\left(\frac{\epsilon U_0}{L_0^2}\frac{\partial^2 w'}{\partial x'^2} + \frac{\epsilon U_0}{L_0^2}\frac{\partial^2 w'}{\partial y'^2} + \frac{\epsilon U_0}{H_0^2}\frac{\partial^2 w'}{\partial z'^2}\right). \tag{A.55}$$

which reduces the equation to,

$$\frac{P_0}{H_0}\frac{\partial p}{\partial z} = \rho g\cos\theta_i, \tag{A.56}$$

which can be re-arranged as,

$$\frac{\partial p}{\partial z} = Bo\cos\theta_i. \tag{A.57}$$

It is known that the boundary condition for pressure at the droplet surface is,

$$p = -\nabla^2 h - \Pi(h) \quad \text{on} \quad z = h, \tag{A.58}$$

where $\Pi(h)$ is the disjoining pressure term for sliding droplets. Integrate equation (A.57) with respect to z and setting the integration constant using equation (A.58) yields the pressure field throughout the film,

$$p = -\nabla^2(h) - \Pi(h) + Bo\cos\theta_i\,(h)\,, \tag{A.59}$$

Spatial discretization of p is given by,

$$p_{ij} + \left(\frac{h_{i+1j} + h_{i-1j} - 2h_{ij}}{\triangle x^2}\right) + \left(\frac{h_{ij+1} + h_{ij-1} - 2h_{ij}}{\triangle y^2}\right) + \frac{(1 - cos\theta_e)\,(n_d - 1)\,(m_d - 1)}{\epsilon^2 h^*(n_d - m_d)}\left[\left(\frac{h^*}{h_{ij}}\right)^{n_d} - \left(\frac{h^*}{h_{ij}}\right)^{m_d}\right] - Bo\cos\theta_i(h_{ij}) = \mathcal{L}_k^p. \tag{A.60}$$

then,

$$\mathcal{L}_k^h\left(h_k^{n_t+1}, p_k^{n_t+1}\right) = f_k^h\left(h_k^{n_t}, p_k^{n_t}\right), \tag{A.61}$$

$$\mathcal{L}_k^p\left(h_k^{n_t+1}, p_k^{n_t+1}\right) = f_k^p\left(h_k^{n_t}, p_k^{n_t}\right). \tag{A.62}$$

Then the Jacobian, J is represented as,

$$J = \frac{\partial\left(\mathcal{L}_k^h, \mathcal{L}_k^p\right)}{\partial\left(h_k^{n_t+1}, p_k^{n_t+1}\right)}. \tag{A.63}$$

Initial guess to the solution is given by $\left(h_{0k}^{n_t+1}, p_{0k}^{n_t+1}\right)$, the Newton iteration proceeds by solving,

$$J\begin{pmatrix} \Delta h \\ \Delta p \end{pmatrix} = \begin{pmatrix} f_k^h - \mathcal{L}_k^h(h_{0k}^{n_t+1}, p_{0k}^{n_t+1}) \\ f_k^p - \mathcal{L}_k^p(h_{0k}^{n_t+1}, p_{0k}^{n_t+1}) \end{pmatrix}. \tag{A.64}$$

Now the terms of the jacobian are calculated. Then from equation (A.60),

$$\frac{\partial \mathcal{L}_k^p}{\partial p_{ij}} = 1 = D, \tag{A.65}$$

$$\frac{\partial \mathcal{L}_k^p}{\partial h_{ij}} = \left(\frac{-2h_{ij}}{\triangle x^2}\right) + \left(\frac{-2h_{ij}}{\triangle y^2}\right) + \frac{(1-\cos\theta_e)\,(n_d-1)\,(m_d-1)}{\epsilon^2 h^*(n_d-m_d)}\left[\frac{m_d}{h_{ij}}\left(\frac{h^*}{h_{ij}}\right)^{m_d} - \frac{n_d}{h_{ij}}\left(\frac{h^*}{h_{ij}}\right)^{m_d}\right] - Bo\cos\theta_i = C, \quad \text{(A.66)}$$

and from equation (A.53),

$$\frac{\partial \mathcal{L}_k^h}{\partial p_{ij}} = \frac{\triangle t}{2}\left[\frac{1}{(\triangle x^2)}\left\{\left(\frac{h_{i+1j}^3 + h_{ij}^3}{6}\right) + \left(\frac{h_{i-1j}^3 + h_{ij}^3}{6}\right)\right\}\right] + \frac{\triangle t}{2}\left[\frac{1}{(\triangle y^2)}\left\{\left(\frac{h_{ij+1}^3 + h_{ij}^3}{6}\right) + \left(\frac{h_{ij-1}^3 + h_{ij}^3}{6}\right)\right\}\right] + \frac{\triangle t}{2}\left[Pm\left(\frac{1}{h_{p\,ij}}\right)\right] = B, \quad \text{(A.67)}$$

$$\frac{\partial \mathcal{L}_k^h}{\partial h_{ij}} = 1 - \frac{\triangle t}{2}\left[\frac{1}{(\triangle x)}\left(\frac{h_{ij}^2}{2}\left(\frac{p_{i+1j} + p_{ij}}{\triangle x}\right) - \frac{h_{ij}^2}{2}\left(\frac{p_{ij} + p_{i-1j}}{\triangle x}\right)\right)\right] - \frac{\triangle t}{2}\left[\frac{1}{(\triangle y)}\left(\frac{h_{ij}^2}{2}\left(\frac{p_{ij+1} - p_{ij}}{\triangle y}\right) - \frac{h_{ij}^2}{2}\left(\frac{p_{ij} + p_{ij-1}}{\triangle y}\right)\right)\right] = A. \quad \text{(A.68)}$$

Equation (A.64) can be expanded,

$$\frac{\partial \mathcal{L}_k^h}{\partial h_{ij}}\Delta h + \frac{\partial \mathcal{L}_k^h}{\partial p_{ij}}\Delta p = f_k^h - \mathcal{L}_k^h\left(h_k^{n_t}, p_k^{n_t}\right), \quad \text{(A.69)}$$

$$\frac{\partial \mathcal{L}_k^p}{\partial h_{ij}}\Delta h + \frac{\partial \mathcal{L}_k^p}{\partial p_{ij}}\Delta p = f_k^p - \mathcal{L}_k^p\left(h_k^{n_t}, p_k^{n_t}\right). \quad \text{(A.70)}$$

This can now be simplified to,

$$\begin{pmatrix} A & B \\ C & D \end{pmatrix}\begin{pmatrix} \Delta h \\ \Delta p \end{pmatrix} = \begin{pmatrix} f_k^h - \mathcal{L}_k^h(h_{0k}^{n_t+1}, p_{0k}^{n_t+1}) \\ f_k^p - \mathcal{L}_k^p(h_{0k}^{n_t+1}, p_{0k}^{n_t+1}) \end{pmatrix}. \quad \text{(A.71)}$$

Expand matrix mentioned in equation (A.71),

$$A\Delta h + B\Delta p = f_k^h - \mathcal{L}_k^h\left(h_k^{n_t}, p_k^{n_t}\right), \quad \text{(A.72)}$$

$$C\Delta h + D\Delta p = f_k^p - \mathcal{L}_k^{h_p}\left(h_k^{n_t}, p_k^{n_t}\right). \quad \text{(A.73)}$$

From equation (A.73),

$$\Delta p = D^{-1}\left(f_k^p - \mathcal{L}_k^p(h_k^{n_t}, p_k^{n_t}) - C\Delta h\right). \quad \text{(A.74)}$$

From equations (A.72) and (A.74),

$$A\Delta h \;+\; BD^{-1}(f_k^p \;-\; \mathcal{L}_k^p(h_k^{n_t}, p_k^{n_t}) \;-\; C\Delta h) \;=\; f_k^h \;-\; \mathcal{L}_k^h\left(h_k^{n_t}, p_k^{n_t}\right), \quad \text{(A.75)}$$

$$\left(A - BD^{-1}C\right)\Delta h = f_k^h - \mathcal{L}_k^h\left(h_k^{n_t}, p_k^{n_t}\right) + \left(-BD^{-1}\right)\left(f_k^p - \mathcal{L}_k^p(h_k^{n_t}, p_k^{n_t}) - C\Delta h\right). \quad \text{(A.76)}$$

The equations (A.74), and (A.76) are applied in the code.

Appendix B

Derivation of the governing equations for non-Newtonian fluid

This derivation is analogous to the one used in references (Ganguly et al., 2012). The stress tensor τ_{ij} for an incompressible power-law fluid is defined by,

$$\tau_{ij} = 2K \left(4D_{kl}D_{lk}\right)^{(n-1)/2} D_{ij}, \tag{B.1}$$

where

$$D_{ij} = \frac{1}{2}\left(\frac{\partial u_i'}{\partial x_j'} + \frac{\partial u_j'}{\partial x_i'}\right) \tag{B.2}$$

D_{ij} is the strain-rate tensor with the spatial components as x_i' and velocity components as u_i'. Making use of equation (B.2), the second invariant of this tensor, $D_{kl}D_{lk}$ (which is the summation with respect to k and l) of the strain-rate tensor D_{ij} is given by,

$$D_{kl}D_{lk} = \frac{1}{4}\left[\left(\frac{\partial u'}{\partial z'} + \frac{\partial w'}{\partial x'}\right)^2 + \left(\frac{\partial v'}{\partial z'} + \frac{\partial w'}{\partial y'}\right)^2 + \left(\frac{\partial u'}{\partial y'} + \frac{\partial v'}{\partial x'}\right)^2\right] - \left[\left(\frac{\partial u'}{\partial x'}\frac{\partial v'}{\partial y'}\right) + \left(\frac{\partial u'}{\partial x'}\frac{\partial w'}{\partial z'}\right) + \left(\frac{\partial w'}{\partial z'}\frac{\partial v'}{\partial y'}\right)\right] \tag{B.3}$$

The mass and momentum balance equations are given as,

$$\frac{\partial u'}{\partial x'} + \frac{\partial v'}{\partial y'} + \frac{\partial w'}{\partial z'} = 0, \tag{B.4}$$

$$\rho\left(\frac{\partial u'}{\partial t'} + u'\frac{\partial u'}{\partial x'} + v'\frac{\partial u'}{\partial y'} + w'\frac{\partial u'}{\partial z'}\right) = \rho g \sin\theta_i - \frac{\partial p'}{\partial x'} + \frac{\partial \tau_{x'x'}}{\partial x'} + \frac{\partial \tau_{x'y'}}{\partial y'} + \frac{\partial \tau_{x'z'}}{\partial z'}, \tag{B.5}$$

$$\rho\left(\frac{\partial v'}{\partial t'}+u'\frac{\partial v'}{\partial x'}+v'\frac{\partial v'}{\partial y'}+w'\frac{\partial v'}{\partial z'}\right)=-\frac{\partial p'}{\partial y'}+\frac{\partial \tau_{y'x'}}{\partial x'}+\frac{\partial \tau_{y'y'}}{\partial y'}+\frac{\partial \tau_{y'z'}}{\partial z'}, \tag{B.6}$$

$$\rho\left(\frac{\partial w'}{\partial t'}+u'\frac{\partial w'}{\partial x'}+v'\frac{\partial w'}{\partial y'}+w'\frac{\partial w'}{\partial z'}\right)=-\rho g\cos\theta_i-\frac{\partial p'}{\partial z'}+\frac{\partial \tau_{z'x'}}{\partial x'}+\frac{\partial \tau_{z'y'}}{\partial y'}+\frac{\partial \tau_{z'z'}}{\partial z'}, \tag{B.7}$$

Convert the dimensional variables into non-dimensional variables, where,

$$U_0=\frac{L_0}{T_0},\ P_0=\frac{\sigma\epsilon}{L_0},\ T_0=\left(\frac{L_0K}{\sigma\epsilon^{n+2}}\right)^{\frac{1}{n}},\ \epsilon=\frac{H_0}{L_0},\ \epsilon\ll 1,$$
$$u'=U_0u,\ v'=U_0v,\ w'=\epsilon U_0w,\ x'=L_0x,\ y'=L_0y,\ z'=H_0z. \tag{B.8}$$

The components of τ_{ij} are:

$$\tau_{x'x'}=2K\left(4D_{kl}D_{lk}\right)^{(n-1)/2}D_{x'x'}, \tag{B.9}$$

$$\tau_{x'y'}=2K\left(4D_{kl}D_{lk}\right)^{(n-1)/2}D_{x'y'}, \tag{B.10}$$

with analogous expressions for $\tau_{x'z'}$, $\tau_{y'x'}$, $\tau_{y'y'}$, $\tau_{y'z'}$, $\tau_{z'x'}$, $\tau_{z'y'}$ and $\tau_{z'z'}$. Using the scalings mentioned above, the dominant terms in the terms $D_{x'x'}$, $D_{x'y'}$, $D_{x'z'}$, $D_{y'y'}$, $D_{y'z'}$, $D_{z'z'}$ and $D_{kl}D_{lk}$ are,

$$\begin{aligned}
D_{x'x'}&=\frac{U_0}{L_0}\frac{\partial u}{\partial x},\\
D_{x'y'}&=D_{y'x'}=\frac{1}{2}\frac{U_0}{L_0}\left(\frac{\partial u}{\partial y}+\frac{\partial v}{\partial x}\right),\\
D_{x'z'}&=D_{z'x'}=\frac{1}{2}\left(\frac{U_0}{H_0}\frac{\partial u}{\partial z}+\frac{\epsilon U_0}{L_0}\frac{\partial w}{\partial x}\right),\\
D_{y'y'}&=\frac{U_0}{L_0}\frac{\partial v}{\partial y},\\
D_{y'z'}&=D_{z'y'}=\frac{1}{2}\left(\frac{U_0}{H_0}\frac{\partial v}{\partial z}+\frac{\epsilon U_0}{L_0}\frac{\partial w}{\partial y}\right),\\
D_{z'z'}&=\frac{\epsilon U_0}{H_0}\frac{\partial w}{\partial z},\\
D_{kl}D_{lk}&=\frac{1}{4}\frac{U_0^2}{H_0^2}\left(\frac{\partial u}{\partial z}\right)^2+\frac{1}{4}\frac{U_0^2}{H_0^2}\left(\frac{\partial v}{\partial z}\right)^2.
\end{aligned} \tag{B.11}$$

The dominant terms in the shear stress terms are only $\tau_{x'z'}$ and $\tau_{y'z'}$ which can be written as,

$$\begin{aligned}\tau_{x'z'} =& \frac{U_0^n}{H_0^n} K \left(\frac{\partial u}{\partial z}\right)^{n-1} \left(\frac{\partial u}{\partial z}\right) + \frac{U_0^n \epsilon}{L_0 H_0^{n-1}} K \left(\frac{\partial u}{\partial z}\right)^{n-1} \frac{\partial w}{\partial x}, \\ \tau_{y'z'} & \frac{U_0^n}{H_0^n} K \left(\frac{\partial v}{\partial z}\right)^{n-1} \left(\frac{\partial v}{\partial z}\right) + \frac{U_0^n \epsilon}{L_0 H_0^{n-1}} K \left(\frac{\partial v}{\partial z}\right)^{n-1} \frac{\partial w}{\partial y}. \end{aligned} \tag{B.12}$$

The shear stress terms $\tau_{x'x'}$, $\tau_{x'y'}$, $\tau_{y'x'}$, $\tau_{y'y'}$, $\tau_{z'x'}$, $\tau_{z'y'}$, and $\tau_{z'z'}$ are all negligible due to ϵ^2 terms in them. Consider the x-axis equation (B.5) and substitute the relevant expressions for τ_{ij} from equation (B.12) in it,

$$\begin{aligned}\rho \left[\frac{U_0}{T_0}\left(\frac{\partial u}{\partial t}\right) + \frac{U_0^2}{L_0}\left(u\frac{\partial u}{\partial x} + v\frac{\partial u}{\partial y} + w\frac{\partial u}{\partial z}\right)\right] &= \rho g \sin\theta_i - \frac{P_0}{L_0}\frac{\partial p}{\partial x} \\ &+ \frac{1}{H_0}\frac{\partial}{\partial z}\left(\frac{U_0^n}{H_0^n} K \left(\frac{\partial u}{\partial z}\right)^{n-1}\left(\frac{\partial u}{\partial z}\right) + \frac{U_0^n \epsilon}{L_0 H_0^{n-1}} K \left(\frac{\partial u}{\partial z}\right)^{n-1} \frac{\partial w}{\partial x}\right). \end{aligned} \tag{B.13}$$

Here $\frac{U_0^n}{L_0 H_0^{n-1}}$ is equal to $\frac{\sigma\epsilon^3}{K L_0}$ using the scalings mentioned above. It is also known through lubrication approximation that $\epsilon^2 = \frac{H_0^2}{L_0^2}$, $\epsilon^2 \ll 1$, which the reduces the equation to,

$$0 = \rho g \sin\theta_i - \frac{P_0}{L_0}\frac{\partial p}{\partial x} + \frac{1}{H_0}\frac{\partial}{\partial z}\left(\frac{U_0^n}{H_0^n} K \left(\frac{\partial u}{\partial z}\right)^{n-1}\left(\frac{\partial u}{\partial z}\right)\right), \tag{B.14}$$

which can be re-arranged as,

$$\frac{\partial}{\partial z}\left(\frac{\partial u}{\partial z}\right)^n = \left[\frac{T_0^n H_0^{n+1} P_0}{K L_0^{n+1}}\frac{\partial p}{\partial x} - \frac{\rho g H_0^{n+1} T_0^n}{L_0^n K}\sin\theta_i\right], \tag{B.15}$$

and $T_0 = \left(\frac{L_0 K}{\sigma\epsilon^{n+2}}\right)^{\frac{1}{n}}$, $P_0 = \frac{\sigma\epsilon}{L_0}$,

$$\frac{\partial}{\partial z}\left(\frac{\partial u}{\partial z}\right)^n = \left[\frac{L_0 K H_0^{n+1} P_0}{\sigma\epsilon^{n+2} K L_0^{n+1}}\frac{\partial p}{\partial x} - \frac{\rho g H_0^{n+1} T_0^n}{L_0^n K}\sin\theta_i\right], \tag{B.16}$$

and $\epsilon = \frac{H_0}{L_0}$,

$$\frac{\partial}{\partial z}\left(\frac{\partial u}{\partial z}\right)^n = \frac{\partial p}{\partial x} - \frac{\rho g L_0^2}{\sigma\epsilon}\sin\theta_i, \tag{B.17}$$

And Bond number, Bo is defined as, $Bo = \frac{\rho g L_0^2}{\sigma}$, so, ,

$$\frac{\partial}{\partial z}\left(\frac{\partial u}{\partial z}\right)^n = \frac{\partial p}{\partial x} - \frac{Bo\sin\theta_i}{\epsilon}. \tag{B.18}$$

Integrate the above equation with respect to "z",

$$\int \frac{\partial}{\partial z}\left(\frac{\partial u}{\partial z}\right)^{n} dz = \int \left(\frac{\partial p}{\partial x} - \frac{Bo\sin\theta_i}{\epsilon}\right) dz, \tag{B.19}$$

$$\left|\left(\frac{\partial u}{\partial z}\right)^{n}\right| = \left(\frac{\partial p}{\partial x} - \frac{Bo\sin\theta_i}{\epsilon}\right)|z + c_1|, \tag{B.20}$$

where c_1 is the constant of integration and at $z = h$, $c = -h$,

$$\left(\frac{\partial u}{\partial z}\right)^{n} = \left(\frac{Bo\sin\theta_i}{\epsilon} - \frac{\partial p}{\partial x}\right)(h - z). \tag{B.21}$$

Re-arranging gives,

$$\frac{\partial u}{\partial z} = \left(\left(\frac{Bo\sin\theta_i}{\epsilon} - \frac{\partial p}{\partial x}\right)(h - z)\right)^{\frac{1}{n}}. \tag{B.22}$$

Integrate again the above equation with respect to "z",

$$\int \frac{\partial u}{\partial z} dz = \left(\frac{Bo\sin\theta_i}{\epsilon} - \frac{\partial p}{\partial x}\right)^{\frac{1}{n}} \int (h - z)^{\frac{1}{n}} dz, \tag{B.23}$$

$$u|_0^u = \left(\frac{Bo\sin\theta_i}{\epsilon} - \frac{\partial p}{\partial x}\right)^{\frac{1}{n}} \left(\frac{n}{n+1}\right)\left|\left[-(h - z)^{(\frac{n+1}{n})} + c_2\right]\right|, \tag{B.24}$$

where c_2 is the constant of integration and at $z = 0$, $u = 0$,

$$c_2 = (h)^{(\frac{n+1}{n})}. \tag{B.25}$$

So the velocity, u in the x-direction is given as,

$$u = \left(\frac{Bo\sin\theta_i}{\epsilon} - \frac{\partial p}{\partial x}\right)^{\frac{1}{n}} \left(\frac{n}{n+1}\right)\left[h^{(\frac{n+1}{n})} - (h - z)^{(\frac{n+1}{n})}\right]. \tag{B.26}$$

The flux in x-direction is given by,

$$Q_x = \int u dz. \tag{B.27}$$

Substitute u in the Q_x,

$$Q_x = \int \left(\frac{Bo\sin\theta_i}{\epsilon} - \frac{\partial p}{\partial x}\right)^{\frac{1}{n}} \left(\frac{n}{n+1}\right)\left[h^{(\frac{n+1}{n})} - (h - z)^{(\frac{n+1}{n})}\right] dz. \tag{B.28}$$

Performing the integration in the above equation gives,

$$Q_x = \left(\frac{Bo\sin\theta_i}{\epsilon} - \frac{\partial p}{\partial x}\right)^{\frac{1}{n}} \left(\frac{n}{n+1}\right) \left|\left[h^{(\frac{n+1}{n})}z + (\frac{n}{2n+1})(h-z)^{(\frac{2n+1}{n})} + c_3\right]\right|. \tag{B.29}$$

where c_3 is the constant of integration and for $z = 0$, $Q_x = 0$,

$$c_3 = -\frac{n}{2n+1}(h)^{(\frac{2n+1}{n})}. \tag{B.30}$$

Substitute c_3 back in the Q_x term,

$$Q_x = \left(\frac{Bo\sin\theta_i}{\epsilon} - \frac{\partial p}{\partial x}\right)^{\frac{1}{n}} \left(\frac{n}{n+1}\right) \left[h^{(\frac{n+1}{n})}z + (\frac{n}{2n+1})(h-z)^{(\frac{2n+1}{n})} - \frac{n}{2n+1}(h)^{(\frac{2n+1}{n})}\right], \tag{B.31}$$

at $z = h$, the Q_x is given as,

$$Q_x = \left(\frac{Bo\sin\theta_i}{\epsilon} - \frac{\partial p}{\partial x}\right)^{\frac{1}{n}} \left(\frac{n}{2n+1}\right) h^{(\frac{2n+1}{n})}, \tag{B.32}$$

Now consider the y-axis equation (B.6) and substitute the relevant expressions for τ_{ij} from equation (B.12) in it,

$$\rho\left[\frac{U_0}{T_0}\left(\frac{\partial v}{\partial t}\right) + \frac{U_0^2}{L_0}\left(u\frac{\partial v}{\partial x}\right) + \frac{U_0^2}{L_0}\left(v\frac{\partial v}{\partial y}\right) + \frac{\epsilon U_0^2}{H_0}\left(w\frac{\partial v}{\partial z}\right)\right] = -\frac{P_0}{L_0}\frac{\partial p}{\partial y} + \\ + \frac{1}{H_0}\frac{\partial}{\partial z}\left(\frac{U_0^n}{H_0^n}K\left(\frac{\partial v}{\partial z}\right)^{n-1}\left(\frac{\partial v}{\partial z}\right) + \frac{U_0^n\epsilon}{L_0H_0^{n-1}}K\left(\frac{\partial v}{\partial z}\right)^{n-1}\frac{\partial w}{\partial y}\right). \tag{B.33}$$

Here $\frac{U_0^n}{L_0H_0^{n-1}}$ is equal to $\frac{\sigma\epsilon^3}{KL_0}$ using the scalings mentioned above. It is also known through lubrication approximation that $\epsilon^2 = \frac{H_0^2}{L_0^2}$, $\epsilon^2 \ll 1$, which the reduces the equation to,

$$0 = -\frac{P_0}{L_0}\frac{\partial p}{\partial y} + \frac{1}{H_0}\frac{\partial}{\partial z}\left(\frac{U_0^n}{H_0^n}K\left(\frac{\partial v}{\partial z}\right)^{n-1}\left(\frac{\partial v}{\partial z}\right)\right), \tag{B.34}$$

which can be re-arranged as,

$$\frac{\partial}{\partial z}\left(\frac{\partial v}{\partial z}\right)^n = \frac{\partial p}{\partial y}. \tag{B.35}$$

Integrate the above equation with respect to "z",

$$\int \frac{\partial}{\partial z}\left(\frac{\partial v}{\partial z}\right)^n dz = \int \left(\frac{\partial p}{\partial y}\right) dz, \tag{B.36}$$

$$\left|\left(\frac{\partial v}{\partial z}\right)^n\right| = \left(\frac{\partial p}{\partial y}\right)|z + c_1|\,, \tag{B.37}$$

where c_1 is the constant of integration and at $z = h,\ c_1 = -h$,

$$\frac{\partial v}{\partial z} = \left(\left(-\frac{\partial p}{\partial y}\right)(h - z)\right)^{\frac{1}{n}}. \tag{B.38}$$

Integrate again the above equation with respect to "z",

$$\int \frac{\partial v}{\partial z} dz = \left(-\frac{\partial p}{\partial y}\right)^{\frac{1}{n}} \int (h - z)^{\frac{1}{n}} dz, \tag{B.39}$$

$$v| = \left(-\frac{\partial p}{\partial y}\right)^{\frac{1}{n}} \left(\frac{n}{n+1}\right) \left|\left[-(h - z)^{(\frac{n+1}{n})} + c_2\right]\right|, \tag{B.40}$$

where c_2 is the constant of integration and at $z = 0,\ v = 0$,

$$c_2 = (h)^{(\frac{n+1}{n})}. \tag{B.41}$$

Then the velocity, v, in the y-direction is given by,

$$v = \left(-\frac{\partial p}{\partial y}\right)^{\frac{1}{n}} \left(\frac{n}{n+1}\right) \left[h^{(\frac{n+1}{n})} - (h - z)^{(\frac{n+1}{n})}\right]. \tag{B.42}$$

The flux in y-direction is given by,

$$Q_y = \int v dz. \tag{B.43}$$

Substituting v in the flux equation gives,

$$Q_y = \int \left(-\frac{\partial p}{\partial y}\right)^{\frac{1}{n}} \left(\frac{n}{n+1}\right) \left[h^{(\frac{n+1}{n})} - (h - z)^{(\frac{n+1}{n})}\right] dz, \tag{B.44}$$

Performing the integration in the above equation gives,

$$Q_y = \left(-\frac{\partial p}{\partial y}\right)^{\frac{1}{n}} \left(\frac{n}{n+1}\right) \left|\left[h^{(\frac{n+1}{n})} z + (\frac{n}{2n+1})(h - z)^{(\frac{2n+1}{n})} + c_3\right]\right|. \tag{B.45}$$

where c_3 is the constant of integration and for $z = 0,\ Q_y = 0$,

$$c_3 = -\frac{n}{2n+1}(h)^{(\frac{2n+1}{n})}. \tag{B.46}$$

Then flux in y-direction is given as,

$$Q_y = \left(-\frac{\partial p}{\partial y}\right)^{\frac{1}{n}} \left(\frac{n}{n+1}\right) \left[h^{(\frac{n+1}{n})} z + (\frac{n}{2n+1})(h-z)^{(\frac{2n+1}{n})} - \frac{n}{2n+1}(h)^{(\frac{2n+1}{n})}\right]. \quad \text{(B.47)}$$

At $z = h$, the Q_y is given as,

$$Q_y = \left(-\frac{\partial p}{\partial y}\right)^{\frac{1}{n}} \left(\frac{n}{n+1}\right) \left[h^{(\frac{2n+1}{n})} \left(\frac{n+1}{2n+1}\right) + (\frac{n}{2n+1})(0)^{(\frac{2n+1}{n})}\right], \quad \text{(B.48)}$$

$$Q_y = \left(-\frac{\partial p}{\partial y}\right)^{\frac{1}{n}} \left(\frac{n}{2n+1}\right) h^{(\frac{2n+1}{n})}. \quad \text{(B.49)}$$

The basic lubrication equation in 3D is given by,

$$\frac{\partial h}{\partial t} + \frac{\partial Q_x}{\partial x} + \frac{\partial Q_y}{\partial y} = 0. \quad \text{(B.50)}$$

Let $\lambda = \frac{1}{n}$,

$$\frac{\partial h}{\partial t} = -\frac{1}{\lambda+2}\left[\frac{\partial}{\partial x}\left(h^{(\lambda+2)}\left(\frac{Bo\sin\theta_i}{\epsilon} - \frac{\partial p}{\partial x}\right)^{\lambda}\right) + \frac{\partial}{\partial y}\left(h^{(\lambda+2)}\left(-\frac{\partial p}{\partial y}\right)^{\lambda}\right)\right]. \quad \text{(B.51)}$$

Let $C_1 = \frac{Bo\sin\theta}{\epsilon}$,

$$\frac{\partial h}{\partial t} = -\left[\frac{\partial}{\partial x}\left(\frac{h^{\lambda+2}}{\lambda+2}\left(C_1 - \frac{\partial p}{\partial x}\right)^{\lambda}\right) + \frac{\partial}{\partial y}\left(\frac{h^{\lambda+2}}{\lambda+2}\left(-\frac{\partial p}{\partial y}\right)^{\lambda}\right)\right]. \quad \text{(B.52)}$$

Spatial discretization in the x-axis only is given as,

$$= \frac{1}{\Delta x}\left[\frac{h_{i+\frac{1}{2}}^{\lambda+2}}{\lambda+2}\left(C_1 - \frac{\partial p_{i+\frac{1}{2}}}{\partial x}\right)^{\lambda} - \frac{h_{i-\frac{1}{2}}^{\lambda+2}}{\lambda+2}\left(C_1 - \frac{\partial p_{i-\frac{1}{2}}}{\partial x}\right)^{\lambda}\right]. \quad \text{(B.53)}$$

$\frac{\partial p_{i+\frac{1}{2}}}{\partial x}$ and $\frac{\partial p_{i-\frac{1}{2}}}{\partial x}$ after spatial discretization can be written as,

$$= \frac{1}{\Delta x}\left[\frac{h_{i+\frac{1}{2}}^{\lambda+2}}{\lambda+2}\left(C_1 - \frac{p_{i+1} - p_i}{\Delta x}\right)^{\lambda} - \frac{h_{i-\frac{1}{2}}^{\lambda+2}}{\lambda+2}\left(C_1 - \frac{p_i - p_{i-1}}{\Delta x}\right)^{\lambda}\right], \quad \text{(B.54)}$$

where by interpolation, $h_{i+\frac{1}{2}}^{\lambda+2} = \frac{h_{i+1}^{\lambda+2}+h_i^{\lambda+2}}{2}$ and $h_{i-\frac{1}{2}}^{\lambda+2} = \frac{h_{i-1}^{\lambda+2}+h_i^{\lambda+2}}{2}$,

$$= \frac{1}{\Delta x}\left[\left(\frac{h_{i+1}^{\lambda+2}+h_i^{\lambda+2}}{2(\lambda+2)}\right)\left(C_1 - \frac{p_{i+1}-p_i}{\Delta x}\right)^{\lambda} - \left(\frac{h_{i-1}^{\lambda+2}+h_i^{\lambda+2}}{2(\lambda+2)}\right)\left(C_1 - \frac{p_i - p_{i-1}}{\Delta x}\right)^{\lambda}\right]. \tag{B.55}$$

Spatial discretization in the y-axis only is given as,

$$= \frac{1}{\Delta y}\left[\frac{h_{j+\frac{1}{2}}^{\lambda+2}}{\lambda+2}\left(-\frac{\partial p_{j+\frac{1}{2}}}{\partial y}\right)^{\lambda} - \frac{h_{j-\frac{1}{2}}^{\lambda+2}}{\lambda+2}\left(-\frac{\partial p_{j-\frac{1}{2}}}{\partial y}\right)^{\lambda}\right]. \tag{B.56}$$

$\frac{\partial p_{j+\frac{1}{2}}}{\partial y}$ and $\frac{\partial p_{j-\frac{1}{2}}}{\partial y}$ after spatial discretization can be written as,

$$= \frac{1}{\Delta y}\left[\frac{h_{j+\frac{1}{2}}^{\lambda+2}}{\lambda+2}\left(-\frac{p_{j+1}-p_j}{\Delta y}\right)^{\lambda} - \frac{h_{j-\frac{1}{2}}^{\lambda+2}}{\lambda+2}\left(-\frac{p_j - p_{j-1}}{\Delta y}\right)^{\lambda}\right], \tag{B.57}$$

where by interpolation, $h_{j+\frac{1}{2}}^{\lambda+2} = \frac{h_{j+1}^{\lambda+2}+h_j^{\lambda+2}}{2}$ and $h_{j-\frac{1}{2}}^{\lambda+2} = \frac{h_{j-1}^{\lambda+2}+h_j^{\lambda+2}}{2}$,

$$= \frac{1}{\Delta y}\left[\left(\frac{h_{j+1}^{\lambda+2}+h_j^{\lambda+2}}{2(\lambda+2)}\right)\left(\frac{p_j - p_{j+1}}{\Delta y}\right)^{\lambda} - \left(\frac{h_{j-1}^{\lambda+2}+h_j^{\lambda+2}}{2(\lambda+2)}\right)\left(\frac{p_{j-1}-p_j}{\Delta y}\right)^{\lambda}\right]. \tag{B.58}$$

Combining the x and y-axis spatial discretizations,

$$\frac{\partial h_{ij}}{\partial t} = -\frac{1}{\Delta x}\left\{\left(\frac{h_{i+1j}^{\lambda+2}+h_{ij}^{\lambda+2}}{2(\lambda+2)}\right)\left(C_1 - \frac{p_{i+1j}-p_{ij}}{\Delta x}\right)^{\lambda} - \left(\frac{h_{i-1j}^{\lambda+2}+h_{ij}^{\lambda+2}}{2(\lambda+2)}\right)\left(C_1 - \frac{p_{ij}-p_{i-1j}}{\Delta x}\right)^{\lambda}\right\}$$
$$\underbrace{-\frac{1}{\Delta y}\left\{\left(\frac{h_{ij+1}^{\lambda+2}+h_{ij}^{\lambda+2}}{2(\lambda+2)}\right)\left(\frac{p_{ij}-p_{ij+1}}{\Delta y}\right)^{\lambda} - \left(\frac{h_{ij-1}^{\lambda+2}+h_{ij}^{\lambda+2}}{2(\lambda+2)}\right)\left(\frac{p_{ij-1}-p_{ij}}{\Delta y}\right)^{\lambda}\right\}}_{\mathcal{F}_h^{n_t}}. \tag{B.59}$$

The right-hand side of the equation (B.59) may be represented as $\mathcal{F}_h^{n_t}$, i.e. $\frac{\partial h_{ij}}{\partial t} = \mathcal{F}_h^{n_t}$. Using the Crank-Nicolson scheme yields,

$$\frac{h_{ij}^{n_t+1} - h_{ij}^{n_t}}{\triangle t} = \frac{1}{2}\left[\mathcal{F}_h^{n_t+1} + \mathcal{F}_h^{n_t}\right]. \tag{B.60}$$

Re-arranging equation (B.60) gives,

$$\underbrace{h_{ij}^{n_t+1} - \frac{\Delta t}{2}\left[\mathcal{F}_h^{n_t+1}\right]}_{\mathcal{L}_k^h} = h_{ij}^{n_t} + \frac{\Delta t}{2}\left[\mathcal{F}_h^{n_t}\right]. \tag{B.61}$$

Now, consider the z-axis equation (B.7) and substitute the relevant expressions for τ_{ij} from equation (B.12) in it,

$$\rho\left(\frac{\epsilon U_0}{T_0}\frac{\partial w}{\partial t}+\frac{\epsilon U_0^2}{L_0}u\frac{\partial w}{\partial x}+\frac{\epsilon U_0^2}{L_0}v\frac{\partial w}{\partial y}+\frac{\epsilon^2 U_0^2}{H_0}w\frac{\partial w}{\partial z}\right) \quad = \quad -\rho g\cos\theta_i \quad - \quad \frac{P_0}{H_0}\frac{\partial p}{\partial z}. \tag{B.62}$$

Applying the lubrication approximation assumption reduces the equation to,

$$\frac{P_0}{H_0}\frac{\partial p}{\partial z}=\rho g\cos\theta_i, \tag{B.63}$$

which can be re-arranged as,

$$\frac{\partial p}{\partial z}=Bo\cos\theta_i. \tag{B.64}$$

It is known that the boundary condition for pressure at the droplet surface is,

$$p=-\nabla^2 h-\Pi(h) \quad \text{on} \quad z=h, \tag{B.65}$$

where $\Pi(h)$ is the disjoining pressure term for sliding droplets. Integrate equation (B.64) with respect to z and setting the integration constant using equation (B.65) yields the pressure field throughout the film,

$$p=-\nabla^2(h)-\Pi(h)+Bo\cos\theta_i\,(h)\,. \tag{B.66}$$

Spatial discretization of p is given by,

$$\begin{aligned} p_{ij}+\left(\frac{h_{i+1j}+h_{i-1j}-2h_{ij}}{\triangle x^2}\right)+\left(\frac{h_{ij+1}+h_{ij-1}-2h_{ij}}{\triangle y^2}\right) \\ +\frac{(1-cos\theta_e)\,(n_d-1)\,(m_d-1)}{\epsilon^2 h^*(n_d-m_d)}\left[\left(\frac{h^*}{h_{ij}}\right)^{n_d}-\left(\frac{h^*}{h_{ij}}\right)^{m_d}\right]-Bo\cos\theta_i(h_{ij})=\mathcal{L}_k^p, \end{aligned} \tag{B.67}$$

then,

$$\mathcal{L}_k^h\left(h_k^{n_t+1},p_k^{n_t+1}\right)=f_k^h\left(h_k^{n_t},p_k^{n_t}\right), \tag{B.68}$$

$$\mathcal{L}_k^p\left(h_k^{n_t+1},p_k^{n_t+1}\right)=f_k^p\left(h_k^{n_t},p_k^{n_t}\right). \tag{B.69}$$

Then the Jacobian, J is represented as,

$$J=\frac{\partial\left(\mathcal{L}_k^h,\mathcal{L}_k^p\right)}{\partial\left(h_k^{n_t+1},p_k^{n_t+1}\right)}, \tag{B.70}$$

Initial guess to the solution is given by $\left(h_{0k}^{n_t+1}, p_{0k}^{n_t+1}\right)$, the Newton iteration proceeds by solving,

$$J\begin{pmatrix}\Delta h\\ \Delta p\end{pmatrix} = \begin{pmatrix} f_k^h - \mathcal{L}_k^h(h_{0k}^{n_t+1}, p_{0k}^{n_t+1}) \\ f_k^p - \mathcal{L}_k^p(h_{0k}^{n_t+1}, p_{0k}^{n_t+1})\end{pmatrix}. \tag{B.71}$$

The terms of the Jacobian are given as,

$$\begin{aligned}\frac{\partial \mathcal{L}_k^h}{\partial h_{ij}} = &-\frac{1}{\Delta x}\left(\frac{h_{ij}^{\lambda+1}}{2}\right)\left(C_1 - \frac{p_{i+1j}-p_{ij}}{\Delta x}\right)^{\lambda} \\ &+\frac{1}{\Delta x}\left(\frac{h_{ij}^{\lambda+1}}{2}\right)\left(C_1 - \frac{p_{ij}-p_{i-1j}}{\Delta x}\right)^{\lambda} \\ &-\frac{1}{\Delta y}\left(\frac{h_{ij}^{\lambda+1}}{2}\right)\left(\frac{p_{ij}-p_{ij+1}}{\Delta y}\right)^{\lambda} \\ &+\frac{1}{\Delta y}\left(\frac{h_{ij}^{\lambda+1}}{2}\right)\left(\frac{p_{ij-1}-p_{ij}}{\Delta y}\right)^{\lambda},\end{aligned} \tag{B.72}$$

$$\begin{aligned}\frac{\partial \mathcal{L}_k^h}{\partial p_{ij}} = &-\frac{\lambda}{(\Delta x)^2}\left(\frac{h_{i+1j}^{\lambda+2}+h_{ij}^{\lambda+2}}{2(\lambda+2)}\right)\left(C_1 - \frac{p_{i+1j}-p_{ij}}{\Delta x}\right)^{\lambda-1} \\ &-\frac{\lambda}{(\Delta x)^2}\left(\frac{h_{i-1j}^{\lambda+2}+h_{ij}^{\lambda+2}}{2(\lambda+2)}\right)\left(C_1 - \frac{p_{ij}-p_{i-1j}}{\Delta x}\right)^{\lambda-1} \\ &-\frac{\lambda}{(\Delta y)^2}\left(\frac{h_{ij+1}^{\lambda+2}+h_{ij}^{\lambda+2}}{2(\lambda+2)}\right)\left(\frac{p_{ij}-p_{ij+1}}{\Delta y}\right)^{\lambda-1} \\ &-\frac{\lambda}{(\Delta y)^2}\left(\frac{h_{ij-1}^{\lambda+2}+h_{ij}^{\lambda+2}}{2(\lambda+2)}\right)\left(\frac{p_{ij-1}-p_{ij}}{\Delta y}\right)^{\lambda-1}.\end{aligned} \tag{B.73}$$

The equations (B.61), and (B.67) are applied the numerical code. The problem lies when terms $\left(C_1 - \frac{p_{ij}-p_{i-1j}}{\Delta x}\right)$ becomes negative. This causes a singularity. To avoid this signum function is introduced such that,

$$\text{sign}_{\text{E}} = \begin{cases} -1 & \text{if } \left(C_1 - \frac{p_{i+1j}-p_{ij}}{\Delta x}\right) < 0, \\ 0 & \text{if } \left(C_1 - \frac{p_{i+1j}-p_{ij}}{\Delta x}\right) = 0, \\ 1 & \text{if } \left(C_1 - \frac{p_{i+1j}-p_{ij}}{\Delta x}\right) > 0. \end{cases}$$

$$\text{sign}_{\text{W}} = \begin{cases} -1 & \text{if } \left(C_1 - \frac{p_{ij}-p_{i-1j}}{\Delta x}\right) < 0, \\ 0 & \text{if } \left(C_1 - \frac{p_{ij}-p_{i-1j}}{\Delta x}\right) = 0, \\ 1 & \text{if } \left(C_1 - \frac{p_{ij}-p_{i-1j}}{\Delta x}\right) > 0. \end{cases}$$

$$\text{sign}_{\text{N}} = \begin{cases} -1 & \text{if } \left(\frac{p_{ij}-p_{ij+1}}{\Delta y}\right) < 0, \\ 0 & \text{if } \left(\frac{p_{ij}-p_{ij+1}}{\Delta y}\right) = 0, \\ 1 & \text{if } \left(\frac{p_{ij}-p_{ij+1}}{\Delta y}\right) > 0. \end{cases}$$

$$\text{sign}_{\text{S}} = \begin{cases} -1 & \text{if } \left(\frac{p_{ij-1}-p_{ij}}{\Delta y}\right) < 0, \\ 0 & \text{if } \left(\frac{p_{ij-1}-p_{ij}}{\Delta y}\right) = 0, \\ 1 & \text{if } \left(\frac{p_{ij-1}-p_{ij}}{\Delta y}\right) > 0. \end{cases}$$

After the introduction of signum function in the code equation (B.59) can be written as,

$$\frac{\partial h_{ij}}{\partial t} = -\frac{1}{\Delta x}\left\{\left(\frac{h_{i+1j}^{\lambda+2}+h_{ij}^{\lambda+2}}{2(\lambda+2)}\right)\text{sign}_{\text{E}}\left|C_1-\frac{p_{i+1j}-p_{ij}}{\Delta x}\right|^{\lambda}-\left(\frac{h_{i-1j}^{\lambda+2}+h_{ij}^{\lambda+2}}{2(\lambda+2)}\right)\text{sign}_{\text{W}}\left|C_1-\frac{p_{ij}-p_{i-1j}}{\Delta x}\right|^{\lambda}\right\} \underbrace{-\frac{1}{\Delta y}\left\{\left(\frac{h_{ij+1}^{\lambda+2}+h_{ij}^{\lambda+2}}{2(\lambda+2)}\right)\text{sign}_{\text{N}}\left|\frac{p_{ij}-p_{ij+1}}{\Delta y}\right|^{\lambda}-\left(\frac{h_{ij-1}^{\lambda+2}+h_{ij}^{\lambda+2}}{2(\lambda+2)}\right)\text{sign}_{\text{S}}\left|\frac{p_{ij-1}-p_{ij}}{\Delta y}\right|^{\lambda}\right\}}_{\mathcal{F}_h^{nt}}, \tag{B.74}$$

and equation (B.72) can be written as,

$$\begin{aligned}\frac{\partial \mathcal{L}_k^h}{\partial h_{ij}} = &-\frac{1}{\Delta x}\left(\frac{h_{ij}^{\lambda+1}}{2}\right)\text{sign}_{\text{E}}\left|C_1-\frac{p_{i+1j}-p_{ij}}{\Delta x}\right|^{\lambda} \\ &+\frac{1}{\Delta x}\left(\frac{h_{ij}^{\lambda+1}}{2}\right)\text{sign}_{\text{W}}\left|C_1-\frac{p_{ij}-p_{i-1j}}{\Delta x}\right|^{\lambda} \\ &-\frac{1}{\Delta y}\left(\frac{h_{ij}^{\lambda+1}}{2}\right)\text{sign}_{\text{N}}\left|\frac{p_{ij}-p_{ij+1}}{\Delta y}\right|^{\lambda} \\ &+\frac{1}{\Delta y}\left(\frac{h_{ij}^{\lambda+1}}{2}\right)\text{sign}_{\text{S}}\left|\frac{p_{ij-1}-p_{ij}}{\Delta y}\right|^{\lambda},\end{aligned} \tag{B.75}$$

and equation (B.73) can be written as,

$$\begin{aligned}\frac{\partial \mathcal{L}_k^h}{\partial p_{ij}} = &-\frac{\lambda}{(\Delta x)^2}\left(\frac{h_{i+1j}^{\lambda+2}+h_{ij}^{\lambda+2}}{2(\lambda+2)}\right)\left|C_1-\frac{p_{i+1j}-p_{ij}}{\Delta x}\right|^{\lambda-1} \\ &-\frac{\lambda}{(\Delta x)^2}\left(\frac{h_{i-1j}^{\lambda+2}+h_{ij}^{\lambda+2}}{2(\lambda+2)}\right)\left|C_1-\frac{p_{ij}-p_{i-1j}}{\Delta x}\right|^{\lambda-1} \\ &-\frac{\lambda}{(\Delta y)^2}\left(\frac{h_{ij+1}^{\lambda+2}+h_{ij}^{\lambda+2}}{2(\lambda+2)}\right)\left|\frac{p_{ij}-p_{ij+1}}{\Delta y}\right|^{\lambda-1} \\ &-\frac{\lambda}{(\Delta y)^2}\left(\frac{h_{ij-1}^{\lambda+2}+h_{ij}^{\lambda+2}}{2(\lambda+2)}\right)\left|\frac{p_{ij-1}-p_{ij}}{\Delta y}\right|^{\lambda-1},\end{aligned} \tag{B.76}$$

The Jacobian terms are calculated from equation (B.67),

$$\frac{\partial \mathcal{L}_k^p}{\partial p_{ij}} = 1 = D, \tag{B.77}$$

$$\begin{aligned}\frac{\partial \mathcal{L}_k^p}{\partial h_{ij}} = &\left(\frac{-2h_{ij}}{\triangle x^2}\right) + \left(\frac{-2h_{ij}}{\triangle y^2}\right) + \\ &\frac{(1-\cos\theta_e)\,(n-1)\,(m-1)}{\epsilon^2 h^*(n-m)}\left[\frac{m}{h_{ij}}\left(\frac{h^*}{h_{ij}}\right)^m - \frac{n}{h_{ij}}\left(\frac{h^*}{h_{ij}}\right)^m\right] - Bo\cos\theta_i = C,\end{aligned} \tag{B.78}$$

and from equation (A.53),

$$\begin{aligned}\frac{\partial \mathcal{L}_k^h}{\partial p_{ij}} = &-\frac{\lambda}{(\Delta x)^2}\left(\frac{h_{i+1j}^{\lambda+2} + h_{ij}^{\lambda+2}}{2(\lambda+2)}\right)\left|C_1 - \frac{p_{i+1j} - p_{ij}}{\Delta x}\right|^{\lambda-1} \\ &-\frac{\lambda}{(\Delta x)^2}\left(\frac{h_{i-1j}^{\lambda+2} + h_{ij}^{\lambda+2}}{2(\lambda+2)}\right)\left|C_1 - \frac{p_{ij} - p_{i-1j}}{\Delta x}\right|^{\lambda-1} \\ &-\frac{\lambda}{(\Delta y)^2}\left(\frac{h_{ij+1}^{\lambda+2} + h_{ij}^{\lambda+2}}{2(\lambda+2)}\right)\left|\frac{p_{ij} - p_{ij+1}}{\Delta y}\right|^{\lambda-1} \\ &-\frac{\lambda}{(\Delta y)^2}\left(\frac{h_{ij-1}^{\lambda+2} + h_{ij}^{\lambda+2}}{2(\lambda+2)}\right)\left|\frac{p_{ij-1} - p_{ij}}{\Delta y}\right|^{\lambda-1} = B,\end{aligned} \tag{B.79}$$

$$\begin{aligned}\frac{\partial \mathcal{L}_k^h}{\partial h_{ij}} = &-\frac{1}{\Delta x}\left(\frac{h_{ij}^{\lambda+1}}{2}\right)\mathrm{sign_E}\left|C_1 - \frac{p_{i+1j} - p_{ij}}{\Delta x}\right|^{\lambda} \\ &+\frac{1}{\Delta x}\left(\frac{h_{ij}^{\lambda+1}}{2}\right)\mathrm{sign_W}\left|C_1 - \frac{p_{ij} - p_{i-1j}}{\Delta x}\right|^{\lambda} \\ &-\frac{1}{\Delta y}\left(\frac{h_{ij}^{\lambda+1}}{2}\right)\mathrm{sign_N}\left|\frac{p_{ij} - p_{ij+1}}{\Delta y}\right|^{\lambda} \\ &+\frac{1}{\Delta y}\left(\frac{h_{ij}^{\lambda+1}}{2}\right)\mathrm{sign_S}\left|\frac{p_{ij-1} - p_{ij}}{\Delta y}\right|^{\lambda} = A,\end{aligned} \tag{B.80}$$

Equation (B.71) can be expanded,

$$\frac{\partial \mathcal{L}_k^h}{\partial h_{ij}}\Delta h + \frac{\partial \mathcal{L}_k^h}{\partial p_{ij}}\Delta p = f_k^h - \mathcal{L}_k^h\left(h_k^{n_t}, p_k^{n_t}\right), \tag{B.81}$$

$$\frac{\partial \mathcal{L}_k^p}{\partial h_{ij}}\Delta h + \frac{\partial \mathcal{L}_k^p}{\partial p_{ij}}\Delta p = f_k^p - \mathcal{L}_k^p\left(h_k^{n_t}, p_k^{n_t}\right). \tag{B.82}$$

To avoid repetition the Jacobian and the rest of the calculations are same as described in Appendix A.

Appendix C

Derivation of the governing equations for Absorption Dynamics

Mass and momentum balance equations along with boundary conditions and scalings mentioned in Chapter 7 reduce the governing equations to a partial differential equation for the height of the droplet which can be written in dimensionless form, h, as,

$$\frac{\partial h}{\partial t} = -\left[\frac{\partial}{\partial x}\left(\frac{h^3}{3}\left(\frac{Bo\sin\theta_i}{\epsilon} - \frac{\partial p}{\partial x}\right)\right) + \frac{\partial}{\partial y}\left(\frac{h^3}{3}\left(-\frac{\partial p}{\partial y}\right)\right)\right] + w_p, \tag{C.1}$$

which is dependent on the sink term, w_p, which describes the mass lost in the porous substrate due to capillary suction. The kinematic boundary condition in the porous medium gives the rate of change of fluid penetration depth, h_p,

$$\phi\frac{\partial h_p}{\partial t} + u_p\frac{\partial h_p}{\partial x} + v_p\frac{\partial h_p}{\partial y} + w_p = 0. \tag{C.2}$$

Let $C_1 = \frac{Bo\sin\theta_i}{\epsilon}$. Pressure gradients in x and y are negligible which reduces the above equation to,

$$\phi\frac{\partial h_p}{\partial t} + w_p = 0, \tag{C.3}$$

that can be simplified to,

$$\frac{\partial h_p}{\partial t} = -\frac{w_p}{\phi}. \tag{C.4}$$

p_p is the pressure in the porous medium which is equal to the capillary pressure, $p_p = -p_c$

where by Darcy's Law,

$$w_p = -\frac{k_p}{\mu}\left(\frac{\partial p_p}{\partial z} + \rho g \cos\theta_i\right). \tag{C.5}$$

It is known that $\frac{\partial w_p}{\partial z} = 0$. Substitute w_p,

$$\frac{\partial}{\partial z}\left(-\frac{k_p}{\mu}\left(\frac{\partial p_p}{\partial z} + \rho g \cos\theta_i\right)\right) = 0. \tag{C.6}$$

Integrate with respect to z,

$$-\frac{k_p}{\mu}\left(\frac{\partial p_p}{\partial z} + \rho g \cos\theta_i\right) = K_1, \tag{C.7}$$

where K_1 is the constant of integration,

$$\frac{\partial p_p}{\partial z} = -\frac{K_1 \mu}{k_p} - \rho g \cos\theta_i. \tag{C.8}$$

Integrate again with respect to z,

$$p_p = \left(-\frac{K_1 \mu}{k_p} - \rho g \cos\theta_i\right) z + K_2, \tag{C.9}$$

where K_2 is the constant of integration. The boundary conditions for the pressure in the porous medium,

$$p_p(z = 0) = p, \tag{C.10}$$

where $p = -\nabla^2(h) - \Pi(h)$. Evaluating the constants of integration, $K_2 = p$,

$$p_p = \left(-\frac{K_1 \mu}{k_p} - \rho g \cos\theta_i\right) z + p. \tag{C.11}$$

But $p_p(z = -h_p) = -p_c$,

$$-p_c = \left(\frac{K_1 \mu}{k_p} + \rho g \cos\theta_i\right) h_p + p. \tag{C.12}$$

Re-arranging gives,

$$K_1 = -\frac{k_p}{\mu}\left(\frac{p_c + p}{h_p} + \rho g \cos\theta_i\right). \tag{C.13}$$

So p_p is given as,

$$p_p = \left(\frac{p_c + p}{h_p}\right) z + p. \tag{C.14}$$

Then w_p is,

$$w_p = -\frac{k_p}{\mu}\left(\frac{p_c + p}{h_p} + \rho g \cos\theta_i\right). \tag{C.15}$$

Scalings and non-dimensional constants are,

$$T_0 = \frac{L_o \mu}{\sigma \epsilon^3}, \quad Pm = \frac{k_p L_0^2}{H_0^4}, \quad Su = \frac{p_c L_0^2}{\sigma H_0}, \quad Bo = \frac{\rho g L_0^2}{\sigma}. \tag{C.16}$$

Equation (C.4) can be written as,

$$w_p = -\phi \frac{\partial h_p}{\partial t}. \tag{C.17}$$

Substitute w_p from equation (C.15) in the above equation,

$$\frac{\partial h_p}{\partial t} = \frac{k_p}{\phi}\frac{L_0^2}{H_0^4}\left(\frac{L_0^2}{\sigma}\frac{p_c + p}{h_p} + \frac{\rho g L_0^2}{\sigma}\cos\theta_i\right). \tag{C.18}$$

Simplifying gives,

$$\frac{\partial h_p}{\partial t} = \frac{Pm}{\phi}\left(\frac{Su + p}{h_p} + Bo\cos\theta_i\right). \tag{C.19}$$

Discretize the above equation in x and y,

$$\frac{\partial h_{p\,ij}}{\partial t} = \underbrace{\frac{Pm}{\phi}\left(Bo\cos\theta_i + \frac{Su + p_{ij}}{h_{p\,ij}}\right)}_{\mathcal{F}_{h_p}^{n_t}}. \tag{C.20}$$

Using the Crank-Nicolson scheme gives,

$$\frac{h_{p\,ij}^{n_t+1} - h_{p\,ij}^{n_t}}{\triangle t} = \frac{1}{2}\left[\mathcal{F}_{h_p}^{n_t+1} + \mathcal{F}_{h_p}^{n_t}\right], \tag{C.21}$$

where $\triangle t = \left(t^{n_t+1} - t^{n_t}\right)$. Substitute $\mathcal{F}_{h_p}^{n_t}$ in (C.21) gives,

$$h_{p\,ij}^{n_t+1} - h_{p\,ij}^{n_t} = \frac{\triangle t}{2}\left[\left(\frac{Pm}{\phi}\left(\frac{Su + p_{ij}}{h_{p\,ij}} + Bo\cos\theta_i\right)\right)^{n_t+1} + \left(\frac{Pm}{\phi}\left(\frac{Su + p_{ij}}{h_{p\,ij}} + Bo\cos\theta_i\right)\right)^{n_t}\right], \tag{C.22}$$

$$\underbrace{h_{p\,ij}^{n_t+1} - \frac{\triangle t}{2}\left[\left(\frac{Pm}{\phi}\left(\frac{Su + p_{ij}}{h_{p\,ij}} + Bo\cos\theta_i\right)\right)^{n_t+1}\right]}_{\mathcal{L}_k^{h_p}} = h_{p\,ij}^{n_t} + \frac{\triangle t}{2}\left[\left(\frac{Pm}{\phi}\left(\frac{Su + p_{ij}}{h_{p\,ij}} + Bo\cos\theta_i\right)\right)^{n_t}\right]. \tag{C.23}$$

Rate of change of height of the droplet above the porous substrate is given by,

$$\frac{\partial h}{\partial t} = -\left[\frac{\partial}{\partial x}\left(\frac{h^3}{3}\left(C_1 - \frac{\partial p}{\partial x}\right)\right) + \frac{\partial}{\partial x}\left(\frac{h^3}{3}\left(-\frac{\partial p}{\partial x}\right)\right)\right] - \phi\frac{\partial h_p}{\partial t}. \tag{C.24}$$

Substitute the rate of change of penetration depth in the above equation,

$$\frac{\partial h}{\partial t} = -\left[\frac{\partial}{\partial x}\left(\frac{h^3}{3}\left(C_1 - \frac{\partial p}{\partial x}\right)\right) + \frac{\partial}{\partial y}\left(\frac{h^3}{3}\left(-\frac{\partial p}{\partial y}\right)\right)\right] - Pm\left(Bo\cos\theta_i + \frac{Su + p}{h_p}\right). \tag{C.25}$$

Spatial discretization the above equation gives,

$$\begin{aligned}\frac{\partial h_{ij}}{\partial t} = &-\frac{1}{\Delta x}\left\{\left(\frac{h^3_{i+1j} + h^3_{ij}}{2(3)}\right)\left(C_1 - \frac{p_{i+1j} - p_{ij}}{\Delta x}\right) - \left(\frac{h^3_{i-1j} + h^3_{ij}}{2(3)}\right)\left(C_1 - \frac{p_{ij} - p_{i-1j}}{\Delta x}\right)\right\} \\ &-\frac{1}{\Delta y}\left\{\left(\frac{h^3_{ij|+1} + h^3_{ij}}{2(3)}\right)\left(\frac{p_{ij} - p_{ij+1}}{\Delta y}\right) - \left(\frac{h^3_{ij-1+}h^3_{ij}}{2(3)}\right)\left(\frac{p_{ij-1} - p_{ij}}{\Delta y}\right)\right\} \\ &\underbrace{-Pm\left(Bo\cos\theta_i + \frac{Su + pij}{h_{pij}}\right)}_{\mathcal{F}_h^{n_t}}.\end{aligned} \tag{C.26}$$

Temporal discretization uses Crank-Nicolson scheme,

$$\frac{h_{ij}^{n_t+1} - h_{ij}^{n_t}}{\triangle t} = \frac{1}{2}\left[\mathcal{F}_h^{n_t+1} + \mathcal{F}_h^{n_t}\right]. \tag{C.27}$$

Re-arranging equation (C.27)

$$\underbrace{h_{ij}^{n_t+1} - \frac{\Delta t}{2}\left[\mathcal{F}_h^{n_t+1}\right]}_{\mathcal{L}_k^h} = h_{ij}^{n_t} + \frac{\Delta t}{2}\left[\mathcal{F}_h^{n_t}\right]. \tag{C.28}$$

Pressure in the droplet is given by,

$$p = -\nabla^2(h) - \Pi(h) + Bo\cos\theta_i\,(h). \tag{C.29}$$

Spatial discretization of the above equation is,

$$p_{ij} + \left(\frac{h_{i+1j} + h_{i-1j} - 2h_{ij}}{\triangle x^2}\right) + \left(\frac{h_{ij+1} + h_{ij-1} - 2h_{ij}}{\triangle y^2}\right) + \frac{(1 - cos\theta_e)\,(n_d - 1)\,(m_d - 1)}{\epsilon^2 h^*(n_d - m_d)} \left[\left(\frac{h^*}{h_{ij}}\right)^{n_d} - \left(\frac{h^*}{h_{ij}}\right)^{m_d}\right] - Bo\cos\theta_i(h_{ij}) = \mathcal{L}_k^p. \quad \text{(C.30)}$$

These equations may be written as,

$$\mathcal{L}_k^h\left(h_k^{n_t+1}, p_k^{n_t+1}, h_{p\,k}^{n_t+1}\right) = f_k^h\left(h_k^{n_t}, p_k^{n_t}, h_{p\,k}^{n_t}\right), \quad \text{(C.31)}$$

$$\mathcal{L}_k^{h_p}\left(p_k^{n_t+1}, h_{p\,k}^{n_t+1}\right) = f_k^{h_p}\left(p_k^{n_t}, h_{p\,k}^{n_t}\right), \quad \text{(C.32)}$$

$$\mathcal{L}_k^p\left(h_k^{n_t+1}, p_k^{n_t+1}\right) = f_k^p\left(p_k^{n_t}, h_k^{n_t}\right), \quad \text{(C.33)}$$

where the local Jacobian, J, which is given for a particular grid level, k, as,

$$J = \frac{\partial\left(\mathcal{L}_k^h, \mathcal{L}_k^p, \mathcal{L}_k^{h_p}\right)}{\partial\left(h_k^{n_t+1}, p_k^{n_t+1}, h_{p\,k}^{n_t+1}\right)}. \quad \text{(C.34)}$$

Initial guess to the solution is given by $\left(h_{0k}^{n_t+1}, p_{0k}^{n_t+1}, h_{p0\,k}^{n_t+1}\right)$, the Newton iteration proceeds by solving,

$$J\begin{pmatrix}\Delta h\\ \Delta p\\ \Delta h_p\end{pmatrix} = \begin{pmatrix} f_k^h - \mathcal{L}_k^h(h_{0k}^{n_t+1}, p_{0k}^{n_t+1}, h_{p0\,k}^{n_t+1}) \\ f_k^p - \mathcal{L}_k^p(h_{0k}^{n_t+1}, p_{0k}^{n_t+1}) \\ f_k^{h_p} - \mathcal{L}_k^{h_p}(p_{0k}^{n_t+1}, h_{p0\,k}^{n_t+1}) \end{pmatrix}. \quad \text{(C.35)}$$

Now, the terms of the Jacobian are calculated. Then from equation (C.30),

$$\frac{\partial \mathcal{L}_k^p}{\partial p_{ij}} = 1 = E, \quad \text{(C.36)}$$

$$\frac{\partial \mathcal{L}_k^p}{\partial h_{p\,ij}} = 0 = F, \quad \text{(C.37)}$$

$$\frac{\partial \mathcal{L}_k^p}{\partial h_{ij}} = \left(\frac{-2h_{ij}}{\triangle x^2}\right) + \left(\frac{-2h_{ij}}{\triangle y^2}\right) + \frac{(1 - \cos\theta_e)\,(n_d - 1)\,(m_d - 1)}{\epsilon^2 h^*(n_d - m_d)} \left[\frac{m_d}{h_{ij}}\left(\frac{h^*}{h_{ij}}\right)^{m_d} - \frac{n_d}{h_{ij}}\left(\frac{h^*}{h_{ij}}\right)^{m_d}\right] - Bo\cos\theta_i = D, \quad \text{(C.38)}$$

and from equation (C.23),

$$\frac{\partial \mathcal{L}_k^{h_p}}{\partial p_{ij}} = -\frac{\triangle t}{2}\left[\frac{Pm}{\phi}\left(\frac{1}{h_{p\,ij}}\right)\right] = H, \tag{C.39}$$

$$\frac{\partial \mathcal{L}_k^{h_p}}{\partial p_{ij}} = 1 - \frac{\triangle t}{2}\left[\frac{Pm}{\phi}\left(\frac{Su + p_{ij}}{h_{p\,ij}^2}\right)\right] = I, \tag{C.40}$$

$$\frac{\partial \mathcal{L}_k^{h_p}}{\partial h_{ij}} = 0 = G, \tag{C.41}$$

and from equation (C.28),

$$\begin{aligned}\frac{\partial \mathcal{L}_k^{h}}{\partial p_{ij}} = {} & \frac{\triangle t}{2}\left[\frac{1}{(\triangle x^2)}\left\{\left(\frac{h_{i+1j}^3 + h_{ij}^3}{6}\right) + \left(\frac{h_{i-1j}^3 + h_{ij}^3}{6}\right)\right\}\right] \\ & + \frac{\triangle t}{2}\left[\frac{1}{(\triangle y^2)}\left\{\left(\frac{h_{ij+1}^3 + h_{ij}^3}{6}\right) + \left(\frac{h_{ij-1}^3 + h_{ij}^3}{6}\right)\right\}\right] + \frac{\triangle t}{2}\left[Pm\left(\frac{1}{h_{p\,ij}}\right)\right] = B,\end{aligned} \tag{C.42}$$

$$\begin{aligned}\frac{\partial \mathcal{L}_k^{h}}{\partial h_{ij}} = 1 & - \frac{\triangle t}{2}\left[\frac{1}{(\triangle x)}\left(\frac{h_{ij}^2}{2}\left(\frac{p_{i+1j} + p_{ij}}{\triangle x}\right) - \frac{h_{ij}^2}{2}\left(\frac{p_{ij} + p_{i-1j}}{\triangle x}\right)\right)\right] \\ & - \frac{\triangle t}{2}\left[\frac{1}{(\triangle y)}\left(\frac{h_{ij}^2}{2}\left(\frac{p_{ij+1} - p_{ij}}{\triangle y}\right) - \frac{h_{ij}^2}{2}\left(\frac{p_{ij} + p_{ij-1}}{\triangle y}\right)\right)\right] = A,\end{aligned} \tag{C.43}$$

$$\frac{\partial \mathcal{L}_k^{h}}{\partial h_{p\,ij}} = -\frac{\triangle t}{2}\left[\frac{Pm}{\phi}\left(\frac{Su + p_{ij}}{h_{p\,ij}^2}\right)\right] = C, \tag{C.44}$$

Equation (C.35) can be expanded as,

$$\frac{\partial \mathcal{L}_k^{h}}{\partial h_{ij}}\Delta h + \frac{\partial \mathcal{L}_k^{h}}{\partial p_{ij}}\Delta p + \frac{\partial \mathcal{L}_k^{h}}{\partial h_{p\,ij}}\Delta h_p = f_k^h - \mathcal{L}_k^h\left(h_k^{n_t}, p_k^{n_t}, h_{p\,k}^{n_t}\right), \tag{C.45}$$

$$\frac{\partial \mathcal{L}_k^{p}}{\partial h_{ij}}\Delta h + \frac{\partial \mathcal{L}_k^{p}}{\partial p_{ij}}\Delta p + \frac{\partial \mathcal{L}_k^{p}}{\partial h_{p\,ij}}\Delta h_p = f_k^p - \mathcal{L}_k^p\left(h_k^{n_t}, p_k^{n_t}\right), \tag{C.46}$$

$$\frac{\partial \mathcal{L}_k^{h_p}}{\partial h_{ij}}\Delta h + \frac{\partial \mathcal{L}_k^{h_p}}{\partial p_{ij}}\Delta p + \frac{\partial \mathcal{L}_k^{h_p}}{\partial h_{p\,ij}}\Delta h_p = f_k^{h_P} - \mathcal{L}_k^{h_p}\left(h_{p\,k}^{n_t}, p_k^{n_t}\right). \tag{C.47}$$

So the equation (C.35) can be written as,

$$\begin{pmatrix} A & B & C \\ D & E & F \\ G & H & I \end{pmatrix}\begin{pmatrix} \Delta h \\ \Delta p \\ \Delta h_p \end{pmatrix} = \begin{pmatrix} f_k^h - \mathcal{L}_k^h(h_{0k}^{n_t+1}, p_{0k}^{n_t+1}, h_{0p\,k}^{n_t+1}) \\ f_k^p - \mathcal{L}_k^p(h_{0k}^{n_t+1}, p_{0k}^{n_t+1}) \\ f_k^{h_p} - \mathcal{L}_k^{h_p}(p_{0k}^{n_t+1}, h_{0p\,k}^{n_t+1}) \end{pmatrix}. \tag{C.48}$$

Equation (C.48) can be expanded with the values of $F = 0$ and $G = 0$,

$$A\Delta h + B\Delta p + C\Delta h_p = f_k^h - \mathcal{L}_k^h \left(h_k^{n_t}, p_k^{n_t}, h_{p\,k}^{n_t} \right), \tag{C.49}$$

$$D\Delta h + E\Delta p = f_k^p - \mathcal{L}_k^p \left(h_k^{n_t}, p_k^{n_t} \right), \tag{C.50}$$

$$H\Delta p + I\Delta h_p = f_k^{h_p} - \mathcal{L}_k^{h_p} \left(h_{p\,k}^{n_t}, p_k^{n_t} \right). \tag{C.51}$$

From equation (C.50),

$$\Delta p = E^{-1} \left(f_k^p - \mathcal{L}_k^p (h_k^{n_t}, p_k^{n_t}) - D\Delta h \right), \tag{C.52}$$

From equations (C.51) and (C.52),

$$HE^{-1} \left(f_k^p - \mathcal{L}_k^p \left(h_k^{n_t}, p_k^{n_t} \right) - D\Delta h \right) + I\Delta h_p = f_k^{h_p} - \mathcal{L}_k^p \left(h_{p\,k}^{n_t}, p_k^{n_t} \right), \tag{C.53}$$

$$\Delta h_p = I^{-1} \left(f_k^{h|_p} - \mathcal{L}_k^{h_p} \left(h_{p\,k}^{n_t}, p_k^{n_t} \right) - HE^{-1} \left(f_k^p - \mathcal{L}_k^p \left(h_k^{n_t}, p_k^{n_t} \right) - D\Delta h \right) \right). \tag{C.54}$$

From equations (C.49), (C.54) and (C.52),

$$\begin{aligned} &A\Delta h + BE^{-1}(f_k^p - \mathcal{L}_k^p(h_k^{n_t}, p_k^{n_t}) - D\Delta h) + \\ &CI^{-1} \left(f_k^{h_P} - \mathcal{L}_k^{h_p}(h_{p\,k}^{n_t}, p_k^{n_t}) - HE^{-1} \left(f_k^P - \mathcal{L}_k^p(h_k^{n_t}, p_k^{n_t}) - D\Delta h \right) \right) = f_k^h - \mathcal{L}_k^h \left(h_k^{n_t}, p_k^{n_t}, h_{p\,k}^{n_t} \right), \end{aligned} \tag{C.55}$$

$$\begin{aligned} \left(A - BE^{-1}D + CI^{-1}HDE^{-1} \right) \Delta h &= f_k^h - \mathcal{L}_k^h \left(h_k^{n_t}, p_k^{n_t}, h_{p\,k}^{n_t} \right) \\ &+ \left(CI^{-1}HE^{-1} - BE^{-1} \right) \left(f_k^p - \mathcal{L}_k^p(h_k^{n_t}, p_k^{n_t}) - D\Delta h \right) - CI^{-1} \left(f_k^{h_P} - \mathcal{L}_k^{h_P}(h_{p\,k}^{n_t}, p_k^{n_t}) \right). \end{aligned} \tag{C.56}$$

The equations (C.52), (C.54) and (C.56) are applied to the numerical code.

Bibliography

Acton, J. M., Huppert, H. E., and Worster, M. G. (2001). Two-dimensional viscous gravity currents flowing over a deep porous medium. *Journal of Fluid Mechanics*, 440:359–380.

Adam, C. D. (2012). Fundamental studies of bloodstain formation and characteristics. *Forensic Science International*, 219(1-3):76–87.

Adam, N. K. and Jessop, G. (1925). Angles of contact and polarity of solid surfaces. *J. Chem. Soc*, 127:1863–1868.

Ahmed, G., Sellier, M., Lee, Y., Jermy, M., and Taylor, M. (2013). Modeling the spreading and sliding of power-law droplets. *Colloids and Surfaces A: Physicochemical and Engineering Aspects*, 432:2–7.

Alleborn, N. and Raszillier, H. (2004a). Spreading and sorption of a droplet on a porous substrate. *Chemical Engineering Science*, 59(10):2071–2088.

Alleborn, N. and Raszillier, H. (2004b). Spreading and sorption of droplets on layered porous substrates. *Journal of Colloid and Interface Science*, 280(2):449–464.

Aradian, A., Raphael, E., and De Gennes, P. G. (1999). Dewetting on porous media with aspiration. *The European Physical Journal E*, 2(4):367–376.

Attinger, D., Moore, C., Donaldson, A., Jafari, A., and Stone, H. A. (2013). Fluid dynamics topics in bloodstain pattern analysis: Comparative review and research opportunities. *Forensic Science International*, 231(1-3):375–396.

Baskurt, O. K. and Meiselman, H. J. (2003). Blood rheology and hemodynamics. *Seminars In Thrombosis And Hemostasis*, 29(5):435–450.

Bertozzi, A. L. and Brenner, M. P. (1997). Linear stability and transient growth in driven contact lines. *Physics of Fluids*, 9(3):530–539.

Betelu, S. and Fontelos, M. (2003). Capillarity driven spreading of power-law fluids. *Applied Mathematics Letters*, 16(8):1315 – 1320.

Bevel, T. and Gardner, R. M. (2008). *Bloodstain pattern analysis: with an introduction to crime scene reconstruction*. CRC Press.

Biswas, G. and Gupta, A. (1987). Spreading of non-newtonian fluid drops on a horizontal plane. *Mechanics Research Communications*, 14(5-6):361–370.

Blake, T. D. (2006). The physics of moving wetting lines. *Journal of Colloid and Interface Science*, 299(1):1–13.

Bonn, D., Eggers, J., Indekeu, J., Meunier, J., and Rolley, E. (2009). Wetting and spreading. *Reviews of Modern Physics*, 81(2):739–805.

Brandt, A. (1982). Guide to multigrid development. *Lecture Notes in Mathematics*, 960:220–312.

Bremmer, R. H., De Bruin, K. G., Van Gemert, M. J. C., Van Leeuwen, T. G., and Aalders, M. C. G. (2012). Forensic quest for age determination of bloodstains. *Forensic Science International*, 216(1-3):1–11.

Brien, O. (2002). Theory and modeling of thin film flows. *Encyclopedia of Surface and Colloid Science*, 84(4):5283–5297.

Brutin, D., Sobac, B., Loquet, B., and Sampol, J. (2010). Patterns formation in drying drops of blood. *Journal of Fluid Mechanics*, 667:1.

Carré, A. and Eustache, F. (2000). Spreading kinetics of shear-thinning fluids in wetting and dewetting modes. *Langmuir*, 16(6):2936–2941.

Cazabat, A. M. and Stuart, M. A. C. (1986). Dynamics of wetting: effects of surface roughness. *Journal of Physical Chemistry*, 90(22):5845–5849.

Chen, J., Wang, J., Han, E., and Ke, W. (2008). Effects of dust and salt particles on the formation and spreading of micro-droplets on az91 magnesium alloy. *Corrosion Science*, 50(5):1449–1459.

Chhabra, R. and Richardson, J. (1999). *Non-Newtonian flow in the process industries: fundamentals and engineering applications*. Chemical, Petrochemical & Process. Butterworth-Heinemann.

Chien, S., Usami, S., Dellenback, R., Gregersen, M., Nanninga, L., and Guest, M. (1967). Blood viscosity: Influence of erythrocyte aggregation. *Science*, 157(3790):829–831.

Christov, C., Pontes, J., Walgraef, D., and Velarde, M. (1997). Implicit time splitting for fourth-order parabolic equations. *Computer Methods in Applied Mechanics and Engineering*, 148(96):1–18.

Chung, C. K., Chen, Y. S., and Shih, T. R. (2008). Fabrication and flow test of long-term hydrophilic fluidic chip without using any surface modification treatment. *Microfluidics and Nanofluidics*, 6(6):853–857.

Clarke, A., Blake, T. D., Carruthers, K., and Woodward, A. (2002). Spreading and imbibition of liquid droplets on porous surfaces. *Langmuir*, 18(8):2980–2984.

Council, N. R. (2009). *Strengthening Forensic Science in the United States: A Path Forward*. Committee on Identifying the Needs of the Forensic Sciences Community, National Research Council.

Dandapat, B. S. and Singh, S. K. (2010). Spreading of a non-newtonian liquid drop over a horizontal plane. *Chemical Engineering Science*, 65:3427–3430.

Daniels, N., Ehret, P., Gaskell, P., Thompson, H., and Decre, M. (2001). Multigrid methods for thin liquid film spreading flows. In Satofuka, N., editor, *Computational Fluid Dynamics 2000*, pages 279–284.

Davis, S. H. and Hocking, L. M. (1999). Spreading and imbibition of viscous liquid on a porous base. *Physics of Fluids*, 11(1):48–57.

Davis, S. H. and Hocking, L. M. (2000). Spreading and imbibition of viscous liquid on a porous base. ii. *Physics of Fluids*, 12(7):1646.

De Gennes, P. G. (1985). Wetting: statics and dynamics. *Rev. Mod. Phys.*, 57:827–863.

De Gennes, P.-G. (2001). Solvent evaporation of spin cast films: crust effects. *Eur Phy J E*, 7(1):8.

Dechelette, A., Sojka, P. E., and Wassgren, C. R. (2010). Non-newtonian drops spreading on a flat surface. *Journal of Fluids Engineering*, 132(10):101302.

Deegan, R., Bakajin, O., Dupont, T., Huber, G., Nagel, S., and Witten, T. (2000). Contact line deposits in an evaporating drop. *Physical Review E Statistical Physics Plasmas Fluids And Related Interdisciplinary Topics*, 62(1 Pt B):756–65.

Deegan, R. D., Bakajin, O., Dupont, T. F., Huber, G., Nagel, S. R., and Witten, T. A. (1997). Capillary flow as the cause of ring stains from dried liquid drops. *Nature*, 389(6653):827–829.

Denesuk, M., Smith, G. L., Zelinski, B. J. J., Kreidl, N. J., and Uhlmann, D. R. (1993). Capillary penetration of liquid droplets into porous materials. *Journal of colloid and*, 158(1):114–120.

Denning, A., Pre, D., and Watson, J. H. (1906). The viscosity of the blood. *Proceedings of the Royal Society of London. Series B,*, 78(526):pp. 328–358.

Deryagin, B. V. (1955). Kolloidn. zh. 17,191.

Desie, G., Allaman, S., Lievens, O., Anthonissen, K., and Soucemarianadin, A. (2002). Influence of substrate properties in drop on demand printing. *International Conference on Digital Printing Technologies, San Diego*, 18:360–365.

Dettre, R. and Johnson, R. (1964). Contact angle, wettability and adhesion. *Edited by F. M. Fowkes, Advances in Chemistry Series (Washington: American Chemical Society)*, 43:136.

Diez, J. A., Kondic, L., and Bertozzi, A. (2001). Global models for moving contact lines. *Physical Review E - Statistical, Nonlinear and Soft Matter Physics*, 63(1 Pt 1):011208.

Drochon, A. (2003). Rheology of dilute suspensions of red blood cells: experimental and theoretical approaches. *The European Physical Journal - Applied Physics*, 22(02):155–162.

Dussan V., E. B. (1985). On the ability of drops or bubbles to stick to non-horizontal surfaces of solids. part 2. small drops or bubbles having contact angles of arbitrary size. *Journal of Fluid Mechanics*, 151:1–20.

Dussan V., E. B. (1987). On the ability of drops to stick to surfaces of solids. part 3. the

influences of the motion of the surrounding fluid on dislodging drops. *Journal of Fluid Mechanics*, 174:381–397.

Dussan V., E. B. and Chow, R. T.-P. (1983). On the ability of drops or bubbles to stick to non-horizontal surfaces of solids. *Journal of Fluid Mechanics*, 137:1–29.

Dutelle, A. W. (2010). *An Introduction to Crime Scene Investigation*. Jones & Bartlett Publishers.

Ehrhard, P. and Davis, S. H. (1991). Non-isothermal spreading of liquid drops on horizontal plates. *Journal of Fluid Mechanics*, 229:365–388.

Elert, G. (1998). Volume of blood in a human. http://hypertextbook.com/facts/1998/LanNaLee.shtml.

Eley, R. R. (2012). *Paint and Coating Testing Manual: 15th Edition of the Gardner-Sward Handbook*. American Society for Testing & Materials, 2012, 2 edition. Rheology and Viscometry.

Eral, H. B., T Mannetje, D. J. C. M., and Oh, J. M. (2013). Contact angle hysteresis: a review of fundamentals and applications. *Colloid and Polymer Science*, 291(2):247–260.

Eres, M. H., Weidner, D. E., and Schwartz, L. W. (1999). Three-dimensional direct numerical simulation of surface-tension-gradient effects on the leveling of an evaporating multicomponent fluid. *Langmuir*, 15(5):1859–1871.

Extrand, C. W. and Kumagai, Y. (1995). Liquid drops on an inclined plane: The relation between contact angles, drop shape, and retentive force. *Journal of Colloid and Interface Science*, 170(2):515–521.

Fan, J., Wilson, M., and Kapur, N. (2011). Displacement of liquid droplets on a surface by a shearing air flow. *Journal of Colloid and Interface Science*, 356:286 – 292.

Fåhræus, R. and Lindqvist, T. (1931). The viscosity of the blood in narrow capillary tubes. *American Journal of Physiology – Legacy Content*, 96(3):562–568.

Frohn, A. and Roth, N. (2000). *Dynamics of Droplets*, volume 255. Springer.

Furmidge, C. G. L. (1962). Studies at phase interfaces. i. the sliding of liquid drops on solid surfaces and a theory for spray retention. *Journal Of Colloid Science*, 17(4):309–324.

Ganguly, A., Reza, M., and Gupta, A. S. (2012). Thin-film flow of a power-law fluid down an inclined plane. *Journal of Fluids Engineering-Transactions of the ASME*, 134(4):044502–1–5.

Gaskell, P. H., Jimack, P. K., Sellier, M., and Thompson, H. M. (2004). Efficient and accurate time adaptive multigrid simulations of droplet spreading. *International Journal for Numerical Methods in Fluids*, 45(11):1161–1186.

Gaskell, P. H., Jimack, P. K., Sellier, M., and Thompson, H. M. (2006). Flow of evaporating, gravity-driven thin liquid films over topography. *Physics of Fluids*, 18(1):013601.

Gaskell, P. H., Koh, Y. Y., Jimack, P. K., Lee, Y. C., and Thompson, H. M. (2009). Droplet migration: quantitative comparisons with experiment. *European Physical Journal-Special topics*, 1:117–120.

Gaskell, P. H., Lee, Y. C., and Thompson, H. M. (2010). Thin film flow over and around surface topography: a general solver for the long-wave approximation and related equations. *CMES-Computer Modeling in Engineering & Sciences*, 62(1):77–112.

Grant, R. (2001). Spray technique takes coating to higher levels. *Pulp & Paper International*, 43:12.

Gratton, J., Minotti, F., and Mahajan, S. M. (1999). Theory of creeping gravity currents of a non-newtonian liquid. *Physical Review E Statistical Physics Plasmas Fluids And Related Interdisciplinary Topics*, 60:6960–6967.

Hocking, L. (1981). Sliding and spreading of thin two-dimensional drops. *Quarterly Journal of Mechanics and Applied Mathematics*, 34(Feb):37–55.

Holbrook, M. (2010). Evaluation of blood deposition on fabric: Distinguishing spatter and transfer stains. *International Association Blood Pattern Analysts Newsletter*, 26-1:3–12.

Holman, R. K., Cima, M. J., Uhland, S. A., and Sachs, E. (2002). Spreading and infiltration of inkjet-printed polymer solution droplets on a porous substrate. *Journal of Colloid and Interface Science*, 249(2):432 – 440.

Howison, S. D., Moriarty, J. A., Ockendon, J. R., Terrill, E. L., and Wilson, S. K. (1997). A mathematical model for drying paint layers. *Journal of Engineering Mathematics*, 32(4):377–394.

Hussain, M., Kar, S., and Puniyani, R. (1999). Relationship between power law coefficients and major blood constituents affecting the whole blood viscosity. *Journal of Biosciences*, 24(3):329–337.

Iyer, R. R. and Bousfield, D. W. (1996). The leveling of coating defects with shear thinning rheology. *Chemical Engineering Science*, 51(20):4611 – 4617.

James, S. H., Kish, P. E., and Sutton, T. P. (2005). *Principles of bloodstain pattern analysis: theory and practice*. CRC Press.

Johnson, R. E. and Dettre, R. H. (1963). Contact angle hysteresis. iii. study of an idealized heterogeneous surface. *Journal of Physical Chemistry*, 107(43):1744–1750.

Karger, B., Rand, S. P., and Brinkmann, B. (1998). Experimental bloodstains on fabric from contact and from droplets. *International Journal of Legal Medicine*, 111:17–21.

Keunings, R. and Bousfield, D. W. (1987). Analysis of surface tension driven leveling in horizontal viscoelastic films. *J. Non-Newtonian Fluid Mech*, 22:219–233.

Kheshgi, H.S.; Scriven, L. (1988). The evolution of disturbances in horizontal films. *Chemical Engineering Science*, 43:793–801.

Kim, H., Lee, H., and Kang, B. (2002). Sliding of liquid drops down an inclined solid surface. *Journal of Colloid and Interface Science*, 247(2):372–380.

Le Grand, N., Daerr, A., and Limat, L. (2005). Shape and motion of drops sliding down an inclined plane. *Journal of Fluid Mechanics*, 541(1):293.

Lee, Y. C., Thompson, H. M., and Gaskell, P. H. (2007). An efficient adaptive multigrid algorithm for predicting thin film flow on surfaces containing localised topographic features. *Computers & Fluids*, 36(5):838 – 855.

Lee, Y. C., Thompson, H. M., and Gaskell, P. H. (2009). Filmpar: A parallel algorithm designed for the efficient and accurate computation of thin film flow on functional surfaces containing micro-structure. *Computer Physics Communications*, 180(12):2634 – 2649.

Lee, Y. C., Thompson, H. M., and Gaskell, P. H. (2011). Three-dimensional thin film and droplet flows over and past surface features with complex physics. *Computers & Fluids*, 46(1):306 – 311.

Livescu, S., Roy, R. V., and Schwartz, L. W. (2011). Leveling of thixotropic liquids. *Journal of non-Newtonian Fluid Mechanics*, 166(7-8):395–403.

Lomas, H. (1970). Calculation of advancing and receding contact angles i. drops on inclined planes. *Interface*, 33(August):548–553.

MacDonell, H. (2005). *Bloodstain Patterns, 2nd ed.* Laboratory of Forensic Sciences, Corning, NY, USA.

MacDonell, H. and Bialousz, L. (1971). Flight characteristics and stain patterns of human blood. *Report to the National Institute of Law Enforcement and Criminal Justice, US Dept of Justice, Law Enforcement Assistance Administration, Washington, DC.*

Merrill, E. (1969). Rheology of blood. *Physiological Reviews*, 49(4):863–&.

Murphy, J. (1968). Rs/t/31/68. Technical report, Paint Research Association Internal Report.

Myers, T. G. (1998). Thin films with high surface tension. *SIAM Review*, 40(3):441–462.

Myers, T. G. (2005). Application of non-newtonian models to thin film flow. *Physical Review E - Statistical, Nonlinear and Soft Matter Physics*, 72(6 Pt 2):066302.

Nguetchue, S. N. N. and Momoniat, E. (2008). Axisymmetric spreading of a thin power-law fluid under gravity on a horizontal plane. *Nonlinear Dynamics*, 52(4):361–366.

Okuzono, T., Kobayashi, M., and Doi, M. (2009). Final shape of a drying thin film. *Physical Review E - Statistical, Nonlinear and Soft Matter Physics*, 80(2 Pt 1):021603.

Orchard, S. (1963). On surface levelling in viscous liquids and gels. *Applied Scientific Research*, 11(4):451–464.

Oron, A., Davis, S. H., and Bankoff, S. G. (1997). Long-scale evolution of thin liquid films. *Rev. Mod. Phys.*, 69:931–980.

Overdiep, W. S. (1986). The levelling of paints. *Coatings*, 14:159–175.

Pan, C., Luo, L. S., and Miller, C. T. (2006). An evaluation of lattice boltzmann schemes for porous medium flow simulation. *Computers and Fluids*, 35(8-9):898–909.

Perazzo, C. A. and Gratton, J. (2003). Thin film of non-newtonian fluid on an incline. *Phys. Rev. E*, 67:016307.

Pizzola, P. A., Roth, S., and De Forest, P. R. (1986). Blood droplet dynamics–i. *Journal of Forensic Sciences*, 31(1):36–49.

Podgorski, T., Flesselles, J. M., and Limat, L. (2001). Corners, cusps, and pearls in running drops. *Physical Review Letters*, 87(3):1–4.

Pomeau, Y. (2002). Recent progress in the moving contact line problem: a review. *Comptes Rendus Mecanique*, 330(3):207–222.

Rafaï, S., Bonn, D., and Boudaoud, A. (2005). Spreading of non-newtonian fluids and surfactant solutions on solid surfaces. *Journal of Fluid Mechanics*, 358(1):58–67.

Raymond, M., Smith, E., and Liesegang, J. (1996). The physical properties of blood - forensic considerations. *Science & Justice*, 36(3):153–160.

Rein, M. (1993). Phenomena of liquid drop impact on solid and liquid surfaces. *Fluid Dynamics Research*, 12(2):61–93.

Reynolds, O. (1886). On the theory of lubrication and its application to mr. beauchamp tower's experiments, including a experimental determination of the viscosity of olive oil. *Philosophical Transactions of the Royal Society of London*, 177(1886):157–234.

Roache, P. (1998a). *Computational Fluid Dynamics*. Hermosa Pub.

Roache, P. (1998b). *Verification and Validation in Computational Science and Engineering*. Hermosa Pub.

Savva, N., Kalliadasis, S., and Pavliotis, G. A. (2010). Two-dimensional droplet spreading over random topographical substrates. *Physical Review Letters*, 104(8):084501.

Schwartz, L., Roux, D., and Cooper-White, J. (2005). On the shapes of droplets that are sliding on a vertical wall. *Physica D*, 209:236–244.

Schwartz, L. W. (1998). Hysteretic effects in droplet motions on heterogeneous substrates: Direct numerical simulation. *Langmuir*, 14(12):3440–3453.

Schwartz, L. W. (1999). Theoretical and numerical modeling of coating flow on simple and complex substrates including theology, drying and marangoni effects. *Advances in Coating and Drying of Thin Films*, pages 105–128.

Schwartz, L. W. and Eley, R. R. (1998). Simulation of droplet motion on low-energy and heterogeneous surfaces. *Journal of Colloid and Interface Science*, 202(1):173 – 188.

Schwartz, L. W., Roy, R. V., Eley, R. R., and Petrash, S. (2001). Dewetting patterns in a drying liquid film. *Journal of Colloid and Interface Science*, 234(2):363–374.

Sellier, M. (2003). *The Numerical Simulation of thin film flow over heterogeneous substrates.* PhD thesis, University of Leeds.

Sellier, M., Baechtel, G., and Taylor, M. (2010). Towards modelling bloodstain formation. In *17th Australasian Fluid Mechanics Conference, Auckland, New Zealand.*

Sellier, M., Nock, V., Gaubert, C., and Verdier, C. (2013). Droplet actuation induced by coalescence: Experimental evidences and phenomenological modeling. *The European Physical Journal Special Topics*, 219(1):131–141.

Sellier, M., Nock, V., and Verdier, C. (2011). Self-propelling, coalescing droplets. *International Journal of Multiphase Flow*, 37(5):462–468.

Seppecher, P. (1996). Moving contact lines in the cahn-hilliard theory. *Science*, 34(9):977–992.

Shaler, R. C. (2011). *Crime Scene Forensics: A Scientific Method Approach.* CRC Press (Taylor & Francis Group).

Sikalo, S., Wilhelm, H. D., Roisman, I. V., Jakirlic, S., and Tropea, C. (2005). Dynamic contact angle of spreading droplets: Experiments and simulations. *Physics of Fluids*, 17(6):062103.

Siregar, D. P., Kuerten, J. G. M., Wijshoff, H. M. A., and van der Linden, L. T. M. (2010). Numerical simulation of the absorption of a droplet in a porous medium. In Vafai, K., editor, *Porous Media and its Applications in Science, Engineering and Industry*, volume 1254 of *AIP Conference Proceedings*, pages 135–140.

Skelland, A. (1967). *Non-Newtonian flow and heat transfer.* Wiley.

Slemko, J. A. (2003). Bloodstains on fabrics: The effect of droplet velocity and fabric composition. *International Association Blood Pattern Analysts Newsletter*, 19(4):3–11.

Sochi, T. (2010). Non-newtonian flow in porous media. *Polymer*, 51(22):5007 – 5023.

Spaid, M. A. and Homsy, G. M. (1996). Stability of newtonian and viscoelastic dynamic contact lines. *Physics of Fluids*, 8(2):460.

Starov, V., Kostvintsev, S., Sobolev, V., Velarde, M., and Zhdanov, S. (2002). Spreading of liquid drops over dry porous layers: Complete wetting case. *Journal of Colloid and Interface Science*, 252(2):397 – 408.

Starov, V. M., Tyatyushkin, A. N., Velarde, M. G., and Zhdanov, S. A. (2003). Spreading of non-newtonian liquids over solid substrates. *Journal of Colloid and Interface Science*, 257(2):284–290.

Steinberg, S. and Roache, P. J. (1985). Symbolic manipulation and computational fluid dynamics. *Journal of Computational Physics*, 57(2):251–284.

Stoiber, B., Zach, C., Izay, B., and Windberger, U. (2005). Whole blood, plasma viscosity, and erythrocyte aggregation as a determining factor of competitiveness in standard bred trotters. *Clin Hemorheol Microcirc*, 32(1):31–41.

Szeri, A. (2010). *Fluid Film Lubrication*. Cambridge University Press.

Thiele, U., Neuffer, K., Bestehorn, M., Pomeau, Y., and Velarde, M. G. (2002). Sliding drops on an inclined plane. *Colloids and Surfaces A Physicochemical and Engineering Aspects*, 206(1-3):87–104.

Thiriet, M. (2008). *Biology and Mechanics of Blood Flows Part II: Mechanics and Medical Aspects*. Springer.

Thurston, G. B. (1979). Rheological parameters for the viscosity, viscoelasticity, and thixotropy of blood. *Biorheology*, 16:149–162.

Thurston, G. B. and Henderson, N. M. (2006). Effects of flow geometry on blood viscoelasticity. *Biorheology*, 43(6):729–746.

Timmons, C. O. and Zisman, W. A. (1966). The effect of liquid structure on contact angle hysteresis. *Science*, 171(2):165–171.

Tsai, B., Carvalho, M. S., and Kumar, S. (2010). Leveling of thin films of colloidal suspensions. *Journal of Colloid and Interface Science*, 343(1):306–313.

Vellingiri, R., Savva, N., and Kalliadasis, S. (2011). Droplet spreading on chemically heterogeneous substrates. *Phys. Rev. E*, 84:036305.

Wang, X. D., Lee, D. J., Peng, X. F., and Lai, J. Y. (2007a). Spreading dynamics and dynamic contact angle of non-newtonian fluids. *Langmuir The Acs Journal Of Surfaces And Colloids*, 23(15):8042–8047.

Wang, X. D., Zhang, Y., Lee, D. J., and Peng, X. F. (2007b). Spreading of completely wetting or partially wetting power-law fluid on solid surface. *Langmuir The Acs Journal Of Surfaces And Colloids*, 23(18):9258–9262.

Warner, M. R. E., Craster, R. V., and Matar, O. K. (2002). Dewetting of ultrathin surfactant-covered films. *Physics of Fluids*, 14(11):4040.

Weidner, D. E., Schwartz, L. W., and Eley, R. R. (1996). Role of surface tension gradients in correcting coating defects in corners. *Journal of Colloid and Interface Science*, 179(1):66–75.

Wilson, S. (1993). The leveling of paint films. *IMA Journal of Applied Mathematics*, 50(2):149–166.

Yeleswarapu, K, K. (1996). *Evaluation of Continuum Models for Characterizing the Constitutive Behavior of Blood*. PhD thesis, University of Pittsburgh.

Young, T. (1805). An essay on the cohesion of fluids. *Philosophical Transactions of the Royal Society of London*, 95(1805):65–87.

Young, T. (1809). The croonian lecture. on the functions of the heart and arteries. *Philosophical Transactions*, 99:1–31.

Zadrazil, A., Stepanek, F., and Matar, O. K. (2006). Droplet spreading, imbibition and solidification on porous media. *Journal of Fluid Mechanics*, 562:1–33.

Zhang, J.-B. and Kuang, Z.-B. (2000). Study on blood constitutive parameters in different blood constitutive equations. *Journal of Biomechanics*, 33(3):355 – 360.

Zografi, G. and Johnson, B. A. (1984). Effects of surface roughness on advancing and receding contact angles. *International Journal of Pharmaceutics*, 22:159–176.